FRACTIONAL ORDER MODELS FOR VIBRATION AND WAVE PROPAGATION APPLICATIONS

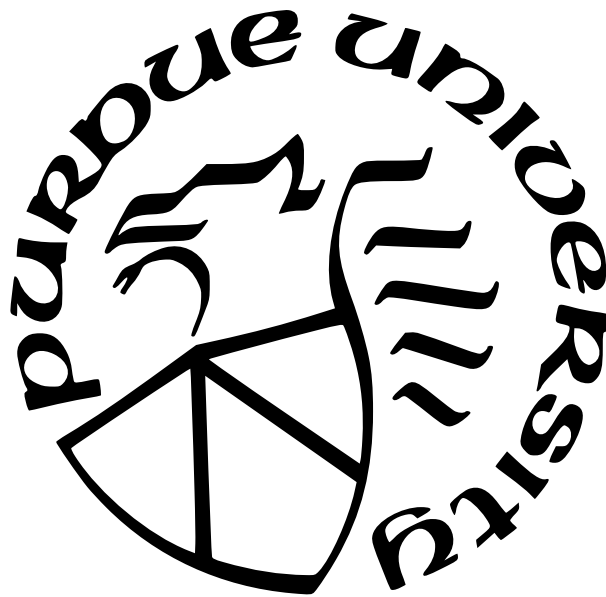by

John Hollkamp

A Dissertation

Submitted to the Faculty of Purdue University

In Partial Fulfillment of the Requirements for the degree of

Doctor of Philosophy

School of Mechanical Engineering

West Lafayette, Indiana

May 2021

My dissertation is dedicated to my parents, Joe & Cathy Hollkamp, as well as my wife

Katherine Hollkamp

ACKNOWLEDGMENTS

TABLE OF CONTENTS

LIST OF TABLES

LIST OF FIGURES

11

12

13

ABBREVIATIONS

1D	one-dimensional
2D	two-dimensional
3D	three-dimensional
ABH	acoustic black hole
BC	boundary condition
DOF	degree of freedom
EOM	equation of motion
FC	fractional calculus
FD	finite difference
FE	finite element
f-FEM	fractional finite element method
FFT	fast Fourier transform
F-NDOF	fractional multiple degree of freedom
F-SDOF	fractional single degree of freedom
GDE	governing differential equation
IC	initial condition
I-MDOF	integer multiple degree of freedom
I-SDOF	integer single degree of freedom
ML	Mittag-Leffler
MOR	model order reduction
RC	Riesz-Caputo
RL	Riemann-Liouville
RMS	root-mean-square
TF	transfer function
TM	transfer matrix
VO	variable order
WKB	Wentzel-Kramers-Brillouin

ABSTRACT

The continuously growing interest in the design and synthesis of heterogeneous structures has further highlighted the need for accurate modeling and efficient simulation techniques. In the context of structural dynamics and elastic wave propagation simulations, theoretical models can be broadly divided into two main categories: discrete and continuous. Discrete parameter models, such as finite difference or finite element analysis, not only provide a simplified representation of complex systems, but also are some of the most powerful structural computational techniques available to-date. In the case of geometrically complex and heterogeneous structures, this class of techniques typically produces numerical models involving a large number of degrees of freedom, ultimately leading to significant computational times and resources. Historically, model order reduction techniques have been one of the most powerful tools to reduce the number of degrees of freedom while maintaining high levels of accuracy and fidelity. On the other hand, continuous parameter models can provide a more accurate and concise representation of the actual physical system, but the underlying mathematical formulation (typically based on partial differential equations with variable coefficients) is typically not well suited to analytical solutions, especially for systems containing complex geometries and boundary conditions. Homogenization techniques are an important class of models that can overcome some of these complexities while still preserving the ability to provide a concise mathematical representation and, possibly, analytical closed-form solutions. Despite the significant advancements and the many successes that the engineering community has achieved in the development of these two classes of methods, both categories still encounter various limitations including, but not limited to, narrow-band frequency accuracy, applicability in the long wavelength regime, and still potentially expensive numerical evaluations. The emergent mathematical field of fractional calculus - the calculus of integrals and derivatives of any real or complex order - provides an excellent opportunity to develop novel, accurate, and efficient models for simulations of heterogeneous structures. Fractional operators, possessing characteristics such as memory effects, nonlocality, multi-scale capabilities, and hybrid behavior, can provide advanced mathematical tools to address the shortcomings of commonly used model order reduction and homogenization techniques. This dissertation

specifically explores the feasibility and potential of fractional calculus to overcome some of the most significant limitations of discrete and continuous parameter methods with specific application to the vibration and wave propagation analysis of structural systems. From the perspective of discrete parameter models, model order reduction methodologies based on time fractional differential equations are presented. The use of a frequency-dependent fractional order is capable of simultaneously delivering high accuracy and high levels of reduction across a wide frequency spectrum. On the other hand, for the case of continuous parameter systems, the research explores how space fractional operators can lead to alternative forms of homogenization for partial order differential equations with application to wave propagation in heterogeneous structures. Specific applications to one-dimensional elastic metamaterials and structural components embedded with acoustic black holes are presented. The physical interpretation, potential, benefits, and even limitations of the developed fractional models are examined in-depth.

1. INTRODUCTION

This dissertation explores novel mathematical models to represent the vibration and wave propagation response of heterogeneous structures. Heterogeneous structures are characterized by spatial variations of either their material or geometrical configuration. Advancements in design and manufacturing techniques have enabled the fabrication of elaborate heterogeneous structures having material and topological properties that were previously unobtainable only a few years ago. As an example, advancements in additive manufacturing technologies have led to the fabrication of composite materials with functionally graded properties as well as the synthesis of porous structures whose pore size can be manipulated across multiple scales. Heterogeneous structures are utilized in engineering thanks to their ability to deliver diverse static and dynamic mechanical properties. For example, a composite material comprised of reinforced fibers can significantly increase the strength and durability compared to its individual constituents. Other composites, such as ceramic matrix composites, reduce the weight of structural components while still meeting, or even improving upon, their performance requirements. The geometry of a heterogeneous structure can be crafted to produce unique dynamical behaviors which can further advance the performance of structural systems. As a result, the modeling and simulation of the vibration and wave propagation in heterogeneous structures is critical to understanding their dynamical behavior and to designing structures that meet challenging engineering requirements or function in extreme and difficult environments. Such models typically use numerical and computational methodologies to represent the structure's intrinsic complexities and to accurately simulate their dynamical behavior. Accurate and computationally efficient models can greatly assist in the design process before constructing physical models or prototypes for experimentation or practical implementation. Thus, advanced modeling and simulation techniques can save much time and resources, and can provide a competitive advantage as well.

Representations of heterogeneous structures include both continuous and discrete models. Continuous representations of heterogeneous structures analyze their governing differential equations and seek to obtain either exact or approximate closed-form solutions accurately describing the dynamics. However, many of the partial differential equations governing the

dynamics of heterogeneous structures do not have known analytical solutions. Nonetheless, the dynamic behavior of continuous structures can be studied using methods such as perturbation techniques or homogenization to avoid relying on the potentially numerically expensive discrete models. Homogenization is a popular approach since the heterogeneous structure is instead represented by a homogeneous structure exhibiting the same dynamic content. In some cases, homogenization techniques produce closed-form analytical solutions of the dynamics since the solution to a homogeneous, constant coefficient differential equation is typically more attainable.

On the other hand, discretization methodologies, such as the finite element method [1]–[5], represent a continuous structure by dividing it into a set of nodal points, also called degrees of freedom (DOF). Usually, the more complex the property spatial distribution (e.g., external loads, material or geometric parameters, boundary conditions), the higher the level of discretization needed to achieve a satisfactory representation of the continuum system. As a result, discrete models of heterogeneous structures often require a large number of degrees of freedom. This high level of discretization for heterogeneous structures leads to a tradeoff between computational time and accuracy of the dynamic response. As a result, the level of achievable accuracy of simulations for heterogeneous structures is limited. In response to this, model order reduction (MOR) methodologies for discrete lumped-parameter systems have been created to maintain accuracy while reducing computational cost. These model order reduction techniques are pivotal for large structural assemblies, such as automobiles, aircraft, buildings and bridges, heating and cooling devices, and bio-mechanical equipment, which can contain many different heterogeneous substructures. The number of DOFs in these large structural assemblies can be on the order of thousands or even more. Design and optimization of these large DOF assemblies requires a thorough understanding of the interactions and connections of the different components and subsystems.

1.1 Approaches to Reduce Model Complexity

1.1.1 Model Order Reduction

As mentioned, discretization approaches including finite difference and finite elements represent a heterogeneous structure or a large structural assembly by a mesh of the degrees of freedom. The discretization of these systems typically takes a form similar to

$$\mathbf{M}\{\ddot{x}\} + \mathbf{K}\{x\} = \{F\}, \tag{1.1}$$

where $\mathbf{M}$ is a NxN inertia matrix, $\mathbf{K}$ is a NxN stiffness matrix, $\{F\}$ is a Nx1 forcing vector, $\{x\}$ is the displacement vector of the generalized coordinates, and N is the number of DOFs. As the level of heterogeneity increases, the number of DOFs increases and so does the order of the system (i.e., the number of ordinary differential equations governing their motion). As N increases, the amount of computational time to evaluate the solutions to the equations increases. If the computational time becomes unreasonable, the number of DOFs must be decreased, reducing the accuracy of model. In response, model order reduction methodologies have been developed to maintain high numerical accuracy and fidelity to the dynamics while reducing the number of degrees of freedom and as a result, the computational time. Model order reduction attempts to represent the essential features of a structure by focusing on the response at selected locations (the active DOFs) such that the DOFs associated with the remaining locations can be omitted. The reduction procedure, exhibited in Fig. 1.1, is not trivial because it must account for the coupling between active and omitted DOFs in order to not change the underlying response of the system. According to [6], model order reduction techniques have typically focused on three main fields: structural dynamics, systems and control, and numerical mathematics. This section specifically considers model order reduction techniques implored in structures (see [6]–[9]) while discussion of MOR techniques in controls and mathematics, including the asymptotic waveform evaluation, Padé-via-Lanczos, truncation methods, and rational interpolation are left to [6], [10].
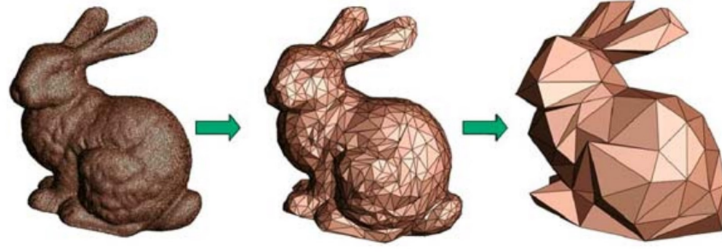
Figure 1.1. Illustration of the concept of model order reduction (Graphics credit: [10] ©2008 Springer).

Structural Model Order Reduction Techniques

To illustrate the concepts of structural model order reduction, this section first presents Guyan reduction [11], [12], also known as static condensation, as the prototypical example of model order reduction. Considering the discrete rabbit model in Fig. 1.1, the left-most rabbit is a fine discretization consisting of degrees of freedom to be retained (the active degrees of freedom) and degrees of freedom to be deleted (the omitted degrees of freedom). Guyan reduction does not account for the system's inertia; instead, it considers the static equation

$$\mathbf{K}\{x\} = \{F\}. \tag{1.2}$$

To reduce the order of the system, Guyan reduction expresses Eq. (1.2) as

$$\begin{bmatrix} \mathbf{K_{AA}} & \mathbf{K_{AO}} \\ \mathbf{K_{OA}} & \mathbf{K_{OO}} \end{bmatrix} \begin{bmatrix} \{x_A\} \\ \{x_O\} \end{bmatrix} = \begin{bmatrix} \{F_A\} \\ \{F_O\} \end{bmatrix}, \tag{1.3}$$

where the subscript A indicates active DOFs and O implies omitted DOFs. Assuming that the forces on the omitted degrees of freedom are zero, the second equation in Eq. (1.3) can be written for the displacements of the omitted DOFs as

$$\{x_O\} = -\mathbf{K_{OO}}^{-1}\mathbf{K_{OA}}\{x_A\}. \tag{1.4}$$

Equation (1.4) thus relates the displacements of the omitted DOFs to the active DOFs. Substituting Eq. (1.4) into Eq. (1.3) yields

$$(\mathbf{K_{AA}} - \mathbf{K_{OO}}^{-1}\mathbf{K_{OA}})\{x_A\} = \{F_A\}. \tag{1.5}$$

The above system of linear equations is equivalent to Eq. (1.3), but is expressed in terms of the active DOFs alone. Thus, Guyan reduction reduces system (the left-most rabbit in Fig. 1.1) by condensing the omitted DOFs (producing the right-most rabbit in Fig. 1.1) while accounting for the relationship between the active and omitted DOFs. This dissertation aims to condense a discrete model in a manner similar to Guyan reduction, but focuses on dynamic reduction. A majority of structural dynamic MOR techniques are based in the modal domain and can be categorized into two classes: global mode superposition [6] and component mode synthesis [7], [9]. Both classes of modal MOR techniques rely on the expansion theorem [13] which gives the displacement of each DOF as a superposition of the eigenvectors of the entire structure. In equation form, this is

$$\{x\} = \sum_{j=1}^{N} \eta_j(t)\{X_j\}, \tag{1.6}$$

where $\{x\}$ is a vector of the nodal displacements, η_j is a modal coordinate, and $\{X_j\}$ is one of the N linearly independent and orthogonal eigenvectors describing the displacement shape of the structure.

The mode displacement MOR reviewed in [6] extracts a limited number P (where $P < N$) of the eigenvectors and eigenfrequencies of the discretized system that can still accurately represent the displacements of the active DOFs. Typically the first P eigenvectors corre-

sponding to eigenfrequencies less than a frequency of interest are retained. In this way, the number of DOFs utilized in the modal basis is reduced, thereby decreasing computational expenses while still retaining the desired accuracy of the displacement. [6] presents two more expansions of this mode superposition reduction method called the mode acceleration method and the mode truncation augmentation method, both of which add a correction vector to the expansion; that is,

$$\{x\} = \sum_{j=1}^{P} \eta_j(t)\{X_j\} + \{x_{\text{cor}}\}. \tag{1.7}$$

In the mode acceleration method, the correction term $\{x_{\text{cor}}\}$ is the static displacement of the active DOFs while $\{x_{\text{cor}}\}$ in the mode truncation augmentation method is a weighted form of the static response.

Component mode synthesis reduction techniques divide the structure into multiple components on which the model order reduction is individually performed, as depicted in Fig. 1.2. As stated by [7], the order reduction of each structural component has multiple advantages, including the effective evaluation of the dynamic behavior of large structural assemblies, identification of local dynamic behavior, the elimination of the evaluation of components which have little to no influence on the overall behavior of the assembled structure, and the ability to dynamically combine modeled parts that have been obtained through different means such as analytical or experimental. Component mode synthesis methodologies require the several substructures to be compatible along their shared boundaries (see Fig. 1.2). Additionally, the MOR must implement a force equilibrium condition along the substructures' interfaces.

One of the most popular component mode synthesis techniques is the Craig-Bampton method [8], [14]. The Craig-Bampton method combines the motion of these boundary points along the shared interface of the substructures with their displacement modes (known as constraint modes). As a result, the dynamics of the system can be reduced to a set of both fixed interface and constraint modes [15]. Additionally, the Craig-Bampton method uses the static modes of the substructures similar to the mode acceleration method and the mode
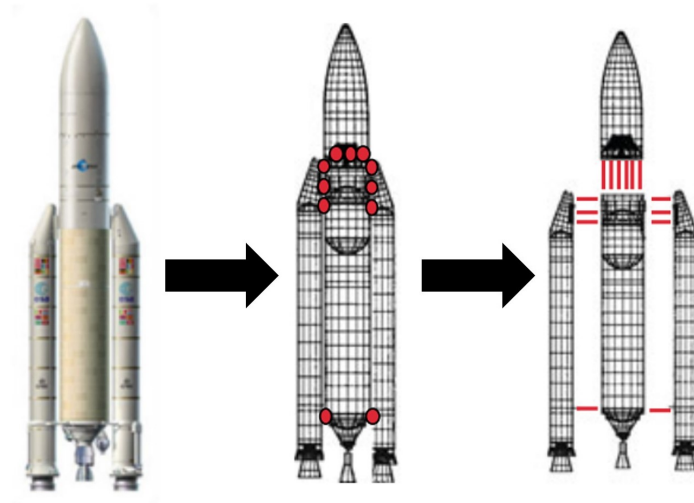
Figure 1.2. Illustration of the dynamic substructuring in component mode synthesis MOR (Graphics credit: [9] ©2019 Springer).

truncation augmentation method. The nearly diagonal reduced mass and stiffness matrices of the Craig-Bampton method lead to efficient computational implementation [7].

Limitations

Despite the advancements of modal superposition and component mode synthesis structural MOR techniques, they still encounter a variety of limitations, as summarized in [6]. These include

- Reduced accuracy for heavily damped structures,

- Decreased accuracy when two resonance frequencies are close to each other,

- The high computational expenses of the determining the eigenvectors for large systems,

- The truncation of the number of eigenvectors used in the modal basis, limiting the accuracy of the reduction to a narrow-band frequency range,

- An a priori selection of the number of retained eigenvectors needed for a desired level of accuracy.

1.1.2 Homogenization Techniques

Homogenization techniques reduce the order of the continuous model by formulating a corresponding homogeneous model via an analytical continuum approach that exhibits the same static or dynamic content as the heterogeneous structure [16]–[23]. Homogenization is a limit theory which uses periodicity, averaging, and asymptotic expansions to replace governing differential equations containing variable coefficients with differential equations possessing constant, or slowly varying, coefficients whose solution approximately represents the behavior of the original heterogeneous medium [19]. Homogenization formulations intrinsically perform averaging operations of the spatially varying material and geometrical properties and leverage specifically crafted convolution kernels to obtain either the homogenized material properties or corrections to the first or second-order homogenized properties. The quantities describing the homogenized models are known as effective properties. By representing the heterogeneous medium as a homogeneous material, computational costs arising from complex geometries, material distributions, interfaces, boundary conditions, and multiple size scales can typically be reduced.

A large class of heterogeneous structures are composite materials, which are materials possessing differing constituents that occupy different regions of the structure [19]. The regular heterogeneity of the composite structure permits the representation of the entire structure as a periodic assembly of a representative volumetric element, also called a unit cell [19], [21]. It is the composition and behavior of the unit cells from which the effective properties of the corresponding homogeneous structure are derived [18], [21]. The homogenization process from the periodic unit cells is illustrated by Fig. 1.3.

Categories of Homogenization Techniques

Broadly speaking, [17] categorizes homogenization theories, also called effective medium theories for composite structures, into four groups: direct homogenization, indirect homogenization, variational methodologies, and mathematical homogenization. In direct homogenization techniques, the average quantities of the microscopic fields of the unit cell, such as stress, strain, displacement, or energy density, are calculated via surface or volume integrals.
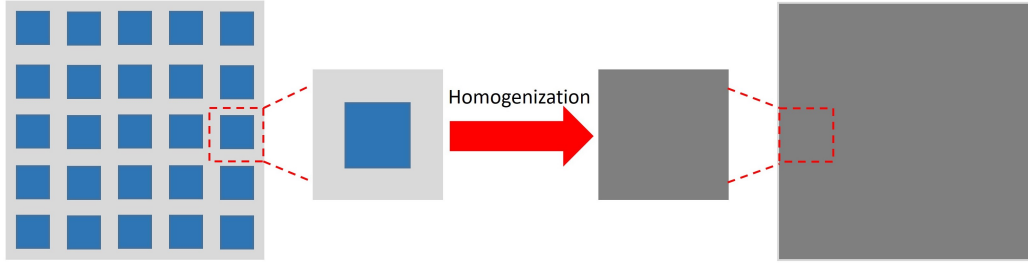
Figure 1.3. Illustration of the concept of homogenization, where the periodic structure is represented by an isotropic, homogeneous material whose effective material properties are chosen so that the dynamics of the two media are equivalent.

The average quantities from the unit cells are then set as the effective properties governing the macroscopic behavior of the homogeneous representation. However, as noted by [16], application of direct homogenization methods, although often used, can produce erroneous models since they fail to consider factors such as localized interactions between various components and the geometrical arrangement and orientation of the unit cell. This has led to the development of indirect methods, which, rather than using the average of quantities, calculate the effective properties by using the volume fraction, geometry orientation, and mechanical properties of each individual component. The third class of homogenization techniques are called variational methods. These homogenization techniques give theoretical upper- and lower-bounds on the values of the effective properties.

As an example, the "rule of mixtures" approach is a variational homogenization method for composites based on a weighted mean of each component's mechanical properties and their percent volume of the total structure [24]–[26]. The rule of mixtures provides a theoretical upper- and lower-bound of the effective mechanical properties depending on if the composite's constitutive components are subjected to uniform strain (Voigt model in Fig. 1.4(a)) or uniform stress (Reuss model in Fig. 1.4(b)). The gray portions in Fig. 1.4 are designated as material #1 while the blue sections are material #2. As seen in the Voigt model in Fig. 1.4(a), the load on the system is applied such that materials #1 and #2 are subject to the same strain. That is, using Hooke's law for uniaxial tension,
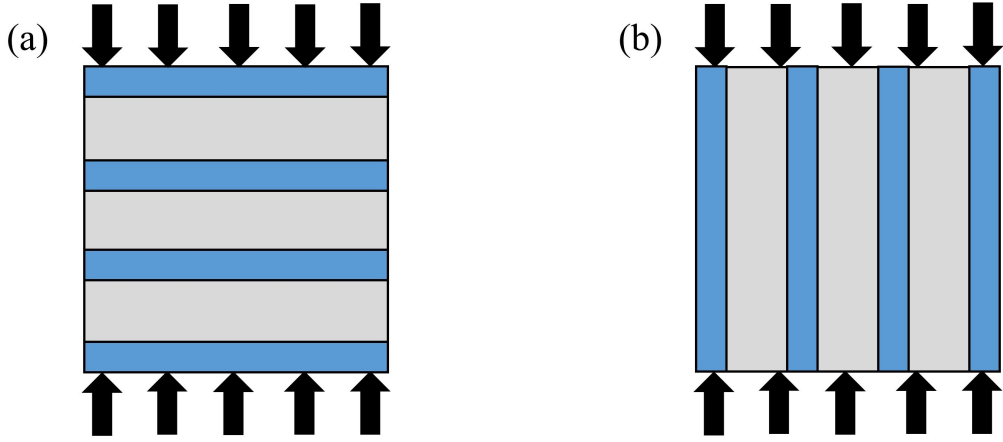
Figure 1.4. (a) Illustration of Voigt iso-strain model of a composite, (b) Illustration of Reuss iso-stress model of a composite.

$$\frac{\sigma_1}{E_1} = \epsilon_1 = \epsilon_2 = \frac{\sigma_2}{E_2}, \tag{1.8}$$

where σ is the stress, ϵ is strain, and E is Young's modulus. The modulus of the corresponding homogenized Voigt model is derived in [24]–[26] as

$$E_H = fE_1 + (1-f)E_2, \tag{1.9}$$

where f is the volume fraction of material #1 and E_H is the effective Young's modulus. On the other hand, the constitutive components in the Reuss model in Fig. 1.4(b) are subjected to the equivalent stress; that is,

$$\epsilon_1 E_1 = \sigma_1 = \sigma_2 = \epsilon_2 E_2. \tag{1.10}$$

The modulus of the Reuss homogenization is

$$E_H = \left(\frac{f}{E_1} + \frac{1-f}{E_2}\right)^{-1}. \tag{1.11}$$

Equations (1.9) and (1.11) are referred to the upper- and lower-bound modulus, respectively, since most heterogeneous structures possess more complex geometries and applied loading such that neither iso-strain or iso-stress is an accurate representation; rather, is it a "mix" of the two.

The final class of homogenization methods are mathematical homogenization, also known as asymptotic homogenization. This class assumes that any field quantity can be represented by an appropriate asymptotic expansion, which is used to calculate the effective properties when substituted in the governing equations [22]. The idea is that each field quantity depends on a slowly varying macroscopic scale and a quickly varying microscopic scale. For instance, the displacement field u could be asymptotically expanded about a point x as

$$u(x) = u^0(x) + \epsilon u^1(x) + \epsilon^2 u^2(x) + \dots, \tag{1.12}$$

where ϵ is a function of the two length scales. The homogenized model and its properties are derived by neglecting high-order terms in the above expansions as the periodicity limit tends to zero [18].

Homogenization techniques can also be classified as low-frequency approaches and high frequency approaches. Low-frequency homogenization procedures, such as the direct, indirect, and variation homogenization methods discussed above, replace the heterogeneous medium by a homogeneous one characterized by constant and uniform material properties. However, they are only valid representations of the behavior of heterogeneous structures when the wavelength is larger than the length of the unit cell. A general rule of thumb for wave propagation in periodic, heterogeneous structures states that the wavelength must be at least twice as long as the unit cell to be an accurate representation. Additionally, in periodic structures, there are frequency ranges where the amplitude of a propagating wave attenuates, or equivalently, where wave propagation through the system does not persist. These frequency ranges, called *band gaps*, are due to multiple scattering from the heterogeneous inclusions in the shorter wavelength regime. The low-frequency homogenization techniques cannot reflect the existence and location of band gaps since the methods are invalid at the high frequencies where the frequency band gaps typically occur. Indeed, the first

band-gap typically marks the approximate limit of validity of low-frequency homogenization approaches. This has prompted high-frequency homogenization approaches, which are expanded asymptotic homogenization methods that use longer asymptotic expansions across multiple scales capable of capturing the aspects of the micro-structural interactions [27]–[29]. Despite providing a successful approach to broadband homogenization, shortcomings of the high-frequency approaches follow from their theoretical formulation and the associated computational cost.

Limitations

Homogenization techniques encounter the following shortcomings:

- The bounds given by variational homogenization methodologies, such as the Voigt and Reuss models, are typically too large to be of any practical use [21],

- The large computational costs of the expansions of the asymptotic homogenization methods, particularly for complex and multiscale structures as well as those containing a large number of variables [22],

- The inability of low-frequency homogenization to accurately model the wave propagation past the long wavelength limit. In particular, these approaches cannot capture the wave attenuation of the frequency band gaps of periodic structures,

- The mathematical complexities and the high computational cost of the theoretical formulations of high-frequency homogenization methodologies.

1.2 Fundamentals of Fractional Calculus

To address the narrow-banded frequency performance of model order reduction for the vibration of discrete, lumped-parameter models possessing multiple DOFs and the long wavelength limit of low-frequency homogenization approaches for the wave propagation through a heterogeneous structure, the dissertation utilizes the mathematical field of fractional calculus.

1.2.1 What is Fractional Calculus?

Fractional calculus (FC) is a branch of mathematics studying integrals and derivatives of non-integer order, which can be either real or complex-valued. Surprisingly, the idea of fractional calculus has existed since the time of classical calculus in a series of letters between Leibniz and de l'Hôpital in 1695 where they discussed the meaning and the interpretation of $\mathrm{d}^\alpha f(t)/\mathrm{d}t^\alpha$ when α is a non-integer. However, it wasn't until the 20th century when the mathematics of FC were more rigorously developed and studied. Despite further enhancement of the mathematics of fractional calculus, practical engineering and scientific applications of the field remained quite limited, mainly due to a lack of understanding and methodologies to link both geometrical and physical properties of a system to the corresponding order of the fractional operator. Luckily, in recent decades, there has been a growing increase in practical applications of fractional calculus as its meaning and significance come into clearer focus. Due to FC's unique properties, areas that have seen the largest boom in number of applications of FC include viscoelasticity [30]–[35], transport processes in complex media [33], [36]–[41], mechanics [42]–[47], nonlocal elasticity [48]–[52], control theory [53], [54], biomedical engineering [55]–[57], and phenomena in fractals [58]–[60]. It is anticipated that applications in fractional calculus will continue to grow across a variety of disciplines in the upcoming years as an understanding of the potential of FC increases.

1.2.2 Mathematical Definitions of Fractional Calculus

Within the last century and a half, the mathematics of FC have been more thoroughly explored and advanced by mathematicians such as Liouville, Riemann, Abel, Riesz, Weyl, and Caputo. The vast study of the mathematics of fractional calculus will be left to sources such as [61]–[65], although this section reviews the most common definitions and properties utilized in this dissertation. In all the following definitions, $f(t)$ is a generic continuous function of the variable t. Before discussing definitions of a fractional derivative, a few specific functions are presented. The gamma function $\Gamma(t)$ can be interpreted as the generalization of the factorial function for all real numbers. The gamma function is

$$\Gamma(t) = \int_0^\infty \mathrm{e}^{-\tau} \tau^{t-1} \mathrm{d}\tau. \tag{1.13}$$

Next, the two term Mittag-Leffler (ML) function, which plays a fundamental role in fractional calculus and can be interpreted as the generalization of the exponential function, is represented by $E(\cdot)$ and is defined as

$$E_{p_1,p_2}(t) = \sum_{q=0}^\infty \frac{t^q}{\Gamma(p_1 q + p_2)}. \tag{1.14}$$

From a theoretical perspective, the quantities p_1, p_2, and t in the Mittag-Leffler definition can be complex quantities, though in most applications of fractional calculus these parameters are purely real.

A multitude of different definitions of fractional derivatives are available in literature, each one created to address a specific need at hand or a shortcoming of another definition. The two most common definitions are the called the Riemann-Liouville and the Caputo derivatives. In the following definitions, the notation $_a^\square D_t^\alpha(\cdot)$ indicates an operator having order α and operating on the interval $[a, t]$ where a is the initial evaluation location. When the fractional operator is performed on the interval $[a, t]$, it is called a left-handed definition. Likewise, the right-handed form of the fractional operator is evaluated on the interval $[t, b]$ where b is the end evaluation point. For the sake of brevity, only the left-handed versions of the fractional operators are presented. The right-handed operators are a straightforward extension of the left-handed versions and can be found in [61]–[65].

Both the Riemann-Liouville and Caputo definitions of a fractional derivative are derived using the definition of a Riemann fractional integral. The fractional integral of order β, denoted as $_aJ_t^\beta(\cdot)$, is

$$_aJ_t^\beta[f(t)] = \frac{1}{\Gamma(\beta)} \int_a^t f(\tau)(t-\tau)^{\beta-1} \mathrm{d}\tau. \tag{1.15}$$

31

Moving to the fractional derivative definitions, let $\alpha \in \mathbb{R}$ (or $\mathbb{C}$) and n be the value of α rounded up to the nearest integer. The Riemann-Liouville fractional derivative of order α is defined by taking the nth derivative of the fractional integral of order $n - \alpha$ of $f(t)$. That is,

$$
{}^{RL}_a D_t^\alpha[f(t)] = D^n {}_a J_t^{n-\alpha}(f(t)) = \frac{1}{\Gamma(n-\alpha)} \frac{\mathrm{d}^n}{\mathrm{d}t^n} \int_a^t f(\tau)(t-\tau)^{n-\alpha-1}\mathrm{d}\tau. \tag{1.16}
$$

On the other hand, the Caputo fractional definition of order α is the $(n - \alpha)^{\text{th}}$ fractional integral of the nth derivative of $f(t)$. That is,

$$
{}^{C}_a D_t^\alpha[f(t)] = {}_a J_t^{n-\alpha} D^n(f(t)) = \frac{1}{\Gamma(n-\alpha)} \int_a^t \frac{\mathrm{d}^n f(\tau)}{\mathrm{d}\tau^n}(t-\tau)^{n-\alpha-1}\mathrm{d}\tau. \tag{1.17}
$$

The Laplace transform of Riemann-Liouville fractional derivative is

$$
\int_0^\infty \mathrm{e}^{-st} D_{RL}^\alpha[f(t)]\mathrm{d}t = s^\alpha F(s) - \sum_{q=0}^{n-1} s^q[D_{RL}^{\alpha-q-1}[f(t)]]_{t=0}, \qquad n-1 < \alpha \leq n \tag{1.18}
$$

while the Laplace Transform of Caputo fractional derivative is

$$
\int_0^\infty \mathrm{e}^{-st} D_{C}^\alpha[f(t)]\mathrm{d}t = s^\alpha F(s) - \sum_{q=0}^{n-1} s^{\alpha-q-1} f^{(q)}(0), \qquad n-1 < \alpha \leq n \tag{1.19}
$$

where $f^{(q)}(0)$ is the qth order derivative of f evaluated at $t = 0$. From Eqs. (1.18) and (1.19), it is evident that the Laplace transform of the Caputo derivative uses the same initial values that a typical integer order problem does (first derivative, second derivative, etc.). The initial values of the Riemann-Liouville definition are actually non-integer order derivative values of the function at $t = 0$. The physical meaning of the necessary initial conditions using the Riemann-Liouville definition is an ongoing research question [66]. On the other hand, the Caputo derivative lends itself to initial values which have a well-defined physical

interpretation (initial position, velocity, acceleration, etc). As a result, Caputo fractional derivatives are more commonly used for actual physical applications.

The finite difference form of fractional derivatives is very important when implementing fractional derivatives in numerical formulations. The finite difference form of the Riemann-Liouville derivative is known as the Grunwald-Letnikov fractional derivative [67], [68] and can be defined recursively as

$$\frac{\partial^\alpha f(x)}{\partial x^\alpha} = \frac{1}{(\Delta x)^\alpha} \sum_{q=0}^{N} g_q f(x_q), \qquad (1.20)$$

where g_q are the Grunwald weights and are

$$g_0 = 1, \qquad (1.21)$$

$$g_q = \left(1 - \frac{\alpha + 1}{q}\right) g_{q-1}. \qquad (1.22)$$

1.2.3   Interpretation and Properties of Fractional Derivatives

The physical interpretation of a fractional derivative has long challenged researchers, although a general consensus has begun to emerge. Unlike an integer order derivative, which can be linked to a clear physical or graphical interpretation (such as the slope of a graph and the first order derivative), the connection between a fractional derivative and its physical or graphical interpretation is not as straightforward. One interpretation of a fractional derivative is an operator that is capable of representing "hybrid" behavior. For example, consider the plot of the derivatives of $f(x) = x^2$, shown in Fig. 1.5. It is evident that the values of the fractional derivatives of $f(x) = x^2$ lie in between the values of the integer order derivatives. From this perspective, fractional derivatives can be interpreted as describing behavior that lies *in-between* models formulated from integer order derivatives.

33
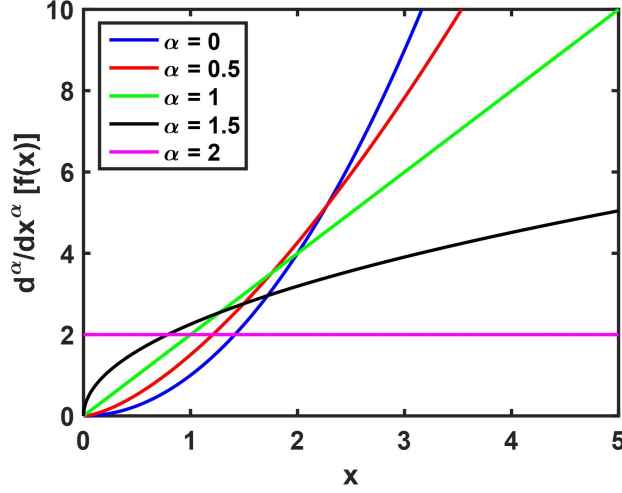
Figure 1.5. Fractional derivatives (order α) of the function $f(x) = x^2$.

The hybrid interpretation of a fractional derivative suggests that it can be a useful mathematical tool for mechanisms that exhibit "hybrid" behavior, such as anomalous diffusion [39], [46], [69] or viscoelasticity [30]–[35]. For instance, the use of fractional derivatives to describe viscoelastic behavior is fairly logical since the overall response of such a system is simultaneously elastic and viscous. Recall that the generalized one-dimensional (1D) relationship between stress σ and strain ϵ of a purely elastic solid is given by the Hooke's law $\sigma = E\epsilon$ where E is Young's modulus. On the other hand, the stress-strain relationship of a viscous medium is given by Newton's law $\sigma = \eta\frac{d\epsilon}{dt}$ where η is the damping coefficient. In Hooke's law, the order of the derivative of strain with respect to time is zero while in Newton's law, the order of the derivative of strain with respect to time is one. Thus, from an empirical standpoint, the stress-strain relationship of a viscoelastic material would be $\sigma = C\frac{d^\alpha\epsilon}{dt^\alpha}$ where $\frac{d^\alpha\epsilon}{dt^\alpha}$ is the fractional derivative of the strain, C is a generalized coefficient, and the value of α is between 0 and 1 (corresponding to the purely elastic and viscous limit cases).

Other interpretations of a fractional derivative are related to their key features. As seen by the definitions in Eqs. (1.16) and (1.17), the fractional operator is a differ-integral operator with a power-law kernel. As a result, a fractional derivative is capable of capturing

the memory of previous states where its power-law kernel acts as a weighting factor for functional values at different domain locations [70]–[72]. Each location's value within the range is weighted where the locations closer to the point of evaluation have a greater influence on the value of the fractional derivative than locations farther away. Systems that are memory-dependent, such as transport processes in complex media [36]–[41], have successfully developed fractional models that reflect this feature. Nonlocal elasticity theory [48]–[52], which is a continuum theory that describes the capability of one location's state variable to be directly influenced by other location's states, even when separated by large distances, has implemented fractional derivatives to model the dynamics of geometrical configurations with inter-connected components and their inherent "spatial memory". Additionally, due to its ability to capture effects across multiple scales, FC has been adopted to model the mechanics of fractals [58]–[60]. Figure 1.6 illustrates the most common systems were fractional models have been shown to be advantageous. These key properties of fractional operators exemplify their potential to accurately represent complicated structures whose mechanical behavior might not be well represented by conventional integer order differential relationships.

Additionally, it is important to note the distinction between fractional derivatives taken with respect to time versus space. A fractional time derivative is a natural tool to model memory-dependent systems [63], [70], [71]. Furthermore, the intrinsic damping nature of a time fractional derivative allows them to accurately represent dissipation in viscoelastic or lossy materials [74]–[77]. Thus, time fractional derivatives are inherently non-conservative operators. While time fractional operators enable memory effects, space fractional operators can account for medium heterogeneity, nonlocal effects, and scale effects. For nonlocal mechanics, for instance, space fractional derivatives provide a power-law kernel where points closer to the location of interest are weighted more than farther off locations. Space fractional derivatives, unlike time fractional derivatives, are indicative of attenuation in systems that potentially are still conservative.
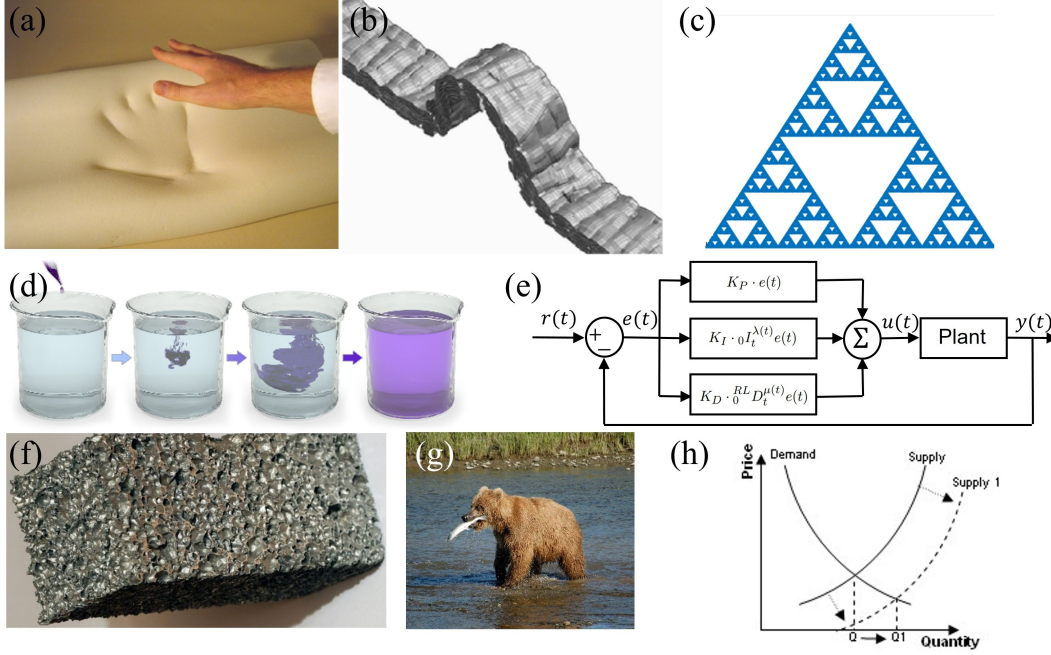
Figure 1.6. Scientific and engineering fields where fractional calculus has been successfully used include (a) viscoelasticity, (b) anisotropic and nonlocal materials (Graphics credit: [73]), (c) fractal geometries, (d) anomalous diffusion, (e) control theory, (f) porosity, (g) population models, and (h) economics (graphics credit for (a),(d), and (f)-(h): Wikipedia).

1.2.4 Complex Order Fractional Derivatives

As will be seen, various portions of this dissertation will implement complex order fractional derivatives. The mathematics of complex fractional derivatives is still a relatively unexplored branch of FC. Additionally, the numerical methods available for complex order fractional differential equations are not nearly as advanced as those for their real order counterparts [68]. Authors such as Love [78], Ortigueira et al. [79], Ross et al. [80], Andriambololona et al. [81], and Valerio et al. [82] have worked on some aspects of complex fractional derivatives; however, applications involving complex fractional orders are rather sparse. While authors such as Atanackovic et al. [83] and Makris et al. [84] have used complex fractional calculus to study various engineering systems, the actual physical significance of a complex fractional order derivative is still not completely evident and continues to garner

attention today. Makris et al. note a link between complex order derivatives to the modulation of both the amplitude and phase of harmonic components of a function. They show that an "*important difference between real-valued and complex-valued time derivatives is that phase modulation in the latter case is frequency-dependent whereas in the former is not*" [84].

The methodologies developed in this dissertation will also yield fractional derivatives that are dependent on forcing frequencies of the system. These fractional derivatives are variable order operators. Contrary to constant order operators, variable order fractional derivatives represent classes of physical phenomena where the order itself is a function of either dependent or independent variables [64], [85], [86]. For example, the order can vary continuously as a function of quantities such as time, space, frequency, or even an independent external variable (e.g., temperature or applied loads).

1.2.5 Why Fractional Calculus for Model Order Reduction and Homogenization?

This dissertation explores the feasibility and potential of fractional calculus as modeling and simulation tools for vibration and wave propagation applications in discrete and continuous structures. While multiple integer order based models have sufficiently modeled complicated mechanics of heterogeneous structures such as multiscale micro-structural behavior, nonlocal interactions, dissipation and damping, and stability, many encounter limitations which this dissertation hypothesizes can be addressed by fractional calculus. Fractional operators, possessing characteristics such as memory effects, intrinsic power-law attenuation, multi-scale functionality, nonlocality, and hybrid behavior can serve as advanced mathematical tools to develop models and simulations more representative of the dynamic behavior of heterogeneous structures.

For model order reduction, the differ-integral nature of the fractional derivative suggests that it is capable of broadband behavior that can overcome the narrow-banded performance of modal-based MOR. Additionally, as a hybrid operator, a fractional derivative appears well suited to reflect the dynamics near closely-spaced resonance frequencies. Also, since the time fractional derivative has been shown to accurately represent dissipation, use of a fractional formulation for a MOR procedure ought to be applicable for discrete systems with

damping. Rather than basing the reduced models on second-order differential equations, use of a fractional MOR will allow the fractional order's value to best represent the vibration of the active DOFs. Lastly, by developing the fractional model order reduction in the frequency domain as opposed to the modal domain, the fractional calculus reduction models will not be subject to the computational costs associated with the calculation of the system's eigenvectors.

The power-law convolution kernel of fractional operators suggests a natural application to homogenization problems, which rely on convolution and averaging approaches to calculate the effective properties. Space fractional derivatives can provide a means to create an effective homogenization tool which captures all spatially variable properties of heterogeneous structures merely through the fractional order. The proposed fractional order techniques are more akin to the class of low-frequency homogenization approaches, in the sense that it replaces the spatially varying material properties (or equivalently, the elastodynamic equation with spatially varying coefficients) with homogenized material properties (or equivalently, constant coefficient elastodynamic equation). Additionally, space fractional derivatives are ideal mathematical tools to capture the dynamics of frequency band gaps in which attenuation is due to multiple back scattering and not to energy dissipation. This provides a means to potential high-frequency homogenization that may not subject to the high computational costs of other theoretical high-frequency asymptotic homogenization approaches.

1.2.6 Fractional Studies Related to Vibration and Wave Propagation

This section reviews previous fractional calculus research in regards to vibration and wave propagation applications and how this dissertation builds upon them. As previously mentioned, viscoelasticity constitutes one of the major fields of application of FC, for both discrete and continuous structures. Multiple studies ([30], [31], [33], [34], [46], [47], [84], [87]–[89]) have developed constitutive equations for viscoelastic structures based on fractional order derivatives (such as the fractional stress-strain relationship given in § 1.2.3), leading to fractional governing equations of motion describing the vibration or wave propagation of the viscoelastic media. Additionally, these studies have found that a fractional model

of the viscoelastic media can be a more accurate representation of their physics. From the perspective of discrete models, integer order models of viscoelasticity are typically modeled as some form of springs and dampers in series or parallel (e.g., Maxwell and Kelvin-Voigt models). Usually, formulating an accurate integer order model across a wide spectrum of parameter variations requires multiple arrays of springs and dampers in series or parallel [33], [90], [91]. On the other hand, the order of the fractional model typically can represent the physics of viscoelastic media accurately without requiring a complex network of springs and dampers. Sources such as [30], [87], [89], [92]–[94] have derived the discrete viscoelastic governing equation as (or similar to)

$$m\ddot{x} + c_\alpha \frac{\mathrm{d}^\alpha x}{\mathrm{d}t^\alpha} = f(t), \tag{1.23}$$

where m is mass, x is the displacement, t is time, f is the load, and c_α is a coefficient for the fractional term.

While FC in viscoelasticity has shown great potential and continues to grow, this dissertation opts to use and expand upon a different discrete fractional equation since the discrete models analyzed in Chapter 2 do not contain viscoelastic components. Sources such as [61]–[63], [74], [76], [95]–[98] have analyzed the vibration of another fractional model called the fractional oscillator. Its governing equation is

$$m \frac{\mathrm{d}^\alpha x}{\mathrm{d}t^\alpha} + kx = f(t), \tag{1.24}$$

where k is the stiffness and $\alpha \in (1, 2]$. From a general perspective, the fractional oscillator behaves very similarly to a classical damped harmonic oscillator [74], [97] with the exception that the damping term does not appear explicitly but is integrated in the time fractional order derivative [76], [97]. As a result, one can physically interpret the time fractional derivative in Eq. (1.24) as viscoinertial. Instead of viewing Eq. (1.24) as a viscoinertial model, Stanislavsky et al. [98] suggests that the fractional oscillator model be considered as an ensemble average

of ordinary multiple harmonic oscillators. Performing a stochastic study of an assembly of classical harmonic oscillators, Stanislavsky relates the fractional order to the phases of the second order oscillators. If the phases are all identical, the resulting motion will be that of a single oscillator; in this case, $\alpha = 2$ in Eq. (1.24). However, if the oscillators are out of phase with one another, the assembly of oscillators will exhibit a dissipative nature over time due to the antiphase contributions each oscillator exhibits on the others [98], resulting in $\alpha \in (1, 2)$.

Although use of Eq. (1.23) is more commonplace since the inertial forces are still the product of the mass and the acceleration in accordance with Newton's second law of motion, this dissertation uses Eq. (1.24) as its basis for a fractional MOR methodology since [98]'s interpretation of the order of the fractional oscillator aligns with the notion of capturing the dynamical relationship between the different DOFs of discrete lumped-parameter oscillators. The hybrid view of a fractional derivative is well-suited to model closely spaced resonance frequencies. Furthermore, use of a time fractional derivative allows the reduced order model to accurately reflect any damping present in the discrete parameter models without needing to explicitly include damping. Additionally, the dissertation extends the concept of a fractional oscillator to possess multiple nodes. Finally, the use of the fractional oscillator as the basis of the MOR represents an application of Eq. (1.24), which to-date has only seen a few practical examples [99]–[101].

Wave propagation through heterogeneous structures is another field where fractional calculus has been implemented [33], [36]–[41], [69]. The hybrid nature of the fractional operator deems it a logical candidate to represent propagation behavior that is both wave-like and diffusive concurrently. Studies of this diffusion-wave equation [69], [95], [102]–[108] derive a governing equation for the propagation as

$$\frac{\partial^\alpha u}{\partial t^\alpha} = c^2 \frac{\partial^2 u}{\partial x^2}, \tag{1.25}$$

where u is a displacement, c is a speed, and $\alpha \in [1, 2]$. Equation (1.25) reduces to the classic diffusion equation for $\alpha = 1$ and the wave equation for $\alpha = 2$. This fractional

differential equation has been applied to describe the wave-like behavior of porous structures [37], [109] and lossy or dissipative materials based on a frequency power-law relationship [38], [110], [111]. Many of these studies derive fractional wave equations similar to Eq. (1.25) by starting with the integer order equations of motion, applying a transformation (such as Laplace or Fourier transform), solving the equation in the transformed domain with the proper assumptions and boundary conditions, and then taking an inverse transform to obtain an equivalent fractional derivative in the time-space domain [31], [37], [38]. This approach is typically utilized when the underlying constitutive relations have an intrinsic power-law dependence and illustrates how the physics of the studied system are inherently fractional.

This dissertation uses governing equations similar to Eq. (1.25) except that the fractional derivative is taken with respect to space rather than time, as seen in [40], [112]–[116]. A space fractional derivative is chosen for heterogeneous systems since the material or geometrical properties vary spatially. Additionally, because of its ability to represent the combined effects of mechanical phenomena, FC homogenizes the varying material and geometry of a heterogeneous structure by a single parameter: a space fractional order. However, unlike the systems such as in [31], [37], [38], many heterogeneous structures are not intrinsically fractional, making it exceedingly difficult to derive a fractional wave equation reflective of the dynamics. Nonetheless, by using fractional models whose governing equation is a space fractional wave equation, the dissertation can develop a novel homogenization tool for 1D heterogeneous structures which can lead to analytical or numerical advantages. In particular, the attenuating, yet conservative, nature of a space fractional derivative is suitable to represent the non-persisting wave propagation that occurs in the frequency band gaps of periodic structures.

1.3 Objectives

This work aims to develop new, advanced, fractional calculus-based modeling techniques applicable to the vibration and wave propagation analysis of discrete and continuous representations of heterogeneous structures. Specifically, this dissertation will explore the use of fractional derivatives to 1) create a model order reduction technique for the vibration

of discrete parameter systems that is capable of broadband accuracy, and to 2) develop a homogenization approach for heterogeneous structures that is based on space fractional operators. In particular, a class of heterogeneous structures called metamaterials [117]–[119] will be studied as a benchmark system. The objectives of this dissertation are summarized as

- To explore the role that time fractional order operators can play in the development of model order reduction techniques capable of simultaneously delivering high accuracy and high levels of reduction. In this context, specific technical objectives are

  - To extend the fractional oscillator model given by Eq. (1.24) to a multiple degree of freedom formulation and to determine their analytical solutions,

  - To analyze the values and physical significance of the time fractional derivatives across a frequency spectrum for multiple reduction examples,

  - To develop a system identification technique based on the fractional oscillator where the amplitude and phase of numerical data is represented by a frequency-dependent fractional order.

- To investigate the role and potential of fractional order operators as the mathematical foundation for the development of material homogenization techniques. Technical objectives are

  - To develop a space fractional model representative of the elastic wave propagation in 1D heterogeneous structures,

  - To demonstrate how the space fractional order derivative accurately captures the spatial wave attenuation of periodic structures in frequency band gaps located beyond the long wavelength limit,

  - To explore both closed-form analytical solutions and numerical solutions of the fractional models of 1D heterogeneous structures.

- To examine and explain the role of space fractional derivatives for heterogeneous geometries implemented in metamaterial waveguides. Technical objectives are

- To analyze the specific example of an acoustic black hole geometry and correlate the fractional order to the geometrical parameters of the acoustic black hole profile,

- To develop a space fractional boundary condition or domain capable of mimicking the effect of an acoustic black hole termination in an acoustic duct,

- To extend the concept of fractional homogenization to variable space fractional order operators and to assess it for a slender, elastic beam containing an acoustic black hole profile.

Along with these technical objectives, an overarching broader objective of this work is to stimulate the engineering community, particularly the structural and dynamics communities, to further consider the feasibility and potential of FC as an important tool for engineering analyses and applications.

1.4 Organization of Dissertation

This dissertation is organized into five chapters. The first chapter here introduced the vibration and wave analysis of heterogeneous structures. Model order reduction techniques for discrete parameter models and homogenization methodologies for continuous models were discussed. Fractional calculus was proposed as a mathematical tool capable of addressing some limitations of MOR and homogenization methodologies. The dissipation characteristic of time fractional derivatives that vary as a function of frequency offers a means to create a highly accurate model order reduction methodology for the vibration of damped discrete parameter systems across a wide frequency spectrum. On the other hand, the ability of the space fractional derivative to capture varying spatial properties suggested its basis for a novel homogenization technique that will represent wave propagation through heterogeneous metamaterials. The objectives, along with their technical tasks, are further analyzed by each of the next three chapters.

Chapter 2 is dedicated to fractional models for the vibration of discrete dynamical systems and model order reduction formulation. Chapter 2 uses time fractional order differential

equations to simulate the dynamic response of non-homogeneous, damped, discrete lumped-parameter systems containing multiple DOFs. FC provides an alternative approach to the traditional integer order approach where discrete dynamical systems can be modeled with compact fractional equations that not only can still guarantee analytical solutions, but can also enable broadband order reduction without compromising on accuracy. In addition, the discussed discrete fractional models can be utilized as a model synthesis technique for system identification.

Next, Chapter 3 formulates homogenized fractional wave models for periodic structures. In particular, this chapter considers elastic wave propagation in a 1D bi-material periodic rod and beam. The governing integer order equations describing the wave propagation in periodic structures consist of partial differential equations with spatially varying coefficients. Numerical solutions for the periodic systems are computationally expensive and low-frequency homogenization fails to reflect the dynamics of frequency band gaps. Instead, FC provides a powerful approach to develop comprehensive mathematical models of periodic structures by serving as a homogenization tool that captures the wave attenuation in band gaps. Analytical and numerical solutions to the space fractional differential equations of the homogenized media are presented.

Then, Chapter 4 extends the notion of fractional homogenization to a heterogeneous geometry known as an acoustic black hole (ABH). This chapter first uses space fractional models for ABH terminations in 1D acoustic ducts whose order results in the equivalent wave reflection into the main host duct. In this way, the effect of the ABH termination on the wave propagation in the duct can be modeled without having the simulate the response within the acoustic black hole itself. Then, this chapter turns its attention to an effective space fractional model for an ABH geometry in a structural elastic beam. However, in this case, the fractional homogenized model aims to also accurately capture the wave propagation within the acoustic black hole by utilizing a variable space fractional order. The proposed fractional models intend to pave the way for alleviating the computational expenses of current numerical simulations of ABHs.

Finally, the last chapter summarizes the work, highlighting how each of the objectives was met. In particular, the conclusion details the contributions and significance of the

dissertation along with its limitations. Recommendations are provided for future work to further promote the marriage of fractional calculus and vibration and wave analysis.

1.5   Remark on Validation of Fractional Models

Before proceeding, we provide a rationale for the use of analytical or numerical results of the heterogeneous systems to assess the fractional models developed in the following chapters. Indeed, the most convincing means to assess and validate the fractional models would be to compare the response predicted by the fractional formulations to experimental data of the corresponding heterogeneous system. However, the heterogeneity of the structures explored in this dissertation are, for the most part, relatively basic. Thus, the analytically or numerically obtained responses of these systems can be considered the "true" response and serve as the reference for assessing the fractional models. Of course, for more complex material and geometrical distributions, experimental data would be needed to serve as the reference for evaluating the fractional model's accuracy and appropriateness. For the more intricate heterogeneous structures considered in this dissertation, references are cited illustrating that experimental data closely aligns with numerical simulations of the systems. In assessing the fractional models, if the heterogeneous structure has a known closed-form analytical solution, it is used as the reference. If an analytical solution is unknown (as is generally the case), a numerical solution (typically obtained using finite elements) of the heterogeneous structure serves as the reference.

2. FRACTIONAL ORDER MODELS FOR DISCRETE DYNAMICAL SYSTEMS

A portion of this chapter was previously published by the Journal of Sound & Vibration and is titled "Model-order reduction of lumped parameter systems via fractional calculus" [120] [DOI: https://doi.org/10.1016/j.jsv.2018.01.011]. Another portion of this chapter is, at the time of the deposit of this dissertation, under review for publication and is titled "Fractional model order reduction of discrete dynamical systems under generalized harmonic loading conditions"

The dissertation begins with the vibration analysis of fractional order models for discrete dynamical systems and develops a fractional model order reduction which permits an accurate broadband frequency response for the reduction of a multi-DOF structure. First, the fractional oscillator, which can be considered as the fractional analog of a single DOF mass-spring-damper, is extended to the case of multiple DOFs. Then, taking inspiration from the modal analysis approach for vibrating systems, a fractional modal analysis is formulated to determine the analytical solution of the displacement of each node of the multiple DOF fractional model. Obtaining a closed-form analytical solution of the displacement via fractional modal analysis will facilitate the assessment of the fractional model order reduction.

Next, the model order reduction procedure is formulated in the frequency domain. The fractional MOR is based on equating the receptance (i.e., the transfer functions relating the displacement and force) of the active DOFs in the multi-DOF structure to the receptance of the DOFs of the corresponding reduced fractional model. The procedure allows the determination of the fractional order of the reduced model such that its dynamics are equivalent to those of the active DOFs. Permitting the fractional order to be a function of the driving frequencies of the applied loads enables the MOR methodology to possess the sought-after broadband accuracy.

Lastly, this chapter concludes by considering fractional calculus for system identification; that is, the analysis of dynamical systems where measured experimental data is available and either the corresponding mathematical model or its coefficients are unknown. The fractional oscillator is chosen to represent the amplitude and phase of an unknown system whose dynamic behavior is given by a Bode plot. By letting the fractional order capture the

amplitude and phase of the response at each frequency, a fractional model order identification method can accurately represent the data across a wide frequency spectrum, including at frequencies between closely spaced resonances. Contents of the chapter include

- Analysis of fractional oscillator models, possessing either a single DOF (F-SDOF) or multiple DOFs (F-NDOF), along with their analytical displacements and transfer functions,

- Reduction methodologies that yield either purely real or complex fractional orders and discussion of their physical meaning,

- The conversion of a damped single DOF mass-spring-damper (I-SDOF) to an un-damped F-SDOF, illustrating how the fractional order is determined by equating of the transfer functions of the systems,

- The reduction of a multiple DOF mass-spring-damper (I-MDOF) to F-SDOF,

- The most generic reduction case of reducing an I-MDOF to a F-NDOF where $N < M$,

- Discussion of how to reduce systems possessing harmonic loads with multiple frequency components or containing loads on both active and omitted DOFs,

- Implementation of the fractional oscillator as the basis for a system identification methodology of the vibration of discrete systems.

2.1 The Fractional Single Degree of Freedom Oscillator

The equation of motion (EOM) of the F-SDOF oscillator, shown in Fig. 2.1(a), is

$$\bar{m}\frac{\mathrm{d}^\alpha \bar{x}}{\mathrm{d}t^\alpha} + \bar{k}\bar{x} = \bar{f}(t), \tag{2.1}$$

where $\bar{x}$ is the displacement from the equilibrium condition, $\bar{m}$ is a mass-like term, $\bar{k}$ is a stiffness term, $\bar{f}(t)$ is the time dependent load acting on the mass, and α is the order of the fractional derivative. The dimensions of these quantities are the same as their counterparts in

47

the classical driven harmonic oscillator equation, except for $\bar{m}$ (dimensions of $[\mathrm{MT}]^{\alpha-2}$). The bar notation (e.g., $\bar{x}$) is used for the reduced fractional models in order to distinguish them from the parameters of the I-SDOF or I-MDOF. As will be observed, while the fractional MOR will result in $\mathrm{Re}(\alpha)$ between 1 and 2, $\mathrm{Im}(\alpha)$ will sometimes be nonzero. Therefore, let $\alpha = a + \mathrm{i}b$, where a and b are the real and imaginary part of α, respectively, and $\mathrm{i} = \sqrt{-1}$.
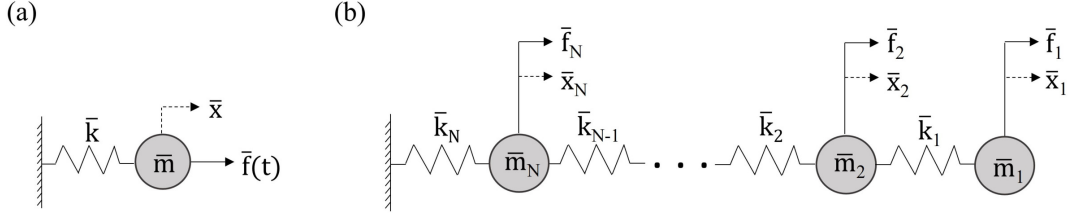
Figure 2.1. (a) The F-SDOF model. (b) The F-NDOF model.

To determine the quantities of the reduced fractional models (chiefly the fractional order), the MOR equates the transfer functions (TF) of the active DOFs in the full scale integer order model to those of the DOFs in the reduced fractional models. Doing so allows the reduction methodology to calculate the value of the fractional order derivative reflective of the interaction between the active and omitted DOFs. To determine the transfer function of the F-SDOF, take the Laplace transform of Eq. (2.1) (see § 1.2.2) with zero initial conditions, obtaining

$$(\bar{m}s^{\alpha} + \bar{k})\bar{X}(s) = \bar{F}(s), \tag{2.2}$$

where s is the Laplace variable. The transfer function of the F-SDOF is

$$G(s) = \frac{\bar{X}(s)}{\bar{F}(s)} = \left(\frac{1}{\bar{m}}\right)\frac{1}{s^{\alpha} + \frac{\bar{k}}{\bar{m}}}. \tag{2.3}$$

Substituting $\alpha = a + \mathrm{i}b$ and $s = \mathrm{i}\omega$ and applying some algebraic manipulation, Eq. (2.3) becomes

$$G(\mathrm{i}\omega) = \left(\frac{1}{\bar{m}}\right)\frac{1}{\gamma_c + \frac{\bar{k}}{\bar{m}}}, \tag{2.4}$$

where

$$\gamma_c = \omega^a \mathrm{e}^{-\frac{b\pi}{2}}\left[\cos\left(\frac{a\pi}{2}\right)\cos\left(b\ln(\omega)\right) - \sin\left(\frac{a\pi}{2}\right)\sin\left(b\ln(\omega)\right) + \mathrm{i}\cos\left(\frac{a\pi}{2}\right)\sin\left(b\ln(\omega)\right) + \mathrm{i}\sin\left(\frac{a\pi}{2}\right)\cos\left(b\ln(\omega)\right)\right]. \tag{2.5}$$

Equation (2.4) can now be rewritten in terms of its real and imaginary parts as

$$G(\mathrm{i}\omega) = \left(\frac{1}{\bar{m}}\right)\frac{1}{\delta + \mathrm{i}\chi}, \tag{2.6}$$

where

$$\delta = \frac{\bar{k}}{\bar{m}} + \omega^a \mathrm{e}^{-\frac{b\pi}{2}}\left[\cos\left(\frac{a\pi}{2}\right)\cos\left(b\ln(\omega)\right) - \sin\left(\frac{a\pi}{2}\right)\sin\left(b\ln(\omega)\right)\right], \tag{2.7}$$

$$\chi = \omega^a \mathrm{e}^{-\frac{b\pi}{2}}\left[\cos\left(\frac{a\pi}{2}\right)\sin\left(b\ln(\omega)\right) + \sin\left(\frac{a\pi}{2}\right)\cos\left(b\ln(\omega)\right)\right]. \tag{2.8}$$

As a result, the magnitude and phase of the transfer function are

$$|G(\mathrm{i}\omega)| = M = \frac{1}{\bar{m}\sqrt{\delta^2 + \chi^2}}, \tag{2.9}$$

$$\angle G(i\omega) = \psi = -\tan^{-1}\left(\frac{\chi}{\delta}\right). \tag{2.10}$$

Additionally, the analytical solution to the fractional oscillator in Eq. (2.1) has been determined through Laplace transformations by [61], [62], [97] as

$$\bar{x}(t) = \frac{1}{\bar{m}}\int_0^t g(\tau)\bar{f}(t-\tau)\mathrm{d}\tau + \frac{x_0}{\bar{m}}E_{\alpha,1}\left(-\frac{\bar{k}}{\bar{m}}t^\alpha\right) + \frac{\dot{x}_0}{t\bar{m}}E_{\alpha,2}\left(-\frac{\bar{k}}{\bar{m}}t^\alpha\right), \tag{2.11}$$

where x_0 is the initial position, $\dot{x}_0$ is the initial velocity, and

$$g(t) = t^{\alpha-1}E_{\alpha,\alpha}\left(-\frac{\bar{k}}{\bar{m}}t^\alpha\right), \tag{2.12}$$

where $E(\cdot)$ is the Mittag-Leffler function (see Eq. (1.14)).

2.2 The Fractional Multiple Degrees of Freedom Oscillator

The F-NDOF model, depicted in Fig. 2.1(b), simply extends the single DOF fractional oscillator to consist of a series of N nodes connected by a set of N springs, whose motion is governed by a fractional derivative. This parallels the extension of a single DOF mass-spring system to a series of multiple masses connected by multiple springs. The EOMs of the F-NDOF are

$$\bar{\mathbf{M}}\frac{\mathrm{d}^\alpha\{\bar{x}\}}{\mathrm{d}t^\alpha} + \bar{\mathbf{K}}\{\bar{x}\} = \{\bar{F}\}(t), \tag{2.13}$$

where $\bar{\mathbf{M}}$ is a diagonal $N \times N$ fractional mass matrix, $\bar{\mathbf{K}}$ is the $N \times N$ stiffness matrix given by

$$
\bar{\mathbf{K}} = \begin{bmatrix} \bar{k}_1 & -\bar{k}_1 & & & & \\ -\bar{k}_1 & \bar{k}_1 + \bar{k}_2 & -\bar{k}_2 & & & \\ & . & . & . & & \\ & & -\bar{k}_{N-2} & \bar{k}_{N-2} + \bar{k}_{N-1} & -\bar{k}_{N-1} & \\ & & & -\bar{k}_{N-1} & \bar{k}_{N-1} + \bar{k}_N \end{bmatrix}, \tag{2.14}
$$

$\{\bar{x}\}$ is the $N \times 1$ vector of nodal displacements $\left(\{\bar{x}\} = \begin{bmatrix} \bar{x}_1 & . & . & . & \bar{x}_N \end{bmatrix}^{\mathrm{T}} \right)$, and $\{\bar{F}\}$ is the $N \times 1$ force vector $\left(\{\bar{F}\} = \begin{bmatrix} \bar{f}_1 & . & . & . & \bar{f}_N \end{bmatrix}^{\mathrm{T}} \right)$. The fractional models considered here do not include any explicit damping terms.

2.2.1 Transfer Functions of the F-NDOF

In obtaining the TF of each DOF in the F-NDOF, a system where there is a force acting on only one DOF is considered (see § 2.4.3 for cases with multiple loads). This section illustrates how to obtain the transfer functions for a F-2DOF. Extension of the process for more DOFs is straightforward. The EOMs are given by

$$
\bar{m}_1 \frac{\mathrm{d}^\alpha \bar{x}_1}{\mathrm{d}t^\alpha} + \bar{k}_1 \bar{x}_1 - \bar{k}_1 \bar{x}_2 = \bar{f}_1(t), \tag{2.15}
$$

$$
\bar{m}_2 \frac{\mathrm{d}^\alpha \bar{x}_2}{\mathrm{d}t^\alpha} - \bar{k}_1 \bar{x}_1 + (\bar{k}_1 + \bar{k}_2)\bar{x}_2 = \bar{f}_2(t). \tag{2.16}
$$

One conceivable analysis would arrange these equations in a state-space form and then obtain the TFs. However, rather than using a fractional state-space to transfer function method, the approach calculates the Laplace transform of Eqs. (2.15) and (2.16) and then applies Cramer's rule. Applying the Laplace transform yields

$$\begin{bmatrix} \bar{m}_1 s^\alpha + \bar{k}_1 & -\bar{k}_1 \\ -\bar{k}_1 & \bar{m}_2 s^\alpha + \bar{k}_1 + \bar{k}_2 \end{bmatrix} \begin{bmatrix} \bar{X}_1 \\ \bar{X}_2 \end{bmatrix} = \begin{bmatrix} \bar{F}_1 \\ \bar{F}_2 \end{bmatrix}. \tag{2.17}$$

Using Cramer's rule, $\bar{X}_1(s)$ and $\bar{X}_2(s)$ are given by

$$\bar{X}_1(s) = \frac{D_1(s)}{D(s)}, \tag{2.18}$$

$$\bar{X}_2(s) = \frac{D_2(s)}{D(s)}, \tag{2.19}$$

where

$$D_1(s) = \begin{vmatrix} \bar{F}_1(s) & -\bar{k}_1 \\ \bar{F}_2(s) & \bar{m}_2 s^\alpha + \bar{k}_1 + \bar{k}_2 \end{vmatrix}, \tag{2.20}$$

$$D_2(s) = \begin{vmatrix} \bar{m}_1 s^\alpha + \bar{k}_1 & \bar{F}_1(s) \\ -\bar{k}_1 & \bar{F}_2(s) \end{vmatrix}, \tag{2.21}$$

$$D(s) = \begin{vmatrix} \bar{m}_1 s^\alpha + \bar{k}_1 & -\bar{k}_1 \\ -\bar{k}_1 & \bar{m}_2 s^\alpha + \bar{k}_1 + \bar{k}_2 \end{vmatrix}. \tag{2.22}$$

The desired transfer functions can then be obtained using Eqs. (2.18) and (2.19). As an example, if $\bar{F}_2(s) = 0$ and $\bar{F}_1(s) = \bar{F}(s)$, one can define $\hat{D}_1(s) = \frac{D_1(s)}{\bar{F}(s)}$ and $\hat{D}_2(s) = \frac{D_2(s)}{\bar{F}(s)}$. The transfer functions of the output displacements relative to the input force on the first node are

$$G_1(s) = \frac{\bar{X}_1(s)}{\bar{F}(s)} = \frac{\hat{D}_1(s)}{D(s)}, \tag{2.23}$$

$$G_2(s) = \frac{\bar{X}_2(s)}{\bar{F}(s)} = \frac{\hat{D}_2(s)}{D(s)}. \tag{2.24}$$

The substitution $s = i\omega$ is made to convert to the frequency domain.

2.2.2 Fractional Modal Analysis of the F-NDOF

To determine the displacements of each DOF in the F-NDOF, this section formulates a fractional modal analysis theory. Previously, Lin et al. [121], [122] have formulated a fractional modal analysis, although it was for a generalized fractional viscoelastic model which included pure elastic and viscous components as well. To generalize the vibration of the fractional viscoelastic models, [121], [122] calculated its eigenvalues, frequency response, and displacement response via their modal analysis algorithm. To develop the fractional modal analysis for the F-NDOF model, the procedure takes inspiration and modifies that proposed by Lin et al. [121], [122] to make it applicable for fractional oscillators instead of the fractional viscoelastic model. Assuming $\{\bar{x}\} = \{\bar{X}\}e^{\lambda t}$ and using the property $\frac{d^\alpha (e^{ax})}{dt^\alpha} = a^\alpha e^{ax}$ (see [123]), Eq. (2.13) becomes

$$\left(\lambda^\alpha \bar{\mathbf{M}} + \bar{\mathbf{K}}\right)\{\bar{X}\} = \{\bar{F}\}. \tag{2.25}$$

When $\{\bar{F}\} = \{0\}$, Eq. (2.25) defines the eigenvalue problem where λ is the eigenvalue and $\{\bar{X}\}$ is the eigenvector. Solving the eigenvalue problem requires $|\lambda^\alpha \bar{\mathbf{M}} + \bar{\mathbf{K}}| = 0$. Assuming that the fractional order $\alpha \in \mathbb{C}$ and $1 < \mathrm{Re}(\alpha) \leq 2$, $|\lambda^\alpha \bar{\mathbf{M}} + \bar{\mathbf{K}}|$ always produces a characteristic equation of the form

$$\lambda^{N\alpha} + c_1\lambda^{(N-1)\alpha} + \ldots + c_{N-1}\lambda^{\alpha} + c_N = 0, \tag{2.26}$$

where the coefficients c_N are real constants. This is a polynomial-like equation that can be transformed into a polynomial equation by adopting the substitution $\xi = \lambda^{2/\alpha}$. Equation (2.26) becomes

$$\xi^{2N} + c_1\xi^{2(N-1)} + \ldots + c_{N-1}\xi^2 + c_N = 0. \tag{2.27}$$

Equation (2.27) has $2N$ complex roots, which occur in complex conjugate pairs. After obtaining the $2N$ roots of Eq. (2.27), the roots of Eq. (2.26) are obtained as $\lambda = \xi^{\alpha/2}$. Each root ξ_r corresponds to an individual value of λ. Therefore, Eq. (2.25) has $2N$ distinct roots. The roots to the $\alpha = 2$ case are all purely imaginary and are indicated as $\pm i\omega_j$, where ω_j are the natural frequencies of the classic second order systems (j ranges from 1 to N). Comparing Eq. (2.25) to the eigenvalue problem for the classic second order set of equations, it is easy to see that the fractional eigenvalues raised to the fractional order (λ_j^{α}) are actually equivalent to the negative of the square of the natural frequencies obtained for the classical $\alpha = 2$ case; that is, $\lambda_j^{\alpha} = -\omega_j^2$. Because of this fact, it is evident that *the eigenvectors of this fractional oscillator system of equations where $1 < \mathrm{Re}(\alpha) \leq 2$ are exactly the same as the eigenvectors that are obtained for the classical $\alpha = 2$ case.*

Equation (2.25) can be written for two different eigensolutions j and k (i.e., $\left(\lambda_j^{\alpha}\bar{\mathbf{M}} + \bar{\mathbf{K}}\right)\{\bar{X}_j\} = \{0\}$ and $\left(\lambda_k^{\alpha}\bar{\mathbf{M}} + \bar{\mathbf{K}}\right)\{\bar{X}_k\} = \{0\}$). Multiplying the j$^{\text{th}}$ eigenvalue equation by $\{\bar{X}_k\}^T$, and the kth eigenvalue equation by $\{\bar{X}_j\}^T$, subtracting the two, and noting that $\bar{\mathbf{K}}$ and $\bar{\mathbf{M}}$ are symmetric, yields

$$(\lambda_j^{\alpha} - \lambda_k^{\alpha})\{\bar{X}_k\}^T\bar{\mathbf{M}}\{\bar{X}_j\} = \{0\}. \tag{2.28}$$

Assuming j $\neq$ k, then $\{\bar{X}_k\}^T\bar{\mathbf{M}}\{\bar{X}_j\} = \{0\}$, showing that the eigenvectors are orthogonal with respect to the fractional mass matrix $\bar{\mathbf{M}}$. If the eigenvectors are normalized with respect to the fractional mass matrix, then

$$\underline{\bar{\mathbf{X}}}^T\bar{\mathbf{M}}\underline{\bar{\mathbf{X}}} = \mathbf{I}, \tag{2.29}$$

$$\underline{\bar{\mathbf{X}}}^T\bar{\mathbf{K}}\underline{\bar{\mathbf{X}}} = -\lambda_j^\alpha\mathbf{I}, \tag{2.30}$$

where $\mathbf{I}$ is the $N \times N$ identity matrix, $-\lambda_j^\alpha\mathbf{I}$ is a diagonal $N \times N$ matrix with the eigenvalues raised to the power α along the diagonal, and $\underline{\bar{\mathbf{X}}}$ is the modal matrix and contains all the eigenvectors $\{\bar{X}\}$ as its columns. Equations (2.29) and (2.30) show that the eigenvectors diagonalize the fractional mass and stiffness matrices, allowing one to use the expansion theorem ([13]) to create a fractional modal analysis. The solution $\bar{\mathbf{x}}$ is expressed as a superposition of the normal modes as

$$\{\bar{x}\} = \sum_{j=1}^{N}\eta_j(t)\{\bar{X}_j\} = \underline{\bar{\mathbf{X}}}\{\eta(t)\}, \tag{2.31}$$

where η_j are the modal coordinates. Substituting Eq. (2.31) into Eq. (2.13) and premultiplying by $\underline{\bar{\mathbf{X}}}^T$ yields

$$\underline{\bar{\mathbf{X}}}^T\bar{\mathbf{M}}\underline{\bar{\mathbf{X}}}\frac{\mathrm{d}^\alpha\{\eta\}}{\mathrm{d}t^\alpha} + \underline{\bar{\mathbf{X}}}^T\bar{\mathbf{K}}\underline{\bar{\mathbf{X}}}\{\eta\} = \{\bar{Q}(t)\}, \tag{2.32}$$

where $\{\bar{Q}(t)\} = \underline{\bar{\mathbf{X}}}^T\{\bar{F}(t)\}$. Equations (2.29) and (2.30) uncouple Eq. (2.32) to give a set of equations of the general form

$$\frac{\mathrm{d}^\alpha \eta_\mathrm{j}(t)}{\mathrm{d}t^\alpha} + (-\lambda_\mathrm{j}^\alpha)\eta_\mathrm{j}(t) = Q_\mathrm{j}(t), \tag{2.33}$$

for $\mathrm{j} = 1, 2, \ldots, N$. Assuming zero initial conditions, the solution to Eq. (2.33) is

$$\eta_\mathrm{j}(t) = \int_0^t \tau^{\alpha-1} E_{\alpha,\alpha}(\lambda_\mathrm{j}^\alpha \tau^\alpha) Q_\mathrm{j}(t-\tau)\mathrm{d}\tau. \tag{2.34}$$

Once the solution is obtained for each modal coordinate, the nodal displacements of the fractional oscillators are obtained using Eq. (2.31). This methodology therefore successfully determines the analytical solution of the displacements of all the nodes in the F-NDOF.

2.3 Conversion from a Damped Integer Single Degree of Freedom to a Fractional Single Degree of Freedom

Now that the models and solutions of the F-SDOF and F-NDOF have been formulated, the reduction methodology is developed. The reduction procedure will be broken into three sections. This first section will consider conversions from a damped I-SDOF to a F-SDOF having an equivalent dynamic response. While the conversion technically does not qualify as a reduction methodology since the number of DOFs remains the same, it illustrates the basic methodology behind the fractional MOR technique. In addition, this section discusses how to handle systems with loads consisting of multiple harmonics.

Next, § 2.4 discusses how to reduce an I-MDOF to a F-SDOF. This is an extreme form of reduction where there is only one active DOF in the I-MDOF which is reduced to a F-SDOF. This section will also discuss how to perform the reduction when there are multiple loads, acting on both active and omitted DOFs.

Finally, § 2.5 analyzes the most general reduction case of reducing an I-MDOF to a F-NDOF where $N < M$. In each of the three sections, two different MOR approaches are considered: one that yields a complex order derivative and one that produces a purely real order fractional derivative.

2.3.1 Approach Using Complex Fractional Orders

The differential equation of a classical mass-spring-damper (Fig. 2.2(a)) is

$$m\ddot{x} + c\dot{x} + kx = f(t), \tag{2.35}$$

where m is the mass, c is the damping coefficient, k is the spring stiffness, x is the displacement of the mass from equilibrium, and f is the external force. Taking the Laplace transform of Eq. (2.35) with zero initial conditions, the TF of the I-SDOF is

$$H(s) = \frac{X(s)}{F(s)} = \frac{1}{ms^2 + cs + k}. \tag{2.36}$$

(a) (b)
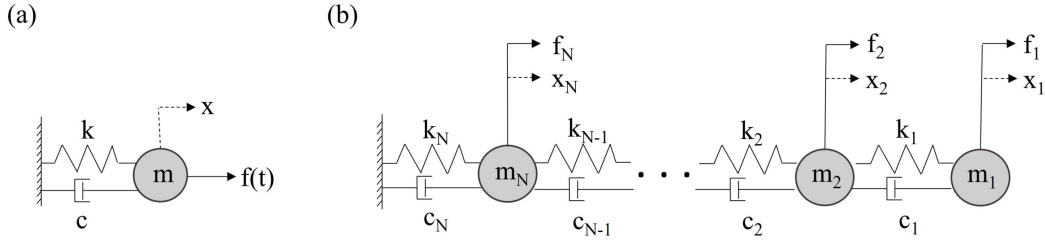
Figure 2.2. (a) A classical mass-spring-damper system. (b) Discrete integer order mass-spring-damper model with multiple DOFs.

To determine the order α of the fractional oscillator such that dynamics of the fractional oscillator and the classical damped oscillator are equivalent, Eq. (2.36) is set equal to Eq. (2.3). According to [63], this operation is allowable only if the external forcing functions satisfy specific conditions and if one seeks an asymptotic form of the dynamic response. Trigonometric harmonic functions are one such example that will yield solutions $\bar{x}(t)$ that, at steady state, are also harmonic [97]. Achar et al. [97] provided a detailed analysis of the closed-form solution to Eq. (2.1) when the external forcing is of the form $\bar{A}\sin(\omega t)$. Based on their results, it is evident that the steady state solution of this kind of harmonically driven fractional

oscillator is still a trigonometric harmonic function whose circular frequency is the same as the frequency of the harmonic external force. Thus, assuming harmonic loads and steady state conditions, setting Eq. (2.36) equal to Eq. (2.3) produces the polynomial equation

$$ms^2 + cs + k = \bar{m}s^\alpha + \bar{k}. \tag{2.37}$$

Solving Eq. (2.37) for α results in a fractional oscillator whose dynamic behavior is equivalent to that of a known integer order oscillator. The use of complex order fractional derivatives here provides much flexibility in the selection of the constant coefficients of the governing equations, which means that the match between transfer functions is not unique and it can occur for different choices of the constants $\bar{k}$ and $\bar{m}$. In this regard, the selection of the parameters is discretionary. In practice, given that these values are connected to physical quantities, they should be selected, at least, within the physical range of validity of their integer order counterpart. The choice of $\bar{m}$ and $\bar{k}$ does affect the final form of the frequency dependency of α but not the ability to match the responses of the two systems. Since the procedure matches the dynamics of the I-SDOF to the F-SDOF, it is logical to set the values of the coefficients of the fractional model equal to their integer model counterparts. This assumption is based on the rationale that the two equations must share the same stiffness and mass-like terms because they represent the same physical system. Another potential approach to obtain $\bar{m}$ would be to invert the definition of the damping ratio (if known) of the integer order system and solve for the value of the mass and then set $\bar{m}$ equal to this value.

Using the strategy of setting the values of the coefficients of the fractional model equal to their integer model counterparts, $\bar{m} = Qm$ and $\bar{k} = k$, where Q is a unit conversion factor necessary to maintain consistency in units. Q is of unitary value and its units are s$^{\alpha-2}$. Substituting this and $s = i\omega$ into Eq. (2.37) and solving for α results in

$$\alpha = 1 + \frac{\text{Ln}(i\omega + \frac{c}{m})}{\text{Ln}(i\omega)}, \tag{2.38}$$

where ω is the forcing frequency and Ln is the complex logarithm function.

From Eq. (2.38), it is seen that for non-damped systems ($c = 0$), Eq. (2.38) returns an integer order derivative with $\alpha = 2$ as expected. On the contrary, for damped systems, the order will never be exactly equal to $\alpha = 2$. However, for asymptotic values of the forcing frequency (in discrete systems this condition translates to frequencies greater than the highest resonance), $\mathrm{Re}(\alpha)$ asymptotically approaches a value of 2 while $\mathrm{Im}(\alpha)$ approaches 0. In the asymptotic regime, the dynamic response is dominated by the inertial term (order of ω^2) so the effect of damping becomes asymptotically small. In fact, this behavior is true also for classical I-SDOF.

Equation (2.38) also reveals that the order α of the equivalent fractional model is both a complex and frequency-dependent quantity. A complex order derivative modulates both the phase and the amplitude [84] of harmonic components therefore allowing for virtually unrestricted matching of the transfer functions. The above results show that if α in Eq. (2.1) is chosen according to Eq. (2.38), then the response of the two systems at the given frequency ω is exactly equivalent.

A numerical example further illustrates that the steady state responses of the two models are exactly equivalent under harmonic loading. Results are presented both in the frequency and the time domain. In the time domain, the steady state response of the I-SDOF subject to a harmonic force $f(t) = F_0 \sin(\omega t)$ is of the well-known general form $x(t) = X \sin(\omega t - \phi)$ [13]. On the other hand, the total (both transient and steady state) time-dependent solution to the fractional oscillator is given by Eq. (2.11), which contains the Mittag-Leffler function. As pointed out by Garrappa [124], while the ML function plays a fundamental role in fractional calculus, there are surprisingly very few methods available for its numerical evaluation. A few MATLAB functions do exist ([125], [126]) to numerically evaluate it but are not valid for complex values of α. In order to evaluate the ML function for complex orders, an edited version of [125] is used.

While the process is independent of the unit system, examples shall use the international system of units (SI) for the sake of illustration. For the numerical evaluation, an I-SDOF with $m = 2$ kg, $c = 1$ N s/m, and $k = 10$ N/m is considered. As discussed, $\bar{m} = 2$ kg s$^{\alpha-2}$ and $\bar{k} = 10$ N/m in the fractional model. The value of α can then be calculated

using Eq. (2.38) for a specified forcing frequency ω. Figure 2.3(a) shows a plot of the value of α as a function of ω for this example. The natural frequency of the I-SDOF in this numerical example is $\omega = \sqrt{\frac{k}{m}} = \sqrt{5}$ rad/s. Figure 2.3(a) shows that for excitation frequencies above the critical frequency, $\mathrm{Re}(\alpha)$ tends towards 2 while $\mathrm{Im}(\alpha)$ tends toward 0. Thus, when the forcing frequency is well above the resonance frequency (i.e., the high frequency asymptotic limit), the fractional model converges to an integer order model. On the contrary, for frequencies below the critical frequency, the model order is fractional and $1 < \mathrm{Re}(\alpha) < 2$ as expected due to the presence of viscous damping in the initial integer order model. With the fractional order as a function of frequency now obtained, the frequency domain response of the fractional model is found using the magnitude and phase given by Eqs. (2.9) and (2.10). The plots of the magnitude and phase of the transfer functions of the integer order model and the fractional order model are plotted in Fig. 2.3(b). Both sets of magnitude and phase show that the TF of the F-SDOF model matches exactly the TF of the corresponding I-SDOF. Thus, the dynamic behavior of the obtained F-SDOF is equivalent to that of the I-SDOF.
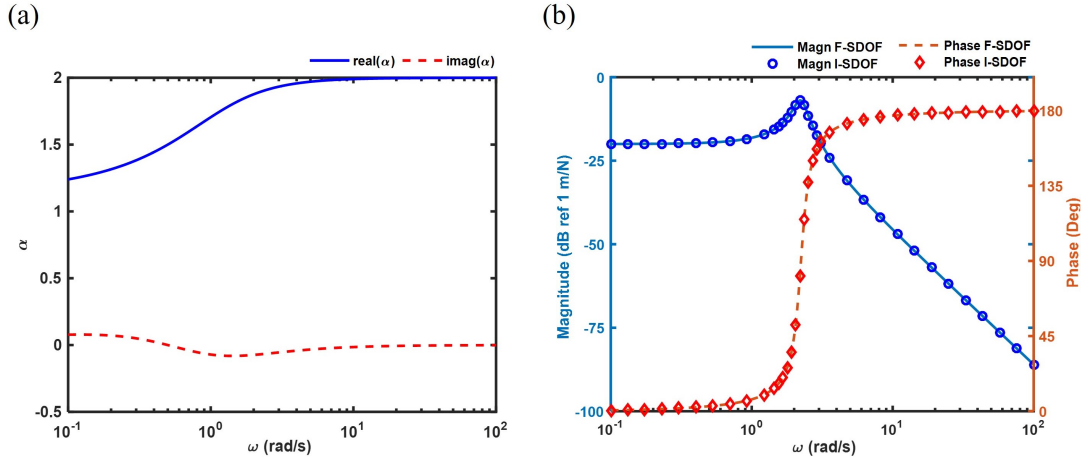
Figure 2.3. (a) The complex fractional order α for the conversion of the damped I-SDOF to a F-SDOF. (b) Magnitude and phase of the transfer functions of I-SDOF and F-SDOF.

To illustrate the match between the I-SDOF and the F-SDOF in the time-domain, a harmonic force of excitation frequency $\omega = 10$ rad/s is considered. From Fig. 2.3(a) or,

equivalently, from Eq. (2.38), this frequency corresponds to an order $\alpha = 1.9903 - 0.0151\mathrm{i}$. Using this value of α in Eqs. (2.11) along with the sinusoidal force $\bar{f}(t) = \sin(10t)$ N, a numerical evaluation of the convolution integral in Eq. (2.11) produces $\bar{x}(t)$. The solution given by Eq. (2.11) includes both the transient and steady state response while the equivalence between the integer and fractional order systems holds only at steady state. Therefore, the comparison will be performed only on the steady state part. The time response of the fractional oscillator is shown in Fig. 2.4 by plotting the real and imaginary parts, separately.

A complex order derivative of a real-valued function is a complex-valued function of time [127], [128] as reflected in the results of Fig. 2.4. However, according to [84], the complex order fractional derivative of a harmonic function is still a harmonic function but subject to amplitude and phase modulations. In particular, the imaginary part of the order allows for the modulation of phase, which are constant for a given frequency. This suggests that the time response of the complex fractional oscillator under harmonic excitation can be treated as an analytic function; therefore the direct comparison of the time responses of the two oscillators requires $x(t) = \mathrm{Re}(\bar{x}(t))$.
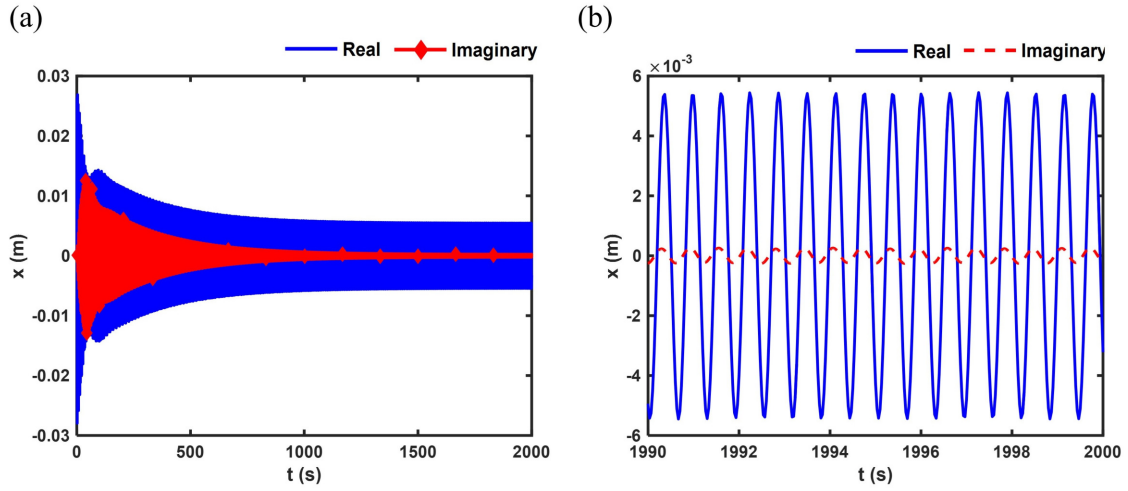
Figure 2.4. (a) The complex-valued displacement of the resulting F-SDOF. (b) A close-up view of the response of the F-SDOF after steady state has been reached.

61

The result of this comparison, seen in Fig 2.5, illustrates a match between the steady state responses of the two systems. A small discrepancy on the order of 3% between the peak values is observed in Fig. 2.5. After further numerical investigations, these differences were attributed to the numerical errors associated with the evaluation of the complex order Mittag-Leffler function in Eq. (1.14). In fact, these numerical errors can sometimes be more substantial depending on the forcing frequencies. As a result, this has prompted the development of a methodology that produces a purely real fractional order while still accurately representing both the amplitude and phase of the harmonic displacement (see § 2.3.2).
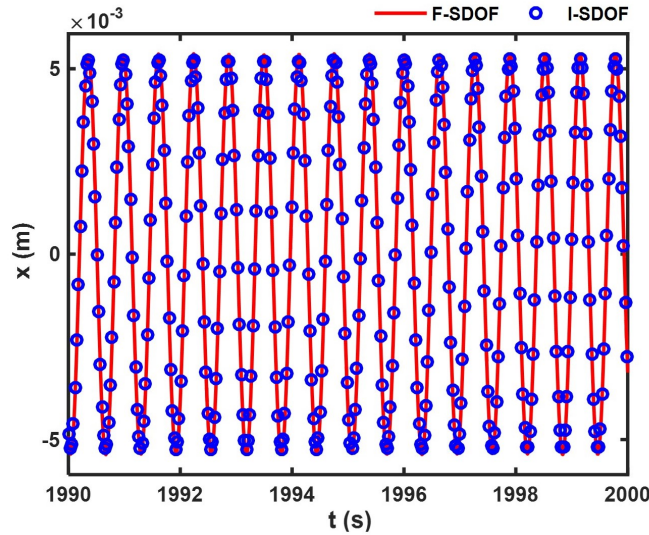
Figure 2.5. Comparison of the steady state response of the I-SDOF to the real part of the steady state response of the corresponding F-SDOF.

The fractional technique is able to obtain complex order fractional oscillators exhibiting an equivalent dynamic response to damped integer order oscillators. Due to the numerical errors associated with the complex order Mittag-Leffler function, comparisons in the dynamic responses of integer and fractional order systems are presented in terms of their TFs since this is sufficient to guarantee that the two systems will behave identically. For the real order approaches, this chapter opts to instead plot the time-domain displacements of the integer and fractional order systems to validate the accuracy of the fractional MOR.

2.3.2 Approach Using Real Fractional Orders

Thus far, the reduction procedure has produced complex order derivatives. As noted, due to the numerical errors of the complex order ML function, an alternative strategy is developed that forces the order to be a purely real quantity. This can be beneficial since the mathematics and numerical methods for real order fractional derivatives are much more developed than their complex order counterpart.

In order for the MOR procedure to produce only real order operators, the value of $\bar{m}$ is not set equal to m, as was previously done. It follows that the expression of the fractional order α (previously given in Eq. (2.38)) becomes

$$\alpha = \frac{\mathrm{Ln}(-\frac{m}{\bar{m}}\omega^2 + \mathrm{i}\frac{c}{\bar{m}}\omega)}{\mathrm{Ln}(\mathrm{i}\omega)}. \tag{2.39}$$

Expanding the definition of the complex logarithm function, Eq. (2.39) is written as

$$\alpha = \frac{\ln\left(\frac{\omega}{\bar{m}}\right) + \frac{1}{2}\ln(m^2\omega^2 + c^2) + \mathrm{i}\tan^{-1}\left(\frac{c}{-m\omega}\right)}{\ln(\omega) + \mathrm{i}\frac{\pi}{2}}. \tag{2.40}$$

Multiplying the numerator and denominator of Eq. (2.40) by the complex conjugate of the denominator, it is observed that the order α will be purely real if

$$\ln(\omega)\tan^{-1}\left(\frac{c}{-m\omega}\right) - \frac{\pi}{2}\left[\ln\left(\frac{\omega}{\bar{m}}\right) + \frac{1}{2}\ln(m^2\omega^2 + c^2)\right] = 0. \tag{2.41}$$

Solving for $\bar{m}$ in Eq. (2.41) yields

$$\bar{m} = \frac{\omega}{\mathrm{e}^{2\Upsilon/\pi}}, \quad \Upsilon = \ln(\omega)\tan^{-1}\left(\frac{c}{-m\omega}\right) - \frac{\pi}{4}\ln(m^2\omega^2 + c^2). \tag{2.42}$$

If the value of the fractional mass $\bar{m}$ is selected according to Eq. (2.42), then the order α of the fractional derivative in the EOM of the F-SDOF will be a purely real quantity. A

plot of $\bar{m}$ for the previous numerical example is given in Fig. 2.6(b). The fractional mass $\bar{m}$ is now a function of the forcing frequency ω and can be regarded as an effective parameter that allows the order α to be real, but still permits the undamped F-SDOF model to exactly represent the damped I-SDOF. At higher frequencies where damping becomes negligible, the value of $\bar{m}$ approaches a constant asymptotic value coinciding with its static value. The order α can be calculated using Eq. (2.39) for a specific forcing frequency ω, where $\bar{m} = \bar{m}(\omega)$. Figure 2.6(a) shows the value of α as a function of ω and confirms that α is a purely real quantity. Other than the fact that $\text{Im}(\alpha) = 0$, the trend of Fig. 2.6(a) is similar to that of Fig. 2.4(a) where α tends to 2 for excitation frequencies above the critical frequency of the oscillator, while $1 < \alpha < 2$ for excitation frequencies below the critical frequency.
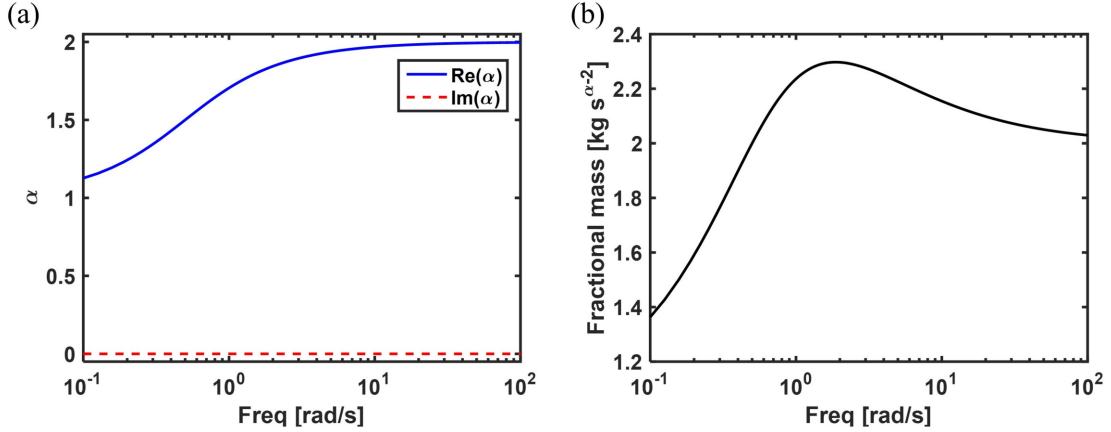
Figure 2.6. (a) The purely real fractional order α for the conversion of the I-SDOF to a F-SDOF. (b) The frequency-dependent fractional mass $\bar{m}$ of the F-SDOF.

While the purely real order formulation is a valid fractional MOR, it should be stressed that once a more accurate numerical means to evaluate the complex order Mittag-Leffler function order is developed, it is more prudent to use the complex order derivative methodology since, in actuality, the system's inertia-like term is not frequency dependent. This allows all frequency dependency to be represented solely by the fractional order.

2.3.3   Methodology for Multi-Harmonic Loads

Thus far, the fractional MOR along with the examples has been limited to single harmonic loads. Here, the question of how to handle multi-harmonic loads is addressed since a large class of vibration problems contain such forcing functions. Both the integer and fractional order derivative operators in all EOMs presented so far are linear operators. As a result, linear superposition can be employed and the extension of the MOR methodology requires the determination of the fractional order α for each frequency component. The total response of the fractional oscillator consists of a summation of the steady state displacements in Eq. (2.11) for each frequency component. The strategy for the fractional reduction procedure for multi-harmonic loads is summarized as

1. Obtain the fast Fourier transform (FFT) of the harmonic load.

2. Select the N_f most prevalent frequencies from the FFT. The selection of the harmonics to be retained is not an exact process and, in general, follows the classical considerations of a Fourier decomposition of a generic function. Hence, in the limit for the number of frequencies $N_f \to \infty$, the approximate function will converge to the exact one. For practical applications, a threshold on the amplitude can be set in order to determine the harmonics to be retained.

3. For each prevalent frequency ω_j (in rad/s), identify the amplitude A_j and the phase ϕ_j for $j = 1, 2, \ldots, N_f$.

4. Calculate the values of the fractional orders α_j corresponding to each frequency ω_j along with any other frequency dependent quantity (such as the fractional mass $\bar{m}_j$ for the real order formulation).

5. Obtain the response for each frequency as

$$\bar{x}_j(t) = \frac{A_j}{\bar{m}_j} \int_0^t \cos(\omega_j t + \phi_j) g_j(t - \tau) d\tau, \quad g_j(t) = t^{\alpha_j - 1} E_{\alpha_j, \alpha_j}\left(-\frac{\bar{k}}{\bar{m}_j} t^\alpha \right). \tag{2.43}$$

6. Obtain the total response by linear superposition as

$$\bar{x}(t) = \sum_{j=1}^{N_f} \bar{x}_j. \tag{2.44}$$

To illustrate the superposition procedure, again consider the numerical example given in § 2.3.1, but with a more complicated harmonic load $f(t)$. The reduction methodology that produces a purely real fractional order is used here so that the plots of the displacement are free of numerical error arising from the complex order Mittag-Leffler function. In this example, the forcing load consists of a square wave superimposed to a harmonic load along with another harmonic frequency, as seen in Fig. 2.7(a). The load is $f(t) = 0.1\big[\mathrm{SQ}(2\pi\Omega_1 t) + \cos(2\pi\Omega_2 t + \phi_1)\big]$ N, where $\mathrm{SQ}(2\pi\Omega_1 t)$ is a square wave with period 2π, $\Omega_1 = 0.08$ Hz, $\Omega_2 = 0.5$ Hz, and $\phi_1 = 0.5$. Figure 2.7(a) depicts discontinuities in the load resulting from the square wave. While these discontinuities excite more frequencies and produce transients, an accurate representation of the steady state response can be obtained by 1) accounting for the effects of multiple prevalent frequencies in the FFT (Fig. 2.7(b)) and by 2) considering the response at a time interval where the damping in the system has decayed all transient behavior (see x-axis in Fig. 2.7(c)). Figure 2.7(c) plots the steady state response of the I-SDOF and the F-SDOF using the values of α and $\bar{m}$ from Fig. 2.6. The curves match quite well, with only a maximum relative error of 1.1%, located at the peaks and valleys. The error in Fig. 2.7(c) is due to the truncation of terms in the superposition of the fractional responses of different frequency components (see Fig. 2.7(b)) and is farther reduced as the value of used frequencies N_f increases.

2.4 Model Order Reduction from Integer Multiple Degrees of Freedom to a Fractional Single Degree of Freedom

A reduction, as opposed to a mere conversion, is now developed having established the basics of the procedure in the I-SDOF to F-SDOF case. Assume that the response of one of the degrees of freedom in the I-MDOF (Fig. 2.2(b)) is the active DOF and that all the remaining DOFs are omitted. An equivalent F-SDOF representation is sought such that
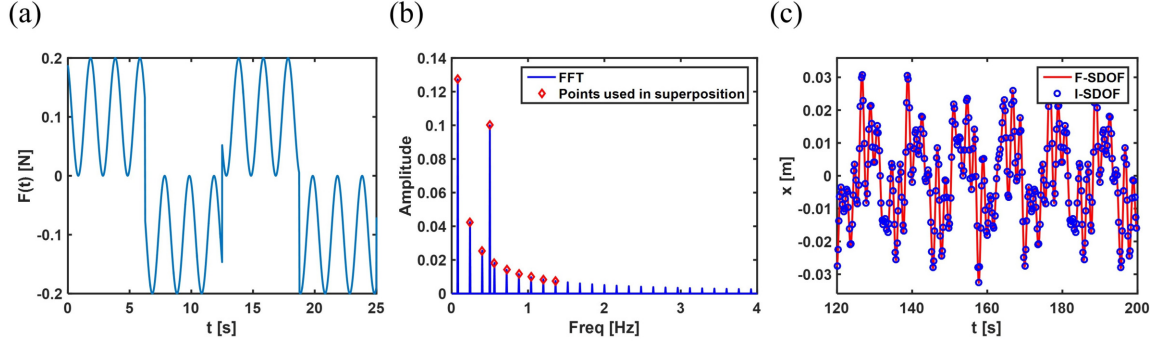
Figure 2.7. (a) The harmonic load in the I-SDOF to F-SDOF example. (b) FFT of the load, depicting the excited frequencies arising from the discontinuities in the square wave. Red markers indicate frequencies used $(N_f = 10)$ to determine the displacement of the F-SDOF. (c) Comparison of the steady state response of the I-SDOF and the F-SDOF subject to the load given in (a).

the F-SDOF's response matches exactly or approximately the response of the corresponding active DOF of the I-MDOF model.

Similar to the methodology of § 2.3, the reduction approach relies on equating the TF of the active DOF to the TF of the F-SDOF and determining the corresponding fractional order α. Recall that the transfer function of the F-SDOF is given by Eq. (2.3). To determine the TF of the I-MDOF, the system is first converted to a state-space form. From the state-space form, the transfer function of any of the nodes in the I-MDOF can be obtained. The process of obtaining the transfer function from state-space is well-established [120], [129], [130]. Note that there are other means to obtain the desired TF of the I-MDOF, such as using Cramer's rule in § 2.2.1.

Like the previous section, two approaches are considered: one that results in a complex fractional order and the other where the order is forced to be purely real. Finally, this section concludes by discussing how to extend the reduction methodology when there are loads on both active and omitted DOFs.

2.4.1 Approach Using Complex Fractional Orders

Let $H(s)$ be the transfer function for the active degree of freedom in the I-MDOF model, obtained from the state-space form. The corresponding fractional model has a mass of $\bar{m}$ and a stiffness of $\bar{k}$, as reflected in Eq. (2.1) and Fig. 2.1(a). By equating the TF of the F-SDOF to the TF of the degree of interest in the I-MDOF, the fractional order α is obtained as

$$\alpha = \frac{\ln\left(\frac{1}{\bar{m}H(s)} - \frac{\bar{k}}{\bar{m}}\right)}{\ln(s)}. \tag{2.45}$$

Equation (2.45) can be made a function of frequency by substituting $s = i\omega$ and provides a fractional order α which guarantees an exact match of the TFs of the two systems. Therefore, as far as the individual function $H(s)$ is exact, the response of the equivalent F-SDOF is an exact match of the initial I-MDOF.

Just like in the I-SDOF case, the selection of the mass $\bar{m}$ and the stiffness $\bar{k}$ in the fractional oscillator is a discretionary decision. However, in § 2.3.1, the selection of the parameters $\bar{m}$ and $\bar{k}$ was a fairly natural decision given the existence of only one set of parameters in the integer order model. Now, in the current configuration with multiple DOFs in the integer order model, multiple choices can be made. Among the possible approaches is to set $\bar{m}$ so that the total mass of the I-MDOF matches that of the F-SDOF; that is

$$\bar{m} = Q \sum_{j=1}^{M} m_j, \tag{2.46}$$

where m_j is the mass of the jth degree of freedom of the I-MDOF and Q is the unit conversion factor. Since the I-MDOF model consists of springs in series, $\bar{k}$ is set equal to the equivalent stiffness of springs in series defined by

$$\bar{k} = \left(\sum_{j=1}^{M} \frac{1}{k_j}\right)^{-1}. \tag{2.47}$$

As in the previous case, the methodology is illustrated with an example. Consider an I-MDOF with M = 4 and non-uniform, periodic coefficients. Specifically, $m_1 = m_3 = 1$ kg, $m_2 = m_4 = 2$ kg, $k_1 = k_3 = 1$ N/m, $k_2 = k_4 = 2$ N/m, $c_1 = c_3 = 1$ N s/m, and $c_2 = c_4 = 2$ N s/m. The natural frequencies are all within the range 0.36 rad/s to 2.22 rad/s. The dynamic response of the first mass (m_1 in Fig. 2.2(b)) is the active degree and therefore the one whose response is reduced to a F-SDOF. Using Eqs. (2.46) and (2.47), the parameters of the fractional model are taken as $\bar{m} = 6$ kg s$^{\alpha-2}$ and $\bar{k} = \frac{1}{3}$ N/m. After obtaining the transfer function $H(s)$ for the first mass in the I-MDOF model, Eq. (2.45) can be applied to find α for a desired forcing frequency.

Figure 2.8(a) shows a plot of the value of α as a function of ω for the example system. The trend of $\alpha(\omega)$ is highly dependent on the methodology used for determining the variables $\bar{m}$ and $\bar{k}$. Following the suggested methodology (Eqs. (2.46) and (2.47)), the fractional system, in the asymptotic limit, tends to a second order system (Re(α) = 2, Im(α) = 0). Thus, in the asymptotic limit, the phase of the response becomes nearly constant and no longer changes with frequency. In the low frequency limit, the behavior of the system is oscillatory ($1 < \text{Re}(\alpha) < 2$) with a phase modulation (Im(α) $\neq 0$). The original system is of order eight with resonances clustered in a narrow frequency range. For this reason, in the frequency range of the local resonances, the equivalent fractional system can exhibit order Re(α) > 2. As highlighted above, the fractional order is affected by the choice made to define the equivalent parameters. Non-monotonic changes in the fractional order should be expected in between resonances, suggesting that the evolution from one local resonance to the next (typically modeled in conventional dynamic theory as a single DOF second order oscillator) occurs via a dynamic behavior that is locally fractional. The dynamic response of the fractional model can be studied using the magnitude and phase as given by Eqs. (2.9) and (2.10). Figure 2.8(b) depicts the match between the magnitude and phase of the first mass of the I-MDOF and the magnitude and phase of the F-SDOF. As desired, the response of the equivalent fractional model is identical to the response of the first mass of the I-MDOF.

The two main advantages of the technique presented above are 1) the approach allows a remarkable reduction in order without any loss in the characteristic features of the original dynamics, and 2) the resulting F-SDOF can pave the way to the use of analytical solu-
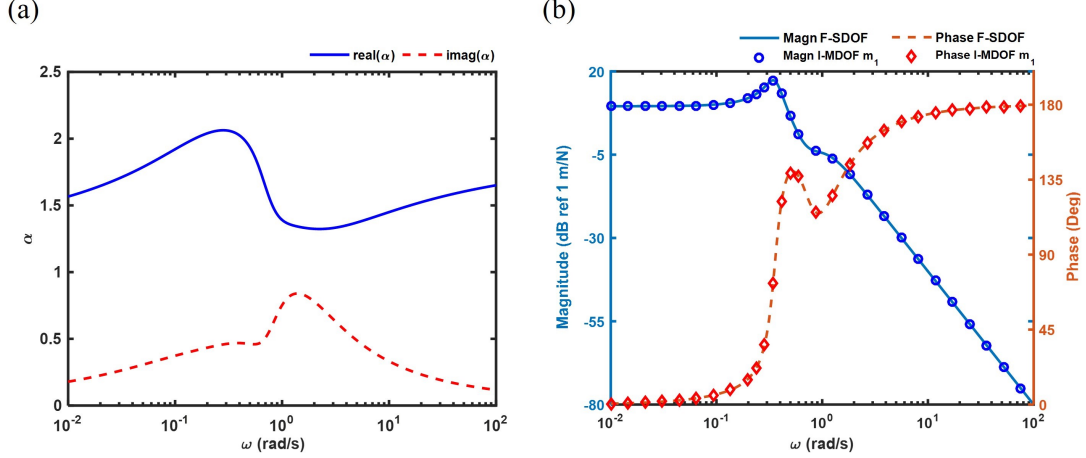
Figure 2.8. (a) The complex fractional order α for the reduction of an I-MDOF to a F-SDOF. (b) Magnitude and phase of the transfer functions of m_1 in the I-MDOF and the F-SDOF.

tions (e.g., Mittag-Leffler function [61]) for the simulation of complex dynamic systems that typically allow only numerical approaches. Of course, the methodology encounters some limitations as well. The methodology assumed that the initial I-MDOF system was known beforehand. To obtain the fractional order α, the transfer function of the active DOF in the I-MDOF must already be known. This is often unknown beforehand and is further discussed in § 2.6 where the corresponding mathematical model or its coefficients are sought via FC.

2.4.2 Approach Using Real Fractional Orders

The procedure to obtain a purely real fractional order when reducing an I-MDOF to a F-SDOF is analogous to that given in § 2.3.2 in that the fractional mass $\bar{m}$ in the F-SDOF varies as a function of the forcing frequency ω. The fractional order α is still given by Eq. (2.45) but $\bar{m}$ is now defined as

$$\bar{m} = \frac{1}{\mathrm{e}^{\Upsilon}}, \quad \Upsilon = \frac{2I_1 \ln(\omega)}{\pi} - \mathrm{Re}\left[\ln\left(\frac{1}{H(\mathrm{i}\omega)} - \bar{k}\right)\right]. \tag{2.48}$$

An example that produces a purely real fractional order is deferred to the next section, where a system with loads on both the active and omitted DOFs is considered.

70

2.4.3 Methodology for Loads on Both Active and Omitted DOF

So far, the MOR procedures and presented examples were limited to a load only acting on the active DOF. Thus, it was immediate to guarantee that the dynamics of the I-MDOF and the F-SDOF were equivalent by matching the TF of the active DOF to that of the F-SDOF. However, since the loads acting on the omitted DOFs and other active DOFs will affect the overall dynamic response, the fractional MOR must be altered to capture the dynamical effects from all the loads. To extend the procedure for systems where there are loads on both the active and omitted DOFs, a *force correlation* procedure is created to translate all the loads in the I-MDOF to be acting on a single active DOF, which is called the *chiefly active DOF*. In the reduction of an I-MDOF to a F-SDOF, the chiefly active DOF is chosen as the lone active DOF. For situations where there are multiple active DOF (as seen in § 2.5), the selection of which active DOF to choose as the chiefly active DOF is a discretionary decision since the dynamics will remain unaltered regardless. The force correlation procedure presented below is valid for reducing an I-MDOF to a F-SDOF and for reducing an I-MDOF to a F-NDOF.

In order to translate the forces to the chiefly active DOF without altering the dynamics of the system, new loads acting on the chiefly active DOF are created while all other loads are eliminated via transfer function analysis. This is illustrated in Fig. 2.9, where the force acting on each DOF in the I-MDOF is replaced by equivalent forces $f_{C,J}(t)$ for $J = 1, 2, \ldots, M$ acting on the chiefly active DOF (in this case, the first node, i.e., $A = 1$) such that the dynamics of the discrete I-MDOF remain unaltered. Let $H(s) = X_A(s)/F_A(s)$ be the TF for the chiefly active DOF in the I-MDOF model. For the chiefly active DOF, $X_A(s)$ is the Laplace transform of the displacement and $F_A(s)$ is the Laplace transform of a load acting directly upon it. Using the state-space to transfer function procedure [129], one can obtain M different transfer functions relating the displacement of the chiefly active DOF to each load in the I-MDOF model; that is, $H_{AJ}(s) = X_A(s)/F_J(s)$ where $F_J(s)$ is the Laplace transform of the load on the Jth DOF ($J = 1, 2, \ldots, M$) (note that the previously defined transfer function $H(s)$ is actually $H_{AA}(s)$). The relationship between the known transfer function $H_{AA}(s)$ and an unknown force $f_{C,J}(t)$ acting on the chiefly active DOF is
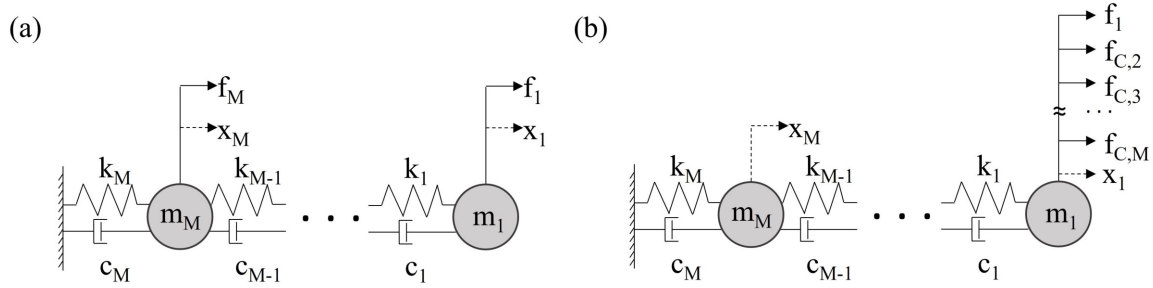
Figure 2.9. (a) I-MDOF with loads on each DOF. (b) Illustration of the force correlation procedure where all of the forces have been *translated* to the chiefly active DOF (the first mass) such that the dynamics remain unaltered.

$$H_{AA}(s) = \frac{X_A(s)}{F_{C,J}(s)}, \tag{2.49}$$

while the relationship between the known transfer function $H_{AJ}(s)$ $(J \neq A)$ and the known force $f_J(t)$ acting on all other DOFs is

$$H_{AJ}(s) = \frac{X_A(s)}{F_J(s)}. \tag{2.50}$$

Solving Eqs. (2.49) and (2.50) for $X_A(s)$ and equating them yields

$$F_{C,J}(s) = C_f(s)F_J(s), \tag{2.51}$$

where

$$C_f(s) = \frac{H_{AJ}(s)}{H_{AA}(s)}, \tag{2.52}$$

is called the correlation function that relates the transfer functions to each other. Taking the inverse Laplace transform of Eq. (2.51) gives each correlation force on the chiefly active DOF as

$$f_{C,J}(t) = \int_0^t f_J(t)c_f(t-\tau)\mathrm{d}\tau. \tag{2.53}$$

Equation (2.53) is a convolution integral that replaces a load on the Jth DOF in the I-MDOF with a corresponding correlated force on the chiefly active DOF such that the displacements of the nodes in the I-MDOF remain unaltered. Since the chiefly active DOF will have multiple loads acting on it with different harmonic components, the linear superposition method in § 2.3.3 will need to be applied to calculate the overall displacements of the reduced fractional models.

Perhaps the best way to illustrate the methodology is with an example. Consider an I-MDOF with $M = 2$ where the first mass is the active DOF (i.e., $A = 1$). The masses, springs, and dampers in this I-MDOF are $m_1 = 1$ kg, $m_2 = 2$ kg, $k_1 = 1$ N/m, $k_2 = 2$ N/m, $c_1 = 1$ N s/m, and $c_2 = 2$ N s/m. The natural frequencies are $\sqrt{2}/2$ rad/s and $\sqrt{2}$ rad/s and the fractional stiffness is chosen as $\bar{k} = 1.5$ N/m. This example uses the real order formulation.

The plots of α and $\bar{m}$ are obtained according to Eq. (2.45) and Eq. (2.48) and are given in Fig. 2.10. It is observed that $1 < \alpha < 2$ in the range of the natural frequencies of the I-2DOF. The value of α in this region captures the damping effects in the system. The plot of $\bar{m}$ in Fig. 2.10(b) indicates that $\bar{m}$ is a large quantity at low frequencies before asymptotically approaching a smaller value at higher frequencies that is closer to the values of the masses in the I-2DOF. In fact, $\bar{m}$ in Fig. 2.10(b) approaches a value of 1 kg $s^{\alpha-2}$, which is the same numerical value of m_1. Thus, at high frequencies, the F-SDOF model becomes a classical second order oscillator with a mass equal to the mass of the active DOF in the I-MDOF.

The loads in this example are $f_1(t) = 0.01\sin(2\pi\Omega_1 t)$ N and $f_2(t) = 0.01\cos(2\pi\Omega_2 t)$ N where $\Omega_1 = 0.08$ Hz and $\Omega_2 = 0.1$ Hz. Using the force correlation procedure, the force $f_2(t)$ acting on the omitted DOF is moved to a new force $f_{C,2}(t)$ acting on the chiefly active DOF.
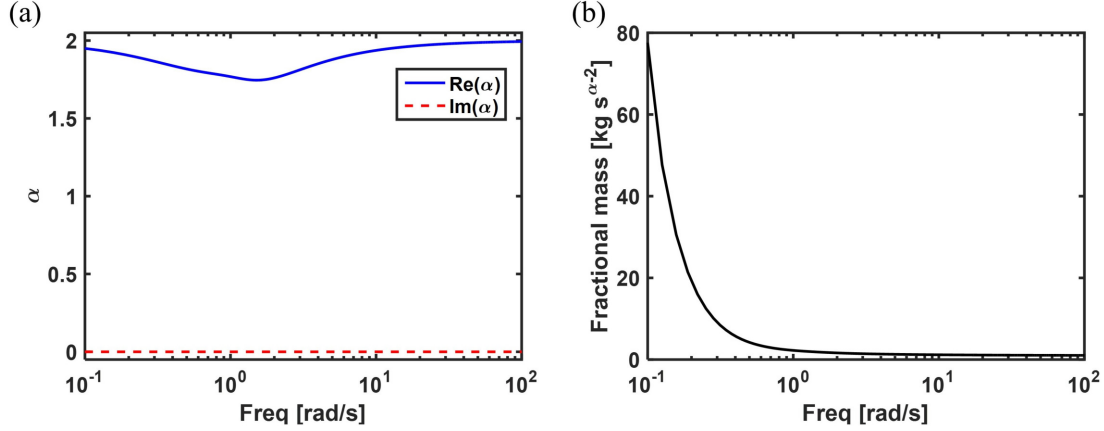
Figure 2.10. (a) The real fractional order α in the I-MDOF to F-SDOF reduction example. (b) The frequency dependent quantity $\bar{m}$ in the F-SDOF.

By taking the inverse Laplace transform of the ratio of transfer functions $H_{1,2}(s)/H_{1,1}(s)$, the correlation function $c_f(t)$ is obtained as

$$c_f(t) = \frac{1}{2}e^{-0.75t}\Big[\cos(0.97t) + 0.26\sin(0.97t)\Big]. \tag{2.54}$$

Thus, the correlated force $f_{C,2}(t)$ acting on the first mass is

$$f_{C,2}(t) = \frac{5}{1000}\int_0^t \cos(2\pi\Omega_2 t)e^{-0.75(t-\tau)}\Big\{\cos\Big[0.97(t-\tau)\Big] + 0.26\sin\Big[0.97(t-\tau)\Big]\Big\}\mathrm{d}\tau. \tag{2.55}$$

A plot of the total force $f_1(t)+f_{C,2}(t)$ on the chiefly active DOF is given in Fig. 2.11(a). The response of the reduced F-SDOF model is determined by taking the FFT of the harmonic load in Fig. 2.11(a) and following the multi-harmonic procedure given in § 2.3.3. The displacement of m_1 in the I-2DOF is obtained by performing a direct time integration using a 4th order Runge-Kutta numerical scheme on the system of differential equations with $f_1(t)$ acting on m_1 and $f_2(t)$ acting on m_2. The steady state response of the displacement of m_1 in the I-2DOF and the displacement of the F-SDOF is plotted in Fig. 2.11(b) (time range chosen after the transient responses had fully decayed). The curves in Fig. 2.11(b) match

74

extremely well, with only a maximum relative error of about 0.25% located at the peaks and valleys of the curves, thus illustrating the accuracy of the reduction procedure when there are multiple loads acting on both active and omitted DOF in the I-MDOF.
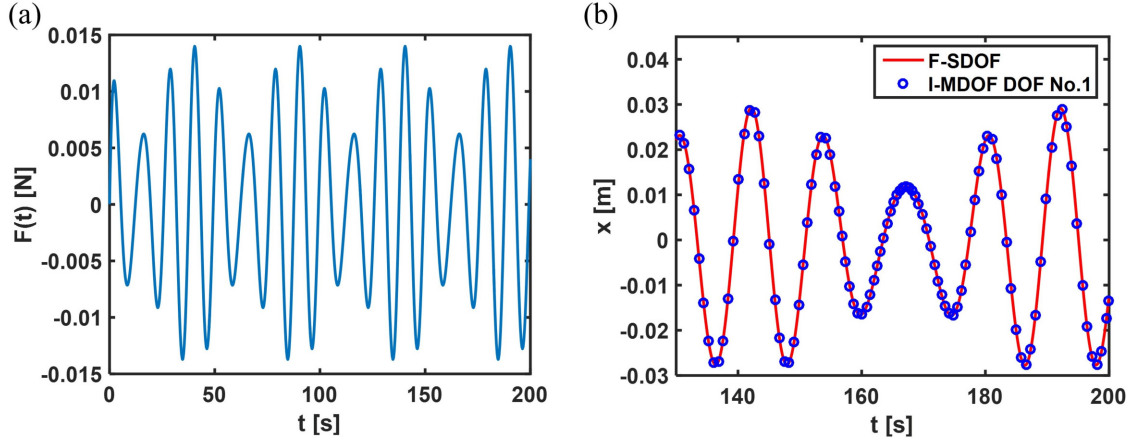
Figure 2.11. (a) The harmonic load acting on the active DOF of the I-MDOF. (b) Comparison of the steady state response of the active DOF of the I-MDOF and the F-SDOF.

2.5 Model Order Reduction from Integer Multiple Degrees of Freedom to Fractional Multiple Degrees of Freedom

Finally, this section considers the most generalized reduction procedure where multiple active DOFs in an I-MDOF are reduced to a dynamically equivalent F-NDOF. Two methods are again developed: one that produces a complex fractional order and the other which forces the fractional order to be real.

2.5.1 Approach Using Complex Fractional Orders

Predictably, the reduction from an I-MDOF to a F-NDOF is once again based on equating the transfer functions of the active DOFs in the I-MDOF to the TFs of the DOFs in the F-NDOF. Having developed the foundation of the fractional MOR in the preceding sections, this section immediately considers the specific reduction of an I-4DOF to a F-2DOF to demonstrate the reduction process. The active DOFs in this demonstration are the first and

third masses of the I-4DOF in Fig. 2.2(b). Furthermore, while all the necessary means to reduce systems with multiple loads consisting of multiple frequencies have been formulated, this example shall only include an external force on the first node in both the I-4DOF and in the F-2DOF to exclusively focus on the reduction process. The reduction technique shall yield responses of the F-2DOF's degrees which are equivalent to the responses of the active degrees in the I-4DOF. The TFs between the displacement and the force of active degrees in the integer order model have been obtained by using state-space to transfer function techniques. These transfer functions are called H_1 and H_3, respectively.

In order to match the responses of the two systems at the selected DOFs, impose $H_1 = G_1$ and $H_3 = G_2$ where G_1 and G_2 are given by Eqs. (2.23) and (2.24), respectively. The values of $\bar{m}_1$, $\bar{m}_2$, $\bar{k}_1$, and $\bar{k}_2$ are determined by lumping masses and springs from the integer model in a logical manner. Although different procedures to assign the fractional parameters can be selected, the proposed method here sets the total mass of the fractional model to be equal to the total mass of the integer model. In this reduction example, $\bar{m}_1 = Q(m_1 + m_2)$ and $\bar{m}_2 = Q(m_3 + m_4)$. Next, a relationship among the stiffness values of the F-NDOF is selected. Recall Eq. (2.47), in which a parameter $\bar{k}$ was the equivalent stiffness of springs in series. Define $\bar{k}_1 = \kappa\bar{k}$ and $\bar{k}_2 = \kappa\bar{k}/(1 - \kappa)$, where κ is an unknown coupling stiffness parameter. Notice that $\bar{k}_1$ and $\bar{k}_2$ are defined such that the equivalent stiffness of these springs in series is equal to the equivalent stiffness of the corresponding integer order model (Eq. (2.47)).

Equating the transfer functions of the fractional and integer order models, a set of two nonlinear equations in two unknowns (α and κ) is obtained. To solve for the complex order α and the stiffness coupling parameter κ (which will also be a complex quantity), a nonlinear numerical solver can be used.

Consider the I-4DOF that was used in the example in § 2.4.1. The equivalent mass coefficients in the F-2DOF are $\bar{m}_1 = \bar{m}_2 = 3$ kg s$^{\alpha-2}$. Using a nonlinear solver, the values of the order α and the coupling parameter κ are obtained over a frequency range. Figure 2.12(a) shows a plot of the value of α as a function of ω while Fig. 2.12(b) plots the value of κ as a function of ω.

The familiar trend in Fig. 2.13(a) where $1 < \text{Re}(\alpha) < 2$ is observed once again. Also, in the asymptotic limit, $\text{Re}(\alpha) \to 2$ while $\text{Im}(\alpha) \to 0$. Concerning κ, when the forcing
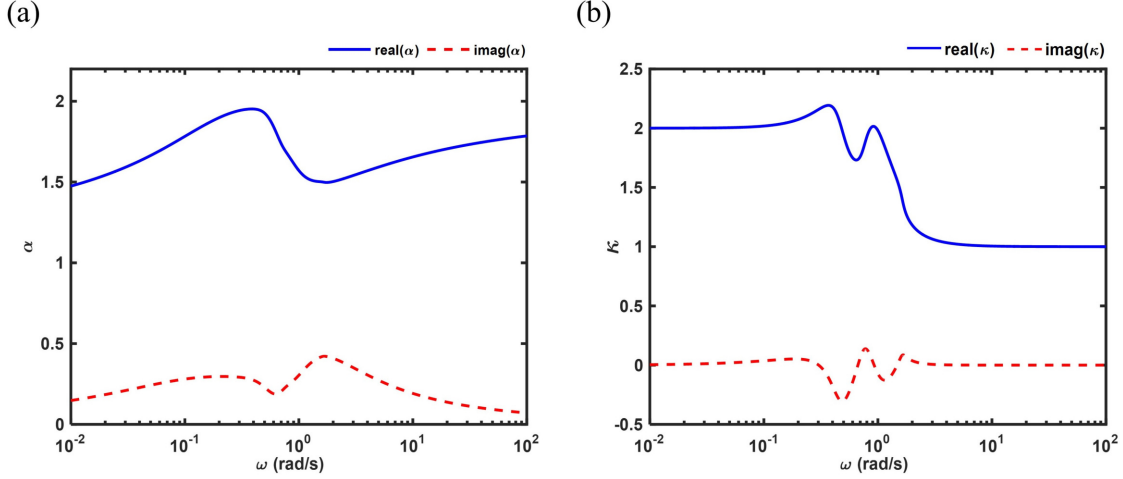
Figure 2.12. (a) The complex fractional order α for the reduction of the I-MDOF to F-NDOF. (b) The stiffness coupling parameter κ for the F-NDOF.

frequency is not near the resonance frequencies, κ is a purely real quantity. In fact, in the low frequency limit, $\kappa = 2$, while in the high frequency limit, $\kappa = 1$. At frequencies near and between the resonance frequencies, κ is a complex quantity. For this range in which the coupling parameter is complex, $\mathrm{Re}(\kappa)$ is representative of the stiffness in the I-4DOF while $\mathrm{Im}(\kappa)$ (along with the complex order α) contributes to the damping of the system. For very high frequencies, where both α and κ are integers, damping no longer plays a significant role in the steady state dynamics.

After obtaining the values of α and κ, the dynamic behavior of the fractional and integer models are verified to be equivalent. The magnitudes and phases over a frequency range are given in Fig. 2.13. Figure 2.13(a) depicts the magnitude and phase of the first degree (mass) in the I-4DOF and the first degree of the F-2DOF while Fig. 2.13(b) shows the magnitude and phase of the third degree in the I-4DOF and the second degree of the F-2DOF. The perfect overlap in the results illustrates that the dynamic response of the F-NDOF was able to exactly match the response of the active degrees of the I-MDOF.
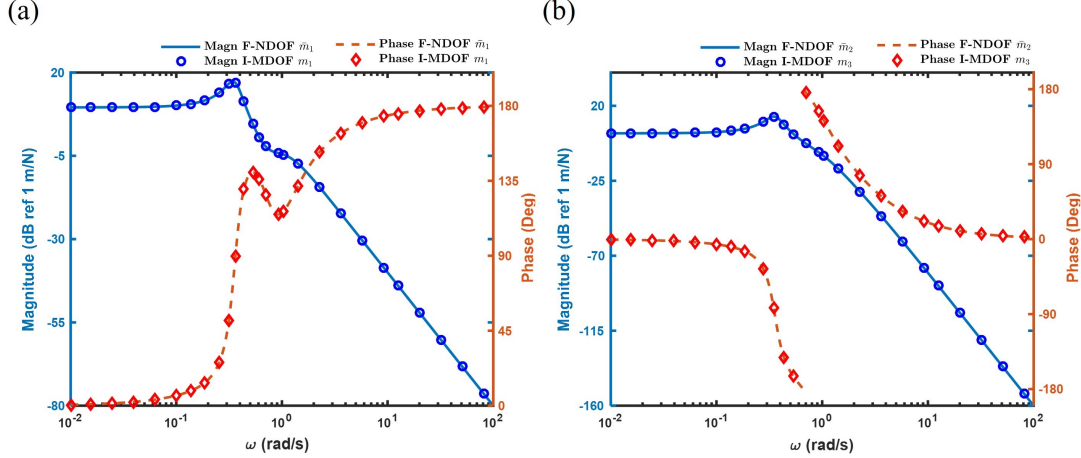
Figure 2.13. (a) Magnitude and phase of the transfer functions of m_1 in the I-MDOF model and $\bar{m}_1$ in the F-NDOF model. (b) Magnitude and phase of the transfer functions of m_3 in the I-MDOF model and $\bar{m}_2$ in the F-NDOF model.

2.5.2 Approach Using Real Fractional Orders

Again, if one wants to determine the displacements of the reduced fractional model, this dissertation strongly suggests using an approach that is restricted to purely real fractional orders to avoid the numerical errors associated with the evaluation of the complex Mittag-Leffler function. Unlike in § 2.3.2 and § 2.4.2, a closed-form expression forcing $\alpha \in \mathbb{R}$ is not easily obtainable. Thus, a nonlinear optimizer is implemented that sets the TFs of the F-NDOF equal to the TFs of the active DOF of the I-MDOF while minimizing the absolute value of the imaginary part of the fractional order α along with other parameters of the reduced F-NDOF including the fractional springs $\bar{k}_j$ and masses $\bar{m}_j$ for $j = 1, 2, \ldots, N$. In this way, the values of the fractional order and parameters can converge to real values while ensuring that the dynamics of the fractional system and the original integer order model remain equivalent. All fractional parameters in this case will be functions of frequency.

Admittedly, this optimization procedure is not the most ideal strategy since the computational expenses of the nonlinear least-squares optimization algorithm will increase quickly for reduced order models with a large number of DOFs and since all of the fractional masses and stiffnesses will vary as a function of frequency. However, due to previous considerations

78

on the accuracy of the complex order ML functions, the procedure is compelled to use this strategy to minimize the imaginary part of the fractional order α so that it can accurately calculate the displacements of the nodes of the F-NDOF according to the fractional modal analysis procedure given in § 2.2.2. Once research has advanced the numerical evaluation of the Mittag-Leffler function, it is suggested to use the complex order methodology in § 2.5.1 along with any additional considerations (e.g., the force correlation procedure from § 2.4.3 and the multi-harmonic procedure from § 2.3.3).

The illustration of the reduction uses the I-4DOF to F-2DOF example given in § 2.5.1 but with a single load $f_1(t) = 0.1\sin(2\pi\Omega t)$ N where $\Omega = 0.15$ Hz, acting on the first mass m_1. As a reminder, the first and third masses are the active DOFs. The optimization determines the values of α, $\bar{m}_1$, $\bar{m}_2$, $\bar{k}_1$, and $\bar{k}_2$ in the F-NDOF such that the TFs of the nodes in the F-NDOF ($G_{11}(s)$ and $G_{21}(s)$) are equal to the TFs of the active DOFs in the I-MDOF ($H_{11}(s)$ and $H_{31}(s)$, respectively). The nonlinear least-squares optimization algorithm used an initial evaluation point of $\alpha = 2$, $\bar{m}_1 = m_1$, $\bar{m}_2 = m_3$, $\bar{k}_1 = \left(\frac{1}{k_1} + \frac{1}{k_2}\right)^{-1}$, and $\bar{k}_2 = \left(\frac{1}{k_3} + \frac{1}{k_4}\right)^{-1}$. The plot of the fractional order α of the F-NDOF is given by Fig. 2.14.
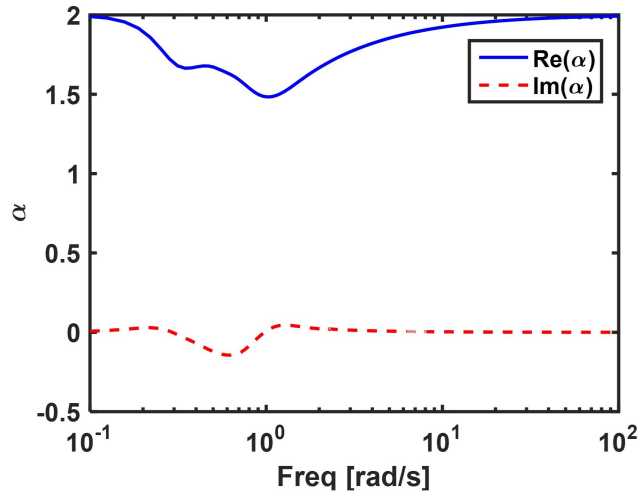
Figure 2.14. The fractional order α in the I-MDOF to F-NDOF reduction where the optimizer minimizes Im(α).

Some of the trends in Fig. 2.14 are similar to those in Fig. 2.10(a), specifically the fact that $1 < \text{Re}(\alpha) < 2$ near and in the range of the natural frequencies of the I-4DOF. This value of α again illustrates that the evolution from one resonance to the next occurs through a dynamic behavior which is locally fractional. For frequencies not near (both above and below) the range of natural frequencies, the fractional order α approaches an integer value of 2. Figure 2.14 also reveals that the fractional order α is not purely real for all frequencies. The imaginary part of α, while small, is non-zero for frequencies near the resonance frequency. Recall that the optimization minimized the imaginary part of α while still guaranteeing that $G_{11}(s) = H_{11}(s)$ and $G_{21}(s) = H_{31}(s)$. Clearly, a purely real value of α could not fully satisfy the equality of the transfer functions for near-resonance frequencies. Although the imaginary part of α is small in these cases, it is anticipated that some additional error in the plots of the displacements of the F-NDOF will occur. Plots of the the fractional masses and stiffnesses indicate that these fractional parameters also possess a small imaginary part just like α.

Having calculated the fractional parameters α, $\bar{m}_1$, $\bar{m}_2$, $\bar{k}_1$, and $\bar{k}_2$ in the F-2DOF, the steady state displacements of the fractional nodes in Fig. 2.15 are plotted by using the fractional modal analysis procedure given in § 2.2.2. In addition, the displacement of the active DOFs in the I-4DOF are obtained by performing a direct time integration using a 4th order Runge-Kutta numerical scheme on the system of integer order differential equations. As seen in Fig. 2.15, the steady state response of the displacement of m_1 and m_3 from the I-4DOF match the displacements of their corresponding reduced fractional nodes quite well, further validating the accuracy of the FC-MOR and fractional modal analysis. The maximum relative error between the curves in Fig. 2.15(a) is approximately 0.8% while it is 1.7% for Fig. 2.15(b). While the match between the I-MDOF and F-NDOF curves in Fig. 2.15 is fairly accurate, it is again stressed that the current means to evaluate complex order Mittag-Leffler functions is not yet nearly as accurate as its real order counterpart and can produce more pronounced errors for different example cases.
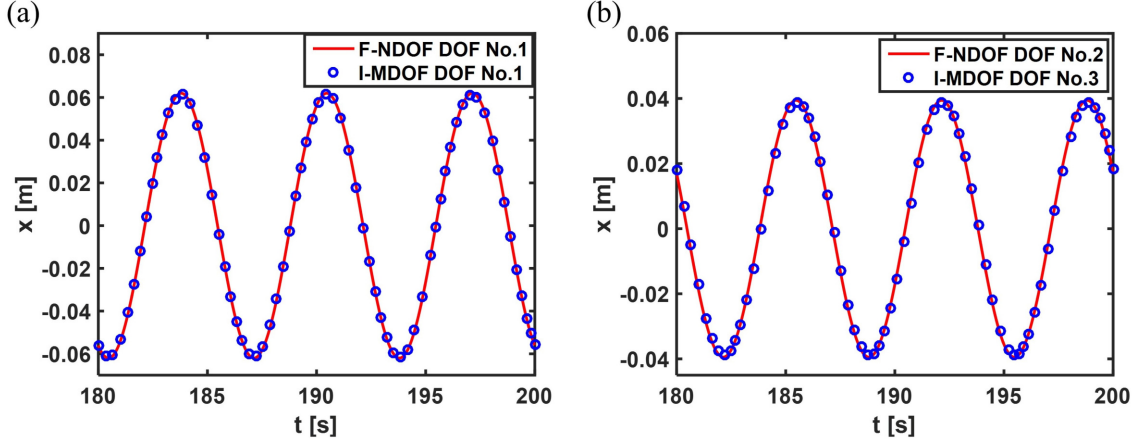
Figure 2.15. (a) The steady state response of the first node in the F-NDOF and the first node in the I-MDOF. (b) The steady state response of the second node in the F-NDOF and the third node in the I-MDOF.

2.6 System Identification from Numerical Data Using Fractional Oscillators

The formulation developed in the previous sections assumed that the initial I-MDOF system was provided and that an equivalent fractional form was sought. However, there are many situations of practical interest in the analysis of dynamical systems where measured experimental data is available and either the corresponding mathematical model or its coefficients are unknown; this class of problems is typically referred to as system identification. Over the years, a variety of system identification techniques have been proposed [130], [131]. One of the most common approaches for vibration problems relies on matching second order systems to individual resonances, therefore approximating the response of the system at resonance as a second order oscillator. This approach is also at the basis of the conventional half-power bandwidth method [13] for damping estimation. However, this approach has some important limitations. When the resonance frequencies of the multiple DOF system are too closely spaced, the local resonance is not well approximated by the single DOF oscillator. Also, in between resonances, the behavior of the system is typically fractional due to the coupling between two or more DOFs. This also explains why, when comparing numerical and experimental data, the largest discrepancies are often observed at frequencies off-resonance (regardless of the accuracy at resonance).

The category of system identification requires the selection of a dynamic model that is matched to the experimental data by properly tuning the model parameters. In this approach, the structure of the mathematical model (typically based on differential operators) is selected *a priori* without any detailed insight into the true physical nature of the system. Further, different operating regimes could require different models to achieve an accurate representation. Fractional models offer a much more general approach to the formulation of the equations of motion because they are capable of capturing in a single mathematical model a variety of physical mechanisms that would otherwise require multiple integer order models. The well-known change in the dynamic behavior of a system when transitioning from the low to the high frequency regime is a classical example of this phenomenon. In addition, it should be considered that typically the most appropriate dynamical model to describe a complex system is not known *a priori*; therefore, the use of a fractional model would allow a general approach in which the system identification process is allowed to converge to the most appropriate form of the governing equations. Therefore, in some respect, this approach would result in a model identification method.

The above considerations suggest that fractional order models can provide a powerful methodology for the dynamic characterization of complex systems from measured data. The system identification approach presented below produces an equivalent F-SDOF model. The data used to synthesize the dynamical models is called *measured* data. In practice, this reference data was generated numerically.

Assume that numerical (or experimental) data describing the dynamics of a system has been obtained at a single location or DOF. Source data will be presented in the form of Bode plots. The magnitude of the measured Bode plot at the desired frequency is M and the phase is ψ. Furthermore, assume that the total mass and stiffness of the system have been measured. An estimation of the system's stiffness could be obtained from the amplitude of the transfer function in the low frequency range (i.e., from the quasi-static limit). The mass and stiffness of the F-SDOF system are $\bar{m}$ and $\bar{k}$, respectively. Using these quantities in Eqs. (2.9) and (2.10), the parameters δ and χ can be obtained at a specific frequency. Rearranging these equations yields

$$\delta^2 + \chi^2 = \frac{1}{(M\bar{m})^2}, \tag{2.56}$$

$$\chi = \delta\tan(-\psi). \tag{2.57}$$

Substituting Eq. (2.57) into Eq. (2.56) results in

$$\delta^2\left[1 + \tan^2(-\psi)\right] = \frac{1}{(M\bar{m})^2}. \tag{2.58}$$

Using the identity $1+\tan^2(\cdot) = \sec^2(\cdot)$, Eq. (2.58) can be written as

$$\delta^2 = \frac{1}{(M\bar{m})^2\sec^2(-\psi)}. \tag{2.59}$$

Taking the positive root,

$$\delta = \frac{\cos(-\psi)}{\bar{m}M}. \tag{2.60}$$

Furthermore,

$$\chi = \frac{\sin(-\psi)}{\bar{m}M}. \tag{2.61}$$

Once δ and χ are obtained for a certain frequency ω, the nonlinear Eqs. (2.7) and (2.8) can be numerically solved to find the coefficients a and b in $\alpha = a + ib$ (assuming a complex order approach). This procedure can then be repeated over a range of frequencies to obtain the order α for many different frequencies for the corresponding F-SDOF model.

To illustrate the procedure, the Bode plot given in Fig. 2.16 is considered the measured data. In this example, $\bar{m} = 2.6044$ kg s$^{\alpha-2}$ and $\bar{k} = 0.4167$ N/m. Equations (2.60) and (2.61) are solved to find δ and χ for 100 different frequencies between 0.01 and 100 rad/s. For each frequency, the value of α can be found using Eqs. (2.7) and (2.8). Figure 2.17(a) shows the plot of $\alpha(\omega)$ for the selected example. To verify that the magnitude and phase of the F-SDOF match that of the synthetically generated data, Eqs. (2.9) and (2.10) are used to plot the magnitude and phase of the obtained F-SDOF. Figure 2.17(b) shows that the magnitude and phase of the F-SDOF match exactly the initial data. In order to assess the effectiveness of the fractional model approach, Fig. 2.17(b) also reports the magnitude and phase of an I-SDOF model created from the same input data. The parameters (mass, stiffness, damping) of the I-SDOF model were obtained by matching the transfer function of a second order system at a selected resonance frequency ($\omega = 0.3$ rad/s). This approach follows the traditional method used to extract physical parameters (e.g., damping) from experimental data. In fact, for sufficiently spaced resonances, the peaks in the magnitude of the TF are fit locally by single DOF systems. While the obtained I-SDOF provides a good match of the data near the resonance, larger discrepancies are observable off-resonance. This is especially evident when analyzing the magnitude and phase of the I-SDOF at higher frequencies in Fig. 2.17(b). In particular, the phase is far off from the synthetically generated data around $\omega = 1$ rad/s. Clearly, the I-SDOF model's range of validity is only valid near the frequency where the second order system was matched ($\omega = 0.3$ rad/s). If the synthetically generated data was represented with an integer order model across a wide frequency spectrum, the use of second order models with multiple DOFs would be required. The fractional model, however, is capable of representing the data across a wide frequency spectrum using only a single DOF whose fractional order is frequency-dependent.

It could be argued that the I-SDOF model in Fig. 2.17(b) was not fairly compared to the obtained F-SDOF since the magnitude and phase of the F-SDOF's transfer function were matched at multiple frequencies while the magnitude and phase of the TF of the I-SDOF were only matched at a single resonance frequency. The variability of the magnitude and phase as a function of frequency was captured by the F-SDOF's order α while no parameter in the I-SDOF was allowed to reflect this variation. In order to make a more fair
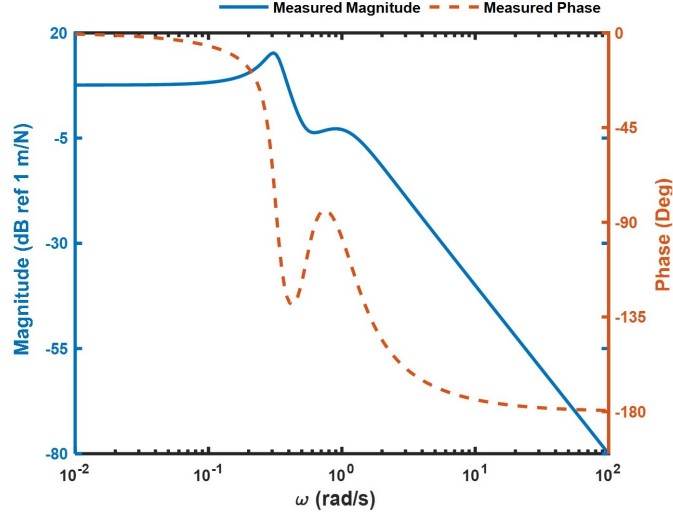
Figure 2.16. The synthetically generated magnitude and phase of a transfer function of position per force. In an experiment setting, this could be understood as the data measured at a specific structural location.
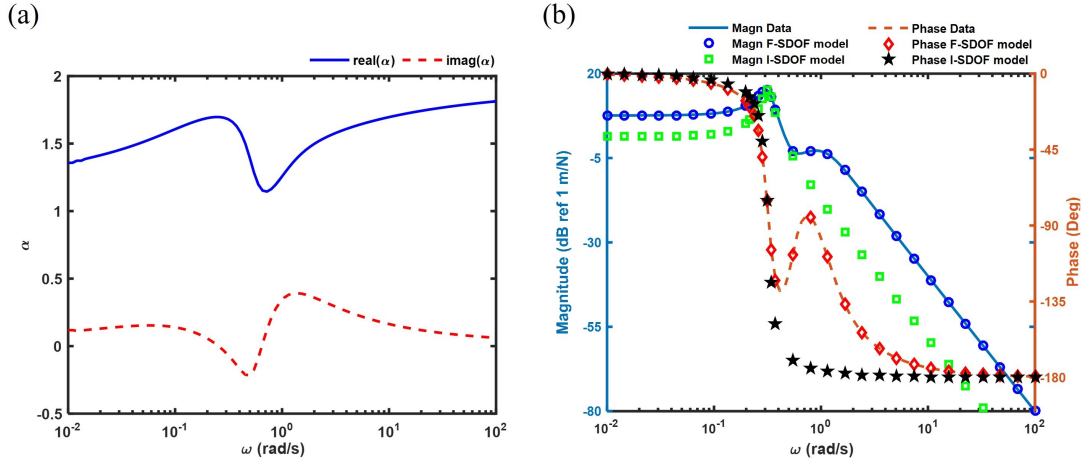
Figure 2.17. (a) The fractional order α corresponding to the F-SDOF model created from the synthetically generated data. (b) The magnitude and phase of synthetically generated data and of the transfer functions of the corresponding F-SDOF and I-SDOF models.

comparison, one can allow the mass and stiffness of the I-SDOF to vary as a function of frequency. The magnitude and phase of the synthetically generated data were matched to the TF of an I-SDOF at multiple frequencies. The damping ratio was set to $\zeta = 0.2$ in the

I-SDOF (value extracted at the resonance peak). The values of the mass and stiffness of the I-SDOF were allowed to vary so that the TF could match the magnitude and phase of the synthetically generated data at various frequencies. The damping coefficient was then obtained using $c = 2\zeta\sqrt{km}$ (and is thus, also a function of frequency). Figure 2.18(a) shows the corresponding frequency-dependent mass and stiffness obtained by such an approach. The values of m and k change rapidly near the resonance frequencies and then recover almost constant values in the asymptotic regimes. Figure 2.18(b) shows the comparison between the response of the I-SDOF and the synthetically generated data clearly indicating an exact match. This is not surprising because the methodology has essentially taken different I-SDOF systems and individually matched them at a given frequency.
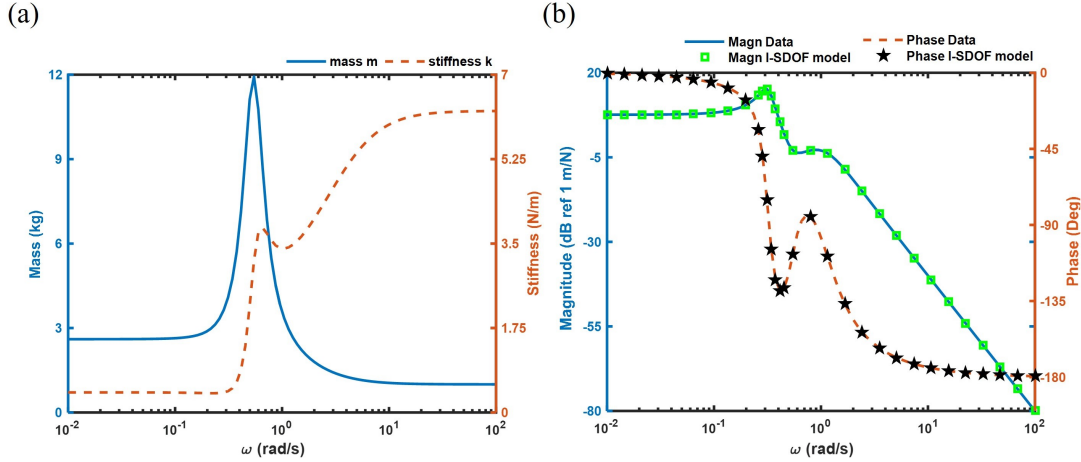
Figure 2.18. (a) The frequency-dependent mass and stiffness of the variable coefficient I-SDOF model. (b) The magnitude and phase of synthetically generated data and of the transfer function of the variable coefficient I-SDOF model.

Physically, this method is not a good reflection of the underlying physical system since the mass and stiffness change depending on the forcing frequency. Again, the F-SDOF model stands in clear contrast with this approach because it captures the frequency dependency entirely in the fractional order of the operator while admitting constant parameters (unless a real fractional order formulation is used; this is why the complex order method can be argued to be a more accurate physical representation). The fractional model is physically more

justifiable because 1) the mass and stiffness as defined in Eq. (2.35) are static properties of the system and their frequency dependence does not have a physical justification, and 2) many mechanical systems of practical interests have already been shown experimentally to exhibit fractional dynamics [31], [132]. Furthermore, the fractional model approach results in a model order identification that is conceptually more general than the parameter identification applicable to integer order models.

In order to perform a more realistic system identification for the I-SDOF, an alternative approach is implemented where both the mass and the stiffness are maintained constant and equal to their (static) low frequency values (as per Fig. 2.18(a), $m = 2.6044$ kg and $k = 0.4167$ N/m). The damping coefficient c varies as a function of frequency and serves as the only unknown parameter. This scenario is more realistic because many mechanical systems do exhibit frequency dependency of the damping properties. This situation results in an overdetermined system when considering the response to be matched as being composed of both magnitude and phase of the synthetically generated data. To solve this issue, only the magnitude of the I-SDOF's transfer function is matched to the magnitude of the data. The results of the parameter identification problem are shown in Fig. 2.19 in terms of the frequency-dependent damping coefficient and of the reconstructed transfer function. For the frequencies above and below the main resonance, it is found that $c = 0$, which is not surprising because the asymptotic response of a damped I-SDOF is not dependent on damping. The match of the TF presents a sufficiently good agreement for the magnitude but it shows a much larger error for the phase. This error is also reflected in the high frequency asymptotic value of the magnitude. The overall behavior is consistent with the fact that the unknown parameter was constructed to match the magnitude.

The results indicate that only the F-SDOF model with constant coefficients and a variable order dependent on frequency is able to exactly represent the synthetically generated data, even at frequencies far off-resonance. In principle, it would be possible to use an integer order model with multiple DOFs to match the data at the same level as the fractional model; however, using less DOFs is typically more desirable since it yields a simpler model. The use of fractional models does not only largely increase the accuracy of the parameter identification but it also effectively results in a model identification approach. In addition,
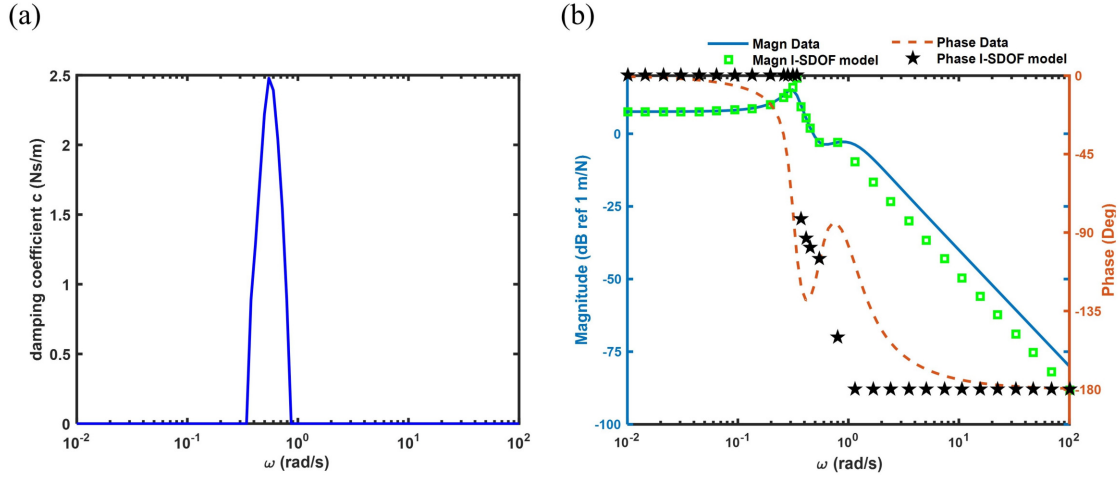
Figure 2.19. (a) The frequency-dependent damping coefficient of an I-SDOF with a constant mass and stiffness ($m = 2.6044$ kg and $k = 0.4167$ N/m). (b) The magnitude and phase of synthetically generated data and of the transfer function of the variable damping I-SDOF model.

the order of many complex dynamical systems of practical interest is not necessarily integer [34], [35], [37], [41]. Hence, it is physically more reasonable to use the fractional order model when fitting experimental data originated by a system with unknown structure.

The system identification method presented can be extended to the case of a multiple DOF system by using, as an example, N measured Bode plots obtained at different locations or degrees of interest. While achievable, a F-NDOF system identification method would be computationally expensive.

2.7 Conclusions

This chapter first advanced the fractional oscillator model to possess multiple degrees of freedom and determined their displacements via fractional modal analysis. Both the single and multiple degree of freedom fractional models served as the foundation of the fractional model order reduction procedure. The numerical results of the reduction examples in § 2.3, 2.4, and 2.5 illustrated the potential and the accuracy of the fractional model order reduction methodology to simulate the vibration of multi-DOF structures. The frequency-

dependency of the fractional operator enabled frequency-dependent modulation of the phase and amplitude which was at the basis of the broad spectrum of problems that can be addressed with this type of modeling. Analytical solutions of the displacements showed that the fractional order reduction procedures were able to 1) accurately (often times exactly) represent the dynamics of the active degrees of the initial system across a wide frequency spectrum, 2) represent the response of heterogeneous discrete parameter systems that included damping, and 3) capture the behavior between closely spaced resonance frequencies where the dynamics were locally fractional. These three features are key advantages over modal-based reduction techniques. However, at this stage, no claims can be made from this analysis about the computational efficiency of the fractional MOR compared to conventional MOR techniques. In fact, the tradeoffs between accuracy and computational time that are in integer, modal-based model order reduction techniques may still be present in the frequency-domain fractional model order reduction methodology for large discrete parameter systems containing hundreds or thousands of DOFs. Further studies are required to compare computational performance. Nonetheless, this chapter laid the groundwork for a new class of order reduction methodologies showing substantial potential to achieve reduced discrete parameter models with broadband applicability. Lastly, the fractional oscillator served as the basis of a system identification tool that permitted the order of the system to best represent the dynamical response at each frequency. This further strengthened the case for using fractional models for the vibration of discrete, heterogeneous structures.

3. FRACTIONAL ORDER MODELS FOR CONTINUOUS DYNAMICAL SYSTEMS

A portion of this chapter was previously published by the Journal of Sound & Vibration and is titled "Analysis of dispersion and propagation properties in a periodic rod using a space-fractional wave equation" [123] [DOI: https://doi.org/10.1016/j.jsv.2018.10.051]. Another portion of this chapter is, at the time of the deposit of this dissertation, under review for publication and is titled "Fractional Order Models for the Homogenization and Wave Propagation Analysis in Periodic Elastic Beams"

This chapter shifts from discrete to continuous models for heterogeneous structures and develops a space fractional homogenization representative of the elastic wave propagation in a 1D heterogeneous, periodic structure. While the periodic, heterogeneous structures considered here are not intrinsically fractional, the use of a space fractional wave equation leads to either closed-form analytical or accurate numerical solutions that well model the wave propagation through the periodic media, particularly for the dynamic attenuation of frequency band gaps. The proposed fractional order techniques are more similar to the low-frequency homogenization approaches discussed in § 1.1.2 where they replace the spatially varying quantities with homogenized material properties. From a mathematical perspective, the methodology converts a wave equation with spatially variable coefficients (i.e., the classical partial differential equation model for a periodic medium) into a space fractional differential equation with constant coefficients. As opposed to the long asymptotic expansions and subsequent computational costs of high-frequency homogenization techniques, the fractional methodology determines the space fractional order by equating the dispersion relationship of the integer order representation of the periodic structures to the dispersion relationship of the space fractional wave equation. The frequency-dependent fractional order is seen to possess a non-zero imaginary part for band gap frequencies, enabling the spatial attenuation of the wave front. Contents of the chapter include

- The derivation of the dispersion relationship of a bi-material, periodic rod, which will be necessary to calculate the corresponding order of the fractional model,

- The determination of the dispersion of a fractional rod model whose governing equation of motion is a space fractional wave equation,

- The values of the frequency-dependent fractional order which allow them to capture the behavior within the band gaps,

- An analysis of two closed-form solutions of the space fractional wave equation: one based on an exponential kernel and the other on a Mittag-Leffler kernel. Both sets of analytical solutions are shown to represent the axial wave propagation through a semi-infinite bi-material, periodic rod,

- The extension of the bi-material rod to a bi-material beam and the determination of its flexural dispersion characteristics based on either Euler-Bernoulli or Timoshenko beam theory,

- The study of the governing equations of a fractional beam model, its corresponding dispersion, and the obtained fractional orders,

- The application of a fractional finite element method to numerically evaluate the flexural displacement of a semi-infinite fractional beam.

3.1 Bi-Material Periodic Rod

3.1.1 Model

To synthesize a space fractional order model capable of capturing the dynamics of a periodic 1D waveguide, a benchmark structure made of two periodically alternating materials was chosen, as illustrated in Fig. 3.1. Figure 3.1 is an example of a 1D elastic metamaterial. This section will consider the structure in Fig. 3.1 as a solid rod whose Young's modulus and density vary periodically and in a step-like fashion between E_1, ρ_1 and E_2, ρ_2. Recall that rods can transmit only axial forces, i.e., no transverse or torsional loads are permitted. The equation of motion for the rod in Fig. 3.1 is

$$\frac{\partial}{\partial x}\left[E(x)A\frac{\partial u}{\partial x}\right] = \rho(x)A\frac{\partial^2 u}{\partial t^2},$$

(3.1)
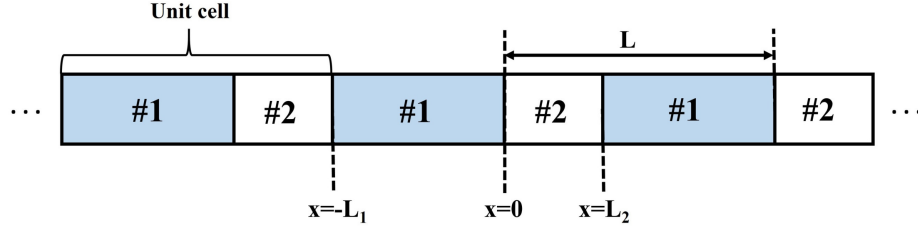
Figure 3.1. The 1D bi-material, periodic structure.

where x is the spatial coordinate, t is the time coordinate, E is Young's modulus, A is the cross-sectional area, ρ is the density, and u is the axial displacement. The value of A in the periodic rod system is taken to be constant. Alternatively, Eq. (3.1) can be written as

$$E_m A_m \frac{\partial^2 u}{\partial x^2} - \rho_m A_m \frac{\partial^2 u}{\partial t^2} = 0, \tag{3.2}$$

where $m = 1 \, \forall \, x \in [-L_1 + NL, NL]$ and $m = 2 \, \forall \, x \in [NL, L_2 + NL]$ $(N \in \mathbb{I})$. The analytical solution of Eq. (3.1) is known only for very specific variations of E, ρ, and A [133].

The corresponding fractional rod model will be formulated in § 3.2. Before that, the dispersion relation of Eq. (3.1) is determined since the dispersion relationship will 1) show where the frequency band gaps of the periodic rod are located and 2) provide a means to calculate the space fractional order of the corresponding fractional rod.

3.1.2 Dispersion Relationship

While there are a variety of means (including experimental) to determine the expression of the dispersion relationship of Eq. (3.1), this section chooses to calculate the dispersion relation via a spectral method along with Block-Floquet theory [134]. The Bloch-Floquet methodology was chosen because it is well established for periodic media [135]. Note that while the Bloch-Floquet theory is helpful to determine the dispersion properties of periodic media, it does not allow obtaining the forced response solution. To obtain these solutions with traditional models, one typically needs to numerically solve the equations.

Consider a generic uniform, homogeneous rod element of length l with two nodes located on the ends. The longitudinal displacement at an arbitrary point in this finite uniform rod can be written as [134]

$$\hat{u}(x) = \hat{g}_1(x)\hat{u}_1 + \hat{g}_2\hat{u}_2, \tag{3.3}$$

where the hat notation (e.g., $\hat{u}$) is a frequency-domain quantity, $\hat{u}_1 = \hat{u}(0)$, $\hat{u}_2 = \hat{u}(l)$, and $\hat{g}_1$ and $\hat{g}_2$ are frequency-dependent shape functions defined as

$$\hat{g}_1 = \frac{\mathrm{e}^{-ikx} - \mathrm{e}^{-ik(2l-x)}}{1 - \mathrm{e}^{-2ikl}}, \tag{3.4}$$

$$\hat{g}_2 = \frac{-\mathrm{e}^{-ik(l+x)} + \mathrm{e}^{-ik(l-x)}}{1 - \mathrm{e}^{-2ikl}}, \tag{3.5}$$

where k is the wavenumber. The wavenumber of a homogeneous rod element is

$$k = \omega\sqrt{\frac{\rho A}{EA}}, \tag{3.6}$$

where ω is the angular frequency. The internal forces in the rod are

$$F = EA\frac{\partial u}{\partial x}. \tag{3.7}$$

The member loads at each end of the rod are $\hat{F}_1 = -F(0)$ and $\hat{F}_2 = F(l)$. Substituting this and Eqs. (3.4), (3.5), (3.7) into Eq. (3.3) yields the matrix equation

$$\begin{bmatrix} \hat{F}_1 \\ \hat{F}_2 \end{bmatrix} = \frac{EA}{l} \frac{ikl}{(1 - \mathrm{e}^{-2ikl})} \begin{bmatrix} 1 + \mathrm{e}^{-2ikl} & -2\mathrm{e}^{-ikl} \\ -2\mathrm{e}^{-ikl} & 1 + \mathrm{e}^{-2ikl} \end{bmatrix} \begin{bmatrix} \hat{u}_1 \\ \hat{u}_2 \end{bmatrix}. \tag{3.8}$$

Equation (3.8) can be written for each uniform portion of the unit cell in Fig. 3.1. Combining the two elements produces three nodes: two at the ends of the unit cell and the other at the discontinuity interface. The node at the discontinuity interface divides the periodic rod element into two subdomains whose matrix equations are

$$\begin{bmatrix} \hat{F}_1 \\ \hat{F}_2 \end{bmatrix} = \begin{bmatrix} \hat{a}_{11} & \hat{a}_{12} \\ \hat{a}_{21} & \hat{a}_{22} \end{bmatrix} \begin{bmatrix} \hat{u}_1 \\ \hat{u}_2 \end{bmatrix}, \tag{3.9}$$

$$\begin{bmatrix} \hat{F}_2 \\ \hat{F}_3 \end{bmatrix} = \begin{bmatrix} \hat{b}_{11} & \hat{b}_{12} \\ \hat{b}_{21} & \hat{b}_{22} \end{bmatrix} \begin{bmatrix} \hat{u}_2 \\ \hat{u}_3 \end{bmatrix}, \tag{3.10}$$

$$\hat{a}_{11} = \hat{a}_{22} = \frac{E_1 A_1}{L_1} \frac{ik_1 L_1}{(1 - \mathrm{e}^{-2ik_1 L_1})} (1 + \mathrm{e}^{-2ik_1 L_1}), \tag{3.11}$$

$$\hat{a}_{12} = \hat{a}_{21} = \frac{E_1 A_1}{L_1} \frac{ik_1 L_1}{(1 - \mathrm{e}^{-2ik_1 L_1})} (-2\mathrm{e}^{-ik_1 L_1}), \tag{3.12}$$

$$\hat{b}_{11} = \hat{b}_{22} = \frac{E_2 A_2}{L_2} \frac{ik_2 L_2}{(1 - \mathrm{e}^{-2ik_2 L_2})} (1 + \mathrm{e}^{-2ik_2 L_2}), \tag{3.13}$$

$$\hat{b}_{12} = \hat{b}_{21} = \frac{E_2 A_2}{L_2} \frac{ik_2 L_2}{(1 - \mathrm{e}^{-2ik_2 L_2})} (-2\mathrm{e}^{-ik_2 L_2}), \tag{3.14}$$

$$k_1 = \omega \sqrt{\frac{\rho_1 A_1}{E_1 A_1}}, \tag{3.15}$$

$$k_2 = \omega \sqrt{\frac{\rho_2 A_2}{E_2 A_2}}. \tag{3.16}$$

Assembling Eqs. (3.9) and (3.10) together yields

$$\begin{bmatrix} \hat{F}_1 \\ \hat{F}_2 \\ \hat{F}_3 \end{bmatrix} = \begin{bmatrix} \hat{a}_{11} & \hat{a}_{12} & 0 \\ \hat{a}_{21} & \hat{a}_{22} + \hat{b}_{11} & \hat{b}_{12} \\ 0 & \hat{b}_{21} & \hat{b}_{22} \end{bmatrix} \begin{bmatrix} \hat{u}_1 \\ \hat{u}_2 \\ \hat{u}_3 \end{bmatrix}. \tag{3.17}$$

Performing a quasi-static condensation on the middle node results in $\hat{F}_2 = 0$. Thus, $\hat{u}_2$ can be written in terms of $\hat{u}_1$ and $\hat{u}_3$ as

$$\hat{u}_2 = -\frac{\hat{a}_{21}}{\hat{a}_{22} + \hat{b}_{11}} \hat{u}_1 - \frac{\hat{b}_{12}}{\hat{a}_{22} + \hat{b}_{11}} \hat{u}_3. \tag{3.18}$$

Substituting Eq. (3.18) into Eq. (3.17) results in

$$\begin{bmatrix} \hat{F}_1 \\ \hat{F}_3 \end{bmatrix} = \begin{bmatrix} \hat{d}_{11} & \hat{d}_{12} \\ \hat{d}_{21} & \hat{d}_{22} \end{bmatrix} \begin{bmatrix} \hat{u}_1 \\ \hat{u}_3 \end{bmatrix}, \tag{3.19}$$

$$\hat{d}_{11} = \hat{a}_{11} - \frac{\hat{a}_{21}\hat{a}_{12}}{\hat{a}_{22} + \hat{b}_{11}}, \tag{3.20}$$

$$\hat{d}_{12} = -\frac{\hat{b}_{12}\hat{a}_{12}}{\hat{a}_{22} + \hat{b}_{11}}, \tag{3.21}$$

$$\hat{d}_{21} = -\frac{\hat{b}_{21}\hat{a}_{21}}{\hat{a}_{22} + \hat{b}_{11}}, \tag{3.22}$$

$$\hat{d}_{22} = \hat{b}_{22} - \frac{\hat{b}_{12}\hat{b}_{21}}{\hat{a}_{22} + \hat{b}_{11}}. \tag{3.23}$$

Equation (3.19) can be arranged as

$$\begin{bmatrix} \hat{u}_L \\ \hat{F}_L \end{bmatrix} = \begin{bmatrix} -\frac{\hat{d}_{11}}{\hat{d}_{12}} & -\frac{1}{\hat{d}_{12}} \\ \hat{d}_{21} - \frac{\hat{d}_{11}\hat{d}_{22}}{\hat{d}_{12}} & -\frac{\hat{d}_{22}}{\hat{d}_{21}} \end{bmatrix} \begin{bmatrix} \hat{u}_0 \\ \hat{F}_0 \end{bmatrix}, \tag{3.24}$$

where $\hat{u}_0 = \hat{u}_1$, $\hat{u}_L = \hat{u}_3$, $\hat{F}_0 = -\hat{F}_1$, and $\hat{F}_L = \hat{F}_3$. Let the 2x2 transfer matrix in Eq. (3.24) be called $\mathbf{T}$. In a periodic arrangement consisting of N unit cells, the general response is given as

$$\begin{bmatrix} \hat{u}_N \\ \hat{F}_N \end{bmatrix} = \mathbf{T} \cdot \mathbf{T} \cdot \mathbf{T} \cdot ... \mathbf{T} \begin{bmatrix} \hat{u}_0 \\ \hat{F}_0 \end{bmatrix}, \tag{3.25}$$

with N $\mathbf{T}$ matrices multiplied by each other. According to Bloch-Floquet theory, the relationships between the displacements and forces at the ends of the rod element can also be written as

$$\begin{bmatrix} \hat{u}_L \\ \hat{F}_L \end{bmatrix} = \begin{bmatrix} \mathrm{e}^{-\mathrm{i}\mu L} & 0 \\ 0 & \mathrm{e}^{-\mathrm{i}\mu L} \end{bmatrix} \begin{bmatrix} \hat{u}_0 \\ \hat{F}_0 \end{bmatrix}, \tag{3.26}$$

where $\hat{u} = \tilde{A}\mathrm{e}^{-\mathrm{i}\mu x}$, $\tilde{A}$ is an unknown and μ is the Floquet wavenumber. Equating Eqs. (3.24) and (3.26) produces

$$\begin{bmatrix} -\frac{\hat{d}_{11}}{\hat{d}_{12}} - \mathrm{e}^{-\mathrm{i}\mu L} & -\frac{1}{\hat{d}_{12}} \\ \hat{d}_{21} - \frac{\hat{d}_{11}\hat{d}_{22}}{\hat{d}_{12}} & -\frac{\hat{d}_{22}}{\hat{d}_{21}} - \mathrm{e}^{-\mathrm{i}\mu L} \end{bmatrix} \begin{bmatrix} \hat{u}_0 \\ \hat{F}_0 \end{bmatrix} = \vec{0}. \tag{3.27}$$

The characteristic equation of the eigenvalue problem given by Eq. (3.27) is

$$\frac{1 + \mathrm{e}^{-2\mathrm{i}\mu L}}{\mathrm{e}^{-\mathrm{i}\mu L}} + \frac{\hat{d}_{11} + \hat{d}_{22}}{\hat{d}_{12}} = 0. \tag{3.28}$$

Simplifying Eq. (3.28) produces the desired dispersion relation relating the wavenumber μ to the frequency ω of the bi-material periodic rod as

$$\cos(\mu L) = \cos\left(\omega\frac{L_1}{c_1}\right)\cos\left(\omega\frac{L_2}{c_2}\right) - \frac{1}{2}\Psi\sin\left(\omega\frac{L_1}{c_1}\right)\sin\left(\omega\frac{L_2}{c_2}\right), \tag{3.29}$$

where

$$\Psi = \frac{A_1 E_1 c_2}{A_2 E_2 c_1} + \frac{A_2 E_2 c_1}{A_1 E_1 c_2}, \tag{3.30}$$

and c_1 is the wave speed in material #1 and c_2 is the wave speed in material #2. Figure 3.2 plots the dispersion relationship for an aluminum-brass periodic rod ($E_1 = 70$ GPa, $\rho_1 = 2700$ kg/m³, $E_2 = 110$ GPa, $\rho_2 = 8100$ kg/m³) where each portion is unit length ($L_1 = L_2 = 1$ m). The frequency band gaps, occurring where $\mathrm{Im}(\mu)$ is nonzero, of the aluminum-brass periodic beam are depicted in Fig. 3.2 and are highlighted in gray. Again, these band gaps are past the long wavelength limit of the classical low-frequency homogenization techniques and thus, are not captured by such models. To develop an effective homogenization model capable of capturing the band gaps, the fractional rod is considered. Note, however, that the bi-material periodic rod is not an intrinsically fractional system (like some viscoelastic or

fractal media). Nonetheless, it is observed that using a fractional rod model will provide an analytical advantage in representing the wave propagation through the bi-material periodic rod.
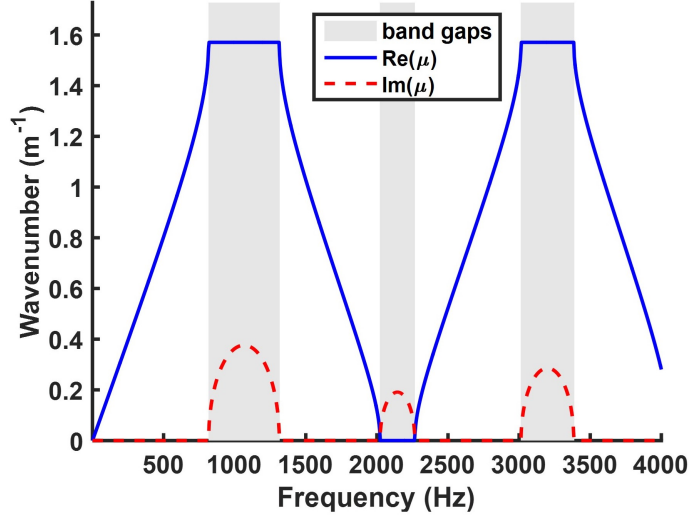
Figure 3.2. Dispersion of the aluminum-brass periodic rod with band gaps depicted. The curve is wrapped over the first Brillouin zone.

3.2 Fractional Rod Model

The fractional rod is very similar to the classical uniform rod, except for the fact its EOM contains a space fractional derivative. The dynamics of the fractional rod are governed by

$$\bar{c}^2 \frac{\partial^\alpha u}{\partial x^\alpha} = \frac{\partial^2 u}{\partial t^2}, \tag{3.31}$$

where α is the order of the fractional derivative and $\bar{c}$ is the fractional wave "speed"; that is, an equivalent wave velocity having dimensions $\frac{(\mathrm{m})^{\alpha/2}}{\mathrm{s}}$. Note how if $\alpha = 2$, Eq. (3.31) becomes the classical wave equation that governs the wave propagation through a uniform rod. For this reason, Eq. (3.31) is often referred to as the space fractional wave equation.

The space fractional derivative in Eq. (3.31) is taken as a left-handed Caputo derivative (see Eq. (1.17)) because it allows a more direct treatment of the boundary conditions. Using the fractional rod model will provide a pathway to obtain a closed-form analytical solution to represent the dynamics of the bi-material, periodic rod. The closed-form analytical solutions can play a major role towards the development of computationally efficient forward and inverse problems and can also have important implications for inverse problems in material design and remote sensing. Before determining the analytical solution to the space fractional wave equation, the homogenization needs to determine the fractional parameters (i.e., α and $\bar{c}$) such that the fractional rod acts as an accurate representation of the bi-material, periodic rod, as shown in Fig. 3.3. As previously stated, the fractional order α is determined by equating the dispersion relationship of Eq. (3.1) to the dispersion relationship of Eq. (3.31).
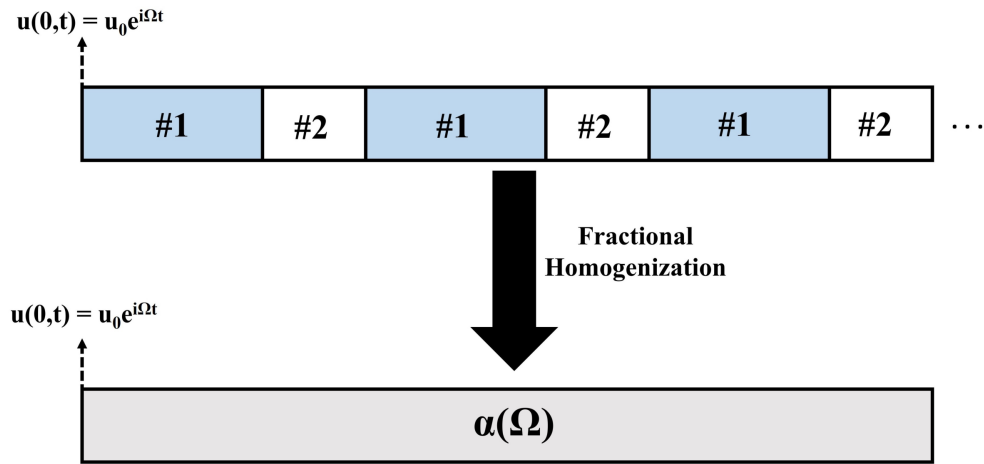
Figure 3.3. Fractional homogenization process where the fractional model is developed so that its dynamic response well represents that of the corresponding bi-material structure.

3.2.1 Dispersion Relationship

To determine the dispersion relationship of Eq. (3.31), the lower bound in the Caputo fractional derivative (quantity a in Eq. (1.17)) must be considered since it has a direct impact

on the evaluation of the derivative. If the fractional derivative in Eq. (3.31) has a lower bound of $-\infty$, then the following the property can be used:

$$^{C}_{-\infty}D^{\alpha}_{x}(\mathrm{e}^{ax}) = a^{\alpha}\mathrm{e}^{ax}, \tag{3.32}$$

where $^{C}_{-\infty}D^{\alpha}_{x}$ is the operational notation for a Caputo fractional derivative of order α [77]. In this case, since the fractional derivative of an exponential function is an exponential function, the solution of the fractional differential Eq. (3.31) can be assumed as the generic complex exponential representation of harmonic waves; that is,

$$u(x,t) = \tilde{A}\mathrm{e}^{\mathrm{i}(\omega t - kx)} + \tilde{B}\mathrm{e}^{\mathrm{i}(\omega t + kx)}. \tag{3.33}$$

Substitution of the first term on the right-hand side of Eq. (3.33) into Eq. (3.31) produces the dispersion relationship of the space fractional wave equation as

$$k = \mathrm{i}\left(-\frac{\omega^{2}}{\bar{c}^{2}}\right)^{1/\alpha}. \tag{3.34}$$

The substitution of the second term of the right hand side of Eq. (3.33) into Eq. (3.31) produces the negative value of Eq. (3.34).

If the Caputo fractional derivative has a lower terminal other than $-\infty$, the property given by Eq. (3.32) is no longer true. The fractional derivative of an exponential function is no longer an exponential function; rather, the fractional derivative of the exponential function is a Mittag-Leffler function (see Eq. (1.14)). For instance, if the lower terminal of the Caputo fractional derivative is 0, the Caputo fractional derivative of the exponential solution is

$$^{C}_{0}D^{\alpha}_{x}(\mathrm{e}^{ax}) = a^{n}x^{n-\alpha}\mathrm{E}_{1,n-\alpha+1}(ax), \tag{3.35}$$

where n is α rounded up to the next integer. Thus, use of Eq. (3.33) as the assumed form of the axial displacement will produce a complicated dispersion relationship consisting of Mittag-Leffler functions. Rather than assuming the axial displacement is given by Eq. (3.33), the solution to Eq. (3.31) can be stated in the form of the following ansatz as

$$u(x,t) = e^{i\omega t}\left\{\tilde{A}\mathrm{E}_{\alpha,1}\left[(-ikx)^{\alpha}\right] + \tilde{B}x\mathrm{E}_{\alpha,2}\left[(-ikx)^{\alpha}\right]\right\}, \tag{3.36}$$

where $\mathrm{E}(\cdot)$ is the ML function, $\tilde{A} = u(0,t)$ and $\tilde{B} = \frac{\mathrm{d}u(0,t)}{\mathrm{d}x}$. It is straightforward to verify that the solution given by Eq. (3.36) satisfies Eq. (3.31) by utilizing the following three formulas. First, the left-handed Riemann-Liouville derivative of a ML function [61] is

$$_{0}^{RL}D_{x}^{\alpha}\left[x^{p_2-1}E_{p_1,p_2}(Cx^{p_1})\right] = x^{p_2-\alpha-1}E_{p_1,p_2-\alpha}(Cx^{p_1}), \tag{3.37}$$

where α is the order of the derivative, C is a constant, and p_1 and p_2 are the generic parameters of the two parameter Mittag-Leffler function. The analytical relation between the Riemann-Liouville and Caputo derivatives is

$$_{0}^{C}D_{x}^{\alpha}[u(x)] = _{0}^{RL}D_{x}^{\alpha}[u(x)] - \sum_{n=0}^{N-1}\frac{\mathrm{d}^{n}u}{\mathrm{d}x^{n}}(0)\frac{x^{-\alpha+n}}{\Gamma(-\alpha+n+1)}, \tag{3.38}$$

where N is α rounded up to the next integer [67]. Finally, an important recurrence relation of the Mittag-Leffler function is [136]

$$E_{p_1,p_2}(z) = zE_{p_1,p_1+p_2}(z) + \frac{1}{\Gamma(p_2)}. \tag{3.39}$$

Substituting Eq. (3.36) into Eq. (3.31) and using the properties from Eq. (3.37) and Eq. (3.38) yields

$$\mathrm{e}^{\mathrm{i}\omega t}\left\{\tilde{A}x^{-\alpha}E_{\alpha,1-\alpha}\Big[(-\mathrm{i}k)^{\alpha}x^{\alpha}\Big] + \tilde{B}x^{1-\alpha}E_{\alpha,2-\alpha}\Big[(-\mathrm{i}k)^{\alpha}x^{\alpha}\Big]\right.$$

$$\left.-\tilde{A}\frac{x^{-\alpha}}{\Gamma(1-\alpha)} - \tilde{B}\frac{x^{1-\alpha}}{\Gamma(2-\alpha)}\right\} = -\frac{\omega^2}{\bar{c}^2}u. \tag{3.40}$$

Using Eq. (3.39) simplifies the expression to

$$\mathrm{e}^{\mathrm{i}\omega t}\left\{\tilde{A}x^{-\alpha}\left[(-\mathrm{i}k)^{\alpha}x^{\alpha}E_{\alpha,1}\Big[(-\mathrm{i}k)^{\alpha}x^{\alpha}\Big] + \frac{1}{\Gamma(1-\alpha)}\right]\right.$$

$$+\tilde{B}x^{1-\alpha}\left[(-\mathrm{i}k)^{\alpha}x^{\alpha}E_{\alpha,2}\Big[(-\mathrm{i}k)^{\alpha}x^{\alpha}\Big] + \frac{1}{\Gamma(2-\alpha)}\right] \tag{3.41}$$

$$\left.-\tilde{A}\frac{x^{-\alpha}}{\Gamma(1-\alpha)} - \tilde{B}\frac{x^{1-\alpha}}{\Gamma(2-\alpha)}\right\} = -\frac{\omega^2}{\bar{c}^2}u.$$

After substituting u according to Eq. (3.36) and canceling like-terms, the dispersion relationship is obtained as

$$k = \mathrm{i}\left(-\frac{\omega^2}{\bar{c}^2}\right)^{1/\alpha}. \tag{3.42}$$

Equation (3.42) is exactly the same as Eq. (3.34). Therefore, both the exponential and Mittag-Leffler solutions produce the same dispersion relationship under the proper assumptions for the bounds of the differ-integral operator. Further discussion on which solution form (Eq. (3.33) or Eq. (3.36)) should be implemented is found in § 3.3.

3.2.2 Calculation of the Fractional Order

In order to identify the fractional order α which guarantees the fractional rod is dynamically equivalent to the bi-material periodic rod, μ from Eq. (3.29) is equated to k from Eq. (3.42). To determine μ from Eq. (3.29), an inverse cosine must be taken which yields a non-unique solution. The theory used to derive Eq. (3.29) used a solution form $\tilde{A}\mathrm{e}^{-\mathrm{i}\mu x}$. For the solution to exponentially decay in the band gaps, the imaginary part of μ must be nega-

tive. In order to meet this requirement, the left hand side of Eq. (3.29) should be $\cos(-\mu L)$. Thus, to solve for the fractional order α, μ from the $\cos(-\mu L)$ solution from Eq. (3.29) is equated to k from Eq. (3.42). The procedure results in

$$\frac{1}{L}\cos^{-1}\left[\cos\left(\omega\frac{L_1}{c_1}\right)\cos\left(\omega\frac{L_2}{c_2}\right) - \frac{1}{2}\Psi\sin\left(\omega\frac{L_1}{c_1}\right)\sin\left(\omega\frac{L_2}{c_2}\right)\right] = -\mathrm{i}\left(-\frac{\omega^2}{\bar{c}^2}\right)^{1/\alpha}, \qquad (3.43)$$

which can be numerically solved for α. Before solving for α, additional assumptions must be made for the value of the equivalent fractional wave speed $\bar{c}$. Two approaches for selecting the value of $\bar{c}$ are considered.

Equivalent Fractional Wave Speed: Constant Speed Assumption

A reasonable assumption for the value of the equivalent wave speed is to take $\bar{c}$ to be a constant value provided by a conventional homogenization approach in the long wavelength limit. According to [23], [137], the effective modulus $\bar{E}$ of the periodic rod can be obtained by the inverse rule of mixtures as

$$\frac{1}{\bar{E}} = \frac{L_1/(L_1 + L_2)}{E_1} + \frac{L_2/(L_1 + L_2)}{E_2}, \qquad (3.44)$$

while the effective density $\bar{\rho}$ is given by a weighted sum as

$$\bar{\rho} = \rho_1 L_1/(L_1 + L_2) + \rho_2 L_2/(L_1 + L_2). \qquad (3.45)$$

The effective wave speed is then defined to be

$$\bar{c} = Q\sqrt{\frac{\bar{E}}{\bar{\rho}}}, \qquad (3.46)$$

103

where Q is a dimensional multiplicative factor that ensures units consistency (here, $Q = \mathrm{m}^{\alpha/2-1}$). Setting $\bar{c}$ according to Eq. (3.46) and substituting into Eq. (3.43) produces the frequency-dependent order α as

$$\alpha = \frac{2\ln(\omega/\bar{c}) + \mathrm{i}\pi}{\ln(\mu) + \mathrm{i}\pi/2}. \tag{3.47}$$

A plot of Eq. (3.47) for the aluminium-brass periodic rod is shown in Fig. 3.4 and reveals the fractional order is a complex number which indicates that the fractional equivalent (homogenized) model will be described by complex order differ-integral operators. A complex order derivative allows for the frequency-dependent modulation of both the phase and the amplitude [84] of harmonic components, therefore allowing for virtually unrestricted matching of the dispersion relations.

In the low frequency range before the first band gap (typically considered as the range of validity for homogenization models under the long wavelength assumption), the value of α is purely real and equal to 2. Thus, within the long wavelength limit, the space fractional wave model with a constant equivalent speed reduces to the classic integer order homogenized model. Moving to higher frequencies within the first band gap shows $\mathrm{Re}(\alpha) < 2$ and $\mathrm{Im}(\alpha) \neq 0$ except for few selected values of ω. This behavior is consistent with the expected amplitude attenuation characteristic of a band gap and with the fact that space fractional wave equations with $1 < \mathrm{Re}(\alpha) < 2$ correspond to spatially attenuated waves [74]–[77]. As band gaps in the higher frequency range are considered, it is observed that, *typically*, $\mathrm{Re}(\alpha) < 2$. This is not always the case, as seen by the fact that $\mathrm{Re}(\alpha)$ is slightly greater than 2 for frequencies at the upper edge of the band gaps (in the third band gap for example, $\mathrm{Re}(\alpha) > 2$ for frequencies in the range 3200-3400 Hz). The frequencies where $\mathrm{Re}(\alpha) > 2$ can raise some potential stability issues (see § 3.3.4). Finally, in the pass bands, $\mathrm{Re}(\alpha) \approx 2$, again consistent with the physical nature of the problem.
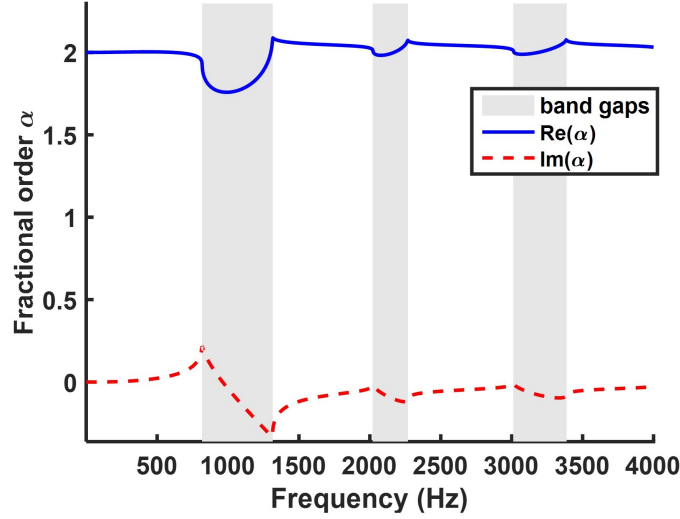
Figure 3.4. The complex, frequency-dependent fractional order α for the aluminum-brass periodic rod using a constant value of $\bar{c}$.

Equivalent Fractional Wave Speed: Frequency-Dependent Speed Assumption

Another approach for $\bar{c}$ is formulated where both α and $\bar{c}$ depend on the frequency ω. Recall the values of $\mu(\omega)$ that are given by Fig. 3.2 and the left hand side of Eq. (3.43). According to Meerschaert et al. [77], the wavenumber can be written as $\mu = \omega/c(\omega) + i\eta$ where $c(\omega)$ is a frequency-dependent wave speed and η is an attenuation factor. From this, the speed $\bar{c}(\omega)$ is

$$\bar{c} = Q \frac{\omega}{\mathrm{Re}(\mu)}. \tag{3.48}$$

A plot of $\bar{c}(\omega)$ for the aluminum-brass periodic rod is given in Fig. 3.5(a). For very low frequencies in the first pass band, the value of $\bar{c}$ is equal to the value given by Eq. (3.46). The trends of $\bar{c}$ in the band gaps are linear while the curves in the pass bands vary smoothly.

Using the frequency-dependent fractional speed $\bar{c}(\omega)$, Eq. (3.43) can be solved for α as a function of frequency. Substituting Eq. (3.48) into Eq. (3.43) and performing some algebraic simplifications results in

105
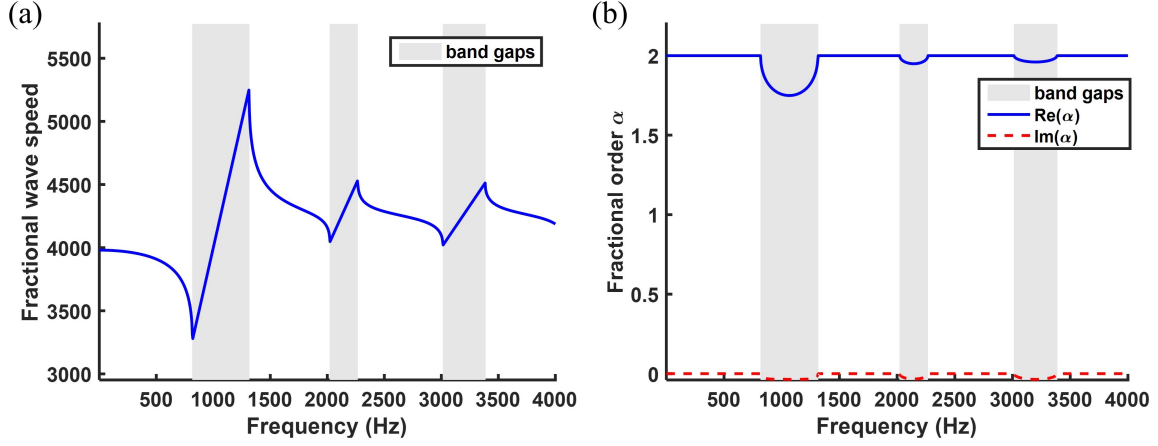
Figure 3.5. (a) The fractional wave speed $\bar{c}$ as a function of frequency. (b) The corresponding fractional order α using the frequency-dependent wave speed from (a).

$$\alpha = \frac{2\ln\left(|\mathrm{Re}(\mu)|\right) + \mathrm{i}\pi}{\ln(\mu) + \mathrm{i}\pi/2}.$$ (3.49)

The plot of Eq. (3.49) for the aluminum-brass periodic rod is given in Fig. 3.5(b). In contrast with the constant speed assumption, $\mathrm{Re}(\alpha) = 2$ for all the frequencies in pass bands. This is again consistent with the physics since a spatial order of two is indicative of propagating waves. It is also not surprising because some degree of variability in the coefficients of the equation has been reinstated, albeit the variability does not occur as a function of space; rather, it is dependent upon frequency. In the band gaps, $\mathrm{Re}(\alpha) < 2$ while $\mathrm{Im}(\alpha) < 0$. The fact that $\mathrm{Re}(\alpha) < 2$ indicates that the wave propagation attenuates in space, consistent with the fact that this frequency is located in a band gap. As already seen in the previous chapter and in § 1.2.4, complex order fractional derivatives are still an ongoing area of research and the physical meaning of the imaginary part of the order is not completely evident, although it is known that the imaginary part does affect the phase of the results.

106

3.3 Analytical Solutions and Assessment of the Fractional Rod

Having obtained the fractional order of the homogenized fractional model, this section analyzes the analytical solution to Eq. (3.31) and compares the plot of its displacement to the displacement of the bi-material periodic rod obtained via finite elements to verify the accuracy and validity of the homogenization. In § 3.2.1, it was seen that the displacement solution to the space fractional wave equation was assumed to be exponential functions or Mittag-Leffler functions depending on the lower limit of the fractional derivative. From a mathematical perspective, it seems that it is appropriate to use the exponential solution when the considered rod is an infinite structure, while the Mittag-Leffler solution is valid if the rod has a boundary at $x = 0$. However, from a physical perspective, the difference between the Mittag-Leffler and exponential solutions is not very intuitive. An exponential function is well-known to describe plane wave propagation, while Mittag-Leffler functions can be interpreted as wave fronts having spatially decaying amplitude when $1 < \alpha < 2$. The following sections analyze both solution forms and argue that either the exponential or ML solution can be considered for a semi-infinite fractional rod.

3.3.1 The Exponential Kernel Solution

The exponential kernel solution seems suited to represent the displacement of an infinite fractional rod. For an infinite rod with an excitation located at $x = 0$, the forward and backward traveling waves propagating from this location are equivalent, hence allowing the study of an infinite rod problem excited at the center location to be accomplished by merely considering half of the domain (i.e., a semi-infinite rod), as seen in Fig. 3.3. If the analysis is limited, for instance, to the positive x-axis and the excitation at $x = 0$ is

$$u(0, t) = u_0 e^{i\Omega t}, \tag{3.50}$$

then $\tilde{A} = u_0$, $\tilde{B} = 0$, and $\omega = \Omega$ in Eq. (3.33). Thus, the displacement throughout the fractional rod is

$$u(x,t) = u_0 e^{i(\Omega t - kx)}. \tag{3.51}$$

Using the dispersion relation from Eq. (3.34), Eq. (3.51) can be rewritten as

$$u(x,t) = u_0 e^{i\Omega t} e^{x(-\Omega^2/\bar{c}^2)^{\frac{1}{\alpha}}} = T(t)U(x). \tag{3.52}$$

Equation (3.52) is the exponential solution to the semi-infinite fractional rod. To analyze the stability of Eq. (3.52) given the fractional order α (see either Fig. 3.4 or Fig. 3.5(b)) of the aluminum-brass periodic rod, consider the spatial term of Eq. (3.52):

$$U(x) = e^{x(-\Omega^2/\bar{c}^2)^{\frac{1}{\alpha}}}. \tag{3.53}$$

Define $\lambda = \frac{\Omega^2}{\bar{c}^2}$ and $\alpha = a + bi$ so that Eq. (3.53) can be written as

$$U(x) = \text{Exp}\left[(-\lambda)^{\frac{a-bi}{a^2+b^2}} x\right]. \tag{3.54}$$

Note that for lengthy mathematical expressions, equations will use both the notations $e^{(\cdot)}$ and $\text{Exp}(\cdot)$ to indicate the exponential function. Let $\tilde{a} = \frac{a}{a^2+b^2}$ and $\tilde{b} = \frac{b}{a^2+b^2}$. After some algebraic work, the solution can be written as

$$U(x) = e^{r_1 x}\left[\cos(r_2 x) + i\sin(r_2 x)\right], \tag{3.55}$$

$$r_1 = \lambda^{\tilde{a}} e^{\tilde{b}\pi} \cos\left[\tilde{a}\pi - \tilde{b}\ln(\lambda)\right], \tag{3.56}$$

$$r_2 = \lambda^{\tilde{a}} e^{\tilde{b}\pi} \sin\left[\tilde{a}\pi - \tilde{b}\ln(\lambda)\right]. \tag{3.57}$$

The real part of Eq. (3.53) is

$$\mathrm{Re}\left[U(x)\right] = e^{r_1 x}\left[\cos(r_2 x)\right], \tag{3.58}$$

while the imaginary part is

$$\mathrm{Im}\left[U(x)\right] = e^{r_1 x}\left[\sin(r_2 x)\right]. \tag{3.59}$$

The trigonometric terms on the right hand side of Eqs. (3.58) and (3.59) are oscillatory and thus are stable. However, the exponential terms will determine if the solution exponentially decays or grows. From Eq. (3.56), the terms $\lambda^{\tilde{a}}$ and $e^{\tilde{b}\pi}$ are always positive. Thus, the term that determines the stability is $\cos\left[\tilde{a}\pi - \tilde{b}\ln(\lambda)\right]$. Cosine is negative if its argument is between $n\frac{\pi}{2}$ and $n\frac{3\pi}{2}$ where n is an odd integer. As a result, Eq. (3.53) is stable if and only if

$$n\frac{\pi}{2} \leq \left[\tilde{a}\pi - \tilde{b}\ln(\lambda)\right] \leq n\frac{3\pi}{2} \quad \text{where } n \text{ is an odd integer.} \tag{3.60}$$

If $\tilde{a}\pi - \tilde{b}\ln(\lambda) = n\frac{\pi}{2}$ (where n is odd), the exponential solution will be marginally stable. If the equality part of Eq. (3.60) is removed, the solution will be unconditionally stable and will always decay. If Eq. (3.60) is not satisfied, then the solution will grow exponentially. Since the values of $\tilde{a}$, $\tilde{b}$, and λ all contribute to whether Eq. (3.60) is satisfied, one cannot definitively conclude what the limiting values of $\tilde{a}$, $\tilde{b}$, and λ are for stability. However, consider a purely real value of $\alpha = 2$ which corresponds to $\tilde{a} = 1/2$ and $\tilde{b} = 0$. Thus, $\tilde{a}\pi - \tilde{b}\ln(\lambda) = \pi/2$, showing that the solution is marginally stable. For purely real orders greater than 2, the value of $\tilde{b}$ is still zero while $\tilde{a} < 1/2$, meaning the solution will be unstable.

However, when α is complex, it may be possible, depending on the values of $\tilde{b}$ and λ, that Eq. (3.60) can be satisfied even though $\tilde{a} < 1/2$. It is obvious then that $\text{Im}(\alpha)$ contributes to the stability of the solution (in addition to the phase). In fact, the values of $\alpha(\omega)$ given in Fig. 3.4 actually always satisfy Eq. (3.60) even when $\text{Re}(\alpha) > 2$. The potential stability issues for $\text{Re}(\alpha) > 2$ can occur when the Mittag-Leffler kernel is implemented.

3.3.2 The Mittag-Leffler Kernel Solution

Previously in § 3.2.1, the ML ansatz given by Eq. (3.36) was assumed to obtain the dispersion relation. Here, the ML solution to Eq. (3.31) is derived when the Caputo fractional derivative has a lower terminal of zero by using separation of variables and Laplace transforms. Using separation of variables,

$$u(x,t) = U(x)T(t). \tag{3.61}$$

Substituting Eq. (3.61) into Eq. (3.31), and separating the time and space variables yields

$$\frac{\ddot{T}}{T} = \frac{\vec{c}^2}{U}\frac{\partial^\alpha U}{\partial x^\alpha} = -\omega^2, \tag{3.62}$$

where ω is a positive constant to guarantee stable oscillatory solutions (and is the frequency). The temporal part of Eq. (3.62) results in the classical second order ordinary differential equation, which is

$$\frac{\mathrm{d}^2 T}{\mathrm{d}t^2} + \omega^2 T = 0. \tag{3.63}$$

Recall the solution to Eq. (3.63) is

$$T(t) = C_1 e^{i\omega t} + C_2 e^{-i\omega t}, \tag{3.64}$$

where C_1 and C_2 are constants to be determined. Alternatively, the solution to Eq. (3.63) could be written using a summation of cosine and sine terms. Let $\xi = \frac{\omega^2}{c^2}$ so that the spatial part of Eq. (3.62) is

$$\frac{\mathrm{d}^\alpha U}{\mathrm{d}x^\alpha} + \xi U = 0. \tag{3.65}$$

Equation (3.65) can be solved by using the Laplace transform, obtaining

$$\hat{U}(s) = \bar{A}\frac{s^{\alpha-1}}{s^\alpha + \xi} + \bar{B}\frac{s^{\alpha-2}}{s^\alpha + \xi}, \tag{3.66}$$

where s is the Laplace variable, $\hat{U}(s)$ is the Laplace transform of $U(x)$, $\bar{A} = U(0)$ and $\bar{B} = \frac{\mathrm{d}U(0)}{\mathrm{d}x}$. The form of Eq. (3.66) will result in Mittag-Leffler functions since the Laplace transform of the Mittag-Leffler function is [61], [138]

$$\mathcal{L}\left[z^{p_2-1}E_{p_1,p_2}(\pm C z^{p_1})\right] = \frac{s^{p_1-p_2}}{s^{p_1} \mp C}. \tag{3.67}$$

Using Eq. (3.67) to take the inverse Laplace transform of Eq. (3.66) yields

$$U(x) = \bar{A}E_{\alpha,1}(-\xi x^\alpha) + \bar{B}x E_{\alpha,2}(-\xi x^\alpha). \tag{3.68}$$

Note that the form of Eq. (3.68) is equivalent to the spatial part of Eq. (3.36) (when $-\xi = (-ik)^\alpha$). Furthermore, when $\alpha = 2$, the exponential and Mittag-Leffler solutions are equivalent (see Appendix B in [123]). This is in accordance with the fact that the expo-

nential function is a special case of the ML functions. Hence the ML kernel can be considered as a set of solutions including the exponential ones.

Returning to the semi-infinite rod, one can argue that the ML solution given by Eq. (3.68) is valid since the structure begins at $x = 0$. Assuming the displacement at $x = 0$ is given by Eq. (3.50), the axial displacement according to the ML solution form is

$$u(x,t) = e^{i\Omega t}\left[u_0 E_{\alpha,1}\left(-\frac{\Omega^2}{c^2}x^\alpha\right) + \tilde{B}x E_{\alpha,2}\left(-\frac{\Omega^2}{c^2}x^\alpha\right)\right]. \tag{3.69}$$

The value of $\bar{B}$, which is equal to $\frac{du(0,t)}{dx}$, is determined using the mechanical impedance at the location $x = 0$, which is

$$F = Zv, \tag{3.70}$$

where F is the force, v is the velocity, and Z is the mechanical impedance. Considering that the displacement is known to be harmonic and has an amplitude of u_0, the velocity amplitude can be obtained by differentiation: $v = i\Omega u_0$. The internal force is given by making use of the constitutive relationship for a rod: $F = EA\frac{du}{dx}$. Hence, Eq. (3.70) becomes

$$EA\frac{du(0,t)}{dx} = i\Omega u_0 Z. \tag{3.71}$$

The mechanical impedance of the rod is $Z = \rho c A$, resulting in

$$EA\frac{du(0,t)}{dx} = i\Omega u_0 \rho c A. \tag{3.72}$$

Recall that the wave speed is $c = \sqrt{\frac{E}{\rho}}$. Finally, $\bar{B}$ is obtained as

$$\frac{du(0,t)}{dx} = \tilde{B} = i\Omega\frac{u_0}{c}. \tag{3.73}$$

In Eq. (3.73), the value of c can be set equal to $\bar{c}$ according to one of the methodologies described in § 3.2.2. Contrary to the exponential solution, the Mittag-Leffler functions in Eq. (3.69) are unstable whenever $\mathrm{Re}(\alpha) > 2$, no matter the value of the imaginary part [63].

3.3.3 Results Using Exponential Kernel

To validate the proposed fractional rod and its performance for the aluminum-brass bi-material periodic rod, the analytical solutions given by Eq. (3.52) or Eq. (3.69) along with the determined fractional order (Fig. 3.4 or Fig. 3.5(b)) are compared to the numerical results of the bi-material rod using a traditional finite element (FE) solution. The simulations are performed at steady state conditions following a harmonic excitation and the comparison is made in terms of the predicted displacement amplitude $u(x)$ as a function of the spatial location. Note that validation of the fractional rod would be stronger if it was compared to experimental data rather than FE numerical results. However, due to the straightforwardness of the bi-material rod's geometrical variation, the numerical results in this case can be considered as the "true" displacement for validation purposes.

Recall that the fractional order α was found to be a complex quantity. A complex order derivative of a real-valued function is a complex-valued function [127], [128], therefore $u(x)$ will also be complex. This aspect was discussed in Chapter 2 where it was concluded that, for harmonic excitations, the time response of a complex fractional oscillator is an analytic function, therefore justifying the physical response being represented by $u(t) = \text{Re}[\bar{u}(t)]$. Thus, in the following displacement plots, the curves corresponding to the analytical solutions are the real parts of the calculated complex-valued function.

Four different forcing frequencies are considered (100, 500, 1000, 3100 Hz). The selection of these values was dictated by the specific position of the pass bands and band gaps for the selected periodic rod (see Fig. 3.2). More specifically, $\Omega = 100$ Hz corresponds to a low frequency regime where the classical homogenization "rule of mixtures" is a valid approach (the wavelength to unit cell size ratio is $\lambda/a \approx 20$). The frequency $\Omega = 500$ Hz is still located in the first pass band, however it approaches the limit of the homogenization assumption ($\lambda/a \approx 4$). The frequency $\Omega = 1000$ Hz is of particular interest since it is located in the first band gap where the wave is attenuated and the classical homogenization assumption starts breaking down [139]. The frequency $\Omega = 3100$ Hz is located in a higher frequency band gap (the third for the studied system) and denotes a regime were the wave is attenuated and the classical low-frequency homogenization assumptions are not applicable.

Each of benchmark studies compares traditional FE results of the bi-material rod with the analytical solutions obtained using the exponential and the Mittag-Leffler kernels. Both approaches for the value of $\bar{c}$ are considered. In the following plots, results obtained using the constant value of $\bar{c}$ as described in § 3.2.2 are labeled as "$\bar{c}$ approach" while those obtained using the frequency-dependent speed are labeled as "$\bar{c}_\omega$ approach." The FE results were obtained by performing steady state analyses using a commercial software package (COMSOL Multiphysics). The specific values of $\bar{c}$ and α for each of the selected frequencies are obtained from Figs. 3.4 and 3.5 and summarized in Table 3.1.

Table 3.1. Values of $\bar{c}$ and α following the approaches given in § 3.2.2.

Ω (Hz)	$\bar{c}$	α using $\bar{c}$	$\bar{c}_\omega$	α using $\bar{c}_\omega$
100	3980.4	2.0003 + 0.0003i	3978.2	2
500	3980.4	2.0031 + 0.0226i	3909.2	2
1000	3980.4	1.7583 - 0.0408i	4000	1.7569 - 0.0357i
3100	3980.4	1.9895 - 0.0550i	4133.3	1.9662 - 0.0307i

Concerning the FE numerical simulations, a harmonic displacement of amplitude $u_0 = 1$ mm was applied at $x = 0$. A low reflecting boundary condition was applied at the right end ($x = 400$ m) to model a semi-infinite structure.

Figure 3.6 presents the spatial exponential solution from Eq. (3.52) for the four selected values of Ω and compares them with the reference FE solution. In all plots, the results using the "$\bar{c}$ approach" and the "$\bar{c}_\omega$ approach" are exactly equivalent. Thus, the exponential solution does not show any sensitivity to the methodology used to select $\bar{c}$. This is also confirmed by the value of the stability parameter $\tilde{a}\pi - \tilde{b}\ln(\lambda)$ (see Eq. (3.60)), which is exactly the same value for both approaches.

The analytical solutions for $\Omega = 100$ Hz match the finite element results quite well with a root-mean-square (RMS) error of 0.018% over the domain, as seen in Fig. 3.6(a). At 500 Hz (Fig. 3.6(b)), the analytical solutions match the phase of the finite element results, but do not match the amplitudes locally. This type of behavior is not unexpected because the frequency is near the long wavelength limit so that the response is increasingly dominated by scattering effects. Unfortunately, like other low-frequency homogenization techniques, the
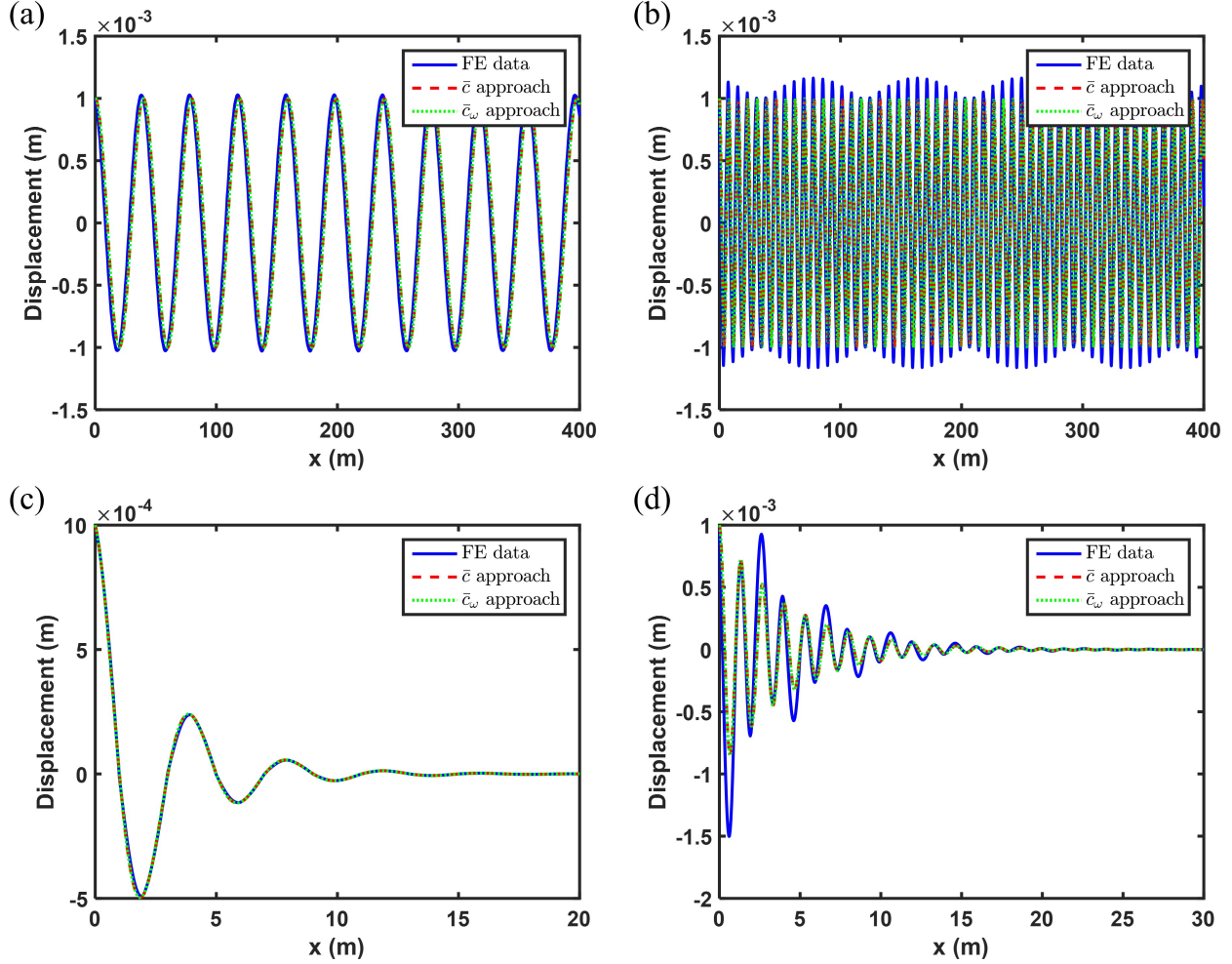
Figure 3.6. The solution to the fractional wave equation using the exponential solution form for a forcing frequency of (a) $\Omega = 100$ Hz, (b) $\Omega = 500$ Hz, (c) $\Omega = 1000$ Hz, (d) $\Omega = 3100$ Hz.

proposed fractional rod model cannot capture localized effects due to wave scattering and interference; however, it still models the wave behavior within the band gaps largely beyond the classical homogenization long-wavelength limit.

The plot at $\Omega = 1000$ Hz (Fig. 3.6(c)) is located in the first band gap. The analytical solution agrees very well with the finite element results with an RMS error as low as 0.0005%. The amplitude of the wave decays in space. The ability of fractional homogenized models

to capture the system response within the band gaps cannot be overstated as an important strength of the fractional modeling approach.

The plot at $\Omega = 3100$ Hz in Fig. 3.6(d) is in the high frequency range where the wavelength is smaller than the length of the unit cell. The analytical solution in this third band gap matches the plot from FE simulations well, except for a few locations (some have a percent difference error as high as 50% between the analytical and numerical solutions). Although this clearly displays high frequency capabilities and can overcome the long wavelength limit of traditional homogenization techniques, it is not necessarily free of error at all frequencies and cannot capture local effects due to high frequencies interference. Nonetheless, the plot still shows, once again, that the fractional homogenization technique is effective in capturing the attenuation in the frequency band gaps.

Concerning the complex nature of the fractional order, the imaginary part of a fractional derivative affects the phase modulation of the response [84]. Considering the "$\bar{c}$ approach", if $\text{Im}(\alpha)$ in Table 3.1 is set equal to zero so that the response is calculated using only the real part of the order α, a distinct phase mismatch between the analytical and numerical solutions is observed. This supports the fact that the imaginary part of a fractional derivative corresponds to controlling the phase of a function. In addition, the imaginary part can also have an effect on the stability. Considering Eq. (3.60), the value of $\tilde{b}$ (related to the imaginary part of α) plays a significant role in determining whether or not Eq. (3.60) is satisfied. While Makris et al. [84] are correct in stating that the physical meaning of the imaginary part of a fractional order corresponds to phase modulation, it appears that this is not the only significance of the imaginary part. Together, the values of the real and imaginary parts of a fractional order dictate stability.

3.3.4   Results Using Mittag-Leffler Kernel

The Mittag-Leffler solution for the semi-infinite rod is given by Eq. (3.69) where $\tilde{B}$ is given by Eq. (3.73). As previously mentioned, the Mittag-Leffler functions in Eq. (3.69) are unstable whenever $\text{Re}(\alpha) > 2$, no matter the value of the imaginary part [63]. As a result, the solutions using the constant $\bar{c}$ might be unstable at any frequency where $\text{Re}(\alpha) > 2$.

116

However, Fig. 3.7 depicts the results using the constant $\bar{c}$ are in fact stable when $\text{Re}(\alpha) > 2$ (except in Fig. 3.7(d)). In actuality, both of the terms in Eq. (3.69) are growing without bound; however, the value of $\tilde{B}$ actually causes the instabilities of the two terms to cancel each other out. Furthermore, the first three plots in Fig. 3.7 show that the results using the two approaches for $\bar{c}$ are equivalent. However, if the value of $\tilde{B}$ is determined in a different manner other than that given by Eq. (3.73) or if the value of $\tilde{B}$ in Eq. (3.73) is rounded off prematurely, an instability occurs in the constant $\bar{c}$ approach, as seen in Fig. 3.7(d). Unfortunately, an expression of the stability (like Eq. (3.60) for the exponential solutions) could not be obtained for ML functions with complex orders. More mathematical theory needs to be developed for complex order Mittag-Leffler functions before a stability expression can be obtained.

Extreme caution must be used whenever it is observed that $\text{Re}(\alpha) > 2$ when using Mittag-Leffler solution kernels. It is recommended that the "$\bar{c}_\omega$ approach" be implemented when using ML functions to avoid a potential instability in the analytical solution since the fractional order never possesses a value where $\text{Re}(\alpha) > 2$. This is precisely why the frequency-dependent fractional wave speed approach was developed.

Another error source is due to the evaluation of the Mittag-Leffler function itself. The evaluation of the infinite summation term in the definition of the ML function is not a trivial task and is actually an ongoing area of computational research [124], [140]. As previously noted in Chapter 2, a few common MATLAB functions do exist [125], [126] to numerically evaluate the Mittag-Leffler function, but they are not valid for complex values of the parameters. The edited version of [125] created to handle complex orders had some intrinsic errors associated with it. In fact, this error associated with the evaluation of the complex order ML function contributes to some of the slight amplitude overshoots and phase mismatches such as those seen in Fig. 3.7(c).

Comparing the exponential and Mittag-Leffler solutions show that both sets are nearly identical. In fact, the plots in Figs. 3.7(a) and 3.7(b) are exactly equivalent to Figs. 3.6(a) and 3.6(b). Comparing Figs. 3.7(c) and 3.6(c) shows that the solution using the exponential function was more accurate at $\Omega = 1000$ Hz than the ML solution. Although the exponential and Mittag-Leffler solutions in Figs. 3.6 and 3.7 are nearly alike, this may not always be
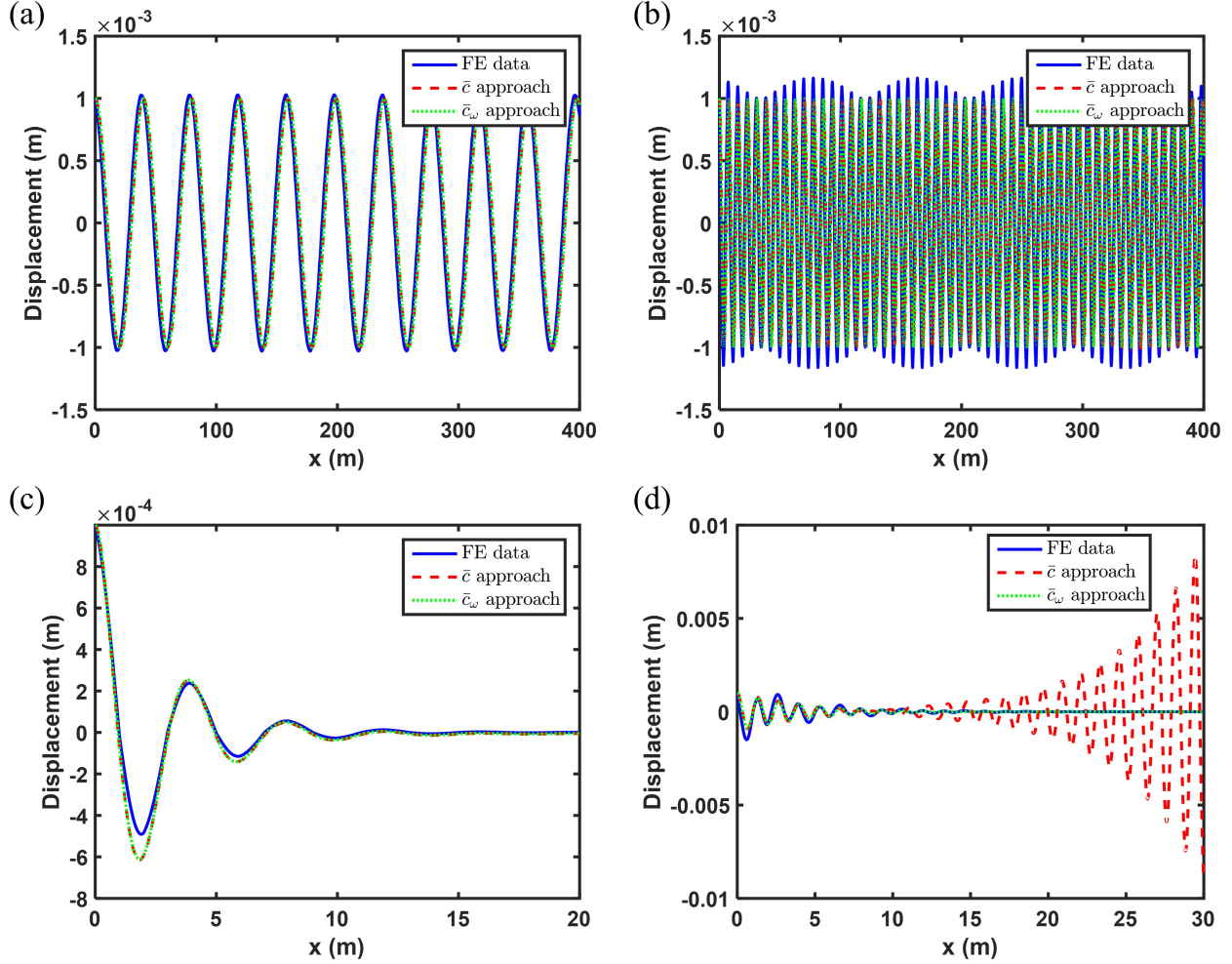
Figure 3.7. The solution to the fractional wave equation using the Mittag-Leffler solution form for a forcing frequency of (a) $\Omega = 100$ Hz, (b) $\Omega = 500$ Hz, (c) $\Omega = 1000$ Hz, (d) $\Omega = 3100$ Hz.

the case. The choice of a specific kernel is important when used to calculate the dynamic response in systems having finite dimensions. In other words, the choice of the kernel and its corresponding analytical solution can be subject to specific boundary conditions.

Overall, the use of the fractional rod model possesses the advantages of 1) accurately representing the wave attenuation in the frequency band gaps as well as the proper spatial phase and 2) providing a means to accurately represent the axial displacement of the transverse wave propagation with a closed-form analytical solution. However, like other low-frequency

118

homogenization techniques, the fractional rod model is locally accurate only for long wavelengths. When approaching short wavelength regimes, local interference effects cannot be accurately captured.

3.4 Bi-Material Periodic Beam

The structure in Fig. 3.1 is now subjected to both transverse and axial loads. Thus, the bi-material periodic structure is now a beam, with each location of the structure capable of both translation and rotation. In particular, this section pursues two main objectives: 1) the extension of the underlying theoretical fractional models to represent the flexural response of the bi-material, periodic beam, particularly within the frequency band gaps, and 2) the development of a computational approach for the solution of fractional complex order differential equations.

As before with the fractional rod, the fractional formulation will rely on first deriving the dispersion relationship of both an Euler-Bernoulli and Timoshenko beam. Recall that the main difference between Euler–Bernoulli and Timoshenko beams is that the Euler-Bernoulli theory neglects shear deformations and assumes plane sections of the beam remain planar and normal to the beam's neutral axis during deformation. On the other hand, Timoshenko beam theory accounts for shear effects and thus, plane sections are no longer normal to the neutral axis. Since it accounts for shear deformation, Timoshenko beam theory is a more accurate representation of the actual physics; however, the assumptions of the Euler-Bernoulli beam theory are valid when the beam geometry is long and slender (typically need a length to thickness ratio of at least 10).

3.4.1 Euler-Bernoulli Beam Model

Consider an infinite periodic beam consisting of two isotropic sections #1 and #2 with different material properties, as shown in Fig. 3.1. The coordinate system is chosen such that the origin lies on the interface between the two layers. The Young's modulus, quadratic moment of inertia, density, and cross-sectional area of the layers are denoted by E_m, I_m, ρ_m and

A_m, where m indicates which uniform portion of the bi-material periodic beam is considered. The governing equation of the bi-material Euler-Bernoulli beam is

$$\frac{\partial^2}{\partial x^2}\left[E(x)I(x)\frac{\partial^2 w(x,t)}{\partial x^2}\right] + \rho(x)A(x)\frac{\partial^2 w(x,t)}{\partial t^2} = 0, \tag{3.74}$$

where $w(x,t)$ is the flexural displacement of the mid-plane of the beam at a spatial location x and at the time instant t. Although the beam properties are a periodic function of the spatial location x, they are isotropic within each individual section. This permits Eq. (3.74) to be re-written as

$$E_m I_m \frac{\partial^4 w(x,t)}{\partial x^4} + \rho_m A_m \frac{\partial^2 w(x,t)}{\partial t^2} = 0, \tag{3.75}$$

where $m = 1 \; \forall \; x \in [-L_1 + NL, NL]$ and $m = 2 \; \forall \; x \in [NL, L_2 + NL]$ for $N \in \mathbb{I}$. Using the method of separation of variables, the flexural displacement is $w(x,t) = W(x)e^{i\omega t}$ where ω is the angular frequency. Substituting $w(x,t) = W(x)e^{i\omega t}$ in Eq. (3.75) results in

$$W(x) = A_{m1}e^{\beta_m x} + A_{m2}e^{-\beta_m x} + A_{m3}e^{i\beta_m x} + A_{m4}e^{-i\beta_m x}, \tag{3.76a}$$

$$\beta_m = \left[\frac{\rho_m A_m \omega^2}{E_m I_m}\right]^{\frac{1}{4}}, \tag{3.76b}$$

where $m \in \{1,2\}$ and A_{m1}, A_{m2}, A_{m3}, and A_{m4} are constants. Since the beam is periodic, Floquet theorem can describe the flexural displacement (and determine the dispersion relationship). According to Floquet theory,

$$W(x) = e^{\mu L}W(x - L) \; \forall \; x \in (-\infty, \infty), \tag{3.77}$$

where μ is the Floquet wavenumber.

3.4.2 Dispersion of the Euler-Bernoulli Beam

The dispersion relations for the periodic beam can now be derived by establishing a relationship between the set of eight constants A_{m1}, A_{m2}, A_{m3}, and A_{m4}. Imposing the

continuity of displacement, slope, bending moment, and shear force at $x = 0$ (i.e., at the interface between the two layers within a unit cell) results in

$$A_{11} + A_{12} + A_{13} + A_{14} = A_{21} + A_{22} + A_{23} + A_{24}, \tag{3.78a}$$

$$\beta_1 A_{11} - \beta_1 A_{12} + i\beta_1 A_{13} - i\beta_1 A_{14} = \beta_2 A_{21} - \beta_2 A_{22} + i\beta_2 A_{23} - i\beta_2 A_{24}, \tag{3.78b}$$

$$E_1 I_1 \left(\beta_1^2 A_{11} + \beta_1^2 A_{12} - \beta_1^2 A_{13} - \beta_1^2 A_{14} \right) = E_2 I_2 \left(\beta_2^2 A_{21} + \beta_2^2 A_{22} - \beta_2^2 A_{23} - \beta_2^2 A_{24} \right), \tag{3.78c}$$

$$E_1 I_1 \left(\beta_1^3 A_{11} - \beta_1^3 A_{12} - i\beta_1^3 A_{13} + i\beta_1^3 A_{14} \right) = E_2 I_2 \left(\beta_2^3 A_{21} - \beta_2^3 A_{22} - i\beta_2^3 A_{23} + i\beta_2^3 A_{24} \right). \tag{3.78d}$$

An additional set of four equations are established by using the Floquet relation in Eq. (3.77) to relate the different physical variables at $x = -L_1$ and at $x = L_2$, giving

$$A_{11}e^{\mu L - \beta_1 L_1} + A_{12}e^{\mu L + \beta_1 L_1} + A_{13}e^{\mu L - i\beta_1 L_1} + A_{14}e^{\mu L + i\beta_1 L_1}$$
$$= A_{21}e^{\beta_2 L_2} + A_{22}e^{-\beta_2 L_2} + A_{23}e^{i\beta_2 L_2} + A_{24}e^{-i\beta_2 L_2}, \tag{3.79a}$$

$$\beta_1 A_{11}e^{\mu L - \beta_1 L_1} - \beta_1 A_{12}e^{\mu L + \beta_1 L_1} + i\beta_1 A_{13}e^{\mu L - i\beta_1 L_1} - i\beta_1 A_{14}e^{\mu L + i\beta_1 L_1}$$
$$= \beta_2 A_{21}e^{\beta_2 L_2} - \beta_2 A_{22}e^{-\beta_2 L_2} + i\beta_2 A_{23}e^{i\beta_2 L_2} - i\beta_2 A_{24}e^{-i\beta_2 L_2}, \tag{3.79b}$$

$$E_1 I_1 \left(\beta_1^2 A_{11}e^{\mu L - \beta_1 L_1} + \beta_1^2 A_{12}e^{\mu L + \beta_1 L_1} - \beta_1^2 A_{13}e^{\mu L - i\beta_1 L_1} - \beta_1^2 A_{14}e^{\mu L + i\beta_1 L_1} \right)$$
$$= E_2 I_2 \left(\beta_2^2 A_{21}e^{\beta_2 L_2} + \beta_2^2 A_{22}e^{-\beta_2 L_2} - \beta_2^2 A_{23}e^{i\beta_2 L_2} - \beta_2^2 A_{24}e^{-i\beta_2 L_2} \right), \tag{3.79c}$$

$$E_1 I_1 \left(\beta_1^3 A_{11} \mathrm{e}^{\mu L - \beta_1 L_1} - \beta_1^3 A_{12} \mathrm{e}^{\mu L + \beta_1 L_1} - \mathrm{i}\beta_1^3 A_{13} \mathrm{e}^{\mu L - \mathrm{i}\beta_1 L_1} + \mathrm{i}\beta_1^3 A_{14} \mathrm{e}^{\mu L + \mathrm{i}\beta_1 L_1} \right)$$
$$= E_2 I_2 \left(\beta_2^3 A_{21} \mathrm{e}^{\beta_2 L_2} - \beta_2^3 A_{22} \mathrm{e}^{-\beta_2 L_2} - \mathrm{i}\beta_2^3 A_{23} \mathrm{e}^{\mathrm{i}\beta_2 L_2} + \mathrm{i}\beta_2^3 A_{24} \mathrm{e}^{-\mathrm{i}\beta_2 L_2} \right).$$
(3.79d)

Equations (3.78) and (3.79) are combined to form a set of eight homogeneous equations of the form $\mathbf{T}\{X\} = 0$, where $\{X\} = \{A_{11}\ A_{12}\ A_{13}\ A_{14}\ -A_{21}\ -A_{22}\ -A_{23}\ -A_{24}\}^T$ is a vector containing the eight constants. The matrix $\mathbf{T}$ is

$$\mathbf{T} = \begin{bmatrix} 1 & 1 & 1 & 1 & 1 & 1 & 1 & 1 \\ 1 & -1 & \mathrm{i} & -\mathrm{i} & \tilde{\beta} & -\tilde{\beta} & \mathrm{i}\tilde{\beta} & -\mathrm{i}\tilde{\beta} \\ 1 & 1 & -1 & -1 & \tilde{Z}\tilde{\beta}^2 & \tilde{Z}\tilde{\beta}^2 & -\tilde{Z}\tilde{\beta}^2 & -\tilde{Z}\tilde{\beta}^2 \\ 1 & -1 & -\mathrm{i} & \mathrm{i} & \tilde{Z}\tilde{\beta}^3 & -\tilde{Z}\tilde{\beta}^3 & -\mathrm{i}\tilde{Z}\tilde{\beta}^3 & \mathrm{i}\tilde{Z}\tilde{\beta}^3 \\ \kappa \mathrm{e}^{-\beta_1 L_1} & \kappa \mathrm{e}^{\beta_1 L_1} & \kappa \mathrm{e}^{-\mathrm{i}\beta_1 L_1} & \kappa \mathrm{e}^{\mathrm{i}\beta_1 L_1} & \mathrm{e}^{\beta_2 L_2} & \mathrm{e}^{-\beta_2 L_2} & \mathrm{e}^{\mathrm{i}\beta_2 L_2} & \mathrm{e}^{-\mathrm{i}\beta_2 L_2} \\ \kappa \mathrm{e}^{-\beta_1 L_1} & -\kappa \mathrm{e}^{\beta_1 L_1} & \mathrm{i}\kappa \mathrm{e}^{-\mathrm{i}\beta_1 L_1} & -\mathrm{i}\kappa \mathrm{e}^{\mathrm{i}\beta_1 L_1} & \tilde{\beta}\mathrm{e}^{\beta_2 L_2} & -\tilde{\beta}\mathrm{e}^{-\beta_2 L_2} & \mathrm{i}\tilde{\beta}\mathrm{e}^{\mathrm{i}\beta_2 L_2} & -\mathrm{i}\tilde{\beta}\mathrm{e}^{-\mathrm{i}\beta_2 L_2} \\ \kappa \mathrm{e}^{-\beta_1 L_1} & \kappa \mathrm{e}^{\beta_1 L_1} & -\kappa \mathrm{e}^{-\mathrm{i}\beta_1 L_1} & -\kappa \mathrm{e}^{\mathrm{i}\beta_1 L_1} & \tilde{Z}\tilde{\beta}^2\mathrm{e}^{\beta_2 L_2} & \tilde{Z}\tilde{\beta}^2\mathrm{e}^{-\beta_2 L_2} & -\tilde{Z}\tilde{\beta}^2\mathrm{e}^{\mathrm{i}\beta_2 L_2} & -\tilde{Z}\tilde{\beta}^2\mathrm{e}^{-\mathrm{i}\beta_2 L_2} \\ \kappa \mathrm{e}^{-\beta_1 L_1} & -\kappa \mathrm{e}^{\beta_1 L_1} & -\mathrm{i}\kappa \mathrm{e}^{-\mathrm{i}\beta_1 L_1} & \mathrm{i}\kappa \mathrm{e}^{\mathrm{i}\beta_1 L_1} & \tilde{Z}\tilde{\beta}^3\mathrm{e}^{\beta_2 L_2} & -\tilde{Z}\tilde{\beta}^3\mathrm{e}^{-\beta_2 L_2} & -\mathrm{i}\tilde{Z}\tilde{\beta}^3\mathrm{e}^{\mathrm{i}\beta_2 L_2} & \mathrm{i}\tilde{Z}\tilde{\beta}^3\mathrm{e}^{-\mathrm{i}\beta_2 L_2} \end{bmatrix},$$
(3.80)

where $\kappa = \mathrm{e}^{\mu L}$, $\tilde{\beta} = \beta_2/\beta_1$, and $\tilde{Z} = E_2 I_2/E_1 I_1$. To solve for a nontrivial solution of the flexural displacement of the periodic beam, the determinant of the matrix $\mathbf{T}$ must be set equal to zero. This yields the dispersion relation for the periodic beam as a fourth degree polynomial of the variable κ:

$$\mathcal{P}(\kappa) = a_4 \kappa^4 + a_3 \kappa^3 + a_2 \kappa^2 + a_1 \kappa + a_0 = 0, \tag{3.81}$$

where a_k are constants. The roots of the above polynomial give the values of κ and subsequently the Floquet wavenumber μ. The coefficients of the characteristic polynomial $\mathcal{P}(\kappa)$ are highly conditioned, preventing the accurate use of typical numerical root-finders. In

order to extract the roots accurately, the procedure takes advantage of the symmetry within the periodic beam, allowing us to factorize $\mathcal{P}(\kappa)$ into two quadratic polynomials:

$$\mathcal{P}(\kappa) \equiv (\kappa^2 + p_1\kappa + 1)(\kappa^2 + p_2\kappa + 1) = 0, \tag{3.82}$$

where $a_0 = a_4$, $a_1 = a_3$, and the coefficients p_1 and p_2 are

$$p_{1,2} = \frac{1}{2}\left[\frac{a_3}{a_4} \pm \sqrt{\left(\frac{a_3}{a_4}\right)^2 - 4\left(\frac{a_2}{a_4} - 2\right)}\right]. \tag{3.83}$$

The solutions for κ can now be found as the roots of quadratic polynomials as

$$\kappa_{1,2} = \frac{1}{2}\left(-p_1 \pm \sqrt{p_1^2 - 4}\right), \tag{3.84a}$$

$$\kappa_{3,4} = \frac{1}{2}\left(-p_2 \pm \sqrt{p_2^2 - 4}\right). \tag{3.84b}$$

The Floquet wavenumber can be found by taking the logarithm of the obtained values of κ as

$$\mu_n = \frac{1}{L}\log(\kappa_n), \tag{3.85}$$

where $n = \{1, 2, 3, 4\}$. It follows from Eq. (3.84) that $\kappa_1\kappa_2 = 1$ and $\kappa_3\kappa_4 = 1$. Thus, $\mu_2 = -\mu_1 + iN_1\pi/L$ and $\mu_4 = -\mu_3 + iN_2\pi/L$ where N_1 and N_2 are integers (this analysis selects $N_1 = 0$ and $N_2 = 0$).

Again consider an aluminum-brass periodic structure. The thickness and width of the beam are 0.005 m while the length of each material portion is 1 m. The dispersion relation of the flexural waves is found using the above procedure and is depicted in Fig. 3.8. Figure 3.8(a) plots the wavenumber versus frequency folded across the first Brillouin zone while Fig. 3.8(b) is the unfolded dispersion curve for the aluminum-brass beam. The frequency regions where $\text{Re}(\mu) \neq 0$, highlighted in the plots as a gray region, are the frequency band gaps of the periodic aluminum-brass beam.
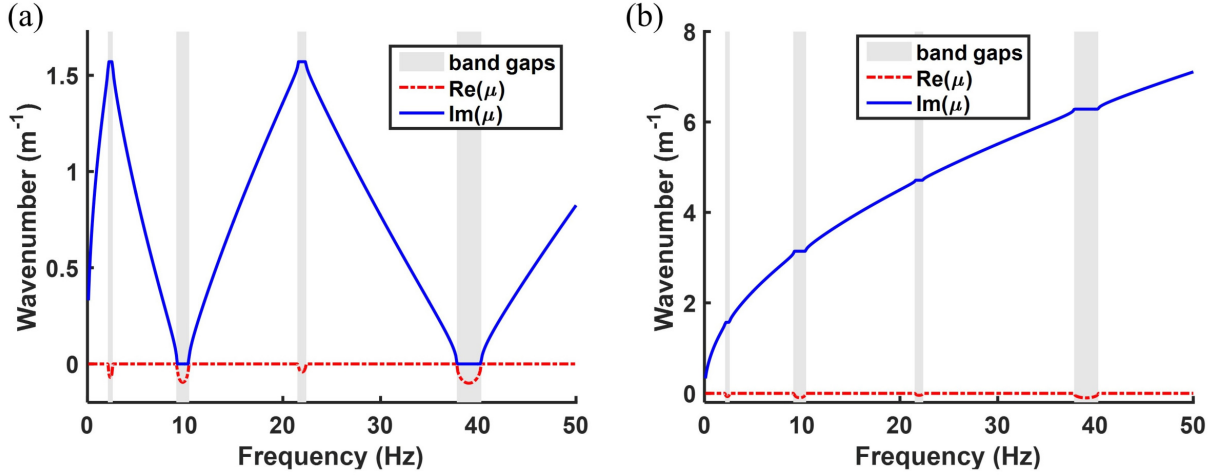
Figure 3.8. The dispersion curve of the aluminium-brass periodic Euler-Bernoulli beam. (a) The dispersion curve is folded across the first Brillouin zone. (b) The unfolded dispersion curve of the periodic beam.

3.4.3 Timoshenko Beam Model

Now consider the bi-material periodic rod according to Timoshenko beam theory. The governing equations of the bi-material Timoshenko beam theory are

$$-\frac{\partial}{\partial x}\left[k_T AG\frac{\partial}{\partial x}\left(\frac{\partial w}{\partial x}-\phi\right)\right]+\rho A\frac{\partial^2 w}{\partial t^2}=f(x,t), \tag{3.86a}$$

$$-\frac{\partial}{\partial x}\left(EI\frac{\partial \phi}{\partial x}\right)-k_T AG\left(\frac{\partial w}{\partial x}-\phi\right)+\rho I\frac{\partial^2 \phi}{\partial t^2}=0, \tag{3.86b}$$

where $w(x,t)$ is the flexural deflection, $\phi(x,t)$ is the angle of rotation of the normal to the mid-surface of the beam, G is the shear modulus, and k_T is the Timoshenko shear coefficient. Typically, $k_T=5/6$ for rectangular cross sections. For each uniform portion of the beam, Eq. (3.86) can be written as

$$-k_T A_m G_m\frac{\partial^2 w}{\partial x^2}+k_T A_m G_m\frac{\partial \phi}{\partial x}+\rho_m A_m\frac{\partial^2 w}{\partial t^2}=0, \tag{3.87a}$$

124

$$-E_m I_m \frac{\partial^2 \phi}{\partial x^2} - k_T A_m G_m \frac{\partial w}{\partial x} + k_T A_m G_m \phi + \rho_m I_m \frac{\partial^2 \phi}{\partial t^2} = 0, \tag{3.87b}$$

for $m \in \{1, 2\}$ corresponding to material #1 and #2. Equation (3.87a) can in fact be combined into a single differential equation as

$$E_m I_m \frac{\partial^4 w}{\partial x^4} + \rho_m A_m \frac{\partial^2 w}{\partial t^2} - \rho_m I_m \left(1 + \frac{E_m}{k_T G_m} \right) \frac{\partial^4 w}{\partial x^2 \partial t^2} + \frac{\rho_m^2 I_m}{k_T G_m} \frac{\partial^4 w}{\partial t^4} = 0. \tag{3.88}$$

Dividing Eq. (3.88) by $\rho_m A_m$ and defining

$$s_m^2 = \frac{E_m I_m}{\rho_m A_m}, \tag{3.89}$$

$$r_m^2 = \frac{I_m}{A_m}, \tag{3.90}$$

Eq. (3.88) can be rewritten as

$$s_m^2 \frac{\partial^4 w}{\partial x^4} + \frac{\partial^2 w}{\partial t^2} - r_m^2 \left(1 + \frac{E_m}{k_T G_m} \right) \frac{\partial^4 w}{\partial x^2 \partial t^2} + \frac{\rho_m r_m^2}{k_T G_m} \frac{\partial^4 w}{\partial t^4} = 0. \tag{3.91}$$

The equations for the bending moment and shear force are, respectively,

$$M = EI \frac{\partial \phi}{\partial x}, \tag{3.92}$$

$$V = k_T A G \left(\frac{\partial w}{\partial x} - \phi \right). \tag{3.93}$$

Using the method of separation of variables, $w(x, t) = W(x) \mathrm{e}^{\mathrm{i}\omega t}$. Substituting $w(x, t)$ in Eq. (3.91) yields

$$W^{IV}(x) + \frac{\omega^2 r_m^2}{s_m^2} \left(1 + \frac{E_m}{k_T G_m} \right) W''(x) + \left(\frac{\omega^4 \rho_m r_m^2}{s_m^2 k_T G_m} - \frac{\omega^2}{s_m^2} \right) W(x) = 0. \tag{3.94}$$

If the form $W(x) = e^{\beta x}$ is assumed, then Eq. (3.91) reduces to

$$\beta^4 + \frac{\omega^2 r_m^2}{s_m^2}\left(1 + \frac{E_m}{k_T G_m}\right)\beta^2 + \frac{\omega^4 \rho_m r_m^2}{s_m^2 k_T G_m} - \frac{\omega^2}{s_m^2} = 0. \tag{3.95}$$

For each material $m \in \{1, 2\}$, solving the above equation will yield four roots: β_{m1}, β_{m2}, β_{m3}, and β_{m4}. The solution for the displacement $W(x)$ is then

$$W_m(x) = A_{m1}e^{\beta_{m1}x} + A_{m2}e^{\beta_{m2}x} + A_{m3}e^{\beta_{m3},x} + A_{m4}e^{\beta_{m4}x}, \tag{3.96}$$

where A_{m1}, A_{m2} A_{m3} and A_{m4} are real or complex constants. Using Floquet theorem for the periodic beam, it can be shown that the displacement, slope, bending moment, and shear force are quasi-periodic across adjoining cells. The Floquet wavenumber is given by Eq. (3.77).

3.4.4 Dispersion of Timoshenko Beam Model

The dispersion relations for the bi-material Timoshenko periodic beam can be derived in a manner similar to that in § 3.4.2. First, a relationship between the set of eight constants A_{m1}, A_{m2}, A_{m3}, and A_{m4} is established. Imposing the continuity of displacement, slope, bending moment, and shear force at $x = 0$ produces four equations. From Eq. (3.96), continuity of displacements implies

$$A_{11} + A_{12} + A_{13} + A_{14} = A_{21} + A_{22} + A_{23} + A_{24}. \tag{3.97}$$

Continuity of slope yields

$$\beta_{11}A_{11} + \beta_{12}A_{12} + \beta_{13}A_{13} + \beta_{14}A_{14} = \beta_{21}A_{21} + \beta_{22}A_{22} + \beta_{23}A_{23} + \beta_{24}A_{24}. \tag{3.98}$$

Recall the moment is given by Eq. (3.92). The value of $\frac{\partial \phi}{\partial x}$ is found by rearranging Eq. (3.87a) as

$$\frac{\partial \phi}{\partial x} = \frac{\partial^2 w}{\partial x^2} - \frac{\rho}{k_T G}\frac{\partial^2 w}{\partial t^2}. \tag{3.99}$$

Continuity of moments produces

$$E_1 I_1 \frac{\partial \phi_1}{\partial x} = E_2 I_2 \frac{\partial \phi_2}{\partial x}. \tag{3.100}$$

Substituting Eq. (3.99) into Eq. (3.100) and applying separation of time and space results in

$$E_1 I_1 \left(\frac{\mathrm{d}^2 W_1}{\mathrm{d}x^2} + \frac{\rho_1 \omega^2}{k_T G_1}W_1\right) = E_2 I_2 \left(\frac{\mathrm{d}^2 W_2}{\mathrm{d}x^2} + \frac{\rho_2 \omega^2}{k_T G_2}W_2\right). \tag{3.101}$$

Now, letting $\tilde{A} = EI$ and $\tilde{B} = \tilde{A}\frac{\rho\omega^2}{k_T G}$, substituting Eq. (3.96) into Eq. (3.101) yields

$$\begin{aligned}
&\tilde{A}_1\left(\beta_{11}^2 A_{11} + \beta_{12}^2 A_{12} + \beta_{13}^2 A_{13} + \beta_{14}^2 A_{14}\right) + \tilde{B}_1\left(A_{11} + A_{12} + A_{13} + A_{14}\right) \\
&= \tilde{A}_2\left(\beta_{21}^2 A_{21} + \beta_{22}^2 A_{22} + \beta_{23}^2 A_{23} + \beta_{24}^2 A_{24}\right) + \tilde{B}_2\left(A_{21} + A_{22} + A_{23} + A_{24}\right).
\end{aligned} \tag{3.102}$$

Lastly, continuity of shear implies

$$A_1 G_1 \left(\frac{\partial w_1}{\partial x} - \phi_1\right) = A_2 G_2 \left(\frac{\partial w_2}{\partial x} - \phi_2\right). \tag{3.103}$$

Unfortunately, the expression for ϕ in terms of w is not directly available. To obtain this, assume $\phi(x,t) = \Phi(x)\mathrm{e}^{i\omega t}$ where the frequency ω is equivalent to the frequency of the displacement $w(x,t) = W(x)\mathrm{e}^{i\omega t}$. Thus, Eq. (3.87a)b is written as

$$k_T AG\Phi - \rho I\omega^2 \Phi = EI\frac{\mathrm{d}^2\Phi}{\mathrm{d}x^2} + k_T AG\frac{\mathrm{d}W}{\mathrm{d}x}. \tag{3.104}$$

Applying separation of variables and differentiating Eq. (3.99) gives $\frac{\mathrm{d}^2\Phi}{\mathrm{d}x^2}$ as

$$\frac{\mathrm{d}^2\Phi}{\mathrm{d}x^2} = \frac{\mathrm{d}^3W}{\mathrm{d}x^3} + \frac{\rho\omega^2}{k_TG}\frac{\mathrm{d}W}{\mathrm{d}x}. \tag{3.105}$$

Substituting Eq. (3.105) into Eq. (3.104),

$$(k_TAG - \rho I\omega^2)\Phi = EI\frac{\mathrm{d}^3W}{\mathrm{d}x^3} + \left(\frac{EI\rho\omega^2}{k_TG} + k_TAG\right)\frac{\mathrm{d}W}{\mathrm{d}x}. \tag{3.106}$$

Using the previously defined constants $\tilde{A}$ and $\tilde{B}$, define $\tilde{C} = \frac{\tilde{A}}{k_TAG-\rho I\omega^2}$ and $\tilde{D} = \frac{\tilde{B}+k_TAG}{k_TAG-\rho I\omega^2}$. Thus, Eq. (3.106) becomes

$$\Phi = \tilde{C}\frac{\mathrm{d}^3W}{\mathrm{d}x^3} + \tilde{D}\frac{\mathrm{d}W}{\mathrm{d}x}. \tag{3.107}$$

Substituting Eq. (3.107) into Eq. (3.103) and applying separation of variables,

$$A_1G_1\left[\tilde{C}_1\frac{\mathrm{d}^3W_1}{\mathrm{d}x^3} + (1 - \tilde{D}_1)\frac{\mathrm{d}W_1}{\mathrm{d}x}\right] = A_2G_2\left[\tilde{C}_2\frac{\mathrm{d}^3W_2}{\mathrm{d}x^3} + (1 - \tilde{D}_2)\frac{\mathrm{d}W_2}{\mathrm{d}x}\right]. \tag{3.108}$$

Defining $\tilde{E} = AG\tilde{C}$ and $\tilde{F} = AG(1 - \tilde{D})$, substituting Eq. (3.96) into Eq. (3.108) finally yields

$$\tilde{E}_1\left(\beta_{11}^3A_{11} + \beta_{12}^3A_{12} + \beta_{13}^3A_{13} + \beta_{14}^3A_{14}\right) + \tilde{F}_1\left(\beta_{11}A_{11} + \beta_{12}A_{12} + \beta_{13}A_{13} + \beta_{14}A_{14}\right)$$
$$= \tilde{E}_2\left(\beta_{21}^3A_{21} + \beta_{22}^3A_{22} + \beta_{23}^3A_{23} + \beta_{24}^3A_{24}\right) + \tilde{F}_2\left(\beta_{21}A_{21} + \beta_{22}A_{22} + \beta_{23}A_{23} + \beta_{24}A_{24}\right). \tag{3.109}$$

An additional set of four relations are established by using the Floquet relations in Eq. (3.77) in order to relate the displacements and other physical variables at $x = -L_1$ and at $x = L_2$. This gives

$$A_{11}e^{\mu L-\beta_{11}L_1} + A_{12}e^{\mu L-\beta_{12}L_1} + A_{13}e^{\mu L-\beta_{13}L_1} + A_{14}e^{\mu L-\beta_{14}L_1}$$
$$= A_{21}e^{\beta_{21}L_2} + A_{22}e^{\beta_{22}L_2} + A_{23}e^{\beta_{23}L_2} + A_{24}e^{\beta_{24}L_2}, \tag{3.110a}$$

$$\beta_{11}A_{11}\mathrm{e}^{\mu L-\beta_{11}L_1} + \beta_{12}A_{12}\mathrm{e}^{\mu L-\beta_{12}L_1} + \beta_{13}A_{13}\mathrm{e}^{\mu L-\beta_{13}L_1} + \beta_{14}A_{14}\mathrm{e}^{\mu L-\beta_{14}L_1}$$
$$= \beta_{21}A_{21}\mathrm{e}^{\beta_{21}L_2} + \beta_{22}A_{22}\mathrm{e}^{\beta_{22}L_2} + \beta_{23}A_{23}\mathrm{e}^{\beta_{23}L_2} + \beta_{24}A_{24}\mathrm{e}^{\beta_{24}L_2},$$

$$(3.110\mathrm{b})$$

$$\tilde{A}_1\left(\beta_{11}^2A_{11}\mathrm{e}^{\mu L-\beta_{11}L_1} + \beta_{12}^2A_{12}\mathrm{e}^{\mu L-\beta_{12}L_1} + \beta_{13}^2A_{13}\mathrm{e}^{\mu L-\beta_{13}L_1} + \beta_{14}^2A_{14}\mathrm{e}^{\mu L-\beta_{14}L_1}\right)$$
$$+\tilde{B}_1\left(A_{11}\mathrm{e}^{\mu L-\beta_{11}L_1} + A_{12}\mathrm{e}^{\mu L-\beta_{12}L_1} + A_{13}\mathrm{e}^{\mu L-\beta_{13}L_1} + A_{14}\mathrm{e}^{\mu L-\beta_{14}L_1}\right)$$
$$= \tilde{A}_2\left(\beta_{21}^2A_{21}\mathrm{e}^{\beta_{21}L_2} + \beta_{22}^2A_{22}\mathrm{e}^{\beta_{22}L_2} + \beta_{23}^2A_{23}\mathrm{e}^{\beta_{23}L_2} + \beta_{24}^2A_{24}\mathrm{e}^{\beta_{24}L_2}\right)$$
$$+\tilde{B}_2\left(A_{21}\mathrm{e}^{\beta_{21}L_2} + A_{22}\mathrm{e}^{\beta_{22}L_2} + A_{23}\mathrm{e}^{\beta_{23}L_2} + A_{24}\mathrm{e}^{\beta_{24}L_2}\right),$$

$$(3.110\mathrm{c})$$

$$\tilde{E}_1\left(\beta_{11}^3A_{11}\mathrm{e}^{\mu L-\beta_{11}L_1} + \beta_{12}^3A_{12}\mathrm{e}^{\mu L-\beta_{12}L_1} + \beta_{13}^3A_{13}\mathrm{e}^{\mu L-\beta_{13}L_1} + \beta_{14}^3A_{14}\mathrm{e}^{\mu L-\beta_{14}L_1}\right)$$
$$+\tilde{F}_1\left(\beta_{11}A_{11}\mathrm{e}^{\mu L-\beta_{11}L_1} + \beta_{12}A_{12}\mathrm{e}^{\mu L-\beta_{12}L_1} + \beta_{13}A_{13}\mathrm{e}^{\mu L-\beta_{13}L_1} + \beta_{14}A_{14}\mathrm{e}^{\mu L-\beta_{14}L_1}\right)$$
$$= \tilde{E}_2\left(\beta_{21}^3A_{21}\mathrm{e}^{\beta_{21}L_2} + \beta_{22}^3A_{22}\mathrm{e}^{\beta_{22}L_2} + \beta_{23}^3A_{23}\mathrm{e}^{\beta_{23}L_2} + \beta_{24}^3A_{24}\mathrm{e}^{\beta_{24}L_2}\right)$$
$$+\tilde{F}_2\left(\beta_{21}A_{21}\mathrm{e}^{\beta_{21}L_2} + \beta_{22}A_{22}\mathrm{e}^{\beta_{22}L_2} + \beta_{23}A_{23}\mathrm{e}^{\beta_{23}L_2} + \beta_{24}A_{24}\mathrm{e}^{\beta_{24}L_2}\right).$$

$$(3.110\mathrm{d})$$

Equations (3.97), (3.98), (3.102), (3.109), & (3.110) are combined to form a set of eight homogeneous equations of the form $\mathbf{T}\{X\} = 0$ where $\{X\}$ is a vector containing the eight constants. The matrix $\mathbf{T}$ (written as $\mathbf{T} = [\mathbf{T_L}][\mathbf{T_R}]$) is obtained as

$$
\mathbf{T_L} =
\begin{bmatrix}
1 & 1 & 1 & 1 \\
\beta_{11} & \beta_{12} & \beta_{13} & \beta_{14} \\
\tilde{A}_1\beta_{11}^2 + \tilde{B}_1 & \tilde{A}_1\beta_{12}^2 + \tilde{B}_1 & \tilde{A}_1\beta_{13}^2 + \tilde{B}_1 & \tilde{A}_1\beta_{14}^2 + \tilde{B}_1 \\
\tilde{E}_1\beta_{11}^3 + \tilde{F}_1\beta_{11} & \tilde{E}_1\beta_{12}^3 + \tilde{F}_1\beta_{12} & \tilde{E}_1\beta_{13}^3 + \tilde{F}_1\beta_{13} & \tilde{E}_1\beta_{14}^3 + \tilde{F}_1\beta_{14} \\
\kappa\mathrm{e}^{-\beta_{11}L_1} & \kappa\mathrm{e}^{-\beta_{12}L_1} & \kappa\mathrm{e}^{-\beta_{13}L_1} & \kappa\mathrm{e}^{-\beta_{14}L_1} \\
\kappa\beta_{11}\mathrm{e}^{-\beta_{11}L_1} & \kappa\beta_{12}\mathrm{e}^{-\beta_{12}L_1} & \kappa\beta_{13}\mathrm{e}^{-\beta_{13}L_1} & \kappa\beta_{14}\mathrm{e}^{-\beta_{14}L_1} \\
\kappa(\tilde{A}_1\beta_{11}^2 + \tilde{B}_1)\mathrm{e}^{-\beta_{11}L_1} & \kappa(\tilde{A}_1\beta_{12}^2 + \tilde{B}_1)\mathrm{e}^{-\beta_{12}L_1} & \kappa(\tilde{A}_1\beta_{13}^2 + \tilde{B}_1)\mathrm{e}^{-\beta_{13}L_1} & \kappa(\tilde{A}_1\beta_{14}^2 + \tilde{B}_1)\mathrm{e}^{-\beta_{14}L_1} \\
\kappa(\tilde{E}_1\beta_{11}^3 + \tilde{F}_1\beta_{11})\mathrm{e}^{-\beta_{11}L_1} & \kappa(\tilde{E}_1\beta_{12}^3 + \tilde{F}_1\beta_{12})\mathrm{e}^{-\beta_{12}L_1} & \kappa(\tilde{E}_1\beta_{13}^3 + \tilde{F}_1\beta_{13})\mathrm{e}^{-\beta_{13}L_1} & \kappa(\tilde{E}_1\beta_{14}^3 + \tilde{F}_1\beta_{14})\mathrm{e}^{-\beta_{14}L_1}
\end{bmatrix},
$$

$$(3.111)$$

$$
\mathbf{T_R} = -
\begin{bmatrix}
1 & 1 & 1 & 1 \\
\beta_{21} & \beta_{22} & \beta_{23} & \beta_{24} \\
\tilde{A}_2\beta_{21}^2 + \tilde{B}_2 & \tilde{A}_2\beta_{22}^2 + \tilde{B}_2 & \tilde{A}_2\beta_{23}^2 + \tilde{B}_2 & \tilde{A}_2\beta_{24}^2 + \tilde{B}_2 \\
\tilde{E}_2\beta_{21}^3 + \tilde{F}_2\beta_{21} & \tilde{E}_2\beta_{22}^3 + \tilde{F}_2\beta_{22} & \tilde{E}_2\beta_{23}^3 + \tilde{F}_2\beta_{23} & \tilde{E}_2\beta_{24}^3 + \tilde{F}_2\beta_{24} \\
\mathrm{e}^{\beta_{21}L_2} & \mathrm{e}^{\beta_{22}L_2} & \mathrm{e}^{\beta_{23}L_2} & \mathrm{e}^{\beta_{24}L_2} \\
\beta_{21}\mathrm{e}^{\beta_{21}L_2} & \beta_{22}\mathrm{e}^{\beta_{22}L_2} & \beta_{23}\mathrm{e}^{\beta_{23}L_2} & \beta_{24}\mathrm{e}^{\beta_{24}L_2} \\
(\tilde{A}_2\beta_{21}^2 + \tilde{B}_2)\mathrm{e}^{\beta_{21}L_2} & (\tilde{A}_2\beta_{22}^2 + \tilde{B}_2)\mathrm{e}^{\beta_{22}L_2} & (\tilde{A}_2\beta_{23}^2 + \tilde{B}_2)\mathrm{e}^{\beta_{23}L_2} & (\tilde{A}_2\beta_{24}^2 + \tilde{B}_2)\mathrm{e}^{\beta_{24}L_2} \\
(\tilde{E}_2\beta_{21}^3 + \tilde{F}_2\beta_{21})\mathrm{e}^{\beta_{21}L_2} & (\tilde{E}_2\beta_{22}^3 + \tilde{F}_2\beta_{22})\mathrm{e}^{\beta_{22}L_2} & (\tilde{E}_2\beta_{23}^3 + \tilde{F}_2\beta_{23})\mathrm{e}^{\beta_{23}L_2} & (\tilde{E}_2\beta_{24}^3 + \tilde{F}_2\beta_{24})\mathrm{e}^{\beta_{24}L_2}
\end{bmatrix},
$$

$$(3.112)$$

where $\kappa = \mathrm{e}^{\mu L}$. The procedure to determine the Floquet wavenumber μ_n is equivalent to that presented in § 3.4.2, where Eqs. (3.81)-(3.85) are used to calculate μ_n. Figure 3.9 plots the dispersion relation of the aluminum-brass beam using the Timoshenko beam theory and compares it to the dispersion relation obtained using the Euler-Bernoulli assumptions. The curves in Fig. 3.9(a) are for the beam geometry given in § 3.4.2 (width and thickness of 0.005 m). It is observed that the dispersion relations of the Euler-Bernoulli and Timoshenko beams coincide, indicating that the assumptions behind the Euler-Bernoulli beam theory are satisfied. Contrast this to the dispersion curves in Fig. 3.9(b) where the beam geometry is

now quite thick (width and thickness of 1 m). As the frequencies increase, the dispersion curve of the Timoshenko beam is shifted slightly to the left of the Euler-Bernoulli curves. This "shift" occurs since the Timoshenko beam considers shearing effects, which are more influential for the thicker beam geometry. A comparison of the dispersion curves to the dispersion curves determined via finite elements (not shown here) shows that the Timoshenko curves more closely match the FE data since the assumptions of the Euler-Bernoulli beam are invalid.
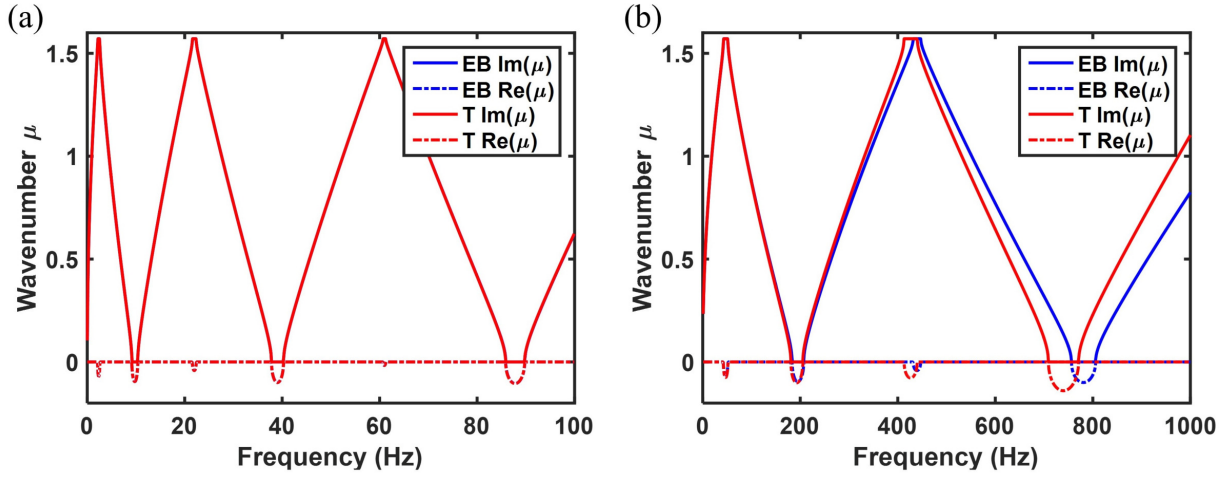
Figure 3.9. (a) The dispersion curve of the aluminium-brass periodic Timoshenko (T) beam compared to an Euler-Bernoulli (EB) beam for a long, slender geometry. (b) Comparison of the dispersion relation of an Euler-Bernoulli and Timoshenko beam for a thick beam geometry where the thickness and width are each 1 m.

3.5   Fractional Beam Model

Having determined the dispersion relation of the bi-material periodic beam, this section develops the corresponding fractional model and determines its fractional order. Although the previous section considered both an Euler-Bernoulli and Timoshenko beam, the remainder of the chapter focuses on developing the fractional beam corresponding to the Euler-Bernoulli beam. A fractional formulation corresponding to the Timoshenko beam theory can be found in [141].

131

3.5.1 Governing Equations

The development of the fractional beam model will take a different route than the fractional rod from § 3.2 because the model is built directly upon the fractional beam model derived in [113]. As with the fractional rod, the fractional beam model can be considered as a homogenized representation of the bi-material periodic beam where the space fractional derivative operator captures the effect of inhomogeneities. According to [113], the nonlocal axial strain ($\bar{\epsilon}$) of the fractional Euler-Bernoulli beam is defined as

$$\bar{\epsilon}(x, z) = -z D_x^\alpha \left[\frac{\partial \bar{w}(x, t)}{\partial x} \right], \tag{3.113}$$

where $\bar{w}$ is the transverse response of the fractional beam. In the above equation, $D_x^\alpha(\cdot)$ is a space fractional Riesz-Caputo (RC) derivative with order $\alpha \in (0, 1)$ defined on the interval $x \in (0, L)$ as

$$D_x^\alpha \Psi(x) = \frac{1}{2} \bar{l}^{\alpha-1} \left[{}_0^C D_x^\alpha \Psi(x) - {}_x^C D_L^\alpha \Psi(x) \right], \tag{3.114}$$

where Ψ is an arbitrary function and $\bar{l}$ is a length-scale factor introduced to ensure dimensional consistency of the fractional-order derivative (and whose value is taken as unity just like Q in Eqs. (2.46) and (3.46)). The operators ${}_0^C D_x^\alpha(\cdot)$ and ${}_x^C D_L^\alpha(\cdot)$ are the left- and right-handed Caputo derivatives of order α, respectively. Note that [112] considered a different version of Eq. (3.114) where different length scales of non-unity value are associated with both the left- and right-handed Caputo derivatives. The RC definition given in [112] (which will be explored further and implemented in § 4.4.1) ensured frame-invariance was satisfied for finite fractional beams. Here, the considered bi-material Euler Bernoulli beam and its corresponding fractional counterpart are infinite structures.

The interval of the RC fractional derivative in Eq. (3.114) defines the horizon of nonlocality of the fractional order beam; that is, the distance beyond which information is no longer accounted for within the fractional derivative. The horizon of nonlocality in Eq. (3.114) coincides with the length of the beam. In this case, the nonlocal convolution corresponding to the intervals of the RC derivative would actually be over the interval $(-\infty, \infty)$. Note

that this assumption on the infinite extent of the nonlocal horizon matches closely with the formulation proposed by Eringen et al. [142]. Also, classical low-frequency homogenization theories often result in integral averaging expressions over the entire domain of the solid [16]. Further, the Caputo fractional derivatives defined in Eq. (3.113) lead to a frame-invariant formulation for an infinite beam. This is important to ensure that no strain is accumulated in the 1D solid under translation [51], [141].

[113] derives the governing equations of the fractional beam using the generalized Hamilton's principle. In this derivation, the total nonlocal potential energy of the fractional beam of volume $\mathcal{V}$ is

$$\Pi = \frac{1}{2} \int_{\mathcal{V}} \bar{\sigma}(x,z)\bar{\epsilon}(x,z) \ \mathrm{d}V - \int_L F_T(x,t) \ \bar{w}(x)\mathrm{d}x, \tag{3.115}$$

where the second integral in the above expression corresponds to the work done by the transverse force $F_T(x,t)$ applied externally on a plane perpendicular to the beam's neutral axis and the fractional stress is defined as

$$\bar{\sigma}(x,z) = \bar{E}\bar{\epsilon}(x,z), \tag{3.116}$$

where $\bar{E}$ is the Young's modulus of the fractional beam. The kinetic energy of the beam is

$$T = \frac{1}{2} \int_{\mathcal{V}} \bar{\rho} \left(\frac{\partial \bar{w}}{\partial t}\right)^2 \mathrm{d}V, \tag{3.117}$$

where $\bar{\rho}$ is the fractional beam's density. Using the potential and kinetic energy, the governing differential equations (GDE), the associated boundary conditions (BC), and the initial conditions (IC) necessary to determine the response of the fractional beam are (see [113] for entire derivation)

$$\text{GDE}: \bar{E}\bar{I}\frac{\partial}{\partial x}\left[\mathfrak{D}_x^\alpha\left[D_x^\alpha\left(\frac{\partial \bar{w}}{\partial x}\right)\right]\right] + \bar{\rho}\bar{A}\frac{\partial^2 \bar{w}}{\partial t^2} = F_T(x,t) \ \ \forall \ \ x \in (0,L) \ \cup \ t \in (0,\infty), \tag{3.118a}$$

133

$$\text{BC} : \begin{cases} \bar{E}\bar{I}\left[\mathcal{I}_x^{1-\alpha}D_x^\alpha\left(\frac{\partial \bar{w}(x,t)}{\partial x}\right)\right] = 0 \ \ \text{or} \ \ \delta\left(\frac{\partial \bar{w}(x,t)}{\partial x}\right) = 0 \ \ \text{at} \ \ x \in \{0,L\} \ \cup \ t \in (0,\infty), \\ \bar{E}\bar{I}\left[\mathfrak{D}_x^\alpha D_x^\alpha\left(\frac{\partial \bar{w}(x,t)}{\partial x}\right)\right] = 0 \ \ \text{or} \ \ \delta\bar{w}(x,t) = 0 \ \ \text{at} \ \ x \in \{0,L\} \ \cup \ t \in (0,\infty), \end{cases}$$

$$(3.118\text{b})$$

$$\text{IC} : \delta\bar{w}(x,t) = 0 \ \ \text{and} \ \ \delta\left(\frac{\partial \bar{w}(x,t)}{\partial t}\right) = 0 \ \ \text{at} \ \ t = 0 \ \cup \ x \in (0,L), \qquad (3.118\text{c})$$

where $\bar{I}$ and $\bar{A}$ are the quadratic moment of inertia and cross-sectional area of the fractional beam, respectively. In Eq. (3.118), $\mathfrak{D}_x^\alpha(\cdot)$ is a Riesz Riemann-Liouville derivative of order α defined on the interval $x \in (0,L)$ as

$$\mathfrak{D}_x^\alpha \Psi(x) = \frac{1}{2}\bar{l}^{\alpha-1}\left[{}^{RL}_0 D_x^\alpha \Psi(x) - {}^{RL}_x D_L^\alpha \Psi(x)\right], \qquad (3.119)$$

where Ψ is an arbitrary function, and ${}^{RL}_0 D_x^\alpha(\cdot)$ and ${}^{RL}_x D_L^\alpha(\cdot)$ are the left- and right-handed Riemann Liouville fractional order derivatives, respectively. Also, $\mathcal{I}_x^{1-\alpha}(\cdot)$ is a Reisz fractional integral defined as

$$\mathcal{I}^{1-\alpha}\Psi(x) = \frac{1}{2}\bar{l}^{\alpha-1}\left[{}_0\mathcal{I}_x^{1-\alpha}\Psi(x) + {}_x\mathcal{I}_L^{1-\alpha}\Psi(x)\right], \qquad (3.120)$$

where ${}_0\mathcal{I}_x^{1-\alpha}(\cdot)$ and ${}_x\mathcal{I}_L^{1-\alpha}(\cdot)$ are the left- and right-handed Riemann Liouville fractional order integrals, respectively. Note that classical beam governing equations are recovered for $\alpha = 1$.

3.5.2 Dispersion and Fractional Order

Just as for the fractional rod, the appropriate value of the fractional order α of the fractional beam is determined by equating the dispersion relation of the bi-material periodic beam (given in Fig. 3.8) to that of the fractional beam. To obtain the dispersion relation of the fractional beam, substitute the ansatz

$$\bar{w}(x,t) = \tilde{A}_1 e^{(kx-\mathrm{i}\omega t)} + \tilde{A}_2 e^{(kx+\mathrm{i}\omega t)}, \qquad (3.121)$$

134

into the fractional beam's governing equation where $\tilde{A}_1$ and $\tilde{A}_2$ are the amplitudes of the wave propagating in the positive and in the negative spatial directions, respectively, k is the wavenumber, and ω is the angular frequency. Equation (3.121) was chosen since it is the standard exponential representation of wave propagation and since the fractional derivative (with bounds of $\pm\infty$) of an exponential is an exponential (see Eq. (3.32)). Given the wave solution assumed in Eq. (3.121), the real and complex parts of the complex wave number k correspond to the attenuating and propagating component of the wave. Note that the ansatz assumed in Eq. (3.121) is contrary to the standard form $A_1 e^{i(kx-\omega t)} + A_2 e^{i(kx+\omega t)}$. The former expression was assumed in order to remain consistent with the form of the Floquet wavenumber assumed in Eq. (3.77).

Substituting Eq. (3.121) into Eq. (3.118a), the dispersion relation for transverse waves in the fractional beam is obtained as

$$k = e^{\frac{2\pi i}{1+\alpha}} \left[\omega^2 \bar{l}^{2(1-\alpha)} \frac{\bar{\rho}\bar{A}}{\overline{EI}} \right]^{\frac{1}{2(1+\alpha)}}. \tag{3.122}$$

The fractional order α for the fractional beam can now be obtained by insisting that the wavenumber obtained through Eq. (3.122) is equal to the wavenumber μ of the bi-material Euler-Bernoulli beam from Eq. (3.77). Recall that the constant $\bar{l}$ is introduced to ensure dimensional consistency of the formulation and is of unity value. Thus, solving Eq. (3.122) for α yields

$$\alpha = \left[\frac{\log\left(\omega^2 \bar{\rho}\bar{A}/\bar{E}\bar{I} \right)}{\log\left(-k^2 \right)} \right] - 1. \tag{3.123}$$

The propagating component of the wavenumber for transverse waves in the beam relates to the angular frequency as $\mathrm{Im}(k)^4 = \omega^2 \rho \bar{A}/\bar{E}\bar{I}$. Using this relation, the expression for α is simplified as

$$\alpha = 4 \left[\frac{\log|\mathrm{Im}(k)|}{\log\left(-k^2 \right)} \right] - 1. \tag{3.124}$$

The formulation for the fractional beam results in a variable order α, where α is a function of the angular frequency ω. A plot of the fractional order α for the aluminum-brass

periodic beam is given in Fig. 3.10. Similar to the fractional rod (specifically the case using a frequency-dependent wave speed in § 3.2.2), the fractional order in Fig. 3.10 is a complex quantity for band gap frequencies while the order is a purely real number ($\alpha = 1$) for band-pass frequencies. This is consistent with the physics of the problem since $\alpha = 1$ is indicative of propagating waves [112]. In the band gaps, $\mathrm{Re}(\alpha) < 1$ and $\mathrm{Im}(\alpha) < 0$. $\mathrm{Re}(\alpha) < 1$ indicates that flexural waves in the periodic beam attenuate spatially, which is again consistent with the fact that this frequency is located within a band gap. Additionally, $\mathrm{Im}(\alpha) < 0$ indicates a frequency-dependent modulation of the phase of the beam response.
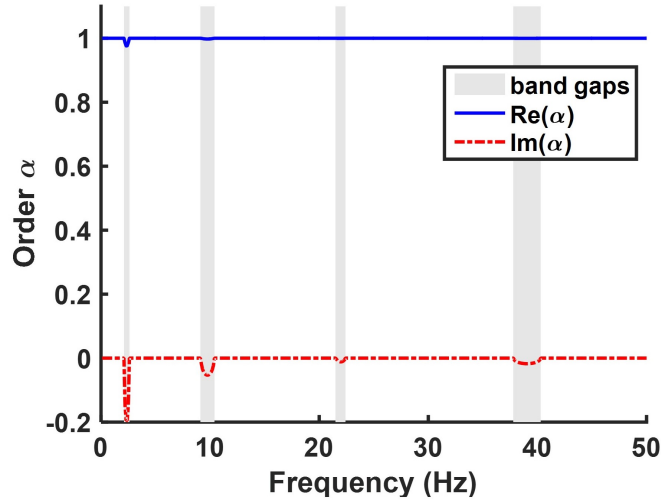
Figure 3.10. The order α for the fractional beam as a function of frequency. The fractional order is equal to 1 for frequencies in the pass-bands, while the order is complex valued for frequencies within the band gaps.

3.6 Numerical Solution and Assessment of the Fractional Beam

Having obtained the governing equation and fractional order for the fractional beam, its solution is compared to the flexural displacement of the bi-material periodic beam to assess the ability of the fractional beam to be an effective homogenization tool. Unlike the space fractional wave equation for the fractional rod, there is no known analytical solution to Eq. (3.118a) of the fractional beam. As a result, this section adopts a fractional finite element method developed in [113] to determine the flexural displacement of the fractional

136

beam. The result is compared to the flexural displacement of the bi-material periodic beam obtained via a commercial finite element software. Again, like the rod, comparing the results of the fractional finite element model of the fractional beam to experimental results would make a more compelling case. In this case, the numerical results obtained via a commercial finite element software are reasonable to use to assess the fractional results because of the relative simplicity of the bi-material beam's geometry.

3.6.1 Fractional Finite Element Method

This section details the alterations made from the fractional finite element method (f-FEM) developed in [113] since the RC derivative used in this analysis for the infinite beam (given by Eq. (3.114)) was different than that implemented in [113] for finite beams. Analogous to classical FEM, the f-FEM is formulated starting from a discretized form of the total potential energy functional given in Eq. (3.115). The domain $\Omega = [0, L]$ is divided into N_e finite elements denoted as Ω_q^e with $q = \{1, .., N_e\}$ such that $\cup_{q=1}^{N_e} \Omega_q^e = \Omega$ and $\Omega_j^e \cap \Omega_k^e = \emptyset \; \forall \; j \neq k$. The transverse displacement at any point $x \in \Omega_q^e$ is evaluated by interpolating the corresponding nodal degrees of freedom of Ω_q^e as

$$\bar{w}(x) = \hat{\mathbf{N}}(\mathbf{x})\{W_q^e\}, \tag{3.125}$$

where $\hat{\mathbf{N}}(\mathbf{x})$ is a matrix containing the interpolation functions and $\{W_q^e\}$ is a vector containing the nodal displacement variables of the element Ω_i^e. From the definition given in Eq. (3.113), the fractional axial strain in the beam is

$$\bar{\epsilon}(x, z) = \frac{-z}{2\Gamma(1-\alpha)} \left[\int_0^L \mathcal{A}(x, x', \alpha)\mathbf{B}(\mathbf{x}')\bar{\mathcal{C}}(\mathbf{x}, \mathbf{x}') \, \mathrm{d}x' \right] \{W\} = -z\bar{\mathbf{B}}(\mathbf{x})\{W\}, \tag{3.126}$$

where x' is a dummy variable used for convolution along the x axis, and $\{W\}$ denotes the global DOF vector. $\mathcal{A}(x, x', \alpha) = 1/|x - x'|^\alpha$ denotes the kernel of the fractional order

derivative. Additionally, the matrix $\mathbf{B}(\mathbf{x}')$ is expressed as the second order derivative of the shape functions given by

$$\mathbf{B}(\mathbf{x}') = \frac{\mathrm{d}^2\hat{\mathbf{N}}(\mathbf{x}')}{\mathrm{d}x'^2}. \tag{3.127}$$

Lastly, $\bar{\mathcal{C}}(\mathbf{x}, \mathbf{x}')$ is a connectivity matrix that is used to attribute the nonlocal contributions from the different elements in the horizon of x to the corresponding nodes of those elements. The connectivity matrix relates the nodes of each element to the global DOFs through

$$\{W_{x'}^{\mathrm{e}}\} = \bar{\mathcal{C}}(\mathbf{x}, \mathbf{x}')\{W\}. \tag{3.128}$$

The connectivity matrix $\bar{\mathcal{C}}(\mathbf{x}, \mathbf{x}')$ is designed such that it is non-zero only if the point x' lies in the nonlocal horizon of x. The fractional strain (Eq. (3.126)) and stress (Eq. (3.116)) are used to determine the total deformation energy of the beam as

$$\mathcal{U} = \frac{1}{2}\{W\}^T\bar{\mathbf{K}}\{W\}, \tag{3.129}$$

where the nonlocal stiffness matrix $\bar{\mathbf{K}}$ is given as

$$\bar{\mathbf{K}} = \bar{E}\bar{I}\int_0^L \mathbf{B}(\mathbf{x})^T\mathbf{B}(\mathbf{x})\mathrm{d}x. \tag{3.130}$$

The f-FEM performs a numerical integration of the nonlocal stiffness matrix $\bar{\mathbf{K}}$ (details in [113]). Although it might appear that this assembly strategy would require the use of larger, global matrices, it is emphasized that simple principles of connectivity are used to avoid the multiplication of large sparse matrices in Eq. (3.126), similar to what is done in local FEM.

The final algebraic equation of the f-FEM model contains an inertial matrix as well such that

$$\bar{\mathbf{M}}\{\ddot{W}\} + \bar{\mathbf{K}}\{W\} = \{F_T\}, \tag{3.131}$$

where the mass-matrix $\bar{\mathbf{M}}$ and the force vector $\{F_T\}$ of the fractional-order beam are the same as obtained in classical FEM for beams [2], [113]. The solution of Eq. (3.131) gives

the nodal generalized displacement coordinates. Additionally, the robust f-FEM described above is still convergent for the complex orders of the frequency band gaps.

3.6.2   Assessment of Numerical Results

The validity of the homogenized fractional beam model is now assessed by comparing the flexural displacement of the fractional beam obtained from the f-FEM to the flexural displacement displacement of the aluminum-brass periodic beam obtained via a commercial finite element software (COMSOL). Similar to the fractional rod in § 3.3, the infinite beam structure is subjected to a prescribed harmonic flexural displacement at its center. Since the forward and backward propagating waves will be equivalent, consider only the section of the infinite periodic beam in the positive x axis. As a result, the analysis is conducted on the rightward propagating wave in a semi-infinite beam.

The flexural transverse displacement is $\bar{w}(0, t) = W_0 e^{i\Omega_0 t}$ at $x = 0$. Thus, the steady-state response across the entire beam is taken as $\{W\} = \{W_0\}e^{i\Omega_0 t}$, where $\{W_0\}$ is the steady-state amplitude. Substituting this into Eq. (3.131) yields

$$\{W_0\} = \left(\bar{\mathbf{K}} - \Omega_0^2 \bar{\mathbf{M}}\right)^{-1} \{F_T\}. \tag{3.132}$$

To simulate a semi-infinite beam and prevent any reflections in the numerical solution, an absorbing boundary condition is implemented at the truncated end of the fractional beam according to [143].

The analysis considers four different forcing frequencies each corresponding to a different region of the dispersion curve in Fig. 3.8: 1) the driving angular frequency $\Omega_0 = 5$ rad/s lies in the first pass-band; 2) the driving angular frequency $\Omega_0 = 15$ rad/s lies in the first band gap; 3) the driving angular frequency $\Omega_0 = 40$ rad/s lies in the second pass-band; and 4) the driving angular frequency $\Omega_0 = 61$ rad/s lies in the second band gap. The fractional order α for these cases are obtained using Eq. (3.124) and are 1, $0.97 - 0.19i$, 1, and $0.99 - 0.05i$, respectively. The results obtained for the four loading cases defined above are shown in Fig. 3.11 where they have been compared against the numerical simulations of the bi-material, periodic beam from COMSOL.
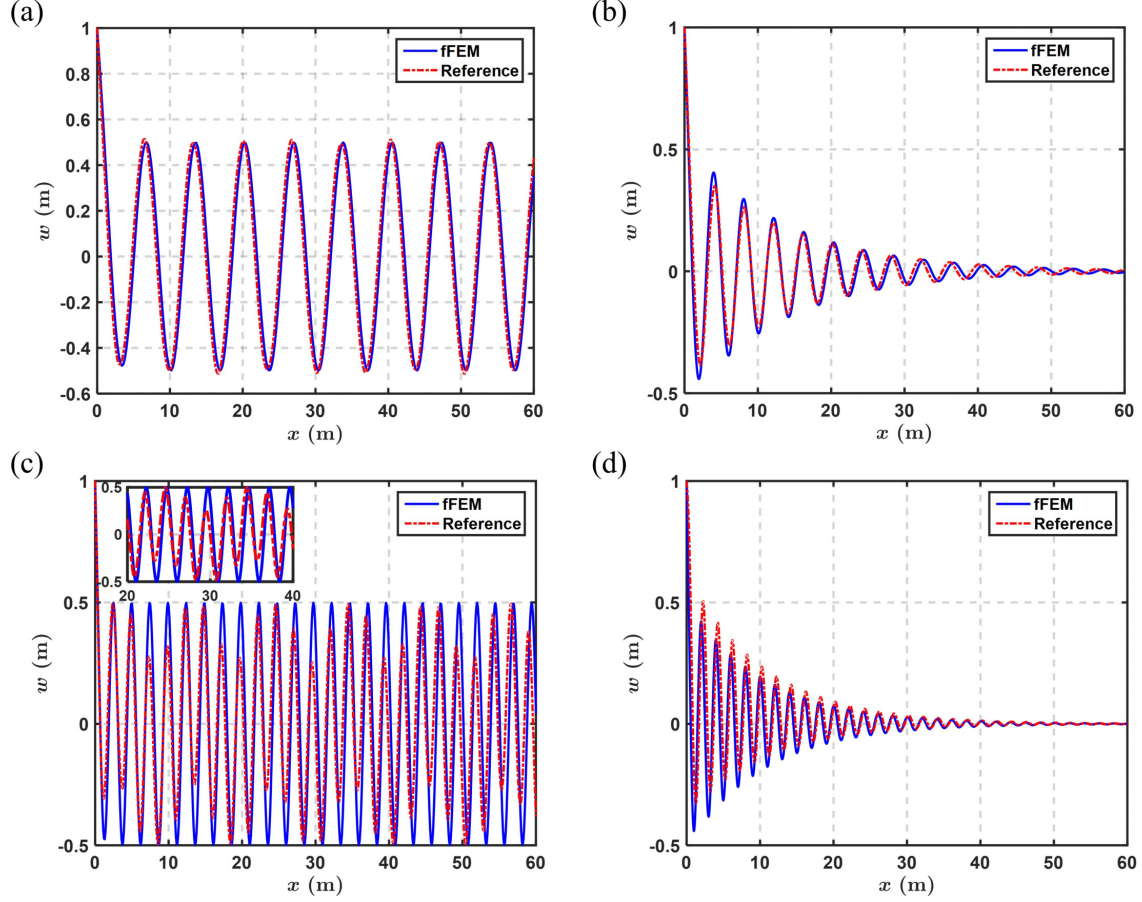
Figure 3.11. The steady state response obtained using the fractional order governing equation for the beam solved via the f-FEM. For the different cases, the forcing frequency of the external load is within the (a) first pass-band: loading #1, (b) first band-gap: loading #2, (c) second pass-band: loading #3, and (d) second band-gap: loading #4. The inset in figure (c) provides a zoomed in view of the response of the beam from $x = 20$ m to $x = 40$ m.

The results in Fig. 3.11(a) and (b) reveal that the match between the results of the aluminum-brass periodic beam and its corresponding fractional model are quite good. However, for loading case #3 where the driving angular frequency lies within the second pass-band, the f-FEM result matches the phase of the COMSOL result, but does not match the amplitude locally. This is past the long wavelength limit of the low-frequency homogenization methods, thus revealing that the fractional model suffers from similar shortcomings as other low-frequency homogenization methods due to scattering effects. One possible route capable of capturing the localized effects would be to use a variable space fractional order,

140

although this needs further research. Moving to loading case #4 where the driving frequency lies in the second band gap, it is again observed that the amplitudes of the two curves do not match due to localization at high frequencies. However, unlike other low-frequency homogenization techniques, the fractional beam model did successfully capture the attenuating flexural displacement within the band gap. This is a key advantage and strength of the fractional beam, making it an ideal homogenization tool for models whose wave propagation occurs in a frequency band gap. For higher-order band gaps, it is expected that the fractional beam model will capture the attenuation due to its complex-valued fractional order, but will experience an increasing mismatch in the amplitude of the response due to the inability of the fractional beam model to capture the localized scattering effects.

3.7 Conclusions

The homogenized space fractional models developed in this chapter serve as a novel homogenization technique which accurately reflected the wave attenuation that occurs in frequency band gaps of periodic, heterogeneous structures. Additionally, the fractional rod model provided a means to obtain a closed-form analytical solution based on either exponential or Mittag-Leffler solution kernels that accurately described the axial displacement of the bi-material periodic rod for band gaps and low-frequency pass bands. These closed-form solutions avoided the computational expenses of asymptotic homogenization approaches. Also, the closed-form solutions can have important implications for inverse problems in material design and remote sensing. Although the governing equation of the fractional beam did not have a known analytical solution, a fractional finite element method was adopted to calculate the flexural displacement of the fractional beam, even for complex orders. This signified an important development for complex order numerical methodologies, which are still relatively young. However, for pass bands located at high frequencies past the long wavelength limit, the fractional models presented here could not capture the localized scattering effects. In this regard, depending on the specific application, the latter aspect may or may not be a disadvantage. For example, if the objective is to simulate the response of a solid with an embedded slab of the periodic medium (e.g., a periodic 1D beam embedded in an otherwise

homogeneous beam), the detailed response inside the periodic medium might not be of interest. Note that this comment is applicable to homogenized models in general and it is neither a consequence nor a peculiarity of the fractional order modeling. Additionally, although some high-frequency homogenization approaches have been more accurate in representing the behavior in the phononic regime, they are based on solving the eigenvalue problem via an asymptotic multiple scale representation of the elastodynamic equation, which is often limited by the computational capabilities of the eigen-solver and becomes progressively more complex as a higher number of terms is used within the multiscale expansion. As such, the performance of the fractional models proposed here may, with modifications, provide a basis for an efficient and accurate broadband homogenization technique for both band gaps and high-frequency pass bands. This chapter successfully illustrated the feasibility and the potential of fractional order homogenization techniques for the dynamic simulation of the band gaps of periodic systems.

4. FRACTIONAL ORDER MODELS FOR ACOUSTIC BLACK HOLE GEOMETRIES

The previous chapter developed a fractional homogenization tool using a 1D bi-material, periodic structure as an example system. While this structure is a classical example of 1D elastic metamaterial, it is not a practical design commonly manufactured. The bi-material, periodic rod and beam would be challenging to manufacture since smoothly joining two different materials at multiple interfaces would be difficult. This chapter advances the space fractional homogenization concepts to a heterogeneous geometry recently manufactured in metamaterial waveguides: the acoustic black hole. Acoustic black holes trap nearly all of the wave energy that propagates through it, making it an ideal tool for passive vibration control and sound attenuation. The acoustic black hole's geometry follows a power-law taper profile. Since fractional derivatives are differ-integral operators based on a power-law kernel, it is hypothesized that a relationship between a space fractional order and the power-law exponent of the taper may exist (see § 4.1.3 for more details relating FC to ABHs). Additionally, common numerical simulations of acoustic black holes tend to computationally expensive due to the need to accurately capture the varying taper of the acoustic black hole. As such, a fractional homogenization of the acoustic black hole may lead to more computationally efficient simulations.

Acoustic black holes have chiefly been studied and manufactured for structural applications such as beams and plates, but have also recently been utilized for acoustic applications as well. The first half of this chapter focuses on developing fractional models to represent the reflection of sound pressure waves in air-filled ducts with ABH terminations. The goal is to mimic the reflection of a planar sound wave into the acoustic duct from the ABH termination using a space fractional model that does not require the simulation of the dynamics within the ABH itself. The latter half creates a homogenized fractional beam model similar to that in § 3.5 for the elastic wave propagation through ABH geometries in structural beams.

However, in this case, the homogenized fractional model aims to not only reflect the effect of the ABH on the rest of the beam, but to also capture the wave propagation within the ABH itself. As will be seen, this will necessitate the use of a variable space fractional order. Contents of the chapter include

- A review of the concepts of acoustic black holes and their applications in structural and acoustic waveguides,

- The calculation of the reflection coefficient of a sound wave produced by an ABH termination in an acoustic duct as a function of its power-law taper,

- A fractional boundary and domain model for the ABH duct which are capable of mimicking the reflection of a sound wave into the main host duct,

- A finite difference formulation of the fractional boundary model to verify its fractional order accurately represents the reflection from the ABH termination,

- Adoption of the fractional beam model presented in the previous chapter to serve as a homogenized model of a portion of a beam containing an ABH profile,

- Use of a governing fractional differential equation containing a variable space fractional order derivative, allowing the fractional homogenized model to capture the dynamic response within the ABH,

- Calculation of the fractional order of the finite fractional beam model of the ABH through an energy-matching approach that provides a link between the fractional order and taper exponent.

4.1 Basic Concepts of Acoustic Black Hole Geometries

Acoustic black holes have been developed for both structural [145]–[166] and acoustic [167]–[170] applications, as reflected in Fig. 4.1. As a waveguide, the main feature of an acoustic black hole is that it can absorb nearly all of the incident energy entering it, which makes it very attractive for applications for passive vibration control and sound attenuation.

144

The dynamic behavior of ABH elements stems from their characteristic geometry that follows a power-law profile as shown in Fig. 4.2. As an acoustic or elastic wave enters the power-law taper, both the phase and group velocities are progressively reduced while the amplitude of the particle displacement increases. In an ideal ABH (i.e., an ABH whose cross-sectional area vanishes at the end of the taper), the incoming wave can never reach the end of the taper; therefore, it is never reflected back. However, in practical implementations, the cross-section of the waveguide can never be reduced to zero. Therefore, reflection should always be expected unless the ABH is combined with a damping mechanism.
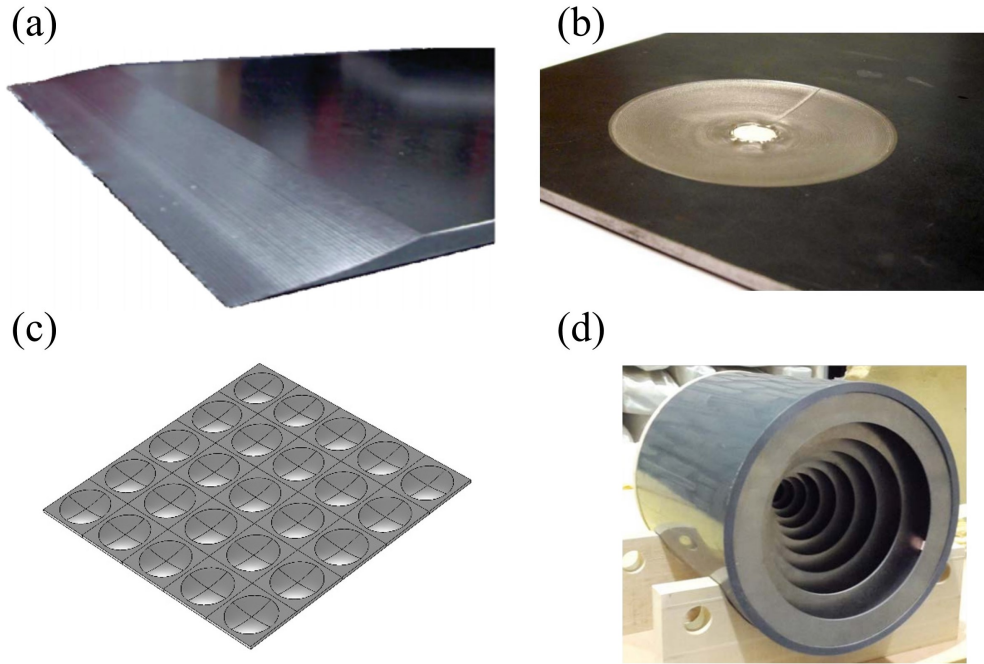
Figure 4.1. ABH waveguides found in literature include (a) 1D ABH plate wedges (Graphics credit: [148] ©2014 IEEE), (b) 2D circular ABH in a plate (Graphics credit: [148] ©2014 IEEE), (c) An array of 2D ABH plate, (d) An ABH termination in an acoustic duct (Graphics credit: [170]).

Finite element models and plane wave expansion have been traditionally used to perform detailed numerical simulations of ABH systems [154], [157], [158]; however, the need to capture the power-law thickness variation dictates minimum requirements on the model's dimensionality which ultimately results in computationally intensive models. For example,
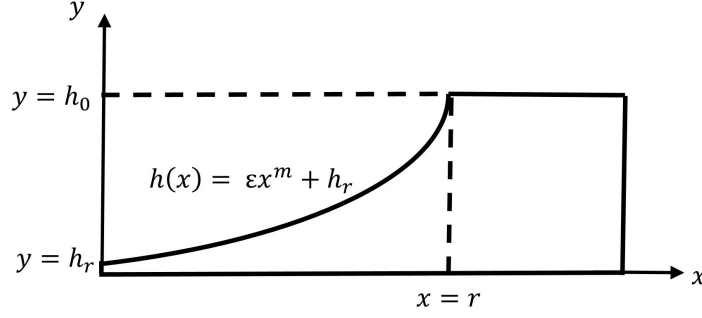
Figure 4.2. Cross section of an acoustic black hole depicting the power-law tapered profile.

a thin plate with ABH terminations on the edges will require a full three-dimensional model instead of a more efficient Kirchhoff plate formulation. Computational efficiency becomes an even more critical consideration for systems with multiple embedded ABHs (e.g., structures with periodic ABHs lattices [155]).

4.1.1   Acoustic Black Holes In Structural Waveguides

In structural waveguides, ABHs have been designed mostly to absorb flexural waves in beams and plates (see Fig. 4.1(a)). Mironov [145], [146] and Krylov [147], [148], [151], [171], [172] pioneered the mathematical work and design approaches for 1D ABHs embedded in beams and plates to achieve efficient reduction of flexural vibrations. In this case, ABHs consist of either embedded tapers or slots having a power-law thickness profile [145], [147], [148], [152]–[155], [157]. To achieve nearly perfect absorption, narrow strips of viscoelastic material cover the power-law wedge. For plate-like structures, the ABH design can be extended in dimensionality to a two-dimensional power-law circular pit as seen in Fig. 4.1(b). In addition, the black hole effect can be more pronounced by arranging the 2D ABH design in a periodic ensemble as shown in Fig. 4.1(c). As seen in [155], when the 2D ABH ensemble is used to create an acoustic metamaterial, many unique behaviors such as zero group velocities, negative group refraction index, collimation, bi-refraction, Dirac-like cones, and mode anisotropy can be achieved.

The latter portion of this chapter will analyze how the fractional beam model introduced in § 3.5 can be used as a homogenization tool for beams with ABH profiles. Mironov [146] provided a thorough analysis of the transverse vibration of a beam with a ABH profile. The equation of motion of the beam is given by Eq. (3.74) where E and ρ are constant, $A(x) = bh(x)$, and $I(x) = bh(x)^3/12$ where b is the beam width. The height $h(x)$ of the beam is given by the power-law relationship of an ABH; in [146], $h(x) = h_0(x/x_0)^m$ where x_0 is the location where the ABH profile begins, h_0 is the height at that location, and m is the power-law exponent. The equation for the harmonic flexural displacement of the beam is

$$(EI(x)w'')'' - \rho A(x)\omega^2 w = 0, \tag{4.1}$$

where w is the flexural displacement, and $'$ indicates differentiation with respect to x. [146] states that the solution of Eq. (4.1), provided that the variation of the cross section is sufficiently smooth, is obtained using a Wentzel–Kramers–Brillouin (WKB) approximation as

$$w_q = \tilde{A}_q(x)\mathrm{e}^{\mathrm{i}\int k_q(x)dx}, \tag{4.2}$$

where the local wavenumber $k_q(x)$ are

$$k_q(x) = \left[\frac{\rho A(x)\omega^2}{EI(x)}\right]^{1/4} \mathrm{e}^{\mathrm{i}\frac{\pi}{2}q}, \tag{4.3}$$

for $q = 0, 1, 2, 3$. The amplitude $\tilde{A}_q(x)$ is determined from energy conservation. [146] further accesses the validity of the WBK approximation and determines that it is only valid for taper exponents of $m \geq 2$. Furthermore, [146] derives the exact solution to Eq. (4.1) for the case $m = 2$; albeit, the mathematics are complicated to the point that obtaining an analytical solution of a beam with a periodic array of imperfect ABHs is exceedingly difficult. By locally approximately any arbitrary power-law thickness profile as a parabola, [146] obtains

the WKB approximation for any taper exponent m. However, once again, implementation of the solution is challenging for practical applications and is not exact since the taper profile must be approximated as parabolic. This prompts the need for other mathematical models of ABH profiles in beams.

4.1.2 Acoustic Black Holes in Acoustic Waveguides

In acoustic waveguides, ABHs absorb pressure waves and are typically used to control pressure and sound levels in ducts [167]–[170]. Influential work in the modeling of acoustic black hole features in air filled ducts was conducted by Mironov et al. [167] and, more recently, by Guasch et al. [168]. Both authors considered a duct having an ABH termination achieved by using a distribution of annular rings whose inner radii decreased following a power-law profile, as depicted in Fig. 4.3. In order to study this system, Mironov et al. [167] proposed an analytical approach leading to a closed-form solution for the case of linear taper ($m = 1$), yielding both the pressure field in the duct and the reflection coefficient from the ABH termination. Later, Guasch et al. [168] extended the analysis of acoustic ducts to obtain the analytical solution and reflection coefficient for a quadratic ($m = 2$) ABH profile. Additionally, El Ouahabi et al. [169], [170] built cylindrical acoustic ducts (see Fig. 4.1(d)) where the radius of the inserted rings varied linearly or quadratically based on the work of [167] and measured the reflection coefficient to illustrate the black hole effect. Unlike the case of structural elements, in acoustic waveguides, the ABH behavior exists for taper exponents less than $m = 2$ due to the combined effect of the variation of the wall admittance (for more details, see Eq. (11) in [167]).

Starting from the linearized form of the continuity and momentum conservation equations, the pressure in the duct of Fig. 4.3 is described by [167] as

$$\frac{\partial^2 p}{\partial x^2} + \frac{\partial p}{\partial x}\frac{\partial(\ln S(x))}{\partial x} + p\left[k_0^2 + \mathrm{i}Z_0 k_0 \frac{2Y(x)}{h(x)}\right] = 0, \tag{4.4}$$

where p is the pressure, $S(x)$ is the cross sectional area of the duct, $k_0 = \omega/c$ is the wavenumber, ω is the frequency, c is the speed of the acoustic wave, $Z_0 = \rho_0 c$ is the characteristic
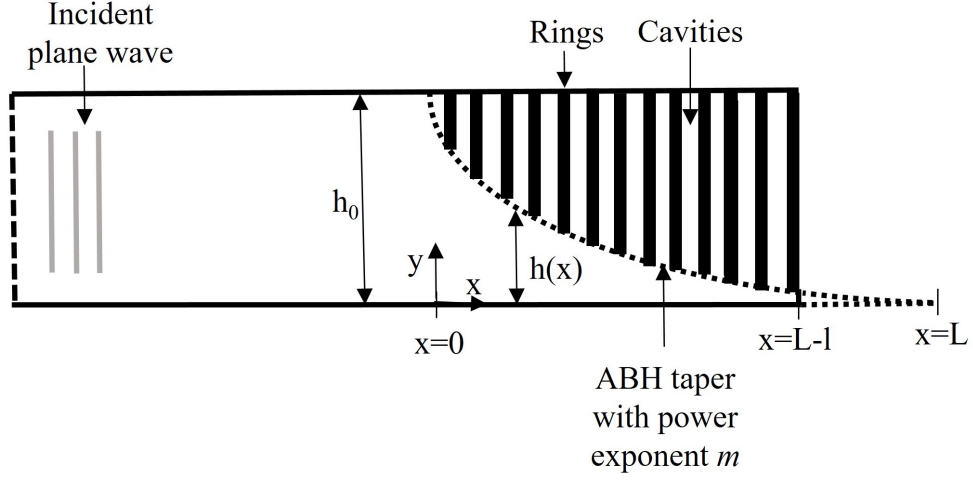
Figure 4.3. Depiction of an acoustic duct with an ABH termination. The drawing shows the top half of the axisymmetric system.

impedance of air, ρ_0 is the air density, $h(x)$ is the radius of the cylindrical duct, $Y(x)$ is the admittance of the wall, and x is the axial coordinate with the origin located at the beginning of the power-law taper. The wall admittance can be approximated by the continuous lumped admittance [167], [168]

$$Y(x) = (-\mathrm{i}\omega)\frac{1}{\rho_0 c^2}\frac{h_0^2 - h(x)^2}{2h(x)}, \tag{4.5}$$

where h_0 is the radius of the section of the duct having constant cross section. The radius of the cylindrical duct in the termination area is given by the power-law equation

$$h(x) = \frac{h_0}{L^m}|x - L|^m, \tag{4.6}$$

where L is the axial length of the ABH and m is the power-law exponent.

149

4.1.3 Relation to Fractional Calculus

The relation between acoustic black holes and fractional calculus is explored for multiple reasons. First, the recent rise of ABHs in passive vibration applications [145]–[149], [151]–[153], [159], [166]–[168] makes them an intriguing geometry to further understand and presents a potential real-world structural application of FC. Second, the complexity of current modeling and simulation techniques for the ABH geometry has prompted the need to further improve them. In many applications involving ABH terminations (and, in some cases, also ABH embedded tapers), models are typically required to evaluate the dynamic response of the host system while the detailed dynamic response within the actual ABH region is often of secondary importance. This suggests that there is a need to identify methodologies capable of capturing the effect of the ABH on the dynamics of the host structure without requiring detailed modeling of the ABH itself. The FC homogenization tools in the previous chapter can be utilized and adapted to formulate an effective model capable of accurate and simpler dynamic simulations of structures with embedded ABH features, thereby relieving some of the computational burdens associated with ABH designs.

Third, the attenuation capabilities of fractional operators makes them an ideal candidate to represent the decreasing wave speed of the ABH geometry. Fourth, the taper profile of the ABH follows a power-law relation, suggesting a possible connection between their physical behavior and the power-law kernel of fractional operators. As such, a relationship between the order of the power-law taper m and the fractional order of the equivalent fractional model should theoretically be achievable. Finally, the dynamics of the acoustic black hole exhibits nonlocal behavior, a mechanical phenomena well represented by space fractional derivatives. For both the ABH duct and beam considered in this chapter, the space fractional derivative can serve as a homogenization of the varying cross-section of an ABH geometry.

4.2 Fractional Boundary Model of the Acoustic Duct

The fractional homogenization of ABHs begins with the development of fractional models for ABH terminations in ducts, as seen in Fig. 4.3. Two different fractional homogenization approaches are explored: 1) a boundary condition of fractional order, and 2) a fractional

order domain that replaces the ABH termination, as shown in Fig. 4.4. This section considers the fractional boundary while the following section explores the fractional domain. Both approaches are built using space fractional derivatives.
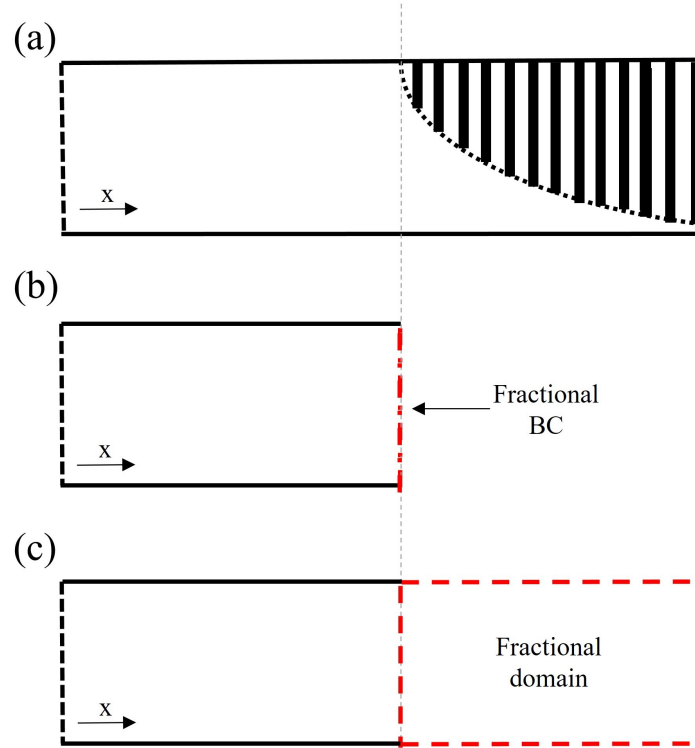
Figure 4.4. Schematic representations of (a) the traditional ABH model for a duct, (b) the fractional order boundary condition model, (c) the fractional order domain model used to represent an ABH.

4.2.1 Fractional Boundary Model

In the fractional boundary condition approach, the entire ABH tapered duct (Fig. 4.4(a)) is replaced by a fractional order BC that mimics the presence of the ABH termination (Fig. 4.4(b)). In this way, there is no need to solve for the actual response within the termination while the response in the main duct remains accurate because the equivalent acoustic impedance from the ABH is properly accounted for.

The general form of a space fractional BC is

$$\frac{\partial p}{\partial t} + \bar{c}\frac{\partial^\beta p}{\partial x^\beta}\bigg|_{x=x_0} = 0, \tag{4.7}$$

where β is the fractional order and $\bar{c}$ is the fractional wave speed (dimensions of $\frac{m^\beta}{s}$). For the specific analyses at hand, the value of $\bar{c}$ is equated to the speed of sound in air. Other considerations to select the value of this constant can be considered similar to the proposed methods in § 3.2.2. Equation (4.7) is similar in form to a typical 1D absorbing boundary condition, which is recovered exactly for $\beta = 1$ [173], [174]. The fractional derivative in Eq. (4.7) is taken as the left-handed Riemann-Liouville derivative (see Eq. (1.16)) to mimic the effect the ABH would have on the dynamics of the main duct located to the left of the ABH.

4.2.2 Reflection Coefficient via Transfer Matrix Method

To determine the equivalent fractional order, it would be preferable to directly relate it to the power-law taper m of the ABH. However, attempts at deriving this relationship thus far have been unsuccessful due to the mathematical complications of obtaining the Laplace or Fourier transform of a variable coefficient differential equation. While it is still believed that this relationship may be obtainable, the approach to determine the fractional order of the fractional boundary given in Eq. (4.7) will depend on a matching scheme between the fractional and integer order models, similar to how the dispersion relationships of the variable coefficient integer order equation and the space fractional wave equation were matched to determine the fractional order in Chapter 3. The reflection coefficient is selected as the matching parameter to determine the fractional order corresponding to the ABH since Mironov [167] and Guasch [168] determined this quantity. However, for ABH tapers with power-law exponents m such that $1 < m < 2$, closed-form analytical solutions are not available. Because of this, the reflection coefficient of air-filled ducts with ABH terminations is determined via the transfer matrix (TM) method as implemented in [168].

In the TM method, the ABH tapered section can be discretized in a series of shorter ducts with constant cross sections, as depicted in Fig. 4.5. This discretization approach is akin to using a rectangular Riemann sum approximation to estimate a definite integral.
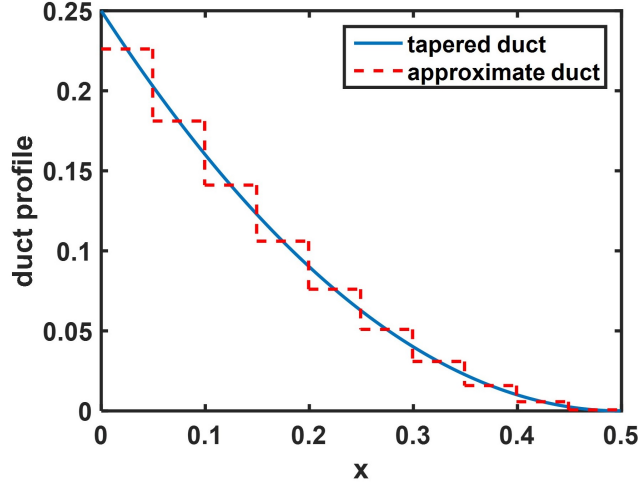
Figure 4.5. Ideal versus discretized duct profile. In the TM approach, the ABH taper is approximated by a series of shorter ducts having constant cross sectional areas.

The transfer matrix for a duct of constant cross section is given by [175] as

$$
\begin{bmatrix} P_{\text{i}} \\ U_{\text{i}} \end{bmatrix} = \begin{bmatrix} \cos(k_0 L_D) & \text{i}\frac{\rho_0 c}{S_D}\sin(k_0 L_D) \\ \text{i}\frac{S_D}{\rho_0 c}\sin(k_0 L_D) & \cos(k_0 L_D) \end{bmatrix} \begin{bmatrix} P_o \\ U_o \end{bmatrix},
\tag{4.8}
$$

where the subscripts i and o indicate the inlet and outlet sections of the duct, P is pressure and U is acoustic volumetric velocity, and L_D and S_D are the length and the cross-sectional area of the duct.

In practical implementation, ABHs exhibit a residual thickness at their end (the ABH terminates at $x = L - l$ in Fig. 4.3 rather than $x = L$). By dividing the ABH domain into N ducts of equal length $L_n = \frac{L-l}{N}$, the cross sectional area of a generic section n is $S_n = \pi h_n^2$ where the radius h_n is determined by taking the value of the radius from Eq. (4.6) at the midpoint of the discretized duct as exemplified in Fig. 4.5. Equation (4.8) does not

account for the variation of the wall admittance along the ABH duct. This contribution can be accounted for by considering the impedance matrix [168]

$$
\begin{bmatrix}
1 & 0 \\
Y_n^{\text{cav}} & 1
\end{bmatrix},
\tag{4.9}
$$

$$
Y_n^{\text{cav}} = \mathrm{i}\frac{k_0}{Z_0}\pi L_n\left(h_0^2 - \frac{1}{3}(h_{n-1}^2 + h_n^2 + h_{n-1}h_n)\right).
\tag{4.10}
$$

Incorporating the matrix of Eq. (4.9) in Eq. (4.8), the resulting transfer matrix for each duct subsection is given by

$$
\mathbf{T}_n =
\begin{bmatrix}
\cos(k_0 L_n) & \mathrm{i}\frac{\rho_0 c}{S_n}\sin(k_0 L_n) \\
\mathrm{i}\frac{S_n}{\rho_0 c}\sin(k_0 L_n) & \cos(k_0 L_n)
\end{bmatrix}
\begin{bmatrix}
1 & 0 \\
Y_n^{\text{cav}} & 1
\end{bmatrix}.
\tag{4.11}
$$

The complete transfer matrix model describing the entire ABH duct can then be assembled as

$$
\begin{bmatrix}
P_{\mathrm{i}} \\
U_{\mathrm{i}}
\end{bmatrix}
= \mathbf{T}_t
\begin{bmatrix}
P_l \\
U_l
\end{bmatrix},
\tag{4.12}
$$

where the subindices i and l represent quantities taken at the inlet and at the termination of the ABH. The complete transfer matrix $\mathbf{T}_t$ is represented as

$$
\mathbf{T}_t =
\begin{bmatrix}
T_{11t} & T_{12t} \\
T_{21t} & T_{22t}
\end{bmatrix}
= \mathbf{T}_1\mathbf{T}_2\mathbf{T}_3....\mathbf{T}_{N-1}\mathbf{T}_N.
\tag{4.13}
$$

For harmonic excitation, the pressure field in the duct before the ABH termination is described by the plane wave solution

$$p(x,t) = \tilde{A}\mathrm{e}^{\mathrm{i}(\omega t - k_0 x)} + \tilde{B}\mathrm{e}^{\mathrm{i}(\omega t + k_0 x)}, \tag{4.14}$$

where $\tilde{A}$ and $\tilde{B}$ are constants. The spatial profile of the pressure is $P(x) = \tilde{A}\mathrm{e}^{-\mathrm{i}k_0 x} + \tilde{B}\mathrm{e}^{\mathrm{i}k_0 x}$. Dividing by $\tilde{A}$, define $R = \tilde{B}/\tilde{A}$ where R is the reflection coefficient. Then, the pressure P_i at the inlet consists of an incident wave of unit amplitude and a reflected wave of amplitude R. That is,

$$P_\mathrm{i} = 1 + R. \tag{4.15}$$

Likewise, using the linear Euler equation [167], the acoustic volumetric velocity at the inlet is

$$U_\mathrm{i} = \frac{S}{\rho_0 c}(1 - R), \tag{4.16}$$

where S is the cross-sectional area at the inlet. Also, the edge termination of the ABH is assumed to be completely rigid meaning that $U_l = 0$. Substituting this assumption along with Eqs. (4.15) and (4.16) into Eq. (4.12) yields

$$1 + R = T_{11t}P_l, \tag{4.17}$$

$$\frac{S}{\rho_0 c}(1 - R) = T_{21t}P_l, \tag{4.18}$$

where P_l is the pressure at the rigid termination. These can accordingly be arranged into the matrix equation

$$
\begin{bmatrix} -1 & T_{11t} \\ \frac{S}{\rho_0 c} & T_{21t} \end{bmatrix} \begin{bmatrix} R \\ P_l \end{bmatrix} = \begin{bmatrix} 1 \\ \frac{S}{\rho_0 c} \end{bmatrix}. \tag{4.19}
$$

Thus, for a given value of ω, R is calculated using Eq. (4.19).

Consider an ABH taper with parameters $h_0 = 0.25$ m, $L = 0.5$ m, $l = 0.001$ m, and $m = 2$. In order to contrast the reflection due to the edge truncation, losses are introduced by using a complex wave speed $c = 340(1 + 0.05i)$. Figure 4.6 plots the absolute value of the reflection coefficient R as a function of frequency. Four discretization cases ($N = 10$, 50, 100, and 500) are considered. As expected, Fig. 4.6 clearly shows that the value of R is very dependent on N. The smaller N is, the larger the oscillation amplitude of the reflection coefficient. As N increases, the trend converges to a smooth curve which coincides with the analytical expression derived in [168]. Given that the methodology presented below to retrieve an equivalent fractional order model of the ABH relies on the value of reflection coefficient obtained via the transfer matrix method, the accuracy of the function $R(\omega)$ is critical. Henceforth, a value $N = 500$ is used to provide a sufficiently smooth approximation of the tapered profile and of the reflection coefficient.

From a practical point of view, the number and size of the rings will affect the black hole behavior of a real duct configuration. According to [168], *"the high number of rings needed to recover the analytic ABHs may pose a severe limitation to practical realizations of the ABH, which aim at a limited number of rings for manufacturing purposes."* It is likely that, for very thin rings, local resonances and structural modes will give rise to fluid-structure interaction that will affect the performance of the ABH. Although [168] does investigate the effects of the size and thickness of the rings in the TM method, a series of experiments or very detailed fluid-structure interaction simulations would be needed to further characterize the influence of the rings on the performance of the ABH. Nevertheless, the experimental work in [169], [170] was able to demonstrate that a design of a finite number of rings could produce an acoustic black hole in a real configuration whose reflection coefficient was similar to the values obtained from the analytical formulas derived in [167].
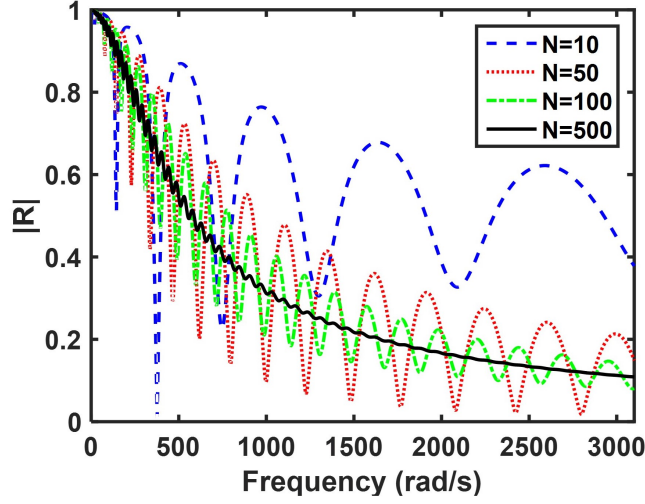
Figure 4.6. The reflection coefficient as a function of frequency for an ABH with taper coefficient $m = 2$. The plot is parameterized in terms of the spatial discretization parameter N.

In a similar fashion, the effect of different values of the taper exponent m on the reflection coefficient is considered to illustrate that the discretized TM approach can calculate the reflection coefficient for non-integer values of the taper exponent m. Consider the ABH where $h_0 = 0.25$ m, $L = 0.5$ m, and $l = 0.001$ m, but m is non-integer. Figure 4.7 plots the reflection coefficient parameterized with respect to the taper exponent m. As m increases, the oscillation of the reflection coefficient is less drastic. In [168], the author notes that the quadratic taper usually produces a reflection coefficient smaller than the linear taper and suggests that the reflection coefficient decreases as m increases. However, this is not necessarily always the case. In fact, the curves in Fig. 4.7 corresponding to the non-integer values of m usually have a smaller reflection coefficient than the $m = 2$ case. Clearly, the optimal value of m in order to reduce the reflection coefficient depends on a variety of factors including the length of the taper, the location of the termination, and the frequency range of interest.
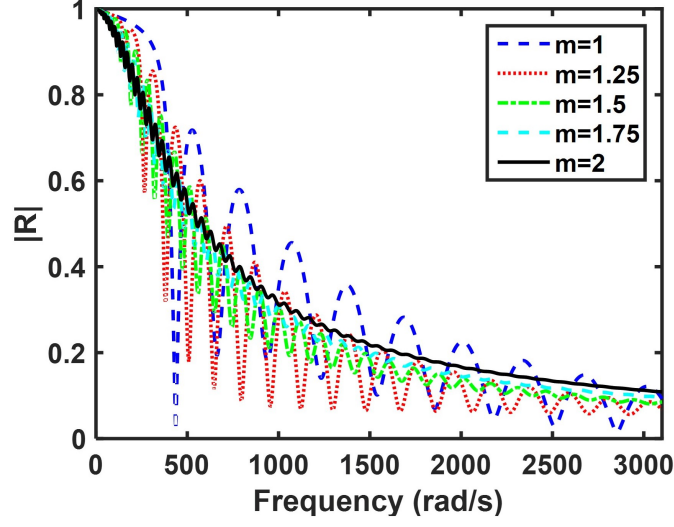
Figure 4.7. The reflection coefficient of the ABH as a function of frequency. The curves are parameterized based on different power-law taper coefficients m. The range of m explored in this plot is consistent with the constraint $m \geq 1$ provided by Mironov [167].

4.2.3 Calculation of Fractional Order

The order β in Eq. (4.7) is determined such that the fractional BC will produce the same reflection coefficient as the tapered termination. Recall that the wave pressure in the main duct is given according to the ansatz

$$p(x,t) = e^{i(\omega t - kx)} + Re^{i(\omega t + kx)}, \qquad (4.20)$$

where $k = \frac{\omega}{c}$ and R is the reflection coefficient. The reflection coefficient at a given frequency ω for a given ABH with power-law exponent m was determined in the previous section using the transfer matrix method. Substituting Eq. (4.20) into Eq. (4.7) yields

$$e^{-ikx_0} + Re^{ikx_0} - i\frac{\bar{c}}{\omega}\left[(-ik)^\beta e^{-ikx_0} + R(ik)^\beta e^{ikx_0}\right] = 0, \qquad (4.21)$$

158

where x_0 marks the location where the ABH taper begins. Since the coordinate system had been set up such that $x_0 = 0$, Eq. (4.21) simplifies to

$$1 + R - \mathrm{i}\frac{\bar{c}}{\omega}\left[(-\mathrm{i}k)^\beta + R(\mathrm{i}k)^\beta\right] = 0. \tag{4.22}$$

It is seen from Eq. (4.22) that, when $R = 0$, the value of β that satisfies the equation is $\beta = 1$. Such a result is consistent with the general observation that when $\beta = 1$, Eq. (4.7) reduces to the typical fully absorbing boundary condition (i.e., $R = 0$).

To calculate the value of β in Eq. (4.22) corresponding to $R(\omega)$ (see Fig. 4.7), a numerical solver is used. Recall that the reflection coefficient is a complex quantity (only the magnitude is plotted in Fig. 4.7). The plot of $\beta(\omega)$ obtained using the coefficients in Fig. 4.7 is given in Fig. 4.8. As expected, Fig. 4.8 shows that the tapers that exhibited larger oscillations of the reflection coefficient also exhibit larger oscillations in their corresponding fractional orders. Furthermore, the order β necessary to match the reflection coefficient is frequency-dependent and is a complex number.
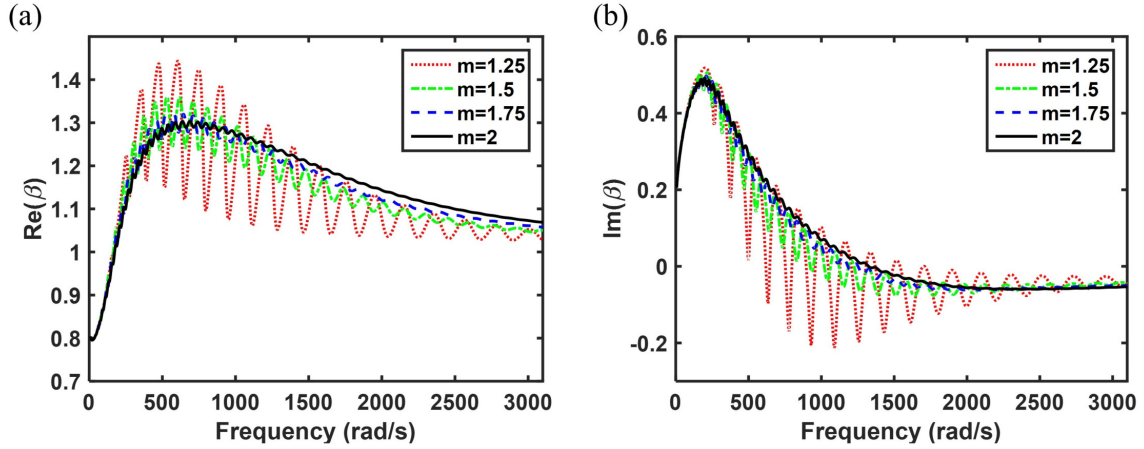
Figure 4.8. (a) The real part of the complex order β of the fractional BC as a function of frequency. (b) The imaginary part of the complex order β of the fractional BC as a function of frequency. The curves are parameterized for different taper coefficients.

159

Certainly, for simple 1D cases, there are other approaches not involving fractional calculus that are capable of modeling partially reflected waves [175], [176] and that could serve a purpose similar to the fractional order boundary. For example, one could replace the ABH taper with the integer order boundary condition (which is referred to as the integer order partial reflection BC)

$$\gamma\frac{\partial p}{\partial t} + c\frac{\partial p}{\partial x}\bigg|_{x=x_0} = 0, \tag{4.23}$$

where $0 \leq \gamma \leq 1$. The case $\gamma = 1$ represents zero reflection while $\gamma = 0$ indicates complete reflection. All the intermediate values of γ represent partial reflection. The use of the fractional BC specifically illustrates how FC could be used for modeling ABH terminations.

4.2.4 Finite Difference Model of the Fractional Boundary

To assess the validity of the fractional boundary condition approach, a numerical simulation of a semi-infinite duct terminated by the proposed fractional order boundary is conducted. The governing equations for such a system can be solved numerically by finite differences (FD) and compared with the predictions from the integer order TM model in order to confirm the amplitude of the reflected waves are indeed equivalent. A more convincing validation of the fractional boundary would compare the measured reflection coefficient from the fractional finite difference model to experimentally measured reflection coefficients of the ABH termination. This would also illustrate, for very thin rings, how fluid-structure interaction may affect the performance of the ABH and affect the accuracy of the fractional boundary. However, use of the reflection coefficients obtained via the TM method as the basis of the validation is supported by the fact that the experiments in [169], [170] matched the analytical and numerical calculations of the reflection coefficients given in [167], [168].

In the fractional boundary condition approach, the governing equation describing the pressure waves in the main duct is still the classical second order wave equation

$$\frac{\partial^2 p}{\partial t^2} = c^2 \frac{\partial^2 p}{\partial x^2}, \tag{4.24}$$

which, by using a second order centered scheme, can be written in the equivalent finite difference form

$$\frac{p_n^{j+1} - 2p_n^{j} + p_n^{j-1}}{\Delta t^2} = c^2 \frac{p_{n+1}^{j} - 2p_n^{j} + p_{n-1}^{j}}{\Delta x^2}, \tag{4.25}$$

where $n = 0, 1, 2, \ldots, N$ is a spatial index, j is the time index, and Δx and Δt describe the spatial and temporal discretization, respectively. If the initial conditions are known (corresponding to j = 0, 1), Eq. (4.25) can be solved for p_n^{j+1} and then subsequently be placed in a computational loop. The explicit FD scheme in Eq. (4.25) is stable if

$$\frac{c\Delta t}{\Delta x} < 1. \tag{4.26}$$

To represent the fractional boundary condition in the computational simulation, discretization of the fractional BC is developed based on a FD formula known as Mur's BC [177]. In a typical 1D wave problem, the Mur BC can be implemented to model the traditional fully absorbing boundary condition. The Mur BC is modified to account for the space fractional derivative in Eq. (4.7). This new form of the Mur BC is called the *fractional Mur BC* and is found by first rewriting Eq. (4.7) as

$$\frac{\partial^\beta p}{\partial x^\beta} = -\frac{1}{c}\frac{\partial p}{\partial t}. \tag{4.27}$$

Following a derivation similar to that given in [177], the space and time derivative approximations must be evaluated at the same point. In a finite difference formulation, this corresponds to averaging the finite differences evaluated at the spatial nodes N and $N-1$ and

161

the temporal points j and j+1 where the sub-index N represents the last spatial node. Thus, the fractional Mur boundary condition will be evaluated at the point $(x_N - \Delta x/2, t_j + \Delta t/2)$. To formulate the finite difference form of Eq. (4.27) requires the use of the FD definition of the Riemann-Liouville fractional derivative, better known as the Grunwald-Letnikov definition of the fractional derivative (see Eq. (1.20)). Note that while the Grunwald-Letnikov definition for the space fractional derivative actually considers all the spatial nodes in the domain, the values of the Grunwald weights are such that the the evaluation of the space fractional derivative occurs at $x_N - \Delta x/2$. Using the Grunwald-Letnikov derivative and weights from Eqs. (1.21) and (1.22), the finite difference form of Eq. (4.27) is

$$\frac{1}{2}\left[\frac{1}{\Delta x^\beta}\left(\sum_{n=0}^{N} g_n p_{N-n}^j + \sum_{n=0}^{N} g_n p_{N-n}^{j+1}\right)\right] = -\frac{1}{2\bar{c}}\left(\frac{p_N^{j+1} - p_N^j}{\Delta t} + \frac{p_{N-1}^{j+1} - p_{N-1}^j}{\Delta t}\right). \qquad (4.28)$$

Defining $\bar{r} = \bar{c}\frac{\Delta t}{\Delta x^\beta}$, pulling out the $n = 0$ terms from the summation, and performing some algebraic steps simplifies Eq. (4.28) to

$$p_N^{j+1} = p_N^j\left(\frac{1-\bar{r}}{\bar{r}+1}\right) + \left(\frac{1}{\bar{r}+1}\right)(p_{N-1}^j - p_{N-1}^{j+1}) - \left(\frac{\bar{r}}{\bar{r}+1}\right)\left(\sum_{n=1}^{N} g_n p_{N-n}^{j+1} + \sum_{n=1}^{N} g_n p_{N-n}^j\right). (4.29)$$

4.2.5   Numerical Assessment

The discretized model developed in § 4.2.4 can be used to obtain the response of the duct with a fractional BC and to compare the response with the traditional model. More specifically, the simulation consists of a wave packet (i.e., a Hanning-windowed wave at a given frequency) traveling in the main duct towards the fractional BC. After encountering the fractional BC, the wave is partially reflected back according to fractional form of the boundary condition. If the fractional BC serves as a representative model of the ABH termination, then the reflected waves should be comparable to the value of R predicted from the TM method. According to this strategy, the simulation in the time domain will only be valid for an impinging harmonic wave possessing the frequency corresponding to that of the

fractional order used. However, the wave equation and the fractional boundary condition are linear, so it is anticipated that linear superposition will still hold.

The modeled duct has the same numerical parameters given in § 4.2.2. The reflection coefficient and the fractional derivative associated with this ABH were shown by the black, solid curves in Figs. 4.7 and 4.8, respectively. For this numerical analysis, a frequency $\Omega = 2988$ rad/s was selected. While, in principle, any frequency could be used in this numerical test, the trend of both the reflection coefficient and the fractional order were particularly smooth at the selected frequency. After considering this specific frequency, the response across a wider frequency range is calculated. From Figs. 4.7 and 4.8, the frequency $\Omega = 2988$ rad/s corresponds to a reflection coefficient of $|R| = 0.1129$ and a fractional order of $\beta = 1.074 - 0.05477\mathrm{i}$. Other parameters for the discretization in both time and space were selected as $\Delta x = 0.01$ and $\Delta t = 1\text{E-}5$.

The incident wave packet was generated by windowing the boundary condition $p(-\infty, t) = \mathrm{e}^{\mathrm{i}\Omega t}$. In the simulation, the location where this BC was applied was selected to be multiple wavelengths away from the fractional BC (to represent a semi-infinite duct in a finite simulation). This harmonic excitation on the initial spatial node persisted for a time of $t = 20.5T$ where T is the duration of a period $(T = 2\pi/\Omega)$. A plot of the incident wave field before it encounters the fractional BC is given in Fig. 4.9(a). As the incident wave encounters the fractional BC at the right end of the domain, it is reflected back as shown in Fig. 4.9(b). The reflected pressure is a complex quantity just like the incident pressure field. If the incident wave had been only a cosine function, the real parts of the plots in Fig. 4.9 would correspond to the actual physical responses of the wave in the duct. Conversely, if the incident wave was given as a sine function, the imaginary parts of the plots in Fig. 4.9 would correspond to the actual physical responses. To measure the reflection coefficient with an incident wave represented using a complex exponential function, the ratio of peak values of the absolute magnitude of the incident and reflected wave packets from Fig. 4.9 is calculated. Doing so yields a reflection coefficient of $R = 0.1119$. Recalling that the reflection coefficient using the traditional TM model shown in Fig. 4.7 was $R = 0.1129$ at $\Omega = 2988$ rad/s, the percent error between the transfer matrix method and the fractional BC model is only 0.9%. However, due to the finite duration of the signal, the spectrum of the incident and reflected signals

will not be a single frequency. Thus, another potentially more accurate way to calculate the reflection coefficient is to analyze the spectrum of either the real or imaginary parts of the incident and reflected waves by taking the fast Fourier transforms of the signals and measuring the ratio of the amplitudes of the FFTs at the wavenumber of interest. This approach yielded $R = 0.112$. It is not surprising that this value is almost nearly equal to the value determined via the ratio of the peak values approach since the Hanning window of the signal was chosen so that contributions of other nearby frequency components were minimal.
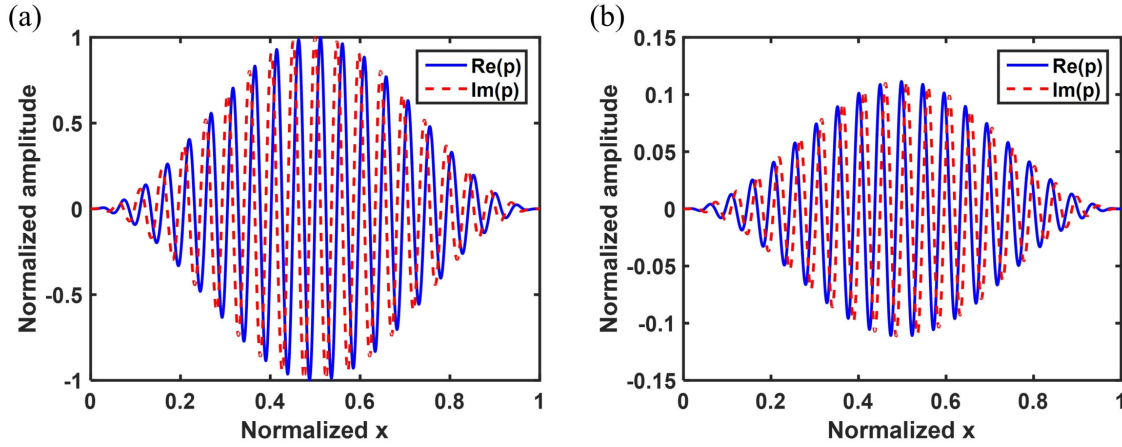
Figure 4.9. Numerical time-domain simulations performed by solving the finite difference model for the fractional BC (§ 4.2.4). The results show the response in the duct due to an incident wave packet at a selected frequency of $\Omega = 2988$ rad/s. (a) Real and imaginary parts of the incident pressure wave. (b) Real and imaginary parts of the reflected pressure wave field after the entire waveform has encountered the fractional Mur boundary (located at the normalized domain x value of 1).

These results confirm the validity of the procedure as well as the satisfactory performance of the fractional order boundary as a means to simulate the effect of the ABH termination on the response of the main duct at the selected frequency of $\Omega = 2988$ rad/s. For further validation, the analysis is extended to a wider range of frequencies. The results are shown in Fig. 4.10 by plotting the reflection coefficients from the TM method and the FD time domain simulation. For the FD simulation curve in Fig. 4.10(a), the reflection coefficient was calculated from the ratio of amplitude of the FFT component at the corresponding

wavenumber of interest. The ratio between the real part of the reflected and the incident wave signal was used. Taking the ratio of the FFTs of the imaginary part of the signals produces the same reflection coefficient curve. The curves in Fig. 4.10(a) nearly lie on top of each other. The percent difference between the curves is plotted in Fig. 4.10(b). The error is always less than 1%, further proving that the fractional BC is an accurate and appropriate means to model the reflection from the acoustic black hole.
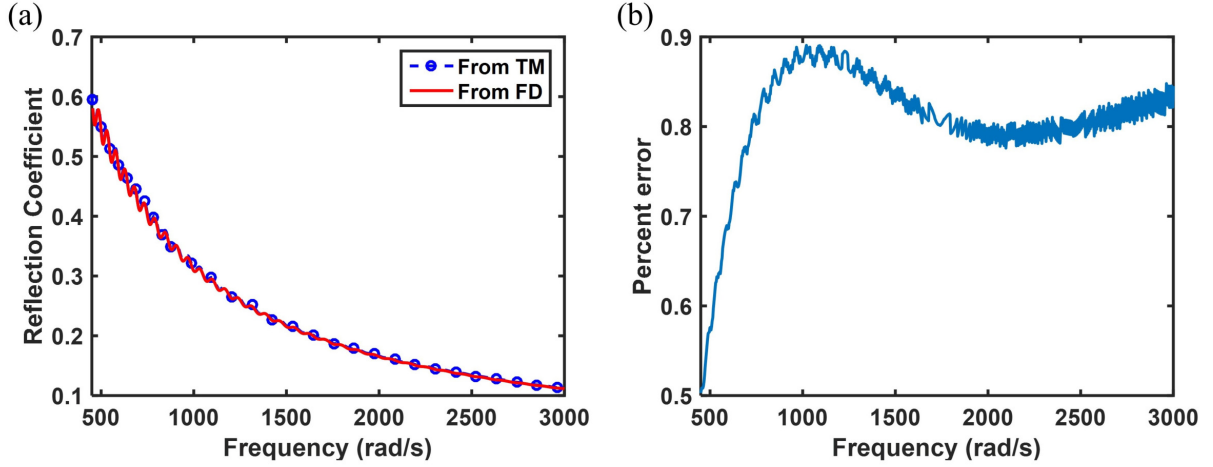
Figure 4.10. (a) The reflection coefficients from the TM method and the FD simulation over a frequency range from 450 to 3000 rad/s. The plot was cut at 450 rad/s due to large computational expenses of the FD simulation for very low frequencies. (b) The percent difference error between the curves of the reflection coefficients. Sources of the error include the inherent error of the finite difference method and a small error in the calculation of a complex-valued fractional derivative.

To compliment the fractional framework, a supplementary analysis is conducted to obtain the results from a FD simulation which used the integer order partial reflection BC (Eq. (4.23)) in order to compare to the results from the FD simulation using the fractional BC (Eq. (4.7)). Substituting Eq. (4.20) into Eq. (4.23) and evaluating at $x_0 = 0$ yields

$$i\omega\gamma(1 + R) + c(-ik + ikR) = 0. \tag{4.30}$$

Simplifying this equation and noting $k = \omega/c$ produces

$$\gamma = \frac{1-R}{1+R}. \tag{4.31}$$

A plot of the coefficient γ for the quadratic tapered ABH (reflection coefficient given by the black, solid curve in Fig. 4.7) is plotted in Fig. 4.11.
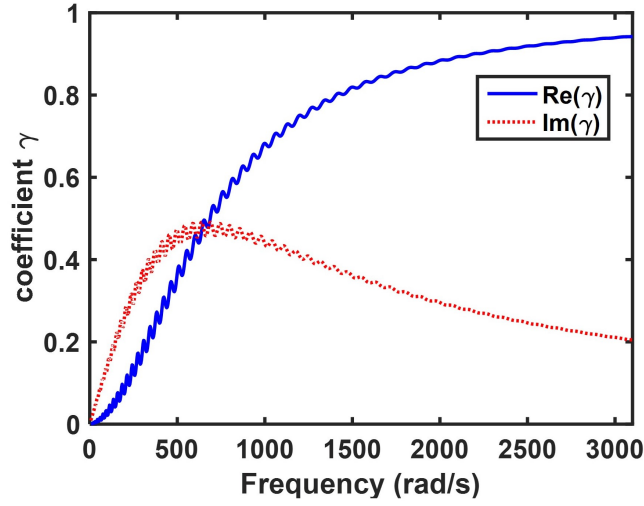
Figure 4.11. The complex-valued coefficient γ for the integer order partial reflection BC.

In a similar fashion as the procedure given in § 4.2.4, a FD method for the integer order partial reflection BC is formulated. The finite difference formula for the fractional Mur BC (Eq. (4.29)) is replaced by the FD Mur formula for the integer order partial reflection BC, which is

$$p_N^{j+1} = p_N^j + \frac{r-\gamma}{r+\gamma}(p_{N-1}^{j+1} - p_N^j), \tag{4.32}$$

where the sub-index N represents the last spatial node and

$$r = c\frac{\Delta t}{\Delta x}. \tag{4.33}$$

The FD simulation for the partial reflection BC is performed across a wide range of frequencies to confirm its validity for the entire frequency range. The results are shown in Fig. 4.12 by plotting the reflection coefficients from the transfer matrix method and the FD time domain simulation. Just as in Fig. 4.10, the reflection coefficient for the FD simulation was calculated from the ratio of amplitude of the FFTs at the corresponding wavenumber for the incident and reflected waves. The curves in Fig. 4.12(a) nearly lie on top of each other. The percent difference between the curves is plotted in Fig. 4.12(b) and is always less than 0.05%. Comparing Fig. 4.10(b) to Fig. 4.12(b), the percent error using the integer order partial reflection BC is an order of magnitude less than the error using the fractional BC. This difference in error most likely arises from a slight error in the calculation of a complex-valued fractional derivative, similar to what was found in Chapter 3.
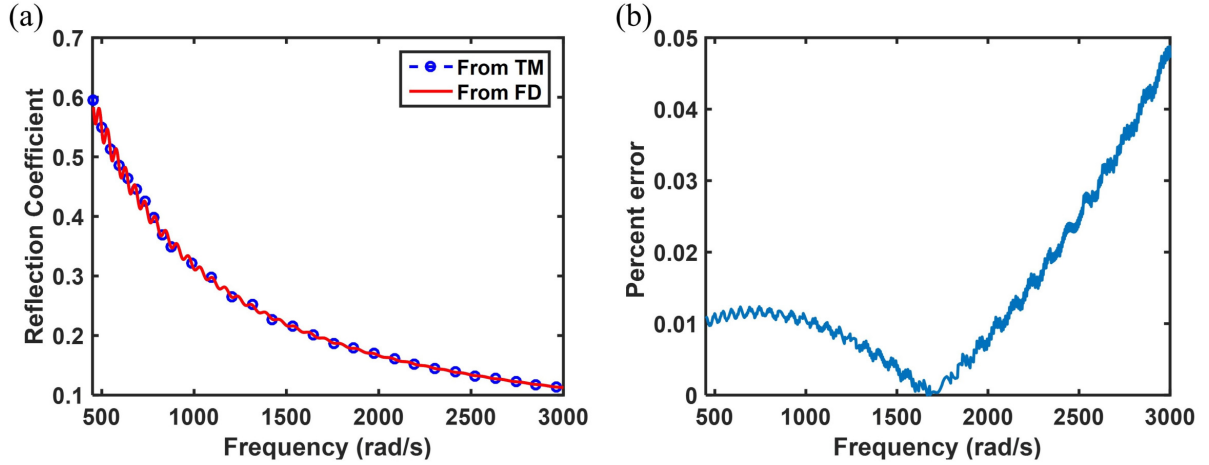
Figure 4.12. (a) The reflection coefficients from the TM method and the FD simulation using the integer order partial reflection BC. (b) The percent difference error between the curves of the reflection coefficients using the integer order partial reflection BC.

One could argue against using a fractional BC due to the lower error associated with the integer order partial reflection BC. However, recall that one of the objectives was to illustrate how fractional order mathematics could be used for modeling metamaterials with ABH terminations and to stimulate future thinking for the application of this mathematical tool to acoustic and vibration analysis. The above results using the fractional order operator certainly exhibited the ability of fractional order operators to serve as a fairly accurate means to model acoustic black hole terminations in ducts.

4.3 Fractional Domain Model of the Acoustic Duct

This section explores the fractional domain model of the ABH termination in an acoustic duct, as shown in Fig. 4.4(c). The fractional domain is governed by the space fractional wave equation, given by Eq. (3.31). To determine the fractional order, the procedure will once again equate the reflection coefficient from the ABH to the reflection coefficient of the fractional domain, which is found through a fractional transfer matrix.

4.3.1 Fractional Transfer Matrix

The governing equation of the fractional domain is the space fractional wave equation

$$\bar{c}^2 \frac{\partial^\alpha p}{\partial x^\alpha} = \frac{\partial^2 p}{\partial t^2}, \tag{4.34}$$

where α is the order of the fractional derivative and $\bar{c}$ is the fractional wave speed with dimensions $\frac{(\text{m})^{\alpha/2}}{\text{s}}$ [77]. As given in § 3.3.1, the solution of the fractional differential Eq. (4.34) (if the lower bound of the integral in the fractional derivative is $-\infty$) is

$$p(x,t) = \tilde{A}\mathrm{e}^{\mathrm{i}(\omega t - \hat{k}x)} + \tilde{B}\mathrm{e}^{\mathrm{i}(\omega t + \hat{k}x)}, \tag{4.35}$$

where $\hat{k}$ is a complex-valued wavenumber. This solution corresponds to forward and backward propagating waves, respectively. Recall from Chapter 3 that the relationship between $\hat{k}$ and the fractional order α is obtained from the dispersion equation of Eq. (4.34) as

$$(\text{-i}\hat{k})^\alpha = -\frac{\omega^2}{\bar{c}^2}. \tag{4.36}$$

The procedure to derive the transfer matrix for the fractional domain is similar to that for an integer order model (see § 4.2.2) since both domain solutions are based on exponential kernels. As such, the fractional transfer matrix is

$$\begin{bmatrix} P_1 \\ U_1 \end{bmatrix} = \begin{bmatrix} \cos(\hat{k}L) & \text{i}\frac{\rho_0 c}{S}\sin(\hat{k}L) \\ \text{i}\frac{S}{\rho_0 c}\sin(\hat{k}L) & \cos(\hat{k}L) \end{bmatrix} \begin{bmatrix} P_2 \\ U_2 \end{bmatrix}, \tag{4.37}$$

where P_1 and U_1 are the pressure and acoustic volumetric velocity of the left end of the fractional domain, P_2 and U_2 are the pressure and acoustic volumetric velocity of the right end of the fractional domain, L is the entire length of the fractional domain, S is the constant cross-sectional area, and $\hat{k}$ is a complex wavenumber.

4.3.2 Calculation of Fractional Order

Obtaining the order α of the ABH-like fractional domain requires guaranteeing the equivalent dynamic behavior of the duct is unchanged when using either a classical ABH termination or a fractional domain model. Equivalently, the two should exhibit the same reflection coefficient. Since the end of the ABH at $x = L - l$ was assumed to be rigidly terminated,

$$U_2 = 0. \tag{4.38}$$

Substituting this into Eq. (4.37), P_1 and U_1 can be written as a function of P_2. Eliminating P_2 from these equations gives the input impedance of the fractional domain as

$$\frac{P_1}{U_1} = -\mathrm{i}\frac{\rho_0 c}{S}\cot(\hat{k}L). \tag{4.39}$$

If the origin of the fractional domain is kept at $x = 0$, then

$$P_1 = 1 + R, \tag{4.40}$$

$$U_1 = \frac{S}{\rho_0 c}(1 - R). \tag{4.41}$$

Substituting these two equations into Eq. (4.39) yields

$$\frac{1 + R}{1 - R} = -\mathrm{i}\cot(\hat{k}L). \tag{4.42}$$

The value of the reflection coefficient R of the ABH was obtained using the transfer matrix method in § 4.2.2. Substituting the value of R into Eq. (4.42), a numerical solver can obtain $\hat{k}$. Once $\hat{k}$ is obtained, α is obtained using Eq. (4.36), which is rearranged as

$$\alpha = \frac{2\ln(\omega/\bar{c}) - \mathrm{i}\pi}{\ln(-\mathrm{i}\hat{k})}. \tag{4.43}$$

Equations (4.42) and (4.43) can be solved to calculate the fractional order α of the fractional domain at the selected frequency. Figure 4.13 depicts the value of the fractional order for the same numerical example used in previous sections.

Figure 4.13 reveals, once again, that the methodology produces fractional differential operators of complex and frequency-dependent order where $1 < \mathrm{Re}(\alpha) < 2$ while $\mathrm{Im}(\alpha) > 0$ (except for very low frequencies). The value of α is responsible for the attenuating effect
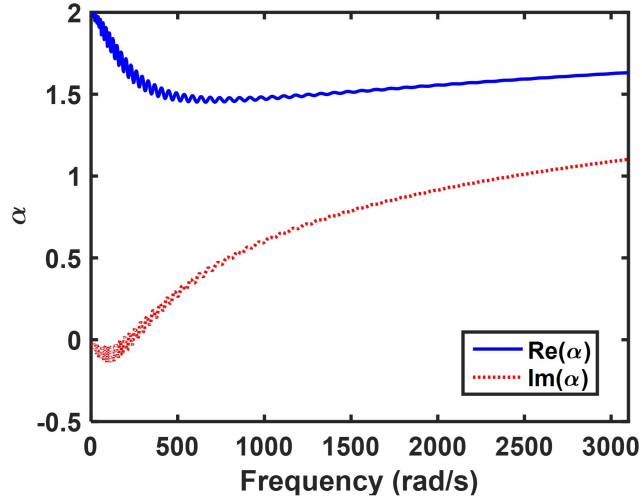
Figure 4.13. Plot of the complex, fractional order α of the fractional domain that replaces the ABH. Using a fractional domain with this order produces the same reflection coefficient as the ABH taper.

characteristic of the fractional domain [74]–[77]. At first, this may seem to contradict the expected behavior inside the ABH termination, since the wave speed should approach zero while the amplitude of the pressure will increase. Recall, however, that the model is not attempting to match the dynamic behavior within the ABH but instead, it focuses on the response of the main duct. To produce a reflected wave with the same reduced amplitude resulting from a classical ABH, the fractional domain itself must attenuate the amplitude of the pressure wave.

It would be ideal to verify that the reflection coefficient from this fractional domain matched the reflection coefficient of the ABH via a finite difference simulation, similar to what was done in § 4.2.4 for the fractional boundary. However, the numerical calculation of complex order fractional derivatives is quite challenging. While a handful of numerical methods are available for purely real order fractional partial differential equations, the analysis of complex order fractional partial differential equations are not quite as advanced. There are few mentions and practically no published results on numerical methods and solutions for these kind of equations. Recall that in Chapter 2, a real order formulation was developed

for the reduction procedure due to the current limitations of evaluating a Mittag-Leffler functions with a complex order. Luckily, § 3.6.1 produced a fractional finite element method that was capable of handling complex orders. However, this does not seem to be the case for the finite difference formulation of the fractional wave equation with complex orders. While the numerical calculation of a complex derivative for just a single location (the fractional boundary) was feasible, the numerical calculation of an entire fractional domain possessing a complex order was observed to always be unstable due to the imaginary component of the order. The instabilities were seen to persist even when an implicit numerical finite difference simulation was conducted. Unfortunately, to the best of our knowledge, there are no available studies on the stability of these complex order numerical solutions. Further research on the numerical evaluation of complex order derivatives is necessary. Nonetheless, based on the results of the fractional boundary model and the accuracy of the fractional methodologies explored throughout the dissertation, we are confident that as more applications and numerical methods for complex order fractional partial differential equations are analyzed and developed, they would validate the obtained fractional orders in Fig. 4.13. To strengthen confidence in the fractional domain, the following section analyzes a homogenized fractional domain as an equivalent model for an ABH profile in a structural beam.

4.4 Fractional Beam Model of an Acoustic Black Hole

This section considers an ABH geometry in a structural beam waveguide. While [146] derived the analytical solution of the flexural displacement of the ABH beam, it was only valid when the taper was approximated as parabolic. Not only that, but the mathematics became rather cumbersome. Rather than focusing on a beam with an ABH termination, this section considers a beam which contains a variable portion that consists of two connected ABH taper profiles with a residual thickness. This ABH beam is depicted in Fig. 4.14(a) where the height of the beam is

$$h(x) = \epsilon|x|^m + h_r, \tag{4.44}$$

172
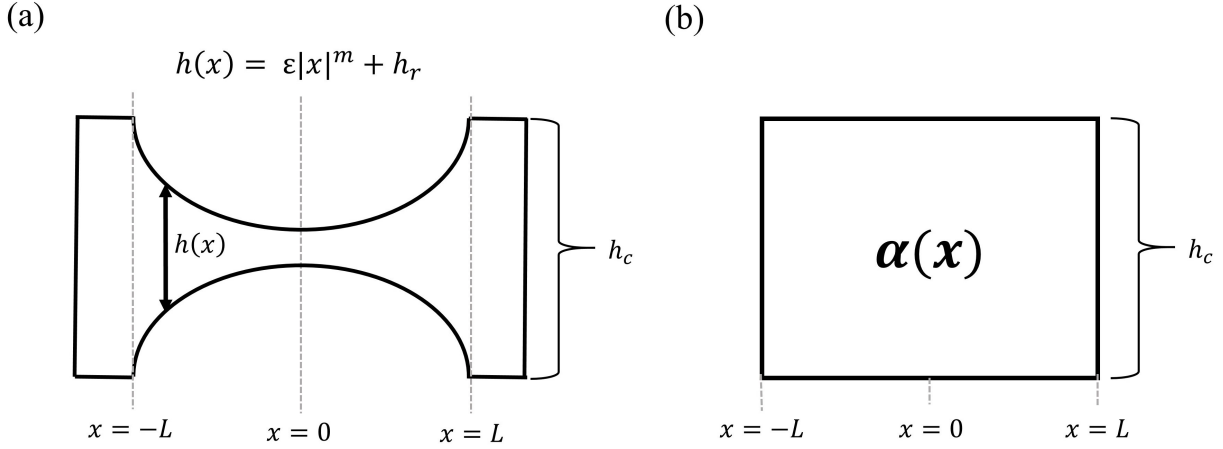
Figure 4.14. (a) The acoustic black hole beam created by two ABH profiles with a residual height h_r (b) The corresponding, homogenized fractional representation of the ABH beam with a constant height h_c equivalent to the height of the beginning and end of the ABH taper.

where h_r is the residual height of the ABH profiles at $x = 0$, and ϵ is a constant given by

$$\epsilon = \frac{h_c - h_r}{L^m}, \tag{4.45}$$

where h_c is the height of the beam at either the start or the end of the ABH tapers and L is the length of the ABH. The geometry of the ABH beam in Fig. 4.14(a) actually consists of two ABH profiles that are symmetric to each other about the line $x = 0$. Thus, the total length of the ABH beam is $2L$. Also, for a rightward propagating wave, the first half of the ABH beam associated with a decreasing thickness will slow down the elastic wave as it propagates toward the center while the second half of the ABH beam accelerates the elastic wave as the cross-sectional area increases. As opposed to the ABH termination in a duct, this section seeks to derive a fractional homogenized model, shown in Fig. 4.14(b), that not only accurately describes the effect of the ABH on the rest of the beam but also better reflects the dynamics within the ABH itself. The fractional beam model consists of a constant cross-sectional area of height h_c. In essence, the variable cross-section of the ABH beam is accounted for entirely by the value of the fractional order. Also, to better

173

represent the dynamics within the ABH beam, a variable space fractional order will need to be implemented. In addition, the homogenization seeks to establish a link between the geometrical parameters, including the power-law taper m, of the ABH to the fractional order of the equivalent fractional model. Recall that in § 4.2 and 4.3, the reflection coefficient from the ABH termination needed to be calculated before determining the fractional order of the fractional boundary or domain. As such, the dynamic response of the integer order system had to be determined first. One could argue that this limited the utility of the fractional models, especially compared to other homogenization tools.

As mentioned in § 1.2.6, a well-documented approach to derive fractional differential equations consists of transforming the integer order equations of motion, solving the equation in the transformed domain with the proper assumptions, approximations, and boundary conditions, and then performing an inverse transform to obtain an equivalent fractional derivative in the time-space domain. This approach works well when the underlying constitutive relations have an intrinsic power-law dependence. While this approach would be ideal, it was still exceedingly difficult to use for the ABH despite its power-law taper. Instead, this section considers an energy-based approach to calculate the corresponding fractional order for the ABH taper. The method equates the total strain and kinetic energy of the ABH beam in Fig. 4.14(a) to the total strain and kinetic energy of the corresponding fractional domain in Fig. 4.14(b) to calculate the fractional order. Although this is still a matching procedure, it is performed at a more fundamental level rather than matching the dynamic response of the integer and fractional models.

4.4.1 Governing Equation of the Fractional Beam

The governing equation of the fractional beam in Fig. 4.14(b) is modified from the beam model considered in § 3.5.1 by changing the definition of the Riesz fractional derivative. The governing equation of the fractional beam is

$$\bar{E}\bar{I}\frac{\partial}{\partial x}\left[\mathfrak{D}_x^{\alpha(x)}\left[D_x^{\alpha(x)}\left(\frac{\partial w}{\partial x}\right)\right]\right] + \bar{\rho}\bar{A}\frac{\partial^2 w}{\partial t^2} = F_T(x,t), \qquad (4.46)$$

where the parameters are equivalent to those in Eq. (3.118a) and $\alpha \in (0, 1)$. It is observed that one difference between Eq. (4.46) and Eq. (3.118a) is that the fractional derivative in Eq. (4.46) is spatially varying [64], [85], [86]. As discussed in [178], there are three types of variable order (VO) fractional derivatives: the first has no order memory, the second has weak order memory, and the third has strong order memory. In view of Eq. (1.17), the difference between the three VO definitions is the dependent variable of the order function: $\alpha = \alpha(t)$ in the no order memory definition, $\alpha = \alpha(\tau)$ in the weak order memory, and $\alpha = \alpha(t - \tau)$ for the strong order memory. This analysis considers the formulation of the variable order derivative without order memory; that is,

$$
{}^{C}_{a}D^{\alpha(x)}_{x}f(x) = \frac{1}{\Gamma(n - \alpha(x))} \int_{a}^{x} \frac{\mathrm{d}^{n}f(\xi)}{\mathrm{d}\xi^{n}}(x - \xi)^{n - \alpha(x) - 1}\mathrm{d}\xi. \tag{4.47}
$$

Again, a variable space order derivative is utilized in order to better reflect the dynamics within the changing geometry and, ultimately, the ABH taper. If one is seeking a homogenization model that reflects the effect of the ABH taper on the host structure without the need to accurately represent the behavior within the ABH itself (in essence, treating the ABH as a "black box"), a constant space fractional order will suffice, as seen in § 4.2 and 4.3. However, if a homogenization model that accurately represents the dynamic content within the ABH itself is sought, a variable order derivative will be necessary to model the variable cross-section of the ABH itself. Selection of a constant or variable space fractional model thus depends on the needs of the model and simulation. One could point out that calling a variable space fractional model a "homogenization" is not entirely accurate because the representation still has a spatially variable quantity. However, the purpose of the VO fractional model is to account for all varying quantities solely by the fractional order. As a result, a mathematical representation of a heterogeneous structure is achieved that contains constant coefficients and lets the order of the derivative account for the heterogeneity.

In contrast to Eq. (3.114), the Riesz-Caputo derivative in Eq. (4.46) is defined as

$$
D^{\alpha(x)}_{x}\Psi(x) = \frac{1}{2}\Gamma(2 - \alpha(x))\left[L^{\alpha(x) - 1}_{A}{}^{C}_{x_A}D^{\alpha(x)}_{x}\Psi(x) - L^{\alpha(x) - 1}_{B}{}^{C}_{x}D^{\alpha}_{x_B}\Psi(x)\right], \tag{4.48}
$$

where x_A is the location where the fractional domain begins and x_B is where the fractional domain terminates (note the Riesz-Riemann-Liouville in Eq. (4.46) is defined in the same manner as Eq. (4.48), but using Riemann-Liouville derivatives). The definition of the Riesz-Caputo derivative given by Eq. (4.48) actually more closely coincides with the definition given in [112], [113]. Recall from § 3.5.1 that Eq. (3.114) was appropriate for an infinite structure. However, to ensure no strain accumulation at the terminations of a finite fractional domain or at fractional-integer domain interfaces, [112] derived a Riesz-Caputo definition where the factors $\Gamma(2 - \alpha)$, $L_A^{\alpha-1}$, and $L_B^{\alpha-1}$ resulted in a frame-invariant formulation. Furthermore, [112] determined that $L_A = x - x_A$ and $L_B = x_B - x$. Since the considered ABH beam is finite and, as will be seen in § 4.4.3, will be embedded in a beam configuration with constant cross-sectional area regions, the fractional derivatives in Eq. (4.46) must be defined according to Eq. (4.48).

4.4.2 Calculation of Fractional Order

To determine the fractional order of the homogenized fractional beam model in Fig. 4.14(b) corresponding to the ABH, an approach where the total strain and kinetic energy of the geometry in Fig. 4.14(a) is equated to the total strain and kinetic energy of the corresponding fractional domain in Fig. 4.14(b) is considered. Ideally, a procedure that determines the fractional order without matching quantities between the fractional and integer order models would be ideal, but such a methodology has been difficult to formulate. Equating the total energy of the ABH in Fig. 4.14(a) to the fractional model in Fig. 4.14(b) is given by

$$\Pi_I + T_I = \Pi_F + T_F, \tag{4.49}$$

where Π is the strain energy, T is the kinetic energy, and the subscripts I and F indicate the variable cross section integer order model and the constant cross section fractional order

model, respectively. Using the definition of the energy of a beam from [179] and the energy of a fractional beam (Eqs. (3.115) and (3.117)), Eq. (4.49) becomes

$$\frac{1}{2} \int_{-L}^{L} EI(x) \left(\frac{\partial^2 w}{\partial x^2} \right)^2 \mathrm{d}x + \frac{1}{2} \int_{-L}^{L} \rho A(x) \left(\frac{\partial w}{\partial t} \right)^2 \mathrm{d}x$$
$$= \frac{1}{2} \int_{-L}^{L} \bar{E}\bar{I} \left[{}_0^C D_L^\alpha \left(\frac{\partial w}{\partial x} \right) \right]^2 \mathrm{d}x + \frac{1}{2} \int_{-L}^{L} \bar{\rho}\bar{A} \left(\frac{\partial w}{\partial t} \right)^2 \mathrm{d}x. \tag{4.50}$$

Using the symmetry about the line $x = 0$ in Fig. 4.14, Eq. (4.50) is simplified to

$$\int_{0}^{L} EI(x) \left(\frac{\partial^2 w}{\partial x^2} \right)^2 \mathrm{d}x + \int_{0}^{L} \rho A(x) \left(\frac{\partial w}{\partial t} \right)^2 \mathrm{d}x$$
$$= \int_{0}^{L} \bar{E}\bar{I} \left[{}_0^C D_L^\alpha \left(\frac{\partial w}{\partial x} \right) \right]^2 \mathrm{d}x + \int_{0}^{L} \bar{\rho}\bar{A} \left(\frac{\partial w}{\partial t} \right)^2 \mathrm{d}x. \tag{4.51}$$

To determine the space order $\alpha(x)$ from Eq. (4.51), a harmonic solution of the flexural displacement is taken as

$$w = \mathrm{e}^{\mathrm{i}(\omega t - \bar{k} x)}, \tag{4.52}$$

where $\bar{k}$ is a constant wavenumber. The selection of the constant parameter $\bar{k}$ is important so that it is accurately reflects the physics of the wave propagation. Recall that the acoustic black hole profile can be considered a nonlocal geometry. The beam given in Fig. 4.14(a) can be viewed as a local beam whose height is equal to the residual height h_r plus nonlocal contributions from the ABH taper located "on top" of the local beam. In this interpretation, $\bar{k}$ is selected as the wavenumber through the local beam; that is, $\bar{k}$ is selected as the local wavenumber of the ABH profile in Fig. 4.14(a) at $x = 0$. The fractional order α, as well as the fractional parameters $\bar{E}$, $\bar{\rho}$, $\bar{I}$, and $\bar{A}$, accordingly serve as effective "tuning" parameters that permit the fractional model to dynamically reflect the speed of the propagation through the ABH accurately.

As will be seen in § 4.4.3, the ABH taper will be positioned in an otherwise homogeneous elastic beam configuration whose height is a constant h_c. As a result, the parameters $\bar{E}$, $\bar{\rho}$, $\bar{I}$, and $\bar{A}$ of the fractional domain are selected to match the homogeneous beam portion. This way, the heterogeneity is represented solely by fractional order. The parameters of the fractional domain are defined as

$$\bar{A} = bh_c, \tag{4.53}$$

$$\bar{I} = \frac{bh_c^3}{12}, \tag{4.54}$$

where b is the constant thickness of the beam. Since the Young's modulus and the density of the beam do not change in the ABH region, $\bar{E} = E$ and $\bar{\rho} = \rho$. Now that the fractional parameters have been selected, the fractional order $\alpha(x)$ is determined by setting the integrands of Eq. (4.51) equal to each other. This is done so that the order $\alpha(x)$ accurately represents the dynamics at each spatial location. Additionally, if the integrands of Eq. (4.51) are equivalent, then the integrals will be equal as well. Equating the integrands and substituting the expressions for the both the variable integer order and the constant fractional areas and moments of inertia yields

$$E\frac{bh(x)^3}{12}\bar{k}^4 w^2 - \rho bh(x)\omega^2 w^2 = \bar{E}\frac{bh_c^3}{12}[(-\mathrm{i}\bar{k})_0^C D_L^\alpha w]^2 - \bar{\rho}bh_c\omega^2 w^2. \tag{4.55}$$

Rearranging and setting $\bar{E} = E$ and $\bar{\rho} = \rho$ produces

$$\left[\frac{h(x)^3}{h_c^3}\bar{k}^4 + \omega^2\frac{12\rho}{Eh_c^3}(h_c - h(x))\right]w^2 = [(-\mathrm{i}\bar{k})_0^C D_L^\alpha w]^2. \tag{4.56}$$

Before further simplifying Eq. (4.56), the fractional derivative of an exponential function is again analyzed. As discussed in § 3.2.1, for a constant space fractional order derivative, the fractional derivative of an exponential is an exponential according to Eq. (3.32) if the lower or upper bound of the fractional derivative is $\pm\infty$. Otherwise the Caputo fractional derivative of an exponential function is a Mittag-Leffler function according to Eq. (3.35). § 3.3 explored both solution kernels and found that the results were nearly equivalent (the main difference

178

between the curves in Figs. 3.6 and 3.7 was due to the numerical evaluation of the Mittag-Leffler function). However, for a variable order derivative, it is not immediately evident which, if either, of the Mittag-Leffler and exponential solution kernels is more appropriate. As a result, the energy-matching approach here will consider both the exponential and ML solution kernels. If the fractional derivative of an exponential is taken according to Eq. (3.32), then Eq. (4.56) reduces to

$$\frac{h(x)^3}{h_c^3}\bar{k}^4 + \omega^2\frac{12\rho}{Eh_c^3}(h_c - h(x)) = (-i\bar{k})^{2(1+\alpha)}\bar{l}^2, \tag{4.57}$$

where

$$\bar{l} = \frac{1}{2}\Gamma(2-\alpha)(L_A^{\alpha-1} + L_B^{\alpha-1}), \tag{4.58}$$

$$L_A = x - x_A, \tag{4.59}$$

$$L_B = x - x_B. \tag{4.60}$$

The parameters L_A and L_B are linear functions of the spatial coordinate and, along with the bounds of the integrals in the definitions of the left and right-handed fractional derivatives, define the horizon of nonlocality of the fractional domain. On the other hand, if the fractional derivative of an exponential is taken according to Eq. (3.35), then Eq. (4.56) reduces to

$$\frac{h(x)^3}{h_c^3}\bar{k}^4 + \omega^2\frac{12\rho}{Eh_c^3}(h_c - h(x)) = \bar{k}^4\bar{l}^2\mathcal{R}^2, \tag{4.61}$$

where

$$\mathcal{R} = \frac{x^{1-\alpha}E_{1,2-\alpha}(-i\bar{k}x)}{e^{-i\bar{k}x}}. \tag{4.62}$$

Both Eqs. (4.57) and (4.61) are transcendental equations that can be numerically solved for α at each spatial coordinate. Additionally, Eqs. (4.57) and (4.61) provide a relationship between fractional order α and the geometrical parameters of the ABH. Thus, the fractional

order can be obtained directly from the geometrical parameters of the ABH without needing to dynamically match the responses of the integer and fractional order models. It should be noted that both the left-hand sides of Eqs. (4.57) and (4.61) are purely real while the right-hand sides will produce a complex quantity. In this instance, the imaginary part of the right-hand side does not have a clear physical meaning since the real and imaginary parts of the parameter $\bar{k}$ would already account for persisting or decaying harmonic oscillations. Therefore, the fractional order α is determined by equating the real part of the right-hand sides of Eqs. (4.57) and (4.61) to the left-hand sides.

4.4.3 Numerical Assessment

To assess the fractional orders given by Eqs. (4.57) and (4.61), consider the ABH geometry in Fig. 4.14(a) with $m = 2$, $L = 3$ m, $h_c = 0.05$ m, $h_r = 0.01$ m, $b = 0.05$ m, $E = 70$ GPa, $\rho = 2700$ kg/m^3, and a harmonic frequency of $\omega = 500$ Hz. The plot of the local wavenumber of the ABH along with its phase velocity is plotted in Fig. 4.15. At the center $x = 0$, the phase velocity is a minimum while the local wavenumber is a maximum. For the selection of these parameters, $\bar{k} = 14.6196$ m^{-1}. The plot of the fractional order calculated from Eqs. (4.57) and (4.61) is shown in Fig. 4.16.
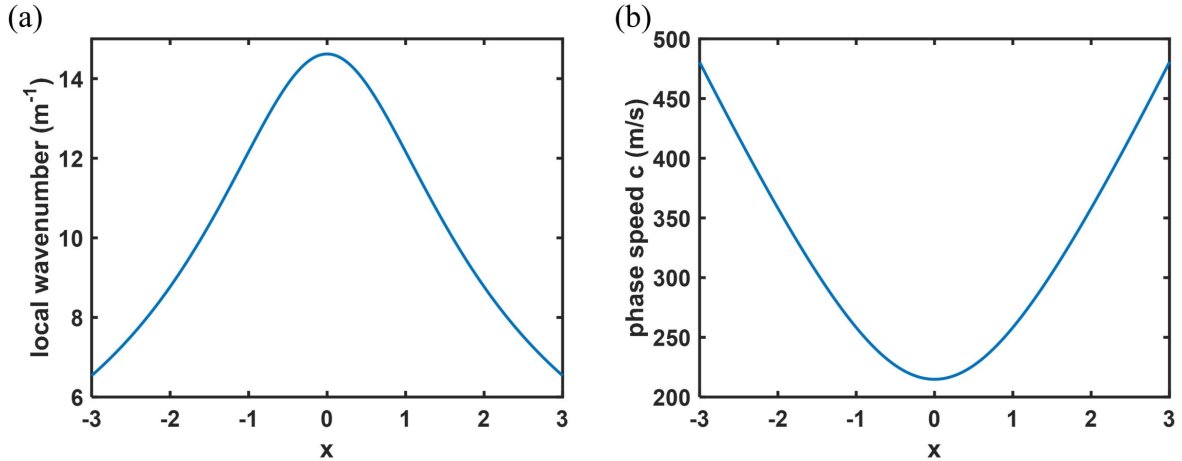

Figure 4.15. (a) The local wavenumber of the ABH as given by Eq. (4.3).
(b) The local phase velocity in the ABH, which is equal to $\omega/k(x)$.
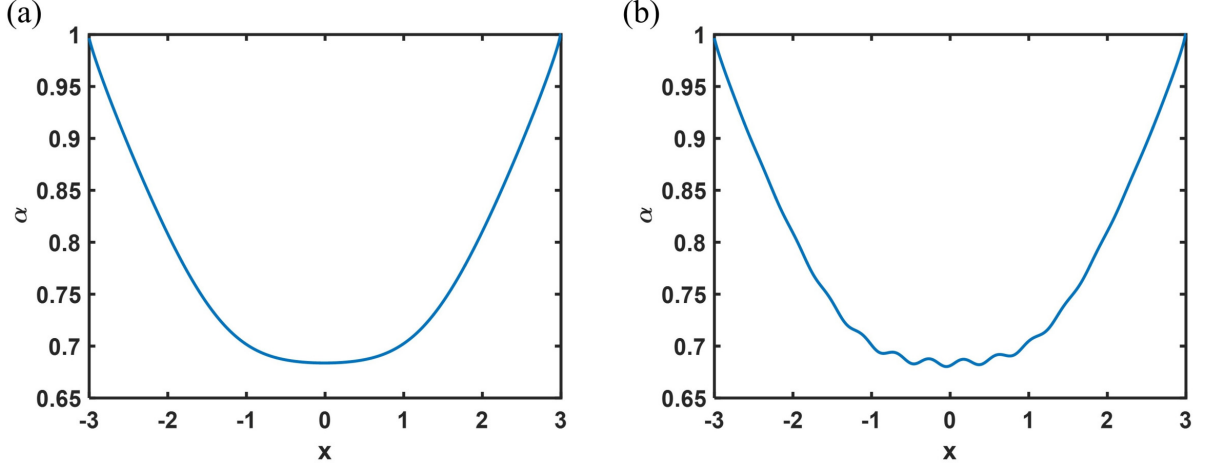
Figure 4.16. (a) The variable space order of the fractional representation of the ABH beam using the exponential solution kernel in the energy-matching approach. (b) The variable space order of the fractional representation of the ABH beam using the Mittag-Leffler formulation in the energy-matching approach.

The fractional orders obtained using the exponential and Mittag-Leffler functions in Fig. 4.16 are identical for spatial locations around $|x| > 1$. However, near the center of the ABH, the plot of the fractional order obtained using the Mittag-Leffler formulation exhibits a small oscillating trend. Both curves have nearly the same minimum point of $\alpha \approx 0.684$ at $x = 0$. Additionally, both curves produce $\alpha = 1$ at the beginning and end of the ABH taper. The fractional parameters $\bar{I}$ and $\bar{A}$ were chosen to produce $\alpha = 1$ at these locations so that when the ABH beam is considered as a portion of a constant cross section beam with height h_c, the fractional order became the integer order $\alpha = 1$, which results in Eq. (4.46) collapsing into the classical fourth-order wave equation for the flexural displacement of a homogeneous beam. The location of the minimum of the fractional order represents the location of the ABH beam where the local phase velocity is a minimum and where the ABH area $A(0)$ and moment of inertia $I(0)$ possess the farthest values from the fractional parameters $\bar{A}$ and $\bar{I}$, respectively. The values of L_A and L_B, plotted in Fig. 4.17, were chosen corresponding to Eqs. (4.59) and (4.60), which are equivalent to the nonlocal horizons of the left and right-hand fractional derivatives given in Eq. (4.48), respectively.
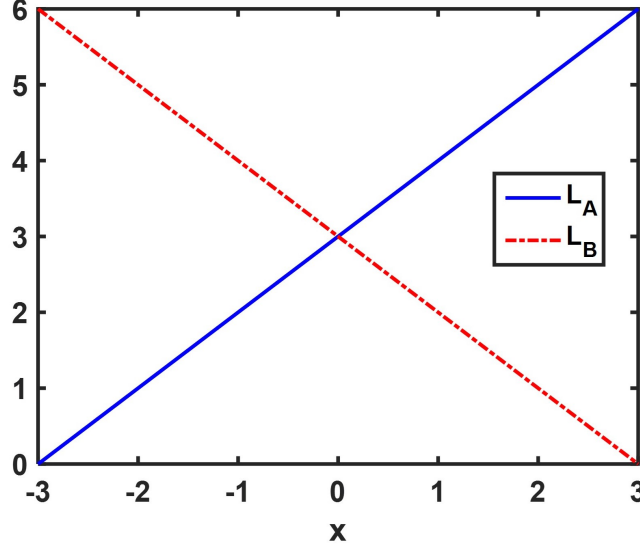
Figure 4.17. The length parameters L_A and L_B in Eq. (4.48) for the fractional beam representation of the ABH.

To validate that the fractional orders given by Eqs. (4.57) and (4.61) are representative of the flexural displacement through the ABH beam, an ABH beam is embedded in a constant cross section beam as depicted in Fig. 4.18. As shown by this figure, the homogenization methodology models the heterogeneity of the acoustic black hole with a fractional domain of constant cross section whose fractional order α is a function of space and frequency. A rightward propagating wave is generated by a prescribed flexural displacement at the left end of the beam, which is designated as $x = 0$. The prescribed flexural displacement in Fig. 4.18 is

$$w(0, t) = w_0 e^{i\omega t}, \tag{4.63}$$

where, for the example considered here, $w_0 = 0.001$ m and $\omega = 500$ Hz. The ABH begins at a location of $x = 7$ m and ends at $x = 13$ m (making its center located at $x = 10$ m). Although most structural acoustic black holes possess some added damping, the ABH considered here does not. Of course, an elastic wave will fully propagate through an imperfect acoustic black hole geometry (i.e., one with a residual thickness) if there is no damping present.

182
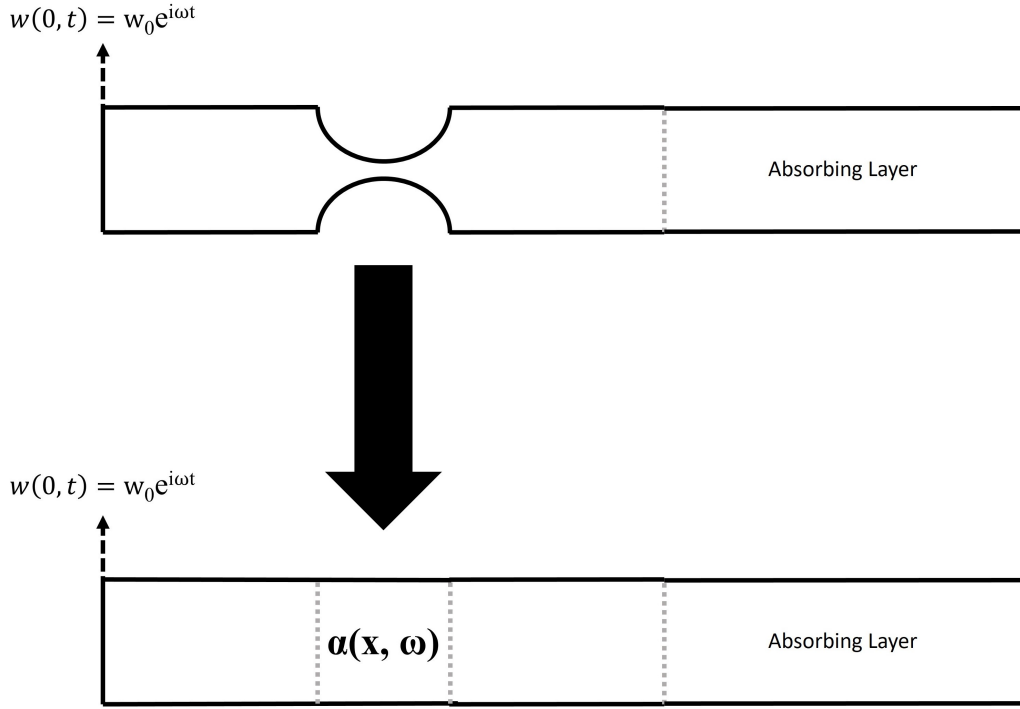
Figure 4.18. Homogenized fractional representation of a beam with an embedded acoustic black hole. Note the right-most part of the beam contains applied structural damping to implement a simplified concept of an absorbing boundary to prevent reflections from the end of the beam.

However, the variation of the wave speed within the ABH geometry will affect the phase of the harmonic flexural displacement in the transmitted region while the amplitude of the flexural displacement within the ABH increases. The right-most portion of the beam configuration in Fig. 4.18 does contain added structural damping. The structural damping acts as an absorbing layer so that the rightward propagating wave is fully attenuated by the time it reaches the right-hand termination of the beam. The added damping is represented by a complex Young's modulus: $E = 70(1+0.5\mathrm{i})$ GPa. This absorbing layer begins at $x = 20$ m and ends at $x = 40$ m.

Figures 4.19 and 4.20 depict the steady state results of the flexural displacement of the beam configuration containing the equivalent fractional domain using the exponential solution kernel and the Mittag-Leffler solution kernel, respectively. The flexural displacements of

the beam configuration were obtained using the fractional finite element method presented in [113] and § 3.6.1 along with the fractional orders calculated in Fig 4.16. To access the accuracy of the fractional domain representation of the ABH obtained via the f-FEM, a reference model of the beam configuration given in Fig. 4.18 with the embedded ABH geometry was constructed and evaluated in the commercial finite element software COMSOL. The steady state flexural displacement obtained using COMSOL is given as the red, dotted curves in Figs. 4.19 and 4.20. Of course, the numerical results obtained from COMSOL may or may not accurately represent the actual dynamic response of the ABH beam. Luckily, comparisons of finite element simulations of structural ABHs to experimental data in [155], [156] assure the results of the COMSOL simulation of the ABH beam can serve as the reference model to assess the homogenization fractional domain. Still, future work involving experimental analysis of the beam with an embedded ABH could be considered for further validation.

Figure 4.19. (a) Comparison of the results from the f-FEM to a reference COMSOL model when using the exponential solution kernel of the energy-matching approach. (b) Closeup of the region where the ABH is located depicting a close phase match of the curves.

Examining the exponential-based results in Fig. 4.19(a), the amplitude and phase of the f-FEM and COMSOL results were in near perfect agreement for the locations before and after the fractional domain with a phase offset on the order of 0.01 m and an amplitude
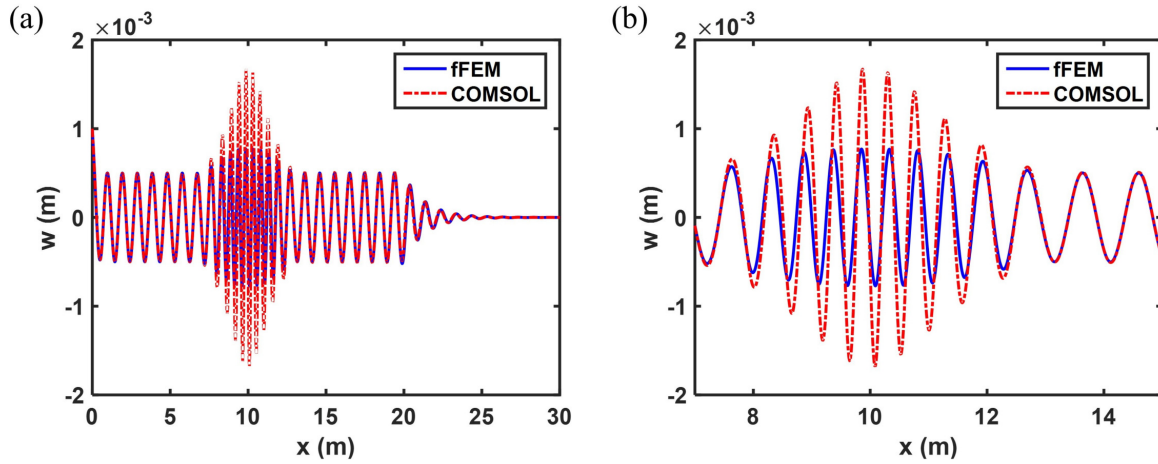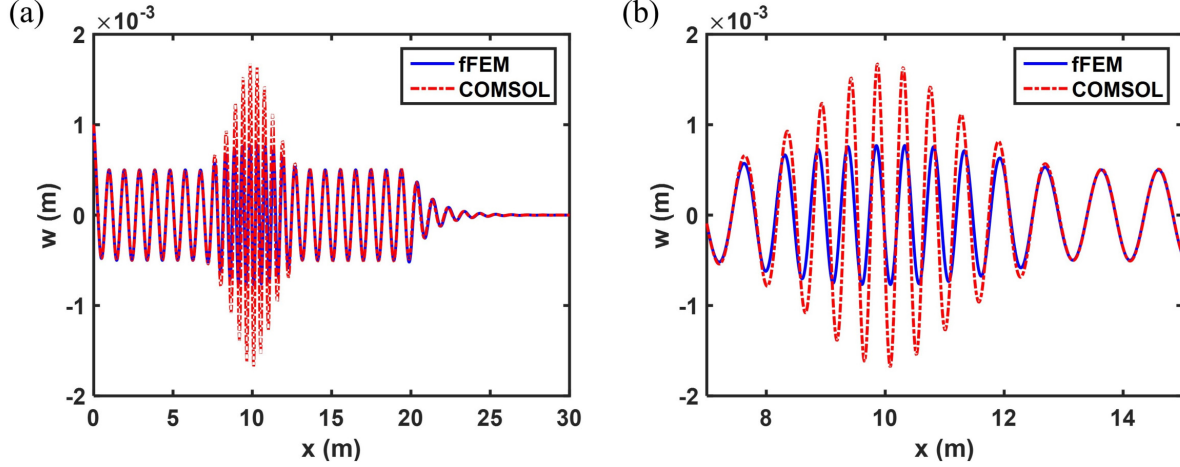
Figure 4.20. (a) Comparison of the results from the f-FEM to a reference COMSOL model when using the Mittag-Leffler solution kernel of the energy-matching approach. (b) Closeup of the region where the ABH is located depicting a close phase match of the curves.

difference approximately 1% or less. The results using the ML kernel are depicted in Fig. 4.20 and are nearly equivalent to the results in Fig. 4.19 (near zero phase mismatch and an amplitude difference on the order of 0.1%). A closer view of the fractional region from $x = 7$ m to $x = 13$ m in Figs. 4.19(b) and 4.20(b) indicates that there is still a relatively small phase mismatch between the f-FEM and COMSOL results (0.06 m is the maximum phase offset between the f-FEM and the reference curves in the fractional domain). This is most likely due to the fact that the exponential and Mittag-Leffler kernels are not exact solutions to the variable space order differential equations seen in Eq. (4.46). However, the results certainly give confidence that the exponential and Mittag-Leffler solution kernels are excellent approximate solutions to the variable order differential equation. While the phase of the curves in Figs. 4.19(b) and 4.20(b) were close to each other, the amplitudes of the curves were not. While Figs. 4.19 and 4.20 do show that the amplitude of the flexural displacement in the fractional domain did increase by approximately 50% at the center of the fractional domain compared to the amplitude of the displacement in the constant cross section beam portions, clearly the flexural displacement did not increase as much as it did in the reference ABH COMSOL model (amplitude increase as large as 230% at the center of the ABH). The

results thus indicate that the space fractional order accurately modeled the phase of the harmonic wave propagation but had a significantly smaller impact on the amplitude of the wave propagation. It is hypothesized that the amplitude of the f-FEM results would better match those of the reference model if the assumed solution form in Eq. (4.52) had a constant non-unity amplitude $\bar{A}$. The selected value of $\bar{A}$ is an open question which needs further investigation, although one potential value would be the mean of $A(x)$ given in Mironov's assumed solution form (Eq. (4.3)).

The results in Figs. 4.19 and 4.20 indicate that the energy-matching formulation of the variable space fractional order produced a homogenized fractional domain that was capable of accurately reflecting the phase of the harmonic wave propagation through the ABH geometry. While this section illustrated that a variable space fractional order derivative is a viable tool, further research should compare the fractional methodologies to integer order homogenization techniques for the ABH. Additionally, most ABH studies implement finite element models (similar to the COMSOL model that was used as the reference flexural displacement) to simulate the wave propagation through structures possessing acoustic black hole geometries. In fact, for the system considered in Fig. 4.14, the results obtained using the f-FEM had a slightly longer computational time compared to the COMSOL results. However, the fractional homogenization may be computationally superior for structures with large periodic arrays of ABH geometries, as illustrated in Fig. 4.21. Also, as previous mentioned, most ABH designs include some amount of damping in order to dissipate the elastic wave energy that is slowed down and trapped in acoustic black hole geometries. While the complex order space fractional derivatives in § 3.2.2 and § 3.5.2 attenuated the displacement field, those periodic, heterogeneous structures were still conservative. Because a time fractional derivative better represents dissipation losses due to damping, the fractional beam model would need to be modified so that its governing differential equation contained a time fractional derivative capable of representing the dissipation characteristics of ABH geometries possessing damping.
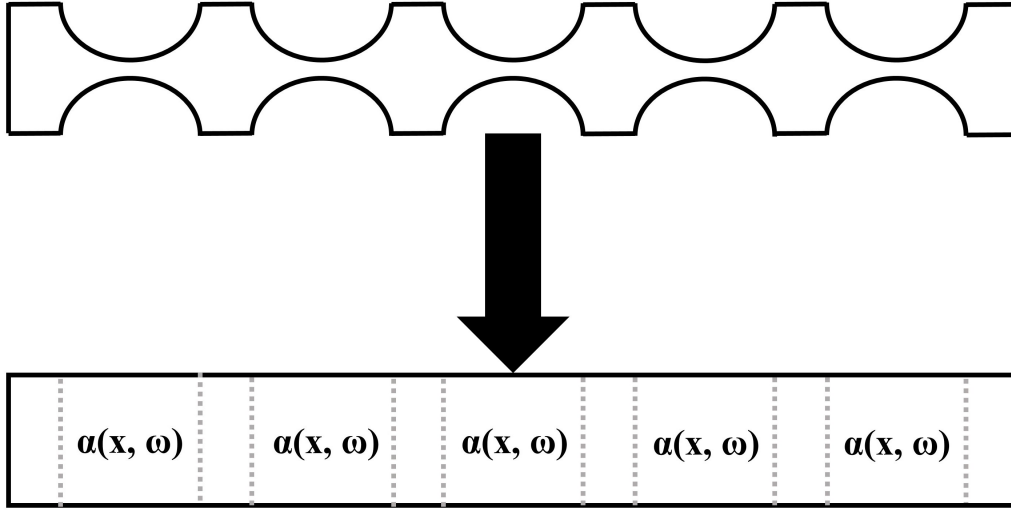
Figure 4.21. Illustration of the fractional homogenization of a beam with a periodic array of acoustic black holes, where the space fractional homogenization may have computational advantages.

4.5 Conclusions

The acoustic black hole geometry was selected as a prototypical system of a geometrical heterogeneous structure in order to implement space fractional order models for homogenization applications. In particular, the chapter studied the possibility of leveraging space fractional order operators to model ABH terminations in air-filled acoustic ducts and ABH tapers in structural beams. For the acoustic black hole terminations in ducts, the fractional formulations replaced the ABH termination with an effective model capable of inducing an equivalent wave reflection of the pressure field in the main duct without requiring the full solution of the pressure field in the termination. Two modeling approaches were used: the first was based on a fractional order boundary condition with a constant space fractional order derivative, while the second implemented a finite fractional order domain. On the other hand, the beam with an acoustic black hole profile was homogenized by a fractional domain whose order varied as a function of space. The approach relied on matching the total energy of the integer and fractional models. Although this was still a matching procedure,

it was performed at a more fundamental level rather than matching the dynamic response of the integer and fractional models. Contrary to the constant space fractional models of the duct, the variable space fractional order produced a homogenized fractional domain where the phase of the harmonic flexural displacement accurately represented the wave propagation through the acoustic black hole. The use of either a constant or variable space fractional order depends on whether the intent of the model is to merely reflect the effect of embedded geometrical heterogeneity on the overall behavior of a structure or to accurately capture the localized behavior within the heterogeneity as well. This chapter illustrated the feasibility and the potential of fractional order homogenization of heterogeneous geometries such as the acoustic black hole. While further research is needed to compare the computational costs of the fractional representation of the ABH to other types of models, use of the fractional models proposed here may provide the basis for an efficient and accurate computational method for structures with periodic arrays of acoustic black holes.

5. CONCLUSIONS

5.1 Summary

This dissertation explored the feasibility and potential of fractional calculus for simulating the vibration and wave propagation in discrete and continuous models of heterogeneous structures. The analysis of the dynamic behavior of heterogeneous structures typically relies on numerical simulations that require proper computational methodologies to overcome their intrinsic complexities. Regarding discrete parameter models, representations of heterogeneous structures often require a large number of degrees of freedom. Despite the continuing growth of computer performance, the large number of degrees of freedom leads to tradeoffs between accuracy of the dynamic simulations and computational time. In response, model order reduction techniques have been developed to reduce the number of degrees of freedom in a discrete parameter model while still retaining the accuracy of finer discretizations. In the introduction, it was discussed how modal-based dynamic model order reduction procedures use the displacement eigenvectors to accurately calculate the displacement field of the retained degrees of freedom. However, these model order reduction techniques experience reduced accuracy for frequency regions where resonance frequencies are closely spaced. Moreover, they are typically valid only for narrow-banded frequency ranges. By developing a reduced order model where the motion of the active degrees of freedom are governed by fractional differential equations, a highly accuracy model order reduction methodology was created. The value of the reduced time fractional order was calculated in the frequency domain and illustrated that the dynamics between resonance frequencies are locally fractional. The frequency-dependency and complex nature of the fractional order enabled modulation of the phase and amplitude of the harmonic displacement. This produced an accurate order reduction across a broad frequency spectrum. In addition, the formulation of the fractional oscillator as a system identification tool for numerical or experimental data further strengthened the case for implementation of fractional oscillators for the vibration of discrete, heterogeneous structures.

For continuous representations of heterogeneous structures, homogenization techniques calculate the effective properties of a corresponding homogeneous medium via averaging or

asymptotic expansions of the spatially varying material and geometrical properties. Mathematically, homogenization approaches represent a heterogeneous structure by replacing their governing differential equations containing variable coefficients with constant coefficient, homogeneous equations. However, low-frequency homogenization techniques can only accurately capture the wave propagation through heterogeneous structures at long wavelengths. As a result, they cannot represent the frequency band gaps observed in periodic, heterogeneous structures. In response, high-frequency homogenization models have successfully been developed to extend past the long wavelength limit, but tend to be mathematically complex and computationally expensive due to necessarily extensive asymptotic expansions. In turn, this work investigated the role of space fractional order operators as the mathematical foundation for the development of material homogenization techniques. In particular, a bi-material, periodic rod and beam was chosen as a prototypical example of a one-dimensional elastic metamaterial. By leveraging the space fractional operator's attenuative and conservative nature, the dynamic response within the frequency band gaps was accurately captured by a frequency-dependent and complex-valued space fractional order. This yielded a homogenization technique that did not rely on long asymptotic expansions to represent the dynamics of the frequency band gaps. In addition, for the periodic rod case, closed-form analytical solutions to the homogenized fractional differential equation were obtained, avoiding reliance on potentially expensive numerical calculations. The closed-form analytical solutions could play a major role towards the development of computationally efficient inverse problems in material design and remote sensing.

Lastly, the dissertation considered another application of the fractional homogenization on a recently studied heterogeneous geometry known as the acoustic black hole. In this case, the order of a space fractional operator captured the heterogeneity of the variable cross-sectional profile of the acoustic black hole. Additionally, the fractional representation of the acoustic black hole was developed with the aim of alleviating current computationally intensive approaches to the simulation of acoustic black holes. The study focused on developing space fractional models for two different systems: 1) an air-filled acoustic duct containing an acoustic black hole termination, and 2) a structural elastic beam embedded with an acoustic black hole profile. For the acoustic duct case, the fractional model replaced

the acoustic black hole termination with a space fractional boundary or domain that was capable of inducing an equivalent dynamic behavior of the pressure field in the main duct without requiring the full solution of the pressure field in the termination. On the other hand, the fractional homogenized model for the acoustic black hole beam sought to also accurately represent the dynamics within the acoustic black hole itself. This required the use of a variable space fractional order. The selection of either a constant or variable space fractional order depends on whether the intent of the homogenized model is to merely reflect the effect of heterogeneity on the overall structure or to additionally capture the localized behavior within the heterogeneity. While the ability of the fractional homogenization to reduce the computation costs of periodic arrays of acoustic black holes requires further study, the work illustrated the potential of using the space fractional operators to model geometrical heterogeneity.

5.2 Contributions and Significance

This section considers the objectives outlined in § 1.3 to analyze the overall contributions and significance of the dissertation. The most significant contributions of this work are

- **The development of fractional model order reduction techniques for damped discrete parameter systems illustrating how time fractional operators can enable high levels of order reduction while simultaneously delivering high accuracy across a broad frequency spectrum. This was achieved via the following technical findings:**.

  - The development of a fractional modal analysis for a multiple degree of freedom fractional oscillator. This produced closed-form analytical solutions of the displacement of each node of the fractional oscillator.

  - The creation of a fractional model order reduction where the active degrees of freedom of the damped discrete parameter system were reduced in order using fractional oscillators. Results indicated that the corresponding fractional or-

191

der was frequency-dependent and complex-valued, which was the basis of the broadband frequency accuracy for the order reduction.

– The extension of the fractional reduction to discrete parameter systems possessing more complicated and multiple harmonic loads, resulting in an reduction procedure well-equipped to handle load cases that commonly arise in vibration analysis.

– The use of the fractional oscillator as the basis for a system identification methodology. This produced a frequency-dependent fractional model which could accurately match the amplitude and phase of numerical or experimental data across a broad frequency spectrum.

• **The creation of a homogenization tool based on space fractional order derivatives for 1D periodic, heterogeneous structures. The approach accounted for the spatially varying properties of a heterogeneous structure by using a homogeneous fractional medium with constant coefficients. This was achieved via the following technical findings:**

– The use of space fractional wave equations to model the wave attenuation of the frequency band gaps of a bi-material periodic rod or beam with a frequency-dependent, complex-valued fractional order.

– The analysis of a closed-form analytical solution of the governing equation of the fractional rod model based on either exponential or Mittag-Leffler solution kernels, yielding accurate representations of the wave propagation through periodic, heterogeneous structures. Additionally, the closed-form solutions can have important implications for inverse problems in material design and remote sensing.

– The implementation of a fractional finite element solution of the fractional beam, which was valid even for complex fractional orders. This signified an important development for complex order numerical methodologies.

192

- **The application of space fractional homogenization concepts to the acoustic black hole geometry, illustrating how fractional operators can simulate the wave propagation in acoustic and structural systems containing geometric heterogeneity. This was achieved via the following technical findings:**

  - The development of an effective model based on a space fractional boundary or domain for an acoustic duct containing an acoustic black hole termination. This fractional homogenization could produce the equivalent reflection from the acoustic black hole termination without having to determine the detailed dynamic response within the acoustic black hole itself.

  - The formulation of an energy-matching methodology to calculate the space fractional order of a fractional representation of a beam containing an acoustic black hole. Equating the kinetic and potential energies of varying cross-sectional profile of the acoustic black hole to a constant cross-sectional fractional model produced a relationship between the value of space fractional order and the geometrical parameters of the acoustic black hole.

  - The use of a variable space fractional order derivative in the fractional beam model that was capable of representing the local dynamical response within the acoustic black hole itself in addition to its effect on the host structure.

- **The illustration of the feasibility and potential of fractional operators for structural dynamic applications serving as 1) a foundation of the application of fractional calculus in the vibration and wave propagation of discrete and continuous heterogeneous structures and 2) a research study which will lead others to consider if, how, and why fractional calculus can be useful for engineering modeling and simulation.**

5.3   Limitations

While this dissertation illustrated the power of fractional calculus for modeling the vibration and wave propagation of discrete and continuous models of heterogeneous structures, it

193

would be remiss if it did not mention its limitations. Starting with the fractional model order reduction in Chapter 2, the approach is most likely still subject to potentially restrictive computational tradeoffs. Even the example of reducing an I-4DOF to a F-2DOF explored in § 2.5 began to require a computational time on the order of ten minutes. While this itself was not too restrictive, if the fractional model order reduction is to gain more widespread use for large discrete assemblies (which can possess thousands of degrees of freedom), the amount of computational time could potentially become unreasonable. More studies into the computational abilities and restrictions of the fractional model order reduction are needed. Additionally, the current state of the art of numerically evaluating complex order derivatives restricted some displacement analyses and introduced error. While the real order reduction formulations were successfully developed to circumvent this issue, the need for advanced complex order numerical methods still persists.

As a homogenization tool in Chapter 3, the space fractional wave equation successfully captured the attenuating wave amplitude of the frequency band gaps of a periodic metamaterial; however, it did not accurately model the response at higher frequency pass bands beyond the long wavelength limit. Like other low-frequency homogenization techniques, the fractional rod and beam failed to capture the local interactions present at smaller wavelengths. This prompts the question of if and how fractional calculus can improve the performance of homogenization techniques at high pass band frequencies. Also, the calculation of the space fractional order occurred by equating the dispersion relationship of the integer order differential equation of the bi-material, periodic structure to that of the corresponding fractional representation. As a result, it could be argued that the dynamic response of the periodic structure had to be determined first in order to calculate the fractional order. This potentially diminishes the impact of the space fractional homogenization depending on the specific application at hand.

Finally, while the fractional operator was illustrated to be a valid means to model acoustic black holes in Chapter 4, questions remain about if it is the optimal means to represent geometric heterogeneity. For example, it was seen that the corresponding integer order boundary condition in Eq. (4.23) and § 4.2.5 had the same or better performance than the developed fractional order boundary condition. In addition, while fractional calculus did

manage to successfully represent the effects of the acoustic black holes on its host structure, a distinct mathematical formulation proving that the physics of the acoustic black hole are inherently fractional was lacking due to its difficulty to derive. For the acoustic duct, this was seen by the fact that the reflection coefficient had to be known beforehand to determine the fractional order. Luckily, a more direct relationship between the space fractional order and geometrical parameters was obtained for the acoustic black hole beam using an approach rooted in the potential and kinetic energy along with a variable space fractional derivative. Although this approach did not rely on first obtaining the dynamic response of an integer order model, it was still a type of matching procedure that did not convincingly indicate that the physics of the acoustic black hole are best described as fractional. Furthermore, the variable space fractional order model still required relatively long computational times compared to the reference COMSOL finite element simulation. Future research would indicate if the fractional models are computationally superior for systems containing large arrays of acoustic black holes.

5.4   Recommendations for Future Work

Recommendations for future work include

- **Further numerical research on the evaluation of complex fractional orders**. Development of an efficient subroutine for the accurate evaluation of the complex order Mittag-Leffler function would immediately strengthen the application of the complex order model order reduction techniques in Chapter 2 and the Mittag-Leffler solution kernels of the space fractional wave equation in Chapter 3. Additionally, while the fractional finite element formulation in § 3.6.1 could evaluate complex order derivatives, an in-depth study of the complex order finite difference formulation (see Eq (1.20)) would be pivotal since a variety of fractional numerical methods are built from the Grunwald-Letnikov definition.

- **Evaluation of the computational performance of fractional operators and methodologies compared to other common integer order-based models.** This

recommendation was alluded to in the previous section when considering the computational expenses of the fractional model order reduction methodology to reduce a discrete model with either hundreds or thousands of degrees of freedom. Comparisons of the computational efficiency of fractional and integer order methodologies would also be useful for the space fractional homogenization of structural heterogeneity. For instance, the analysis of structures with large, periodic assemblies of acoustic black holes could illustrate if and how fractional calculus may improve computational efficiency.

- **Extension of fractional homogenization methodologies to higher dimensional structures.** The development and application of fractional homogenization methodologies for two and three-dimensional structures, along with other structural elements such as plates or shells, would continue to further strengthen the argument for the use of fractional models in structural dynamic simulations.

In conclusion, this dissertation addressed the question "*Can fractional calculus be a potentially feasible tool for generic vibration and wave propagation analyses in discrete and continuous structures? If so, how?*". The work here argued for the versatility of fractional models and simulations for discrete and continuous heterogeneous structures by illustrating how these fractional models addressed shortcomings of model order reduction and homogenization methodologies. Future research should continue to seek the answer to the question "*Are the physics and dynamics of a structural system best represented using a fractional calculus model? If so, why?*". If the knowledge and practical applications of fractional calculus is to steadily grow, this is the next fundamental question research must answer.

REFERENCES

[1] D. Logan, *A First Course in the Finite Element Method*. Stamford, CT: Cengage Learning, 2011, ISBN: 9780495668251.

[2] J. Reddy, *Introduction to the Finite Element Method*, 4th ed. New York, NY: McGraw-Hill Education, 2018, ISBN: 9781259861918.

[3] T. Hughes, *The Finite Element Method: Linear Static and Dynamic Finite Element Analysis*. New York, NY: Dover Publications, 2003, ISBN: 9780486411811.

[4] S. Rao, *The Finite Element Method in Engineering*. Cambridge, MA: Elsevier Science, 2005, ISBN: 9780750678285.

[5] I. Koutromanos, *Fundamentals of Finite Element Analysis: Linear Finite Element Analysis*. Hoboken, NJ: Wiley, 2018, ISBN: 9781119260080.

[6] B. Besselink, U. Tabak, A. Lutowska, N. van de Wouw, H. Nijmeijer, D. Rixen, M. Hochstenbach, and W. Schilders, "A comparison of model reduction techniques from structural dynamics, numerical mathematics and systems and control," *Journal of Sound and Vibration*, vol. 332, no. 19, pp. 4403–4422, 2013. [Online]. Available: http://dx.doi.org/10.1016/j.jsv.2013.03.025.

[7] D. de Klerk, D. Rixen, and S. Voormeeren, "General framework for dynamic substructuring: History, review, and classification of techniques," *AIAA Journal*, vol. 46, no. 5, pp. 1169–1181, 2008. [Online]. Available: http://dx.doi.org/10.2514/1.33274.

[8] R. Craig and M. Bampton, "Coupling of substructures for dynamic analyses," *AIAA Journal*, vol. 6, no. 7, pp. 1313–1319, 1968. [Online]. Available: http://dx.doi.org/10.2514/3.4741.

[9] M. Allen, D. Rixen, M. van der Seijs, P. Tiso, T. Abrahamsson, and R. Mayes, *Substructuring in Engineering Dynamics: Emerging Numerical and Experimental Techniques*, ser. CISM International Centre for Mechanical Sciences. Cham, Switzerland: Springer International Publishing, 2019, ISBN: 9783030255329.

[10] W. Schilders, H. van der Vorst, and J. Rommes, *Model Order Reduction: Theory, Research Aspects and Applications*. Berlin, Germany: Springer, 2008, ISBN: 9783540788409.

[11] R. Guyan, "Reduction of stiffness and mass matrices," *AIAA Journal*, vol. 3, no. 2, pp. 380–380, 1965. DOI: 10.2514/3.2874. [Online]. Available: https://doi.org/10.2514/3.2874.

[12] O. Flodén, K. Persson, and G. Sandberg, "Reduction methods for the dynamic analysis of substructure models of lightweight building structures," *Computers & Structures*, vol. 138, pp. 49–61, 2014, ISSN: 0045-7949. [Online]. Available: https://doi.org/10.1016/j.compstruc.2014.02.011.

[13] S. Rao, *Mechanical Vibrations*, 5th ed. Indianapolis, IN: Prentice Hall, 2011, ISBN: 9780132128193.

[14] R. Craig and A. Kurdila, *Fundamentals of Structural Dynamics*, 2nd ed. Hoboken, NJ: John Wiley & Sons, 2006.

[15] R. Kuether, M. Allen, and J. Hollkamp, "Modal substructuring of geometrically nonlinear finite-element models," *AIAA Journal*, vol. 54, no. 2, pp. 691–702, 2016. [Online]. Available: http://dx.doi.org/10.2514/1.J054036.

[16] L. Manevitch, I. Andrianov, and V. Ošmjan, *Mechanics of Periodically Heterogeneous Structures*. New York, NY: Springer, 2002, ISBN: 9783540416302.

[17] Q. Qin and Q. Yang, *Macro-micro Theory on Multifield Coupling Behavior of Heterogeneous materials*. Beijing, China: Springer, 2008, ISBN: 9783642096914.

[18] A. Kalamkarov, I. Andrianov, and V. Danishevskyy, "Asymptotic homogenization of composite materials and structures," *Applied Mechanics Reviews*, vol. 62, May 2009. DOI: 10.1115/1.3090830.

[19] B. Hassani and E. Hinton, "A review of homogenization and topology optimization i—homogenization theory for media with periodic structure," *Computers & Structures*, vol. 69, no. 6, pp. 707–717, 1998, ISSN: 0045-7949. [Online]. Available: https://doi.org/10.1016/S0045-7949(98)00131-X.

[20] M. Yang, G. Ma, Y. Wu, Z. Yang, and P. Sheng, "Homogenization scheme for acoustic metamaterials," *Physical Review B*, vol. 89, no. 6, p. 064 309, 2014. DOI: 10.1103/PhysRevB.89.064309. [Online]. Available: https://link.aps.org/doi/10.1103/PhysRevB.89.064309.

[21] W. Yu and T. Tang, "Variational asymptotic method for unit cell homogenization of periodically heterogeneous materials," *International Journal of Solids and Structures*, vol. 44, no. 11, pp. 3738–3755, 2007, ISSN: 0020-7683. [Online]. Available: https://doi.org/10.1016/j.ijsolstr.2006.10.020.

[22] S. Arabnejad and D. Pasini, "Mechanical properties of lattice materials via asymptotic homogenization and comparison with alternative homogenization methods," *International Journal of Mechanical Sciences*, vol. 77, pp. 249–262, 2013, ISSN: 0020-7403. [Online]. Available: https://doi.org/10.1016/j.ijmecsci.2013.10.003.

[23] J. Mei, Z. Liu, W. Wen, and P. Sheng, "Effective dynamic mass density of composites," *Physical Review B*, vol. 76, no. 13, pp. 134 205–1, 2007, ISSN: 1098-0121. [Online]. Available: https://link.aps.org/doi/10.1103/PhysRevB.76.134205.

[24] Z. Hashin, "Analysis of composite materials—a survey," *Journal of Applied Mechanics*, vol. 50, no. 3, pp. 481–505, Sep. 1983, ISSN: 0021-8936. DOI: 10.1115/1.3167081. [Online]. Available: https://doi.org/10.1115/1.3167081.

[25] M. Alger, *Polymer Science Dictionary*. Dordrecht, Netherlands: Springer Netherlands, 1996, ISBN: 9780412608704.

[26] D. Askeland and W. Wright, *Science and Engineering of Materials, SI Edition*. London: Cengage Learning, 2015, ISBN: 9781305446335.

[27] R. Craster, J. Kaplunov, and A. Pichugin, "High-frequency homogenization for periodic media," *Proceedings of the Royal Society A: Mathematical, Physical and Engineering Sciences*, vol. 466, no. 2120, pp. 2341–2362, 2010. DOI: 10.1098/rspa.2009.0612.

[28] T. Antonakakis, R. Craster, S. Guenneau, and J. Kaplunov, "High frequency homogenization: Going from the microscale to the macroscale," in *Proceedings of the 9th International Conference on Structural Dynamics, EURODYN*, Porto, Portugal, 2014, pp. 3413–3416, ISBN: 9789727521654. [Online]. Available: https://paginas.fe.up.pt/~eurodyn2014/CD/papers/478_MS23_ABS_1079.pdf.

[29] T. Antonakakis, R. Craster, and S. Guenneau, "High-frequency homogenization of zero-frequency stop band photonic and phononic crystals," *New Journal of Physics*, vol. 15, no. 10, pp. 103 014–103 014, 2013, ISSN: 1367-2630. [Online]. Available: http://stacks.iop.org/1367-2630/15/i=10/a=103014.

[30] R. Bagley and P. Torvik, "A theoretical basis for the application of fractional calculus to viscoelasticity," *Journal of Rheology*, vol. 27, no. 3, pp. 201–10, 1983, ISSN: 0148-6055. [Online]. Available: http://dx.doi.org/10.1122/1.549724.

[31] P. Torvik and R. Bagley, "On the appearance of the fractional derivative in the behavior of real materials," *Journal of Applied Mechanics, Transactions ASME*, vol. 51, no. 2, pp. 294–298, 1984. [Online]. Available: https://doi.org/10.1115/1.3167615.

[32] A. Chatterjee, "Statistical origins of fractional derivatives in viscoelasticity," *Journal of Sound and Vibration*, vol. 284, no. 3-5, pp. 1239–1245, 2005. [Online]. Available: https://doi.org/10.1016/j.jsv.2004.09.019.

[33] F. Mainardi, *Fractional Calculus And Waves In Linear Viscoelasticity: An Introduction To Mathematical Models*. San Diego, CA: World Scientific Publishing Company, 2010, ISBN: 9781908978578.

[34] A. Wharmby and R. Bagley, "Generalization of a theoretical basis for the application of fractional calculus to viscoelasticity," *Journal of Rheology*, vol. 57, no. 5, pp. 1429–1440, 2013. [Online]. Available: http://dx.doi.org/10.1122/1.4819083.

[35] B. Narahari Achar and J. Hanneken, "Microscopic formulation of fractional calculus theory of viscoelasticity based on lattice dynamics," *Physica Scripta Volume T*, vol. 2009, no. T136, pp. 014 011–014 018, 2009. [Online]. Available: stacks.iop.org/PhysScr/T136/014011.

[36] D. Benson, S. Wheatcraft, and M. Meerschaert, "Application of a fractional advection-dispersion equation," *Water resources research*, vol. 36, no. 6, pp. 1403–1412, 2000. [Online]. Available: https://inside.mines.edu/~dbenson/current/2000WR900031.pdf.

[37] Z. Fellah, M. Fellah, and C. Depollier, "Transient wave propagation in inhomogeneous porous materials: Application of fractional derivatives," *Signal Processing*, vol. 86, no. 10, pp. 2658–2667, 2006. [Online]. Available: http://dx.doi.org/10.1016/j.sigpro.2006.02.014.

[38] W. Chen and S. Holm, "Modified Szabo's wave equation models for lossy media obeying frequency power law," *The Journal of the Acoustical Society of America*, vol. 114, no. 5, pp. 2570–2574, 2003. DOI: 10.1121/1.1621392.

[39] S. Buonocore, M. Sen, and F. Semperlotti, "Occurrence of anomalous diffusion and non-local response in highly-scattering acoustic periodic media," *New Journal of Physics*, vol. 21, no. 3, p. 033 011, 2019. DOI: 10.1088/1367-2630/aafb7d. [Online]. Available: https://doi.org/10.1088/1367-2630/aafb7d.

[40] G. Casasanta and R. Garra, "Fractional calculus approach to the acoustic wave propagation with space-dependent sound speed," *Signal, Image and Video Processing*, vol. 6, no. 3, pp. 389–392, 2012. DOI: 10.1007/s11760-012-0314-4.

[41] V. Tarasov, "Acoustic waves in fractal media: Non-integer dimensional spaces approach," *Wave Motion*, vol. 63, pp. 18–22, 2016. [Online]. Available: http://dx.doi.org/10.1016/j.wavemoti.2016.01.003.

[42] F. Riewe, "Mechanics with fractional derivatives," *Physical Review E*, vol. 55, no. 3, p. 3581, 1997. [Online]. Available: https://doi.org/10.1103/PhysRevE.55.3581.

[43] O. Agrawal, "Fractional variational calculus in terms of Riesz fractional derivatives," *Journal of Physics A: Mathematical and Theoretical*, vol. 40, no. 24, p. 6287, 2007. DOI: 10.1088/1751-8113/40/24/003.

[44] Y. Rossikhin and M. Shitikova, "Application of fractional calculus for dynamic problems of solid mechanics: Novel trends and recent results," *Applied Mechanics Reviews*, vol. 63, no. 1, p. 010 801, 2010. [Online]. Available: https://doi.org/10.1115/1.4000563.

[45] V. Tarasov, "Review of some promising fractional physical models," *International Journal of Modern Physics B*, vol. 27, no. 09, p. 1 330 005, 2013. [Online]. Available: https://doi.org/10.1142/S0217979213300053.

[46] T. Atanackovic, S. Pilipovic, B. Stankovic, and D. Zorica, *Fractional Calculus with Applications in Mechanics: Vibrations and Diffusion Processes*, ser. ISTE. Hoboken, NJ: Wiley, 2014, ISBN: 9781118577462.

[47] T. Atanackovic, S. Pilipovic, B. Stankovic, and D. Zorica, *Fractional Calculus with Applications in Mechanics: Wave Propagation, Impact and Variational Principles*, ser. ISTE. Hoboken, NJ: Wiley, 2014, ISBN: 9781118909133.

[48] K. Lazopoulos, "Non-local continuum mechanics and fractional calculus," *Mechanics Research Communications*, vol. 33, no. 6, pp. 753–757, 2006. [Online]. Available: https://doi.org/10.1016/j.mechrescom.2006.05.001.

[49] G. Cottone, M. Di Paola, and M. Zingales, "Fractional mechanical model for the dynamics of non-local continuum," in *Advances in Numerical Methods*, Springer, 2009, pp. 389–423. [Online]. Available: https://link.springer.com/chapter/10.1007/978-0-387-76483-2_33.

[50] G. Cottone, M. Di Paola, and M. Zingales, "Elastic waves propagation in 1d fractional non-local continuum," *Physica E: Low-dimensional Systems and Nanostructures*, vol. 42, no. 2, pp. 95–103, 2009. [Online]. Available: https://doi.org/10.1016/j.physe.2009.09.006.

[51] A. Carpinteri, P. Cornetti, and A. Sapora, "A fractional calculus approach to nonlocal elasticity," *The European Physical Journal Special Topics*, vol. 193, no. 1, p. 193, 2011. [Online]. Available: https://doi.org/10.1140/epjst/e2011-01391-5.

[52] W. Sumelka, "Thermoelasticity in the framework of the fractional continuum mechanics," *Journal of Thermal Stresses*, vol. 37, no. 6, pp. 678–706, 2014. [Online]. Available: https://doi.org/10.1080/01495739.2014.885332.

[53] H. Sheng, H. Sun, C. Coopmans, Y. Chen, and G. Bohannan, "A physical experimental study of variable-order fractional integrator and differentiator," *The European Physical Journal Special Topics*, vol. 193, no. 1, pp. 93–104, Mar. 2011, ISSN: 1951-6401. DOI: 10.1140/epjst/e2011-01384-4. [Online]. Available: https://doi.org/10.1140/epjst/e2011-01384-4.

[54] L. Liu, F. Pan, and D. Xue, "Variable-order fuzzy fractional pid controller," *ISA Transactions*, vol. 55, pp. 227–233, 2015, ISSN: 0019-0578. [Online]. Available: https://doi.org/10.1016/j.isatra.2014.09.012.

[55] R. Magin, "Fractional calculus in bioengineering, part 1," *Critical Reviews in Biomedical Engineering*, vol. 32, no. 1, 2004. DOI: 10.1615/CritRevBiomedEng.v32.i1.10.

[56] R. Magin, "Fractional calculus in bioengineering, part 2," *Critical Reviews in Biomedical Engineering*, vol. 32, no. 2, 2004. DOI: 10.1615/critrevbiomedeng.v32.i2.10.

[57] R. Magin, "Fractional calculus in bioengineering, part3," *Critical Reviews in Biomedical Engineering*, vol. 32, no. 3&4, 2004. DOI: 10.1615/critrevbiomedeng.v32.i34.10.

[58] A. Carpinteri and F. Mainardi, *Fractals and fractional calculus in continuum mechanics*. London: Springer, 1997, ISBN: 9783211829134.

[59] A. Carpinteri, B. Chiaia, and P. Cornetti, "The elastic problem for fractal media: Basic theory and finite element formulation," *Computers & Structures*, vol. 82, no. 6, pp. 499–508, 2004, ISSN: 0045-7949. [Online]. Available: https://doi.org/10.1016/j.compstruc.2003.10.014.

[60] J. Li and M. Ostoja-Starzewski, "Fractal solids, product measures and fractional wave equations," *Proceedings of the Royal Society : Mathematical, Physical and Engineering Sciences*, vol. 465, no. 2108, pp. 2521–2536, 2009, ISSN: 1364-5021. [Online]. Available: http://rspa.royalsocietypublishing.org/content/465/2108/2521.

[61] I. Podlubny, *Fractional Differential Equations An Introduction to Fractional Derivatives, Fractional Differential Equations, to Methods of Their Solution and Some of Their Applications*. New York, NY: Academic Press, 1999, ISBN: 9780080531984.

[62] R. Herrmann, *Fractional Calculus: An Introduction for Physicists*, 2nd ed. New Jersey: World Scientific Publishing Company, 2014, ISBN: 9789814551090.

[63] K. Diethelm, *The Analysis of Fractional Differential Equations*. New York, NY: Springer, 2004, ISBN: 9783642145742.

[64] S. Samko, A. Kilbas, and O. Marichev, *Fractional Integrals and Derivatives*. New York, NY: Taylor & Francis, 1993, ISBN: 9782881248641.

[65] R. Hilfer, *Applications Of Fractional Calculus In Physics*. London: World Scientific Publishing Company, 2000, ISBN: 9789814496209.

[66] N. Heymans and I. Podlubny, "Physical interpretation of initial conditions for fractional differential equations with riemann-liouville fractional derivatives," *Rheol. Acta*, vol. 45, pp. 765–771, 2006. [Online]. Available: https://doi.org/10.1007/s00397-005-0043-5.

[67] E. Sousa, "How to approximate the fractional derivative of order $1 < \alpha \leq 2$," *International Journal of Bifurcation and Chaos in Applied Sciences and Engineering*, vol. 22, no. 4, pp. 1 250 075–1 250 075, 2012, ISSN: 0218-1274. [Online]. Available: https://doi.org/10.1142/S0218127412500757.

[68] C. Li and F. Zeng, *Numerical Methods for Fractional Calculus*, ser. Chapman & Hall/CRC Numerical Analysis and Scientific Computing Series. Bota Raton, FL: CRC Press, 2015, ISBN: 9781482253818.

[69] Y. Povstenko, *Linear Fractional Diffusion-Wave Equation for Scientists and Engineers*. New York, NY: Springer International Publishing, 2015, ISBN: 9783319179544.

[70] H. Wang J.and Li, "Surpassing the fractional derivative: Concept of the memory-dependent derivative," *Computers and Mathematics with Applications*, vol. 62, no. 3, pp. 1562–1567, 2011, ISSN: 0898-1221. [Online]. Available: https://doi.org/10.1016/j.camwa.2011.04.028.

[71] V. Tarasova and V. Tarasov, "Fractional dynamics of natural growth and memory effect in economics," *European Research*, vol. 23, pp. 30–37, Dec. 2016. DOI: 10.20861/2410-2873-2016-23-004.

[72] H. Sun, W. Chen, and H. Wei, "A comparative study of constant-order and variable-order fractional models in characterizing memory property of systems," *Eur. Phys. J. Spec. Top.*, vol. 193, p. 185, 2011. [Online]. Available: https://doi.org/10.1140/epjst/e2011-01390-6.

[73] B. El Said, D. Ivanov, A. Long, and S. Hallett, "Multi-scale modelling of strongly heterogeneous 3d composite structures using spatial voronoi tessellation," *Journal of the Mechanics and Physics of Solids*, vol. 88, pp. 50–71, 2016, ISSN: 0022-5096. [Online]. Available: https://doi.org/10.1016/j.jmps.2015.12.024.

[74] B. Narahari Achar, J. Hanneken, and T. Clarke, "Damping characteristics of a fractional oscillator," *Physica A*, vol. 339, no. 3-4, pp. 311–19, 2004. [Online]. Available: http://dx.doi.org/10.1016/j.physa.2004.03.030.

[75] Y. Ryabov and A. Puzenko, "Damped oscillations in view of the fractional oscillator equation," *Physical Review B (Condensed Matter and Materials Physics)*, vol. 66, no. 18, pp. 184 201–1, 2002. [Online]. Available: http://dx.doi.org/10.1103/PhysRevB.66.184201.

[76] A. Tofighi, "The intrinsic damping of the fractional oscillator," *Physica A*, vol. 329, no. 1-2, pp. 29–34, 2003, ISSN: 0378-4371. [Online]. Available: http://dx.doi.org/10.1016/S0378-4371(03)00598-3.

[77] M. Meerschaert and R. McGough, "Attenuated fractional wave equations with anisotropy," *Journal of Vibration & Acoustics.*, vol. 136, no. 5, 2014, ISSN: 0739-3717. [Online]. Available: http://doi.org/10.1115/1.4025940.

[78] E. Love, "Fractional derivatives of imaginary order," *J. London Math. Soc.*, vol. 3, no. 2, pp. 241–259, 1971. [Online]. Available: https://doi.org/10.1112/jlms/s2-3.2.241.

[79] M. Ortigueira, L. Rodriguez-Germa, and J. Trujillo, "Complex grunwald-letnikov, liouville, riemann-liouville, and caputo derivatives for analytic functions," *Communications in Nonlinear Science and Numerical Simulation*, vol. 16, no. 11, pp. 4174–4182, 2011. [Online]. Available: http://dx.doi.org/10.1016/j.cnsns.2011.02.022.

[80] B. Ross and F. Northover, "A use of a derivative of complex order in the fractional calculus," *Indian J. Pure Appl. Math.*, vol. 9, no. 4, pp. 400–406, 1978. [Online]. Available: https://insa.nic.in/writereaddata/UpLoadedFiles/IJPAM/20005a85_400.pdf.

[81] Andriambololona, Tokiniaina, and Rakotoson, "Definitions of complex order integrals and complex order derivatives using operator approach," *International Journal of Latest Research in Science and Technology*, vol. 1, no. 4, pp. 317–323, 2012. [Online]. Available: https://arxiv.org/ftp/arxiv/papers/1209/1209.0400.pdf.

[82] D. Valerio and J. Sa Da Costa, "Variable-order fractional derivatives and their numerical approximations," *Signal Processing*, vol. 91, no. 3, pp. 470–483, 2011. [Online]. Available: http://dx.doi.org/10.1016/j.sigpro.2010.04.006.

[83] T. Atanackovi, S. Konjik, S. Pilipovi, and D. Zorica, "Complex order fractional derivatives in viscoelasticity," *Mechanics of Time-Dependent Materials*, vol. 20, no. 2, pp. 175–195, 2016. [Online]. Available: http://dx.doi.org/10.1007/s11043-016-9290-3.

[84] N. Makris and M. Constantinou, "Models of viscoelasticity with complex-order derivatives," *Journal of Engineering Mechanics*, vol. 119, no. 7, pp. 1453–1464, 1993. [Online]. Available: https://doi.org/10.1061/(ASCE)0733-9399(1993)119:7(1453).

[85] C. Lorenzo and T. Hartley, "Variable order and distributed order fractional operators," *Nonlinear Dynamics*, vol. 29, no. 1, pp. 57–98, Jul. 2002, ISSN: 1573-269X. DOI: 10.1023/A:1016586905654. [Online]. Available: https://doi.org/10.1023/A:1016586905654.

[86] S. Patnaik, J. Hollkamp, and F. Semperlotti, "Applications of variable-order fractional operators: A review," *Proceedings of the Royal Society A: Mathematical, Physical and Engineering Sciences*, vol. 476, no. 2234, p. 20 190 498, 2020. DOI: 10.1098/rspa.2019.0498. [Online]. Available: https://royalsocietypublishing.org/doi/abs/10.1098/rspa.2019.0498.

[87] C. Coimbra, "Mechanics with variable-order differential operators," *Annalen der Physik*, vol. 12, no. 11-12, pp. 692–703, 2003. DOI: 10.1002/andp.200310032. [Online]. Available: https://onlinelibrary.wiley.com/doi/abs/10.1002/andp.200310032.

[88] D. Ingman and J. Suzdalnitsky, "Response of viscoelastic plate to impact," *Journal of Vibration and Acoustics*, vol. 130, no. 1, p. 011 010, Sep. 2008. [Online]. Available: https://doi.org/10.1115/1.2731416.

[89] M. Di Paola, J. Reddy, and E. Ruocco, "On the application of fractional calculus for the formulation of viscoelastic reddy beam," *Meccanica*, vol. 55, pp. 1365–1378, 2020. [Online]. Available: https://doi.org/10.1007/s11012-020-01177-3.

[90] L. Ramirez and C. Coimbra, "A variable order constitutive relation for viscoelasticity," *Annalen der Physik*, vol. 16, no. 7-8, pp. 543–552, 2007. DOI: 10.1002/andp.200710246. [Online]. Available: https://onlinelibrary.wiley.com/doi/abs/10.1002/andp.200710246.

[91] S. Park, "Analytical modeling of viscoelastic dampers for structural and vibration control," *International Journal of Solids and Structures*, vol. 38, no. 44-45, pp. 8065–8092, 2001. [Online]. Available: http://dx.doi.org/10.1016/S0020-7683(01)00026-9.

[92] D. Ingman and J. Suzdalnitsky, "Control of damping oscillations by fractional differential operator with time-dependent order," *Computer Methods in Applied Mechanics and Engineering*, vol. 193, no. 52, pp. 5585–5595, 2004, ISSN: 0045-7825. [Online]. Available: https://doi.org/10.1016/j.cma.2004.06.029.

[93] C. Soon, C. Coimbra, and M. Kobayashi, "The variable viscoelasticity oscillator," *Annalen der Physik*, vol. 14, no. 6, pp. 378–389, 2005. DOI: 10.1002/andp.200410140. [Online]. Available: https://onlinelibrary.wiley.com/doi/abs/10.1002/andp.200410140.

[94] S. Sakakibara, "Properties of vibration with fractional derivative damping of order 1 / 2," *JSME International Journal Series C*, vol. 40, no. 3, pp. 393–399, 1997. DOI: 10.1299/jsmec.40.393.

[95] F. Mainardi, "Fractional relaxation-oscillation and fractional diffusion-wave phenomena," *Chaos, Solitons & Fractals*, vol. 7, no. 9, pp. 1461–1477, 1996. [Online]. Available: https://doi.org/10.1016/0960-0779(95)00125-5.

[96] R. Gorenflo and R. Rutman, "On ultraslow and intermediate processes, transform methods & special functions," *Sofia'94, Proc. of Intern. Workshop*, pp. 61–81, Jan. 1994. [Online]. Available: https://www.researchgate.net/publication/292002712_On_ultraslow_and_intermediate_processes_Transform_Methods_Special_Functions.

[97] B. Narahari Achar, J. Hanneken, and T. Clarke, "Response characteristics of a fractional oscillator," *Physica A*, vol. 309, no. 3-4, pp. 275–288, 2002, ISSN: 0378-4371. [Online]. Available: http://dx.doi.org/10.1016/S0378-4371(02)00609-X.

[98] A. Stanislavsky, "Fractional oscillator," *Physical Review E (Statistical, Nonlinear, and Soft Matter Physics)*, vol. 70, no. 5, pp. 51 103–1, 2004. [Online]. Available: http://dx.doi.org/10.1103/PhysRevE.70.051103.

[99] K. Fa, "Fractional ornstein–uhlenbeck noise," *Annals of Physics*, vol. 393, pp. 327–334, 2018, ISSN: 0003-4916. [Online]. Available: https://doi.org/10.1016/j.aop.2018.04.019.

[100] K. Fa, "Effect of the fractional oscillator noise in the overdamped linear oscillator with the presence of a periodic force," *Physica Scripta*, vol. 95, no. 2, p. 025 004, Dec. 2019. DOI: 10.1088/1402-4896/ab41e4.

[101] G. Bohannan and B. Knauber, "A physical experimental study of the fractional harmonic oscillator," in *2015 IEEE International Symposium on Circuits and Systems (ISCAS)*, 2015, pp. 2341–2344. DOI: 10.1109/ISCAS.2015.7169153.

[102] F. Zeng, "Second-order stable finite difference schemes for the time-fractional diffusion-wave equation," *Journal of Scientific Computing*, vol. 65, Jul. 2014. DOI: 10.1007/s10915-014-9966-2.

[103] M. Heydari, Z. Avazzadeh, and M. Haromi, "A wavelet approach for solving multi-term variable-order time fractional diffusion-wave equation," *Applied Mathematics and Computation*, vol. 341, pp. 215–228, 2019, ISSN: 0096-3003. [Online]. Available: https://doi.org/10.1016/j.amc.2018.08.034.

[104] O. Agrawal, "Solution for a fractional diffusion-wave equation defined in a bounded domain," *Nonlinear Dynamics*, vol. 29, pp. 145–155, 2002. [Online]. Available: https://doi.org/10.1023/A:1016539022492.

[105] K. Sakamoto and M. Yamamoto, "Initial value/boundary value problems for fractional diffusion-wave equations and applications to some inverse problems," *Journal of Mathematical Analysis and Applications*, vol. 382, no. 1, pp. 426–447, 2011, ISSN: 0022-247X. [Online]. Available: https://doi.org/10.1016/j.jmaa.2011.04.058.

[106] R. Du, W. Cao, and Z. Sun, "A compact difference scheme for the fractional diffusion-wave equation," *Applied Mathematical Modelling*, vol. 34, no. 10, pp. 2998–3007, 2010, ISSN: 0307-904X. [Online]. Available: https://doi.org/10.1016/j.apm.2010.01.008.

[107] J. Chen, F. Liu, V. Anh, S. Shen, Q. Liu, and C. Liao, "The analytical solution and numerical solution of the fractional diffusion-wave equation with damping," *Applied Mathematics and Computation*, vol. 219, no. 4, pp. 1737–1748, 2012, ISSN: 0096-3003. [Online]. Available: https://doi.org/10.1016/j.amc.2012.08.014.

[108] F. Mainardi, "The time fractional diffusion-wave equation," *Radiophys Quantum Electron*, vol. 38, pp. 13–24, 1995. [Online]. Available: https://doi.org/10.1007/BF01051854.

[109] A. Choudhary, D. Kumar, and J. Singh, "A fractional model of fluid flow through porous media with mean capillary pressure," *Journal of the Association of Arab Universities for Basic and Applied Sciences*, vol. 21, pp. 59–63, 2016, ISSN: 1815-3852. [Online]. Available: https://doi.org/10.1016/j.jaubas.2015.01.002.

[110] T. Szabo, "Time domain wave equations for lossy media obeying a frequency power law," *The Journal of the Acoustical Society of America*, vol. 96, no. 1, pp. 491–500, 1994. DOI: 10.1121/1.410434. [Online]. Available: https://doi.org/10.1121/1.410434.

[111] W. Chen, S. Hu, and W. Cai, "A causal fractional derivative model for acoustic wave propagation in lossy media," *Arch. Appl. Mech.*, vol. 86, pp. 529–539, 2016. [Online]. Available: https://doi.org/10.1007/s00419-015-1043-2.

[112] S. Patnaik and F. Semperlotti, "A generalized fractional-order elastodynamic theory for nonlocal attenuating media," *Proceedings of the Royal Society A: Mathematical, Physical and Engineering Sciences*, vol. 476, no. 2238, p. 20 200 200, 2020. DOI: 10.1098/rspa.2020.0200. [Online]. Available: https://royalsocietypublishing.org/doi/abs/10.1098/rspa.2020.0200.

[113] S. Patnaik, S. Sidhardh, and F. Semperlotti, "A ritz-based finite element method for a fractional-order boundary value problem of nonlocal elasticity," *International Journal of Solids and Structures*, vol. 202, pp. 398–417, 2020. [Online]. Available: https://doi.org/10.1016/j.ijsolstr.2020.05.034.

[114] B. Treeby and B. Cox, "Modeling power law absorption and dispersion in viscoelastic solids using a split-field and the fractional laplacian," *The Journal of the Acoustical Society of America*, vol. 136, no. 4, pp. 1499–1510, 2014. DOI: 10.1121/1.4894790. [Online]. Available: https://doi.org/10.1121/1.4894790.

[115] X. Zhao and R. McGough, "Time-domain analysis of power law attenuation in space-fractional wave equations," *The Journal of the Acoustical Society of America*, vol. 144, no. 1, pp. 467–477, 2018. DOI: 10.1121/1.5047670. [Online]. Available: https://doi.org/10.1121/1.5047670.

[116] T. Atanackovic, M. Janev, L. Oparnica, S. Pilipovic, and D. Zorica, "Space-time fractional zener wave equation," *Proceedings of the Royal Society A: Mathematical, Physical and Engineering Sciences*, vol. 471, no. 2174, p. 20 140 614, 2015. DOI: 10.1098/rspa.2014.0614. [Online]. Available: https://royalsocietypublishing.org/doi/abs/10.1098/rspa.2014.0614.

[117] N. Engheta and R. Ziolkowski, *Metamaterials: Physics and Engineering Explorations*. Hoboken, NJ: Wiley, 2006, ISBN: 9780471784180.

[118] P. Pai and G. Huang, *Theory and Design of Acoustic Metamaterials*. Bellingham, WA: SPIE, 2015, ISBN: 9781628418354.

[119] P. Deymier, *Acoustic Metamaterials and Phononic Crystals*. New York, NY: Springer, 2013, ISBN: 9783642312328.

[120] J. Hollkamp, M. Sen, and F. Semperlotti, "Model-order reduction of lumped parameter systems via fractional calculus," *Journal of Sound & Vibration*, vol. 419, pp. 526–543, 2018, ISSN: 0022-460X. [Online]. Available: https://doi.org/10.1016/j.jsv.2018.01.011.

[121] R. Lin and T. Ng, "Development of a theoretical framework for vibration analysis of the class of problems described by fractional derivatives," *Mechanical Systems and Signal Processing*, vol. 116, pp. 78–96, 2019, ISSN: 0888-3270. [Online]. Available: https://doi.org/10.1016/j.ymssp.2018.06.020.

[122] R. Lin and T. Ng, "Eigenvalue and eigenvector derivatives of fractional vibration systems," *Mechanical Systems and Signal Processing*, vol. 127, pp. 423–440, 2019, ISSN: 0888-3270. [Online]. Available: https://doi.org/10.1016/j.ymssp.2019.03.014.

[123] J. Hollkamp, M. Sen, and F. Semperlotti, "Analysis of dispersion and propagation properties in a periodic rod using a space-fractional wave equation," *Journal of Sound and Vibration*, vol. 441, pp. 204–220, 2019, ISSN: 0022-460X. [Online]. Available: https://doi.org/10.1016/j.jsv.2018.10.051.

[124] R. Garrappa, "Numerical evaluation of two and three parameter mittag-leffler functions," *SIAM Journal on Numerical Analysis*, vol. 53, no. 3, pp. 1350–1369, 2015, ISSN: 00361429. [Online]. Available: http://dx.doi.org/10.1137/140971191.

[125] R. Garrappa, *The mittag-leffler function*, MATLAB Central File Exchange, file ID: 48154, 2015. [Online]. Available: https://www.mathworks.com/matlabcentral/fileexchange/48154-the-mittag-leffler-function.

[126] I. Podlubny, *The matlab mlf code*, MATLAB Central File Exchange, file ID: 8738, 2012. [Online]. Available: https://www.mathworks.com/matlabcentral/fileexchange/8738-mittag-leffler-function.

[127] D. Valerio and J. Sa da Costa, "Fractional derivatives and their numerical approximations ii: " complex orders," in *Symposium on Fractional Signals and Systems*, Lisbon, Portugal, 2009. [Online]. Available: http://web.ist.utl.pt/duarte.valerio/FSS2009I.pdf.

[128] J. L. Adams, T. T. Hartley, and C. F. Lorenzo, "Complex order-distributions using conjugated order differintegrals," in *Advances in Fractional Calculus: Theoretical Developments and Applications in Physics and Engineering*, J. Sabatier, O. P. Agrawal, and J. A. T. Machado, Eds. Dordrecht: Springer Netherlands, 2007, pp. 347–360, ISBN: 978-1-4020-6042-7. DOI: 10.1007/978-1-4020-6042-7_24. [Online]. Available: https://doi.org/10.1007/978-1-4020-6042-7_24.

[129] G. Franklin, J. Powell, and A. Emami-Naeini, *Feedback Control of Dynamic Systems*, 7th ed. Indianapolis, IN: Pearson, 2015, ISBN: 9780133496598.

[130] J. Juang and M. Phan, *Identification and Control of Mechanical Systems*. Cambridge, UK: Cambridge University Press, 2001, ISBN: 9781139430111.

[131] R. Isermann and M. Munchhof, *Identification of Dynamic Systems*. New York, NY: Springer, 2011, ISBN: 9783540788782.

[132] A. Di Matteo, F. Lo Iacono, G. Navarra, and A. Pirrotta, "Innovative modeling of tuned liquid column damper motion," *Communications in nonlinear science and numerical simulation*, vol. 23, no. 1, pp. 229–244, 2015, ISSN: 1007-5704. [Online]. Available: https://doi.org/10.1016/j.cnsns.2014.11.005.

[133] K. Graff, *Wave Motion in Elastic Solids*. New York, NY: Dover Publications, 1991, ISBN: 9780486667454.

[134] J. Doyle, *Wave Propagation in Structures: Spectral Analysis Using Fast Discrete Fourier Transforms*. New York, NY: Springer, 1997, ISBN: 9780387949406.

[135] L. Brillouin, *Wave Propagation in Periodic Structures: Electric Filters and Crystal Lattices*. Mineola, NY: Dover Publications, 1953, ISBN: 9780486600345.

[136] R. Gorenflo, A. A. Kilbas, F. Mainardi, and S. V. Rogosin, *Mittag-Leffler Functions, Related Topics and Applications*. Berlin, Germany: Springer Publishing Company, 2014, ISBN: 9783662439296.

[137] J. Berryman, "Effective medium theories for multicomponent poroelastic composites," *Journal of Engineering Mechanics*, vol. 132, no. 5, pp. 519–531, 2006, ISSN: 0733-9399. [Online]. Available: https://doi.org/10.1061/(ASCE)0733-9399(2006)132:5(519).

[138] J. Duan, Z. Wang, Y. Liu, and X. Qiu, "Eigenvalue problems for fractional ordinary differential equations," *Chaos, Solitons, and Fractals*, vol. 46, pp. 46–53, 2013, ISSN: 0960-0779. [Online]. Available: https://doi.org/10.1016/j.chaos.2012.11.004.

[139] Y. Wu, J. Li, Z. Zhang, and C. Chan, "Effective medium theory for magnetodielectric composites: Beyond the long-wavelength limit," *Physical Review B*, vol. 74, no. 8, pp. 85 111–1, 2006, ISSN: 1098-0121. [Online]. Available: https://link.aps.org/doi/10.1103/PhysRevB.74.085111.

[140] R. Garrappa and M. Popolizio, "Computing the matrix mittag-leffler function with applications to fractional calculus," *Journal of Scientific Computing*, pp. 1–25, 2018, ISSN: 0885-7474. [Online]. Available: https://doi.org/10.1007/s10915-018-0699-5.

[141] S. Patnaik, S. Sidhardh, and F. Semperlotti, "Towards a unified approach to nonlocal elasticity via fractional-order mechanics," *International Journal of Mechanical Sciences*, vol. 189, p. 105 992, 2021, ISSN: 0020-7403. [Online]. Available: https://doi.org/10.1016/j.ijmecsci.2020.105992.

[142] A. Eringen and D. Edelen, "On nonlocal elasticity," *International journal of engineering science*, vol. 10, no. 3, pp. 233–248, 1972. [Online]. Available: https://doi.org/10.1016/0020-7225(72)90039-0.

[143] L. Andersen, S. Nielsen, and P. Kirkegaard, "Finite element modelling of infinite euler beams on kelvin foundations exposed to moving loads in convected co-ordinates," *Journal of Sound and Vibration*, vol. 241, no. 4, pp. 587–604, 2001. DOI: 10.1006/jsvi.2000.3314.

[144] J. Hollkamp and F. Semperlotti, "Application of fractional order operators to the simulation of ducts with acoustic black hole terminations," *Journal of Sound and Vibration*, vol. 465, p. 115 035, 2020, ISSN: 0022-460X. [Online]. Available: https://doi.org/10.1016/j.jsv.2019.115035.

[145] M. Mironov, "Propagation of a flexural wave in a plate whose thickness decreases smoothly to zero in a finite interval," *Sov. Phys. Acoust.*, vol. 34, no. 3, pp. 318–319, 1988. [Online]. Available: https://www.scopus.com/record/display.uri?eid=2-s2.0-3042686028&origin=inward.

[146] M. Mironov, "Exact solutions of equation of transverse vibrations for a bar with a specific cross section variation law," *Acoust. Phys.*, vol. 63, pp. 1–6, 2017. [Online]. Available: https://doi.org/10.1134/S1063771016060129.

[147] V. Krylov and F. Tilman, "Acoustic 'black holes' for flexural waves as effective vibration dampers," *Journal of Sound and Vibration*, vol. 274, no. 3, pp. 605–619, 2004, ISSN: 0022-460X. [Online]. Available: https://doi.org/10.1016/j.jsv.2003.05.010.

[148] V. Krylov, "Acoustic black holes: Recent developments in the theory and applications," *IEEE Transactions on Ultrasonics, Ferroelectrics, and Frequency Control*, vol. 61, no. 8, pp. 1296–1306, Aug. 2014, ISSN: 0885-3010. DOI: 10.1109/TUFFC.2014.3036. [Online]. Available: https://ieeexplore.ieee.org/document/6863850?arnumber=6863850.

[149] V. Krylov, "Acoustic black holes for flexural waves: A smart approach to vibration damping," *Procedia Engineering*, vol. 199, pp. 56–61, 2017, X International Conference on Structural Dynamics, EURODYN 2017, ISSN: 1877-7058. [Online]. Available: https://doi.org/10.1016/j.proeng.2017.09.150.

[150] V. Krylov and R. Winward, "Experimental investigation of the acoustic black hole effect for flexural waves in tapered plates," *Journal of Sound and Vibration*, vol. 300, no. 1, pp. 43–49, 2007, ISSN: 0022-460X. [Online]. Available: https://doi.org/10.1016/j.jsv.2006.07.035.

[151] V. Krylov, "New type of vibration dampers utilising the effect of acoustic black holes," *Acta Acustica United With Acustica*, vol. 90, no. 5, pp. 830–7, 2004, ISSN: 1610-1928. [Online]. Available: https://www.researchgate.net/publication/233521336_New_type_of_vibration_dampers_utilising_the_effect_of_acoustic_'black_holes'.

[152] D. O'Boy, V. Krylov, and V. Kralovic, "Damping of flexural vibrations in rectangular plates using the acoustic black hole effect," *Journal of Sound and Vibration*, vol. 329, no. 22, pp. 4672–4688, 2010, ISSN: 0022-460X. [Online]. Available: https://doi.org/10.1016/j.jsv.2010.05.019.

[153] D. O'Boy and V. Krylov, "Damping of flexural vibrations in circular plates with tapered central holes," *Journal of Sound and Vibration*, vol. 330, no. 10, pp. 2220–2236, 2011, Dynamics of Vibro-Impact Systems, ISSN: 0022-460X. [Online]. Available: https://doi.org/10.1016/j.jsv.2010.11.017.

[154] S. Conlon, J. Fahnline, and F. Semperlotti, "Numerical analysis of the vibroacoustic properties of plates with embedded grids of acoustic black holes," *The Journal of the Acoustic Society of America*, vol. 137, pp. 447–457, 2015. [Online]. Available: https://doi.org/10.1121/1.4904501.

[155] H. Zhu and F. Semperlotti, "Phononic thin plates with embedded acoustic black holes," *Phys. Rev. B*, vol. 91, p. 104 304, 10 Mar. 2015. DOI: 10.1103/PhysRevB.91.104304. [Online]. Available: https://link.aps.org/doi/10.1103/PhysRevB.91.104304.

[156] H. Zhu and F. Semperlotti, "Two-dimensional structure-embedded acoustic lenses based on periodic acoustic black holes," *Journal of Applied Physics*, vol. 122, no. 6, p. 065 104, 2017. DOI: 10.1063/1.4998524. [Online]. Available: https://doi.org/10.1063/1.4998524.

[157] L. Zhao and F. Semperlotti, "Embedded acoustic black holes for semi-passive broadband vibration attenuation in thin-walled structures," *Journal of Sound and Vibration*, vol. 388, pp. 42–52, 2017, ISSN: 0022-460X. [Online]. Available: https://doi.org/10.1016/j.jsv.2016.10.029.

[158] V. Denis, A. Pelat, C. Touzé, and F. Gautier, "Improvement of the acoustic black hole effect by using energy transfer due to geometric nonlinearity," *International Journal of Non-Linear Mechanics*, vol. 94, pp. 134–145, 2017, ISSN: 0020-7462. [Online]. Available: https://doi.org/10.1016/j.ijnonlinmec.2016.11.012.

[159] A. Pelat, F. Gautier, S. Conlon, and F. Semperlotti, "The acoustic black hole: A review of theory and applications," *Journal of Sound and Vibration*, vol. 476, p. 115 316, 2020, ISSN: 0022-460X. [Online]. Available: https://doi.org/10.1016/j.jsv.2020.115316.

[160] P. Feurtado and S. Conlon, "Wavenumber transform analysis for acoustic black hole design," *The Journal of the Acoustical Society of America*, vol. 140, no. 1, pp. 718–727, 2016. DOI: 10.1121/1.4959023. [Online]. Available: https://doi.org/10.1121/1.4959023.

[161] P. Feurtado, S. Conlon, and F. Semperlotti, "A normalized wave number variation parameter for acoustic black hole design," *The Journal of the Acoustical Society of America*, vol. 136, no. 2, EL148–EL152, 2014. DOI: 10.1121/1.4890205. [Online]. Available: https://doi.org/10.1121/1.4890205.

[162] K. Hook, J. Cheer, and S. Daley, "A parametric study of an acoustic black hole on a beam," *The Journal of the Acoustical Society of America*, vol. 145, no. 6, pp. 3488–3498, 2019. DOI: 10.1121/1.5111750. [Online]. Available: https://doi.org/10.1121/1.5111750.

[163] J. Deng, L. Zheng, O. Guasch, H. Wu, P. Zeng, and Y. Zuo, "Gaussian expansion for the vibration analysis of plates with multiple acoustic black holes indentations," *Mechanical Systems and Signal Processing*, vol. 131, pp. 317–334, 2019, ISSN: 0888-3270. [Online]. Available: https://doi.org/10.1016/j.ymssp.2019.05.024.

[164] S. Foucaud, G. Michon, Y. Gourinat, A. Pelat, and F. Gautier, "Artificial cochlea and acoustic black hole travelling waves observation: Model and experimental results," *Journal of Sound and Vibration*, vol. 333, no. 15, pp. 3428–3439, 2014, ISSN: 0022-460X. [Online]. Available: https://doi.org/10.1016/j.jsv.2014.03.016.

[165] J. Lee and W. Jeon, "Exact solution of euler-bernoulli equation for acoustic black holes via generalized hypergeometric differential equation," *Journal of Sound and Vibration*, vol. 452, pp. 191–204, 2019, ISSN: 0022-460X. [Online]. Available: https://doi.org/10.1016/j.jsv.2019.02.016.

[166] J. Lee and W. Jeon, "Vibration damping using a spiral acoustic black hole," *The Journal of the Acoustical Society of America*, vol. 141, no. 3, pp. 1437–1445, 2017. DOI: 10.1121/1.4976687. [Online]. Available: https://doi.org/10.1121/1.4976687.

[167] M. Mironov and V. Pislyakov, "One-dimensional acoustic waves in retarding structures with propagation velocity tending to zero," *Acoustical Physics*, vol. 48, no. 3, pp. 347–352, May 2002, ISSN: 1562-6865. DOI: 10.1134/1.1478121. [Online]. Available: https://doi.org/10.1134/1.1478121.

[168] O. Guasch, M. Arnela, and P. Sánchez-Martín, "Transfer matrices to characterize linear and quadratic acoustic black holes in duct terminations," *Journal of Sound and Vibration*, vol. 395, pp. 65–79, 2017, ISSN: 0022-460X. [Online]. Available: https://doi.org/10.1016/j.jsv.2017.02.007.

[169] A. El Ouahabi, V. Krylov, and D. O'Boy, "Experimental investigation of the acoustic black hole for sound absorption in air," in *Proceedings of the 22nd International Congress on Sound and Vibration*, Florence, Italy, Jul. 2015. [Online]. Available: https://www.researchgate.net/publication/282186662_Experimental_investigation_of_the_acoustic_black_hole_for_sound_absorption_in_air.

[170] A. El Ouahabi, V. Krylov, and D. O'Boy, "Investigation of the acoustic black hole termination for sound waves in cylindrical waveguides," in *INTER-NOISE and NOISE-CON Congress and Conference Proceedings, Institute of Noise Control Engineering*, San Francisco, CA, Jul. 2015. [Online]. Available: https://repository.lboro.ac.uk/articles/conference_contribution/Investigation_of_the_acoustic_black_hole_termination_for_sound_waves_propagating_in_cylindrical_waveguides/9221027.

[171] V. Krylov, "Conditions for validity of the geometrical-acoustics approximation in application to waves in an acute-angle solid wedge," *Soviet Physics - Acoustics*, vol. 35, pp. 176–180, Mar. 1989. [Online]. Available: https://repository.lboro.ac.uk/articles/journal_contribution/Conditions_for_validity_of_the_geometrical-acoustics_approximation_in_application_to_waves_in_an_acute-angle_solid_wedge/9225362.

[172] V. Krylov, *Geometrical-acoustics approach to the description of localized vibrational modes of an elastic solid wedge*, Jan. 1990. [Online]. Available: https://hdl.handle.net/2134/6176.

[173] M. Israeli and S. Orszag, "Approximation of radiation boundary conditions," *Journal of computational physics*, vol. 41, no. 1, pp. 115–135, 1981, ISSN: 0021-9991. [Online]. Available: https://doi.org/10.1016/0021-9991(81)90082-6.

[174] J. Dea, "Absorbing boundary conditions for the fractional wave equation," *Applied Mathematics and Computation*, vol. 219, no. 18, pp. 9810–9820, 2013, ISSN: 0096-3003. [Online]. Available: https://doi.org/10.1016/j.amc.2013.03.113.

[175] L. Cremer, M. Heckl, and B. Petersson, *Structure-Borne Sound: Structural Vibrations and Sound Radiation at Audio Frequencies*. New York, NY: Springer, 2005, ISBN: 9783540265146.

[176] K. Hamanaka, "Open, partial reflection and incident-absorbing boundary conditions in wave analysis with a boundary integral method," *Coastal Engineering*, vol. 30, no. 3, pp. 281–298, 1997, ISSN: 0378-3839. [Online]. Available: https://doi.org/10.1016/S0378-3839(96)00049-X.

[177] G. Mur, "Absorbing boundary conditions for the finite-difference approximation of the time-domain electromagnetic-field equations," *IEEE Transactions on Electromagnetic Compatibility*, vol. 23, no. 4, pp. 377–382, Nov. 1981, ISSN: 0018-9375. DOI: 10.1109/TEMC.1981.303970.

[178] M. Jokar, S. Patnaik, and F. Semperlotti, *Variable-order approach to nonlocal elasticity: Theoretical formulation and order identification via deep learning techniques*, 2020. arXiv: 2008.13582 [math.NA].

[179] S. Rao, *Vibration of Continuous Systems*. Hoboken, NJ: Wiley, 2019, ISBN: 9781119424147.

VITA

JOHN P. HOLLKAMP

EDUCATION

Purdue University

Ph.D. in Mechanical Engineering

May 2021

GPA: 4.00/4.00

Dissertation: "Fractional order models for vibration and wave propagation applications"
Advisor: Prof. Fabio Semperlotti

Purdue University

M.S. in Mechanical Engineering

December 2017

GPA: 4.00/4.00

Note: Received while enrolled in Direct Ph.D. program

University of Notre Dame

B.S. in Mechanical Engineering

May 2015

GPA: 3.93/4.00

Graduated Summa Cum Laude

RESEARCH INTERESTS

- Structural dynamics and vibration control

- Elastic wave propagation

- Design of periodic structures and acoustic metamaterials

- Structural acoustics and passive noise control

- Vibration modeling and simulation

- Development of mathematical models

RESEARCH EXPERIENCE

Graduate Research Assistant, Ph.D Candidate

June 2015-May 2021

Purdue University

- Developed an accurate and effective model order reduction methodology rooted in fractional order differential equations to simulate the dynamic response of non-homogeneous discrete systems

- Contributed to a study of implicit and fractional-derivative operators in infinite networks of integer-order components

- Created a fractional homogenization technique to model wave propagation in complex, heterogeneous media by studying the elastic wave propagation through a one-dimensional periodic rod and beam

- Investigated the potential of fractional order operators to develop accurate and efficient models for embedded acoustic black hole geometries in ducts and beams

- Authored an extensive and thorough review of the available applications of variable order fractional calculus in the general area of scientific and engineering modeling

WORK EXPERIENCE

Thermal Systems Design Intern

June 2014-August 2014

General Electric Aviation

- Enhanced a ticketing system for assisting engineers with thermal analysis software

- Updated and created tutorials on finite element heat transfer software

Engine Controls Intern

May 2013-August 2013

General Electric Transportation

- Investigated locomotive diesel engine problems to determine root causes of performance issues

- Analyzed data and performed tests to replicate fuel rail pressure instability in a locomotive engine

Engineering Aid

June 2010-August 2011

Air Force Research Laboratory Sensors Directorate, Wright-Patterson AFB

- Employed through the Wright Scholar program

- Tracked vehicles in video imagery to provide truth models for automatic tracking software

- Conducted calibration tests on video imaging systems

- Attended seminars and workshops on various engineering fields

TEACHING EXPERIENCE

Teaching Assistant

August 2013-December 2014

University of Notre Dame

- Served as a teaching assistant for two years for AME 20214: Introduction to Engineering Computing, an undergraduate course averaging 120 students per semester

- Assisted sophomore engineering students to develop computation skills using Fortran and Linux OS through leading extended office hours two times a week

- Graded homework and exams

HONORS AND AWARDS

- National Defense Science & Engineering Graduate Fellowship

- National Science Graduate Research Fellowship Honorable Mention

- INCE-USA paper award at NOISE-CON 2020

- Midwest Mechanics Workshop Presentation Award 3rd place

- Syndey Kelsey Excellence Prize for Structural Mechanics - University of Notre Dame

- Dean's List - University of Notre Dame

- William E. Fotsch Family Engineering Scholarship - University of Notre Dame

- Jerome L. Novotny Design Award Honorable Mention - University of Notre Dame

- Ingersoll-Rand Engineering Scholarship - University of Notre Dame

PUBLICATIONS

<u>Journal Publications</u>

Patnaik, S., Hollkamp, J.P. and Semperlotti, F., "Applications of Variable-Order Operators: A Review", Proceedings of the Royal Society A., 476(2234):20190498, 2020. https://doi.org/10.1098/rspa.2019.0498.

Hollkamp, J.P. and Semperlotti, F., "Application of fractional-order operators to the simulation of ducts with acoustic black hole terminations", Journal of Sound & Vibration, 465:115035, 2019. https://doi.org/10.1016/j.jsv.2019.115035.

Hollkamp, J.P., Sen, M., and Semperlotti, F., "Analysis of dispersion and propagation properties in a periodic rod using a space-fractional wave equation", Journal of Sound & Vibration, 441:204 – 220, 2019. https://doi.org/10.1016/j.jsv.2018.10.051.

Hollkamp, J.P., Sen, M., and Semperlotti, F., "Model-order reduction of lumped parameter systems via fractional calculus", Journal of Sound & Vibration, 419:526 – 543, 2018. https://doi.org/10.1016/j.jsv.2018.01.011.

Sen, M., Hollkamp, J.P., Semperlotti, F., and Goodwine, B. "Implicit and fractional-derivative operators in infinite networks of integer-order components", Chaos, Solitons & Fractals, 114:186– 192, 2018. https://doi.org/10.1016/j.chaos.2018.07.003.

<u>Journal Papers in Review</u>

Hollkamp, J.P. and Semperlotti, F., "Fractional model order reduction of discrete dynamical systems under generalized harmonic loading conditions", Submitted to: ASME Journal of Vibrations and Acoustics.

Patnaik, S., Hollkamp, J.P., Sidhardh, S. and Semperlotti, F., "Fractional Order Models for the Homogenization and Wave Propagation Analysis in Periodic Elastic Beams", Submitted to: Meccanica.

<u>Conference Papers (Peer-Reviewed)</u>

Hollkamp, J.P. and Semperlotti, F., "Fractional Calculus Models for Simulating the Reflection of Sound Waves in Ducts with Acoustic Black Hole Terminations", INTER-NOISE and NOISE-CON Congress and Conference Proceedings, New Orleans, LA, Nov. 16-20, 2020, Conference Proceeding 1, pp. 246-252(7). https://www.ingentaconnect.com/content/ince/incecp/2020/00000262/00000001/art00029.

Hollkamp, J.P., Sen, M., and Semperlotti, F., "Vibration Analysis of lumped parameter systems via fractional order models", Proceedings of SPIE Smart Structures & Nondestructive Evaluation, Portland, OR, Mar. 25-29, 2017, PAPERID-101682V. doi: 10.1117/12.2258736.

PRESENTATIONS

"Vibration analysis of lumped parameter systems via fractional order models", SPIE Smart Structures & Nondestructive Evaluation Conference, Portland, OR, Mar. 25-29, 2017.

"Vibration analysis of lumped parameter systems via fractional order models", Engineering Mechanics Institute Conference, San Diego, CA, June 4-7, 2017.

"Vibration analysis of lumped parameter systems via fractional order models", Midwest Mechanics Workshop, West Lafayette, IN, Aug. 11, 2017.

"Analysis of dispersion and propagation properties in a periodic rod via fractional wave equation", SPIE Smart Structures & Nondestructive Evaluation Conference, Denver, CO, Mar. 4-8, 2018.

"Development of fractional order models in the fields of vibrations and elastic wave propagation", NDSEG Fellows Conference, San Diego, CA, Aug. 5-8, 2019.

"Fractional Calculus Models for Simulating the Reflection of Sound Waves in Ducts with Acoustic Black Hole Terminations", NOISE-CON, New Orleans, LA, Nov. 16-20, 2020.

PROFESSIONAL AFFILIATIONS

- Society of Photographic Instrumentation Engineers

- American Society of Mechanical Engineers

- Pi Tau Sigma Mechanical Engineering Honor Society

- Tau Beta Pi National Engineering Honor Society

PROFESSIONAL SERVICE

Graduate Student Representative Committee

January 2018-December 2020 (President from June 2019 - August 2020)

Herrick Laboratories, Purdue University

- Act as an intermediary between graduate students and members of the Industrial Advisory Committee

- Coordinate and host seminar series with Industrial Advisory Committee

- Organize student-led events throughout the year

Peer-Reviewed Articles for

- Journal of Sound & Vibration

- IETE Technical Review

COMMUNITY SERVICE

Volunteer at Blessed Sacrament Church

September 2018-May 2019

- Assisted in preparing high school students to receive the sacrament of Confirmation

Volunteer at University Place

April 2016-March 2017

- Visited residents of assisted living and retirement home once a week

Volunteer for Liturgy at University of Notre Dame

September 2011-May 2015

- Served as a lector and a Eucharistic minister at Mass

COMPUTER SKILLS

Programming: MATLAB, Mathematica, Fortran

Applications: Creo, COMSOL, Microsoft Office, LaTeX, Linux OS